Ferromagnetism and interlayer exchange coupling in thin metallic films

DISSERTATION

zur Erlangung des akademischen Grades
doctor rerum naturalium

(Dr. rer. nat.)

im Fach Physik

eingereicht an der

Mathematisch-Naturwissenschaftlichen Fakultät I

Humboldt-Universität zu Berlin

von
Jochen Kienert
geboren am 16.07.1973 in Neunkirchen/Saar

Präsident der Humboldt-Universität zu Berlin:
Prof. Dr. Dr. h.c. Christoph Markschies

Dekan der Mathematisch-Naturwissenschaftlichen Fakultät I:
Prof. Dr. Lutz-Helmut Schön

Gutachter:

1. Prof. Dr. Wolfgang Nolting
2. Priv.-Doz. Dr. Bernd Esser
3. Prof. Dr. Michael Potthoff

eingereicht am: 28. März 2008
Tag der mündlichen Prüfung: 15. Juli 2008

Abstract

This thesis is concerned with the ferromagnetic Kondo lattice (s-d, s-f) model for film geometry. The spin-fermion interaction of this model refers to substances in which localized spins interact with mobile charge carriers like in (dilute) magnetic semiconductors, manganites, or rare-earth compounds. The carrier-mediated, indirect interaction between the localized spins comprises the long-range, oscillatory RKKY exchange interaction in the weak-coupling case and the short-range double-exchange interaction for strong spin-fermion coupling.

Both limits are recovered in this work by mapping the problem onto an effective Heisenberg model. The influence of reduced translational symmetry on the effective exchange interaction and on the magnetic properties of the ferromagnetic Kondo lattice model is investigated. Curie temperatures are obtained for different parameter constellations. The consequences of charge transfer and of lattice relaxation on the magnetic stability at the surface are considered. Since the effective exchange integrals are closely related to the electronic structure in terms of the density of states and of the kinetic energy, the discussion is based on the modifications of these quantities in the dimensionally-reduced case. The important role of spin waves for thin film and surface magnetism is demonstrated.

Interlayer exchange coupling represents a particularly interesting and important manifestation of the indirect interaction among localized magnetic moments. The coupling between monatomic layers in thin films is studied in the framework of an RKKY approach. It is decisively determined by the type of in-plane and perpendicular dispersion of the charge carriers and is strongly suppressed above a critical value of the Fermi energy. Finally, the temperature-dependent magnetic stability of thin interlayer-coupled films is addressed and the conditions for a temperature-driven magnetic reorientation transition are discussed.

Keywords:
Kondo lattice model, magnetic thin films, interlayer exchange coupling, ferromagnetism

Zusammenfassung

Die vorliegende Arbeit befasst sich mit dem ferromagnetischen Kondo-Gitter-Modell (s-d-, s-f-Modell) für Filmstrukturen. Die Spin-Fermion-Wechselwirkung des Modells kommt in Materialien vor, in denen lokalisierte Spins mit beweglichen Ladungsträgern wechselwirken, wie etwa in (verdünnten) magnetischen Halbleitern, Manganaten, oder Seltene-Erd-Verbindungen. Die durch die Ladungsträger vermittelte, indirekte Wechselwirkung zwischen den lokalisierten Spins reicht von der langreichweitigen, oszillierenden RKKY-Austauschwechselwirkung im Falle schwacher Kopplung bis zur kurzreichweitigen Doppelaustausch-Wechselwirkung bei starker Spin-Fermion-Kopplung.

Beide Grenzfälle werden in dieser Arbeit durch die Abbildung des Problems auf ein effektives Heisenberg-Modell erfasst. Der Einfluss von reduzierter Translationssymmetrie auf die effektive Austauschwechselwirkung und auf die magnetischen Eigenschaften des ferromagnetischen Kondo-Gitter-Modells wird untersucht. Curie-Temperaturen werden für verschiedene Parameterkonstellationen berechnet. Die Auswirkungen von Ladungstransfer und von Gitter-Relaxation auf die magnetische Oberflächenstabilität werden betrachtet. Die Diskussion bezieht sich auf die Modifizierungen der Zustandsdichte und der kinetischen Energie im dimensionsreduzierten Fall, da die effektiven Austauschintegrale eng mit diesen Größen verknüpft sind. Die Bedeutung von Spinwellen für den Magnetismus dünner Filme und an der Oberfläche wird gezeigt.

Die Interlagen-Austauschkopplung stellt ein besonders interessantes und wichtiges Beispiel der indirekten Wechselwirkung zwischen lokalisierten Momenten dar. Im Rahmen einer RKKY-Behandlung wird die Kopplung zwischen Monolagen in dünnen Filmen untersucht. Sie wird entscheidend durch die Art der ebenen und senkrechten Ladungsträgerdispersion bestimmt und ist jenseits eines kritischen Wertes der Fermi-Energie stark unterdrückt. Schließlich wird die temperaturabhängige magnetische Stabilität von interlagen-gekoppelten dünnen Filmen behandelt und die Bedingungen für einen temperaturgetriebenen magnetischen Reorientierungsübergang werden diskutiert.

Schlagwörter:
Kondo-Gitter-Modell, magnetische dünne Filme, Interlagen-Austauschkopplung, Ferromagnetismus

Contents

Chapter 1

Introduction

Magnetic ultrathin structures are receiving growing attention in both theoretical and experimental condensed-matter physics [1]. On the one hand this is caused by the fast progress in experimental growing techniques like molecular-beam epitaxy, producing ever thinner, well-defined systems of high quality. On the other hand the aspect of technological applications in the fields of nano-electronics and nano-magnetism becomes increasingly relevant. The promising field of spintronics as a combination of both [2], aspiring to extend the practical implications of magnetic ordering phenomena from data storage and sensor technology to data processing, fuels the great effort to manufacture dimensionally-reduced systems and to understand their physics from a fundamental point of view.

The scope of this thesis is twofold. First, the physical system under consideration is subject to reduced translational symmetry. This work is on magnetic films and surfaces, i.e. translational invariance is broken in one spatial direction. An ideal film or layer is obtained by cutting a slab consisting of atomic planes of some crystallographic orientation out of a perfect bulk crystal lattice. If non-identical slabs are combined a multilayer system is obtained. Secondly, this thesis deals with model considerations based on the many-body theory of magnetism. The central interest of the present work is the coupling and collective ordering of localized magnetic moments in thin films and at surfaces.

Spontaneous magnetic order has been a very active field of research in solid-state physics for a long time. Starting with the Ising model [3] and with effective theories like the Weiss mean-field theory for the ferromagnet, a first step towards a more realistic theoretical description was achieved with the quantum mechanical Heisenberg model [4]. The origin of the magnetic moment of an atom has been known since Dirac's relativistic derivation of the electron spin and the spin-orbit coupling, and a microscopic many-body Hamiltonian for a crystal lattice could be readily formulated. However, it is impossible to solve the problem in the general case due to the enormously large number of degrees of freedom.

The Density Functional Theory (DFT) in the Local-Density Approximation (LDA) has turned out to be a very useful tool for computing ground-state properties of realistic many-particle systems. The Coulomb interactions, however, are not adequately taken into account for strongly correlated electrons. In order to obtain transport and finite-temperature properties and to have more transparent physical pictures governing the magnetic and other properties of a strongly correlated many-body system, it is indispensable to resort to model considerations. It goes without saying that these models must be sufficiently simple in order to be as much analytically tractable as possible but must still contain all essential interactions which govern the effects to be explained. A prominent example of such a many-body model is the Hubbard model. It allows to investigate the interplay between kinetic energy, lattice structure, Pauli's principle, and (a selected but essential part of) the Coulomb interaction and has been intensively employed for studying magnetic order in the $3d$-transition metals Fe, Co or Ni, the metal-insulator transition in transition-metal oxides, and high-T_{C} superconductivity.

This work is concerned with the Kondo lattice (s-d-, s-f-) model (KLM) for reduced translational symmetry. In contrast to the purely fermionic Hubbard model, the Kondo lattice is a coupled spin-fermion system. In its simplest form it comprises non-degenerate, s-like conduction electrons which interact with localized spins of quantum number S via a local spin interaction of the type

$$-J\mathbf{S}\cdot\boldsymbol{\sigma}\,. \tag{1.1}$$

The spin operators denote the localized and the conduction electron spin, respectively. J is an effective interaction strength which results from some coupling mechanism. It corresponds to the on-site part of the s-d-exchange interaction, also referred to as kinetic-exchange interaction, introduced by Zener to model the magnetism in transition metals like Mn [5]. Here, the effective spin coupling is due to the Coulomb interaction between s-like conduction electrons and d-like core electrons. The weak-coupling limit is known as the RKKY theory of indirect exchange interaction between d-shell moments first discussed by Kasuya [6] and Yosida [7].

The spin-fermion coupling (1.1) is one of the most intensively studied model interactions in current solid-state research. It refers to a variety of different material classes and phenomena, some of which are summarized in the following. A more detailed account of ways to treat the many-body problem associated with (1.1) is given in Chapter 2.

Magnetic $4f$-systems

(1.1) has been used in connection with the so-called magnetic $4f$-systems and is usually known as s-f-interaction in this context [8]. The well-shielded and partially filled $4f$-shell gives rise to a strongly-localized permanent magnetic moment due to the Hund's rule alignment of the $4f$-electron spins. Some kind of exchange interaction among these localized spins leads to spontaneous magnetic order below a critical temperature. Well-known examples of magnetic $4f$-systems are the rare-earth metals Gd, Tb, Dy and the Europium chalcogenides EuX (X=O, S, Se, Te), the latter belonging to the class of magnetic semiconductors. The ferromagnetic semiconductor EuO became famous in 1964 when a red shift of the absorption edge of the optical $4f$-$5d_{t_{2g}}$-transition was found by Wachter [9] and by Busch et al. [10]. This shift can be obtained already in a mean-field treatment of (1.1) and is a direct consequence of the strong influence of the intra-atomic spin coupling on the electronic structure in $4f$-systems [11]. The magnetism in metallic rare earths such as Gd is RKKY-like, i.e. is mediated by the conduction electrons [12, 13, 14]. Since Gd has a half-filled f-shell the localized spin has the magnitude S=7/2.

Manganites

Transition metal oxides like La_{1-x}Ca_xMnO_3 (manganites, manganese perovskites) have attracted considerable attention in the last years due to the colossal magnetoresistance near the ferromagnetic transition temperature [15, 16]. The mother compound LaMnO_3 is an insulator consisting of antiferromagnetic planes. Upon doping ($x > 0$) one observes a conducting ferromagnetic state below a critical temperature which has a maximum as a function of x. For higher doping the system becomes an antiferromagnetic insulator again. The importance of electron-phonon coupling [16, 17, 18] and of orbital degeneracy [16, 19, 20, 21] for the physics of manganites has been emphasized. Despite the apparently complicated structure of the full Hamiltonian and of its phase diagrams, the crucial exchange interaction to account for the magnetism of this class of materials is believed to be of the type (1.1). The five-fold degenerate Mn-3d-level is split by the crystal field into a threefold degenerate t_{2g}-state and a twofold degenerate e_g-state. By the earth alkali doping, Mn^{4+}-ions are present in addition to the Mn^{3+}-ions of the mother compound. Three of the resulting average $4 - x$ electrons per site fill the energetically lower t_{2g}-states and form a rather localized Hund's-rule S=3/2-spin state. The remaining $1-x$ electrons per site occupy the e_g-states and interact ferromagnetically with the localized spins, again due to Hund's rules coupling. The hopping of the Mn-e_g-electrons between Mn^{3+}- and Mn^{4+}-ions in the crystal lattice is made possible by the double-exchange mechanism via the O-p-states which was introduced by Zener [22, 23]. For this reason the model including the interaction

(1.1) is often referred to as double-exchange model in connection with the manganites. Since the ferromagnetic coupling between the localized and the conduction electron spin is quite strong, the double-exchange model actually corresponds to the strong-coupling limit ($J \to \infty$) of (1.1). A parallel alignment of the localized magnetic moments is favored because it increases the hopping probability of the mobile charge carriers and therefore decreases their kinetic energy.

Dilute magnetic semiconductors

Dilute (ferro)magnetic semiconductors (DMS) are among the most interesting systems as concerns the combined manipulation of charge and spin degrees of freedom (for a review on (III,Mn)V systems see Ref. [24]). The interest in these substances was triggered by the discovery of a Curie temperature as high as 110 K in (Ga,Mn)As by Ohno and co-workers [25]. The driving mechanism behind the ferromagnetic order was readily identified as charge-carrier (hole) mediated. In (Ga,Mn)As, which has been the focus of attention in many experimental and theoretical studies of DMS systems since then, the Mn-impurities act both as acceptors and localized magnetic moments. The microscopic source of the ferromagnetism was traced back to an antiferromagnetic coupling between valence-band holes of As-4*p*-character and the five aligned Mn *d*-electrons forming a localized S=5/2-spin due to a spin-dependent hybridization similar to the Zener kinetic-exchange interaction. In a simplified form this corresponds to the spin-exchange interaction (1.1). For high Mn-doping, corresponding to the metallic limit of (Ga,Mn)As, a lot of theoretical approaches have been based on the Zener model and its weak-coupling RKKY limit [24, 26, 27, 28, 29, 30, 31, 32, 33]. On the other hand, for low doping, and in general for wider-gap (III,Mn)V-materials like (Ga,Mn)N, there are indications that the *p*-*d*-exchange is rather strong and the double-exchange mechanism prevails [24]. The important role of defects and disorder must be strongly emphasized in the context of DMS [34, 35, 36, 37]. One of the key issues in the field of ferromagnetic semiconductors is the quest for higher Curie temperatures. With regard to the electrical and optical control of ferromagnetism in future device applications, the dependence of ferromagnetism on the charge carrier density is of particular interest.

The sign of the intra-atomic exchange coupling J in (1.1) plays a very important role. For $J < 0$, an antiparallel coupling of the localized spin and the electron spin is favored, and one may therefore speak of the 'antiferromagnetic Kondo lattice model' when considering (1.1) on a lattice and supplementing it with a kinetic part. The antiferromagnetic KLM corresponds to the periodic generalization of the Kondo model which describes the interaction of a single impurity spin with an uncorrelated conduction band. The Kondo (lattice) problem is closely connected with heavy-fermion systems - as the name suggests these are strongly correlated systems characterized by an exceptionally high effective electron mass - and has been the subject of intense research in condensed-matter physics for the past decades [38]. One of the key issues here is the interplay between RKKY coupling and spin screening effects. The latter are responsible for the resistivity minimum in dilute magnetic alloys ('Kondo effect').

The present work exclusively deals with a positive (ferromagnetic) exchange coupling ($J > 0$) favoring a parallel alignment of the spins in (1.1). For the sake of clarity the expression 'ferromagnetic Kondo lattice model' should be used, however the adjective 'ferromagnetic' will be omitted later. A positive exchange coupling refers to Gd and manganese perovskite compounds. Some considerations in this thesis are based on the conventional RKKY picture. In this case, the sign of the intra-atomic coupling J does not play a role.

As regards the aspect of reduced dimensionality, a further model parameter, namely the number of monatomic layers of a film, comes into play. The lost translational invariance leads to a layer-dependence of all observables, in particular of the density of states. The presence of a surface imposes a restriction on the charge carrier hopping and gives rise to a reduced effective bandwidth of the surface layer. Generally, one can therefore expect the surface layers to be governed to a greater extent by strong-coupling physics than the inner layers.

There has been growing interest recently in (ultra)thin films, layered structures, or the surface of materials in which (1.1) is assumed to play an important role. In connection with dimensionally reduced $4f$-systems, a possible magnetic Gd(0001)-surface transition and electronic surface states have been discussed vividly. The issue is not finally settled: while there has been experimental evidence of surface magnetic order up to 85 K above the bulk transition [39, 40, 41, 42], other works have not found any [43, 44]. Regarding the theoretical description, some authors have proposed results in favor of an enhanced magnetic order at the surface [45, 46, 47]. Furthermore, the thickness dependence of the Curie temperatures and the anisotropy of thin Gd-films have been studied both experimentally [48, 49, 50, 51, 52, 53] and theoretically [54].

Concerning dilute magnetic semiconductors, strongly confined local-moment systems like quantum wells draw increasing attention. The physical properties of quantum wells, and likewise of ultrathin 'freestanding' films representing quantum-well systems with infinitely high potential barriers, are very sensitive to geometric modulation. Ferromagnetism and spin waves have been investigated theoretically in DMS quantum wells in Refs. [55, 56, 57, 58, 59, 60]. The RKKY exchange interaction was studied between magnetic impurities within a single quantum well [61] and between magnetic impurities located in a (Ga,Mn)As/GaAs double well [62].

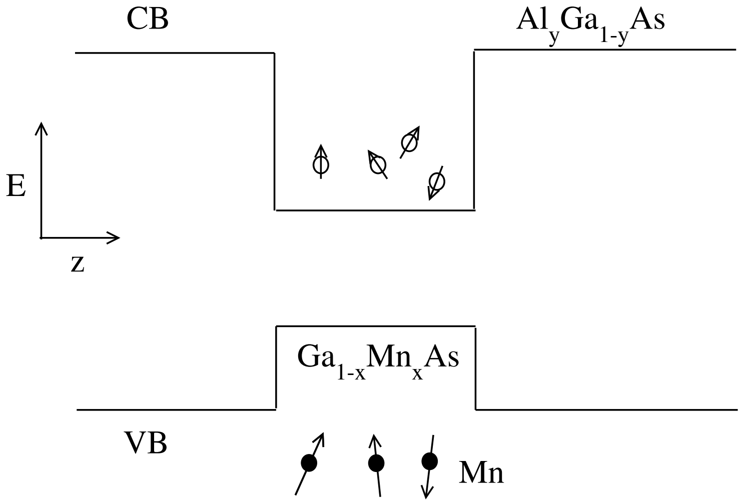

Figure 1.1: Sketch of a quantum-well system with localized Mn-moments and confined conduction-band electrons.

A disordered lattice mean-field RKKY theory was proposed for a DMS monolayer in Ref. [32].

So-called digital ferromagnetic heterostructures can be grown by incorporating monolayer planes of MnAs into GaAs using molecular-beam epitaxy ('δ-doping') [63]. Ferromagnetic order was observed over large distances between the Mn-layers. Confined III-V heterostructures like (Ga,Mn)As/(Al,Ga)As (Fig. 1.1) with δ-doped Mn-planes have attracted particular attention due to a confinement-induced increase of the Curie temperature [64, 65, 66, 67]. In addition, they are highly interesting because the density of the magnetic ions and of the itinerant charge carriers can be modulated independently. The quantum confinement may also modify the sign of the conduction-band exchange-coupling constant [68].

Moreover, interlayer exchange coupling (IEC) between ferromagnetic layers separated by a non-magnetic spacer was studied in DMS-systems [29, 69, 70, 71, 72]. The IEC is an important quantity since it determines the relative orientation of the magnetization of the coupled layers and thereby governs the spin-dependent electrical transport properties. It was first detected in Fe/Cr/Fe [73, 74] and has been investigated in a variety of different materials since then. Chapter 7 contains a more detailed introduction to IEC. The sensitive dependence of the transport properties on the magnetic configuration is known as the giant magnetoresistance effect (GMR) and was discovered independently by Grünberg and Fert (Nobel Prize 2007) two decades ago [75, 76, 77]. Today, the standard technology used in magnetic data-storage media is based on the GMR-effect.

Theoretical approaches to thin film and surface magnetism in general, and particularly in KLM-type systems, are dominated by localized-spin Heisenberg-like models [45, 54, 78, 79, 80, 81, 82, 83, 84, 85]. Early studies on surface magnetism based on the Landau-mean-field theory [86, 87, 88, 89] yielded a reduced surface magnetization which depends rather linearly on temperature (more details on the mean-field theory are given in Chap. 6.6). Although the localized-spin picture is generally adequate for the Kondo lattice model, it is desirable to keep the hybrid local-moment/itinerant character of the problem. There seem to be only few works which take the itinerant character of the charge carriers explicitly into account, most of them focussing on rather specific aspects of the magnetism or of the exchange coupling in Kondo lattice films [90, 91, 92, 93]. This is surprising because one of the most interesting aspects of (1.1) in connection with a finite charge carrier density is the mutual dependence between the layer-dependent electronic structure and the carrier-mediated magnetic properties.

Within mean-field treatments, spin wave excitations are neglected from the outset. Non-local spin correlations, however, are expected to be more important in lower dimensions where the mean-field picture generally becomes less reliable due to the decreased effective coordination number. Spin fluctuations even exclude magnetic order for finite temperatures in 1D- and 2D- systems with isotropic interactions (Mermin-Wagner theorem) [94, 95]. Furthermore, they were shown to be important for coupling phenomena in layered structures [96, 97, 98]. Taking spin wave excitations into account is therefore a central concern of the present work on Kondo lattice films.

This thesis treats ideal, single-orbital Kondo lattice model films. It is clear that using a simplified band structure, neglecting other interactions apart from (1.1), and ignoring disorder effects forbids a quantitative comparison with experiments. The intention is rather to study the effects of reduced dimensionality on the electronic and magnetic properties and on the effective local-moment interaction originating from (1.1). It is thus necessary to disregard other factors which may possibly obscure these effects in a first step before making the model more realistic by including further interactions or disorder. The investigations are carried out for the ferromagnetic and the paramagnetic phase of the KLM. It is the ferromagnetic, conducting phase which is relevant for Gd [99], which dominates large parts of the phase diagrams of the manganites [16], and which is the phase of primary interest in DMS systems [24].

The structure of the thesis is as follows. In Chapter 2 the Kondo lattice Hamiltonian is first introduced in detail. Then some technical aspects are addressed. The single-electron Green function is briefly discussed and important quantities and relations are listed for reference. A short survey of exact results and approximative approaches is given. Two exactly solvable limits, the zero-bandwidth limit and the ferromagnetically saturated semiconductor, are discussed.

Chapter 3 summarizes the notation and the physical quantities for film geometry. It closes with a short discussion of the one-particle excitation spectrum of non-interacting Kondo lattice films.

In Chapter 4 some approximative solutions for the single-electron Green function in the interacting case are given. One of these approaches, an equation-of-motion approach based on a physically motivated decoupling scheme, is then used to calculate the one-particle excitation spectrum. The temperature-dependent electronic density of states and the spectral density of Kondo lattice films are discussed. The chapter concludes with an analysis of charge transfer.

Chapter 5 focusses on the local-moment subsystem. A modified RKKY approach is presented which maps the spin-fermion interaction (1.1) onto an effective Heisenberg Hamiltonian with exchange integrals that depend on the spin-dependent electronic structure. A uniaxial magnetic anisotropy is introduced and the transversal spin Green function is obtained by a combined RPA and Anderson-Callen theory for the exchange and anisotropy terms, respectively. The method is generalized to arbitrary orientations of the magnetizations by a layer-dependent rotation of the local frame.

The effective localized-spin Hamiltonian is used in Chapter 6 to calculate the layer-dependent local-moment magnetization and the Curie temperature of Kondo lattice films. The second part concentrates on exchange interactions and ferromagnetism at the film surface. Charge transfer and relaxation effects on the ferromagnetic stability are discussed and interpreted in terms of the modified electronic structure of the surface layers. The importance of spin wave excitations for a proper treatment of surface magnetism becomes evident in the investigation of the ferromagnetic order for an enhanced surface exchange interaction.

The last chapter treats the problem of interlayer exchange coupling in thin Kondo lattice films. Using conventional RKKY theory the IEC between confined monatomic layers is studied focussing on the carrier-density dependence. The second part deals with the temperature dependence of the interlayer coupling for a parallel and for an antiparallel alignment of two ferromagnetic layers. In particular, the influence of the spacer and of the magnetic layer thickness are analyzed. Finally, the conditions for a temperature-induced magnetic reorientation transition are explored.

Chapter 2

Kondo lattice (*s-d, s-f*) model

The model Hamiltonian for the Kondo lattice is now introduced in detail. As the many-body problem is treated using Green functions in this work, some basic quantities and relations are listed for reference. For more detailed accounts of Green functions see Refs. [100, 101, 102, 103, 104]. In the third section of this chapter, several rigorous results and approximative treatments of the model are summarized. Finally, two analytically solvable limits are presented that give insight into the elementary excitations. Film geometry and the notation for reduced translational symmetry will be introduced in the next chapter.

2.1 Model Hamiltonian

In its simplest form the Kondo lattice Hamiltonian consists of a non-degenerate, s-like conduction band and an intra-atomic interaction term which accounts for the coupling between the itinerant electron spin and the localized spin:

$$H_{\mathrm{KLM}} = H_0 + H_I \tag{2.1}$$

$$H_0 = -\sum_{ij\sigma}(t_{ij} + \mu\delta_{ij})c^\dagger_{i\sigma}c_{j\sigma} \tag{2.2}$$

$$H_I = -J\sum_i \mathbf{S}_i \cdot \boldsymbol{\sigma}_i \tag{2.3}$$

$$= -\frac{1}{2}J\sum_{i\sigma}\left(z_\sigma S^z_i n_{i\sigma} + S^{-\sigma}_i c^\dagger_{i\sigma}c_{i-\sigma}\right) \ . \tag{2.4}$$

$c^{(\dagger)}_{i\sigma}$ annihilates (creates) a Wannier electron of spin $\sigma =\uparrow,\downarrow$ on the lattice site $\mathbf{R}_i$ and $n_{i\sigma} = c^\dagger_{i\sigma}c_{i\sigma}$ is the particle density operator. $\boldsymbol{\sigma}_i$ and $\mathbf{S}_i$ are the electron and the localized spin operator, respectively. In order to obtain (2.4) the electron spin operator was rewritten according to

$$\sigma_i^{\uparrow} = c_{i\uparrow}^{\dagger} c_{i\downarrow}, \;\; \sigma_i^{\downarrow} = c_{i\downarrow}^{\dagger} c_{i\uparrow}, \;\; \sigma_i^z = \frac{1}{2}(n_{i\uparrow} - n_{i\downarrow}) \tag{2.5}$$

using $z_{\uparrow} = +1$, $z_{\downarrow} = -1$ ($\hbar$ is set to unity from now on). The raising ('$\uparrow$' or '+') and lowering ('$\downarrow$' or '$-$') operators are defined as

$$\sigma_i^{\sigma} = \sigma_i^x + \mathrm{i} z_{\sigma} \sigma_i^y, \qquad S_i^{\sigma} = S_i^x + \mathrm{i} z_{\sigma} S_i^y\,. \tag{2.6}$$

The first term of H_I represents an Ising-like interaction between the z-components of the spins and the second term describes spinflips.

t_{ij} is the hopping amplitude from site i to site j. In the tight-binding approximation [105] used throughout this work, only nearest-neighbor (nn) hopping (i.e. between adjacent lattice sites) is considered:

$$t_{ij} \longrightarrow t_{\langle ij \rangle} \equiv t\,. \tag{2.7}$$

The chemical potential μ fixes the particle density $n = \sum_{\sigma} \langle n_{i\sigma} \rangle$.

The fundamental (anti-)commutator rules reflect the quite different nature of the two subsystems in (2.1). For the fermions the anticommutator relations read

$$\left[c_{i\sigma}, c_{j\sigma'}^{\dagger}\right]_+ = \delta_{ij}\delta_{\sigma\sigma'}, \qquad \left[c_{i\sigma}, c_{j\sigma'}\right]_+ = \left[c_{i\sigma}^{\dagger}, c_{j\sigma'}^{\dagger}\right]_+ = 0 \tag{2.8}$$

while the spin operators obey the angular momentum commutator rules

$$\left[S_i^{\alpha}, S_j^{\beta}\right]_- = \mathrm{i}\epsilon_{\alpha\beta\gamma}\delta_{ij} S_i^{\gamma} \qquad (\alpha, \beta, \gamma = x, y, z)\,. \tag{2.9}$$

$\epsilon_{\alpha\beta\gamma}$ is the third-rank totally antisymmetric unit tensor.

It may be necessary to take additional interactions in a Kondo lattice system into account. Examples of these are antiferromagnetic exchange interactions between the localized spins or the intra- and interband Coulomb matrix elements in manganite systems [16, 106, 107, 108].

Heisenberg interaction

The interaction term (2.3) represents the on-site coupling between a localized and an itinerant spin. The same bilinear form of the interaction, however referring to the non-local coupling among localized magnetic moments, defines the well-known Heisenberg model [4, 109, 110]:

$$H_{\mathrm{H}} = -\sum_{ij} J_{ij} \mathbf{S}_i \mathbf{S}_j\,. \tag{2.10}$$

This Hamiltonian is often employed to model the magnetism of insulators containing localized magnetic moments due to incompletely filled shells [11, 111]. In case of ferromagnetic coupling $J_{ij} > 0$ the ground state corresponds to a parallel alignment of all spins. Low-temperature excitations from this ground state can be described by spin wave theory [112, 113]. A spin wave (magnon) is a collective excitation which reduces the total angular momentum by $\hbar$.

Hubbard interaction

If the Coulomb interaction among the conduction electrons cannot be neglected, higher-order terms in the charge carrier density must be considered. The simplest case comprises H_0 as in (2.2) and an on-site repulsive Coulomb interaction and is known as the Hubbard model [114, 115, 116]:

$$H_U = H_0 + \frac{U}{2} \sum_{i\sigma} n_{i\sigma} n_{i-\sigma} \,. \tag{2.11}$$

The Hubbard model is the most elementary model to study the magnetism and electronic correlation effects of the so-called 'band magnets' [117, 118]. In more refined versions which include additional matrix elements and combined with DFT-LDA, it has been used to describe real materials [119, 120]. Mott-Hubbard insulators represent another field of intense application of the Hubbard model [121]. The standard method to study a strongly-correlated fermionic many-body problem like (2.11) is the Dynamical Mean Field Theory (DMFT) [122, 123, 124, 125]. DMFT relies on the fact that the self-energy of correlated lattice fermions does not depend on the quasi-momentum in infinite dimensions ($D = \infty$).

2.2 One-particle Green function

The retarded Green function (GF) is defined as

$$G^{\mathrm{ret}}_{AB}(t,t') = -\mathrm{i}\Theta(t-t')\langle [A(t), B(t')]_{-\epsilon}\rangle \,. \tag{2.12}$$

A, B are Heisenberg operators, $\epsilon = +(-)$ denotes the (anti)commutator Green function, and $\langle .. \rangle$ means the quantum statistical average (usually within the grand-canonical ensemble). The step function $\Theta(x)$ is equal to 1 for $x > 0$ and zero for $x < 0$.

Another important quantity is the spectral density,

$$S_{AB}(t,t') = \frac{1}{2\pi}\langle [A(t), B(t')]_{-\epsilon}\rangle \,, \tag{2.13}$$

which can be used to calculate correlation functions. The spectral theorem for the anticommutator spectral density ($\epsilon = -$) reads

$$\langle B(t')A(t)\rangle = \int\limits_{-\infty}^{+\infty} dE \frac{S_{AB}(E)}{\mathrm{e}^{\beta E}+1}\mathrm{e}^{-\mathrm{i}E(t-t')} \tag{2.14}$$

where the Fourier transformation

$$S_{AB}(E) = \int\limits_{-\infty}^{+\infty} d(t-t') S_{AB}(t-t')\mathrm{e}^{\mathrm{i}E(t-t')} \tag{2.15}$$

has been used. It is sometimes convenient to consider the spectral (Lehmann) representation of the spectral density:

$$S_{AB}(E) = \frac{1}{\Xi}\sum_{m,n}\langle E_n|B|E_m\rangle\langle E_m|A|E_n\rangle \mathrm{e}^{\beta E_n}\left(\mathrm{e}^{\beta E}-\epsilon\right)\delta\left[E-(E_n-E_m)\right] \,. \tag{2.16}$$

E_n and $|E_n\rangle$ are the eigenenergies and eigenstates of the considered Hamiltonian, respectively, and Ξ denotes the grand-canonical partition function. The spectral representation of the (retarded) Green function is as follows:

$$G_{AB}(E) \equiv \langle\langle A;B\rangle\rangle_E = \frac{1}{\Xi}\sum_{m,n}\langle E_n|B|E_m\rangle\langle E_m|A|E_n\rangle \mathrm{e}^{\beta E_n}\frac{\mathrm{e}^{\beta(E_n-E_m)}-\epsilon}{E-(E_n-E_m)+\mathrm{i}0^+} \,. \tag{2.17}$$

If the spectral density is real there is a simple relation to the Green function:

$$S_{AB}(E) = -\frac{1}{\pi}\mathrm{Im}G_{AB}(E)\,. \tag{2.18}$$

From the equation of motion for Heisenberg operators one obtains the equation of motion for the Green function:

$$\begin{aligned} E\langle\langle A;B\rangle\rangle_E &= \langle[A,B]_{-\epsilon}\rangle + \langle\langle[A,H]_-\,;B\rangle\rangle_E && (2.19)\\ &= \langle[A,B]_{-\epsilon}\rangle + \langle\langle A;[H,B]_-\rangle\rangle_E\,. && (2.20)\end{aligned}$$

It can be exploited to obtain approximative solution by decoupling higher-order Green functions.

The key quantity of interest regarding the fermionic part of the many-body problem associated with (1.1) will be the one-electron (single-electron) Green function

$$G_{ij\sigma}(E) \equiv \langle\langle c_{i\sigma}; c_{j\sigma}^{\dagger}\rangle\rangle_E = \frac{1}{2\pi}\int\limits_{-\infty}^{+\infty} d(t-t')G_{ij\sigma}(t-t')\mathrm{e}^{\mathrm{i}E(t-t')}\,. \tag{2.21}$$

From the real-space (Wannier) representation of the construction/annihilation operator the (Bloch) representation in reciprocal space is obtained using Fourier transformation:

$$c_{i\sigma}^{(\dagger)} = \frac{1}{\sqrt{N}}\sum_{\mathbf{k}} \mathrm{e}^{(-)\mathrm{i}\mathbf{k}\mathbf{R}_i} c_{\mathbf{k}\sigma}^{(\dagger)}\,. \tag{2.22}$$

$\mathbf{R}_i$ is a vector referring to the ith of N sites composing a Bravais crystal lattice, and the sum is over all wave vectors of the first Brillouin zone. With (2.22) the Fourier transform of (2.21) reads

$$G_{\mathbf{k}\sigma}(E) \equiv \langle\langle c_{\mathbf{k}\sigma}; c_{\mathbf{k}\sigma}^{\dagger}\rangle\rangle_E = \frac{1}{N}\sum_{ij} \mathrm{e}^{-\mathrm{i}\mathbf{k}(\mathbf{R}_i-\mathbf{R}_j)} G_{ij\sigma}(E)\,. \tag{2.23}$$

Similarly, the Bloch energy dispersion $\epsilon(\mathbf{k})$ is given by the Fourier-transformed hopping integrals:

$$\epsilon(\mathbf{k}) = -\frac{1}{N}\sum_{ij} \mathrm{e}^{-\mathrm{i}\mathbf{k}(\mathbf{R}_i-\mathbf{R}_j)} t_{ij}\,. \tag{2.24}$$

The conduction electron bandwidth is defined as $W = \epsilon_{max} - \epsilon_{min}$. For the simple-cubic 3D-lattice the tight-binding dispersion reads

$$\epsilon(\mathbf{k}) = -2t\left[cos(k_x a) + cos(k_y a) + cos(k_z a)\right] \tag{2.25}$$

where a is the lattice constant.

The equation of motion (2.19) for the one-electron anticommutator Green function (2.23) using the Hamiltonian (2.1) reads

$$EG_{\mathbf{k}\sigma}(E) = 1 + \langle\langle [c_{\mathbf{k}\sigma}, H_0 + H_I]_-\,; c_{\mathbf{k}\sigma}^{\dagger}\rangle\rangle_E\,. \tag{2.26}$$

Defining the self-energy $M_{\mathbf{k}\sigma}$ as

$$\langle\langle [c_{\mathbf{k}\sigma}, H_I]_-\,; c_{\mathbf{k}\sigma}^{\dagger}\rangle\rangle_E = M_{\mathbf{k}\sigma}(E)G_{\mathbf{k}\sigma}(E)\,, \tag{2.27}$$

(2.26) can be formally solved:

$$G_{\mathbf{k}\sigma}(E) = \frac{1}{E + \mu - \epsilon(\mathbf{k}) - M_{\mathbf{k}\sigma}(E) + \mathrm{i}0^+}\,. \tag{2.28}$$

With the non-interacting Green function

$$G^{(0)}_{\mathbf{k}\sigma}(E) = \frac{1}{E + \mu - \epsilon(\mathbf{k}) + \mathrm{i}0^+}\,, \tag{2.29}$$

(2.28) is equivalent to Dyson's equation:

$$G_{\mathbf{k}\sigma}(E) = G^{(0)}_{\mathbf{k}\sigma}(E) + G^{(0)}_{\mathbf{k}\sigma}(E) M_{\mathbf{k}\sigma}(E) G_{\mathbf{k}\sigma}(E)\,. \tag{2.30}$$

Summing the single-electron spectral density over $\mathbf{k}$ yields the spin-dependent local density of states (LDOS):

$$\rho_\sigma(E) = \frac{1}{N}\sum_{\mathbf{k}} S_{\mathbf{k}\sigma}(E-\mu) = -\frac{1}{\pi N}\sum_{\mathbf{k}} \mathrm{Im} G_{\mathbf{k}\sigma}(E-\mu)\,. \tag{2.31}$$

By applying the spectral theorem (2.14) one obtains the average occupation of a site in a translationally invariant lattice (charge carrier density, band filling),

$$n \equiv \langle n \rangle = \langle n_i \rangle = \langle n_{i\uparrow} \rangle + \langle n_{i\downarrow} \rangle\,, \tag{2.32}$$

by integration of the LDOS:

$$\langle n_\sigma \rangle = \langle c^\dagger_{i\sigma} c_{i\sigma} \rangle = \int\limits_{-\infty}^{+\infty} dE f_-(E) \rho_\sigma(E)\,. \tag{2.33}$$

$f_-(E)$ denotes the Fermi-Dirac distribution function,

$$f_-(E) = \frac{1}{\mathrm{e}^{\beta(E-\mu)} + 1}\,, \tag{2.34}$$

with the inverse temperature $\beta = 1/k_{\mathrm{B}}T$.

The (central) moments of the spectral density ('spectral moments')

$$m^{(n)}_{\mathbf{k}\sigma} = \int\limits_{-\infty}^{+\infty} dE E^n S_{\mathbf{k}\sigma}(E) \quad (n = 0,\, 1,\, 2, ..) \tag{2.35}$$

can be computed equivalently via

$$m^{(n)}_{\mathbf{k}\sigma} = \frac{1}{N}\sum_{ij} \mathrm{e}^{-\mathrm{i}\mathbf{k}(\mathbf{R}_i - \mathbf{R}_j)} \langle \Big[\big[.. \left[c_{i\sigma}, H \right]_- .., H \big]_- , c^\dagger_{j\sigma} \Big]_+ \rangle\,, \tag{2.36}$$

including an n-fold commutator with the Hamiltonian. The spectral moments are closely related to the high-energy expansion of the Green function:

$$G_{\mathbf{k}\sigma}(E) = \sum_{n=0}^{\infty} \frac{m^{(n)}_{\mathbf{k}\sigma}}{E^{n+1}}\,. \tag{2.37}$$

The above relations for the moments may be exploited to devise approximations by constructing an ansatz for the single-electron Green function and then fitting the parameters using (2.36) and (2.37). This method has been applied to the Kondo lattice model (see Chap. 4.2) [126, 127], the Hubbard model [128, 129, 130] and the periodic Anderson model [131].

2.3 Rigorous results and approximative methods

Exact statements

While the majority of exact treatments has focussed on the antiferromagnetic KLM, in particular in one dimension ($D = 1$), [132, 133, 134, 135, 136], some rigorous statements have been made for the ferromagnetic Kondo lattice model. For $S = 1/2$, besides the trivial result that the ground state in $D = 1$ for one conduction electron forms a completely saturated ferromagnet with $S_{tot} = (N + 1)/2$ [132], it was proven for a half-filled conduction band that the ground state is unique and antiferromagnetic (a total spin singlet) for both positive and negative J on a bipartite lattice of any dimension [137]. For intermediate conduction band occupation $0.12 < n < 0.45$ it was shown by means of a variational approach that the totally saturated ferromagnetic state for $S = 1/2$ is unstable against single-particle spin-flip excitations even for $J \to \infty$ on a simple-cubic lattice in $D = 3$ [138]. The excitation spectra of two solvable limits, the zero-bandwidth limit and the ferromagnetically saturated semiconductor, are discussed in Secs. 2.4 and 2.5.

Perturbative approaches

The hybrid character of the Hamiltonian (2.1) prohibits a direct application of standard diagrammatic perturbation theory in the interaction parameter based on Wick's theorem [139]. Attempts in this direction by using a generalized Wick theorem could not establish an accepted formalism [140, 141]. The localized spins, however, allow for an $1/S$-expansion which has been employed to obtain the spin wave excitation spectrum in the strong-coupling limit [142, 143, 144, 145]. In the $1/S$-expansion, the localized spins are bosonized using the Holstein-Primakov transformation [112] and the KLM Hamiltonian (2.1) is rewritten in powers of $1/S$ by means of a suitable unitary transformation. A proposal to treat the electronic and the spin subsystem formally on the same footing uses projection operator techniques [146, 147]. This method yields a second-order weak-coupling theory in J for the electronic self-energy [126, 127, 148, 149].

Conventional Schrödinger perturbation theory for a Hamiltonian of the form (2.1) in the weak-coupling regime $JS/W \ll 1$ leads to an effective spin Hamiltonian. The exchange integrals of this so-called Ruderman-Kasuya-Kittel-Yosida

(RKKY) interaction [6, 7, 150] essentially correspond to the free electron gas susceptibility and have long-range oscillatory character. A more detailed discussion of the RKKY interaction is given in Chap. 5. Standard RKKY theory has been studied extensively in all dimensions for homogeneous and inhomogenous situations, see e.g. Refs. [61, 62, 151, 152, 153, 154, 155, 156, 157, 158]. It is believed to play a crucial role for the magnetic properties of various systems. Besides the heavy-fermion compounds these are the 'normal' rare-earth materials like Gd [13, 14]. More recently the RKKY interaction has attracted renewed interest in connection with dilute magnetic semiconductors. While several authors promote its relevance for the magnetism in these materials [24, 26, 27, 31, 32, 33, 37], this is disputed by others [159, 160].

RKKY theory was used to model one of the first observations of interlayer exchange coupling between ferromagnetic layers separated by a non-magnetic spacer layer, namely in Gd/Y multilayers [161, 162, 163, 164]. Chap. 7 presents a discussion of the interlayer exchange coupling in thin Kondo lattice films using conventional RKKY theory as well as a modified version. The latter accounts for the exchange splitting of the conduction band in the ferromagnetic phase.

Non-perturbative approaches

Before commenting on the methods used in this work, a short summary of other approximative treatments of the KLM shall be given.

The application of DMFT to the Kondo lattice was pioneered by Furukawa [165, 166, 167] who calculated the one-particle excitation spectrum, transport properties, and other thermodynamical quantities in the double-exchange limit ($J \to \infty$). Assuming a local self-energy, one can treat the lattice problem as an effective single-site problem. Similar to the mean field of the Weiss theory for a ferromagnet, the degrees of freedom of all other lattice sites are put into an effective (Weiss-)propagator, which together with the local self-energy forms an impurity problem. On the other hand the single-site Green function of the impurity problem can be calculated from the effective action resulting from the Weiss-field and the on-site interaction. In the case of the KLM this is usually achieved using Monte Carlo techniques. Identifying the local lattice Green function with the single-site impurity Green function and calculating the average value of the localized spin by integration over the directions of the (classical) spin vector, one has a closed system of dynamical mean-field equations which can be iterated until self-consistency is reached [124, 165, 166, 168].

DMFT was subsequently employed extensively for studying the transition temperature [106, 169, 170, 171], the optical conductivity [106, 169, 170], the magnetic phase diagram [172, 173, 174, 175, 176], and superlattices [177] in manganite systems using the single- or double-band Kondo lattice model without or including

Coulomb correlations [106] (see also [168]). It was also used to investigate ferromagnetism and transport in dilute magnetic semiconductor systems [178, 179, 180]. Based on DMFT, the magnetic susceptibility including the local-moment and electronic susceptibility as well as the cross terms has been evaluated, and transition temperatures and magnetic phases have been obtained [181, 182, 183].

A common feature to all of the above works is the assumption of classical spins ($S \to \infty$), which significantly facilitates the formulation of the DMFT for the Kondo lattice. In view of the fact that the localized spins in the manganites have the magnitude $S = 3/2$ one may raise the question if this assumption is justified. At least for $S = 1/2$ a marked influence of quantum spins has been found in the one-particle excitation spectrum using DMFT based on a fermionization of the localized spins [148]. In particular, a finite $\downarrow$-scattering spectral weight below the Fermi energy leads to an incomplete polarization of the conduction band in the ferromagnetic state. This finding is corroborated also for $S > 1/2$ by other approaches which take the quantum character of the localized spins into account and which were put forward by Nolting and co-workers [107, 126, 127, 148, 184, 185, 186]. Classical spins suppress spinflips that are inherent to the Hamiltonian (2.1) and therefore the ferromagnetic ground state is always completely polarized (see e.g. [166]). While some other authors find a fully polarized conduction band at $T = 0$ for certain parameter constellations [187], there are analytical results [138] as well as numerical indications [188] which stress an incomplete polarization. This point is discussed further in Chap. 4.4.

As far as magnetism for $T = 0$ in the strong-coupling limit is concerned, there is numerical evidence in $D = 1$ that the influence of the quantum nature for $S = 3/2$ is not very important [172, 173]. This is corroborated and found to hold also in higher dimensions by the magnetic phase diagrams using quantum spins proposed by Kienert and Nolting [189]. Here, the internal energy was calculated using the approach of Chap. 4.3. Fig. 2.1 shows the phase diagram for the square lattice ($D = 2$) including the paramagnetic, ferromagnetic, and ferromagnetic/antiferromagnetic phase-separated states. For comparison the results of other methods are also shown. The special case $S = 1/2$ exhibits an instability of the ferromagnetic state with respect to paramagnetism for intermediate charge densities. For $S = 3/2$ and classical spin there is a stable FM ground state over a wide range of band fillings n and a phase-separated region near half-filling. The FM state evolves to higher band fillings as the coupling strength increases. An important result is that the phase boundaries for $S = 3/2$ and $S \to \infty$ do not differ much. This gives support to the usage of classical localized spins when modelling the manganites, at least as far as the magnetic stability at low temperatures is concerned.

In a very recent work, DMFT using the Numerical Renormalization Group

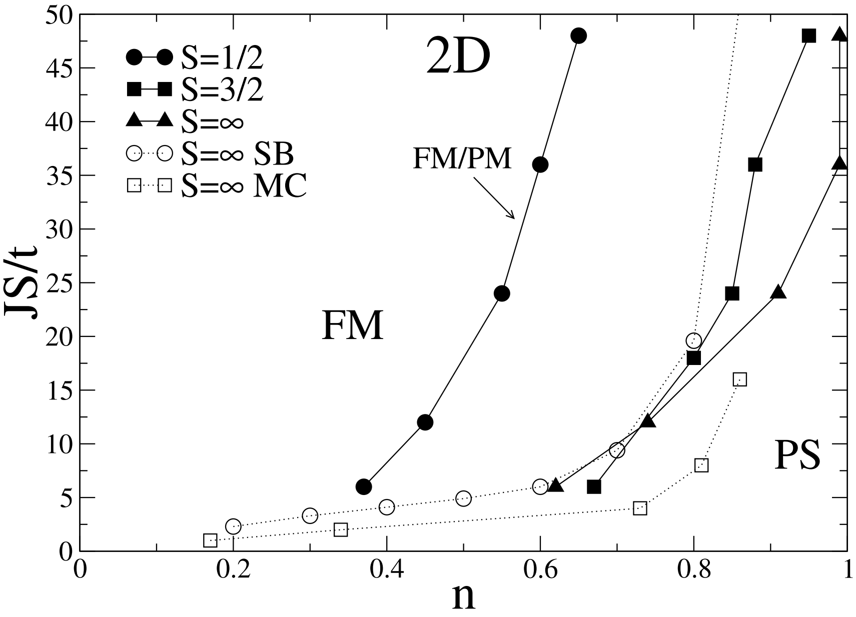

Figure 2.1: Ground-state phase diagram for $S = 1/2$, $S = 3/2$, and classical spin (square lattice). Open circles from Ref. [191] ($S = \infty$) indicate the boundary between the FM state and FM/AFM-phase separation above $JS/t \approx 7$ and between FM and a spiral phase at weaker coupling. SB stands for the Schwinger-boson approach. The open squares denoting the Monte Carlo results of Ref. [172] ($S = \infty$) mark the transition from FM to FM/AFM-phase separation above $JS/t \approx 4$ and from FM to incommensurate order for weaker coupling. Lines are guides to the eye (from Ref. [189]).

(NRG) as an impurity solver was applied to the correlated ferromagnetic and antiferromagnetic Kondo lattice model with quantum spins [190]. The discussion of the collinear magnetic phases, however, is restricted to $S = 1/2$. The FM state is found to be unstable with respect to an undetermined magnetic phase for moderate coupling at $n \approx 0.45$, consistent with the instability of the FM phase observed in Fig. 2.1. In order to throw more light on the issue of classical versus quantum spins, further results for $S > 1/2$-quantum spins using DMFT and other methods appear highly desirable.

Among many other non-perturbative approaches to the ferromagnetic Kondo lattice model, the Coherent Potential Approximation (CPA) is finally mentioned [192]. The many-body CPA treats the interaction effectively as spin disorder by means of an alloy analogy. The electrons of a given spin projection are frozen while calculating the Green function for the opposite spin. In Ref. [148] a self-consistent CPA using the atomic-limit excitation energies and weights (Chap. 2.4) is used for $S = 1/2$ and for parametrized magnetization in order to compare the LDOS with that obtained by other approaches. When applied to the Hubbard model the alloy analogy with atomic limit levels and weights corresponds to a Green function decoupling scheme introduced by Hubbard himself [193]. With respect to the Kondo lattice model, however, this correspondence holds only in the zero-field, paramagnetic phase. In the symmetry-broken phase, the equation-of-motion approach on the one hand and the atomic-limit CPA on the other yield deviating results as pointed out by Edwards et al. [18, 194]. These authors propose a decoupling procedure analogous to Hubbard's for arbitrary S. For $S = \infty$, Furukawa's DMFT expression for the one-electron Green function is obtained. However, no ferromagnetism is possible within the CPA treatment. It is therefore suggested to generalize the DMFT probability distribution function for the spin vector to finite S so that the correct Curie-law behavior for empty and half-filled band is ensured. With this extension, ferromagnetic solutions are possible and transition temperatures can be calculated [18, 194].

Numerical simulations

There is a great number of numerical simulations particularly concerning the strong-coupling regime of the Kondo lattice. They can be roughly divided into two parts. Monte Carlo simulations for classical localized spins allow for an exact diagonalization of the fermionic Hamiltonian. They have been carried out mostly in order to obtain magnetic phase diagrams or critical temperatures, or to study phase separation [172, 173, 195, 196, 197, 198, 199, 200]. Simulations based on the Density Matrix Renormalization Group (DMRG) allow for a quantum-mechnical treatment of the localized spins [201]. They are usually restricted to the one-dimensional model due to the heavy computational cost. Besides being employed for the comparison with classical spins [172, 173], DMRG has revealed new magnetic phases like antiferromagnetically coupled FM islands and magnetic polarons on the ferromagnetic correlated Kondo lattice [202, 203, 204].

Methods used in this work

In this work a combined approach to Kondo lattice films is chosen. The electronic self-energy (2.27) is obtained using an equation-of-motion approach. In a separate step, the intra-atomic interaction (2.3) is mapped onto an effective localized-spin Hamiltonian in order to calculate the magnetization. This generalized RKKY approach accounts for the effect of the conduction band polarization on the interaction among the localized spins. Both methods have been applied to bulk model systems [107, 184, 186] and real materials [11, 99] on periodic lattices, and including configurational disorder [37]. One of the main tasks of this work is to formulate and evaluate the two approaches for film geometry [185, 205].

As concerns the electronic self-energy, no restrictions on the localized quantum spins are required. Regarding the spin subsystem, it must be seen as a strong argument in favor of the modified RKKY theory that it interpolates between the weak-coupling RKKY limit and the strong-coupling double-exchange physics. The two regimes refer to quite different relations between the indirect interaction and the conduction band structure: while the exchange integrals of the conventional RKKY limit depend sensitively on the density of states at the Fermi level, they are closely related to the kinetic energy of the charge carriers in the double-exchange regime, implying that details of the DOS are less important.

The modified RKKY method yields the interaction among the localized spins 'directly' in terms of effective exchange integrals. This turns out to be particularly useful for the study of the interlayer exchange coupling, which is essentially given by summing up the exchange integrals between the coupled layers.

2.4 Atomic limit

If the hopping between lattice sites is switched off one speaks of the atomic or zero-bandwidth limit [206]. The single-site Hamiltonian including the Hubbard interaction reads:

$$H_{\mathrm{at}} = -\sum_{i\sigma}(t_0+\mu)n_{i\sigma} - J\sum_i \mathbf{S}_i\cdot\boldsymbol{\sigma}_i + \frac{U}{2}\sum_{i\sigma} n_{i\sigma}n_{i-\sigma}\,. \tag{2.38}$$

$-t_0$ denotes the atomic energy level. Since all sites are equivalent, the site index can be dropped.

According to elementary angular momentum algebra the total spin on a site with one electron can assume the values

$$S_{tot} = S-\frac{1}{2},\, S+\frac{1}{2}\,. \tag{2.39}$$

For $S = 1/2$ this corresponds to a singlet and a triplet spin state, respectively. It is straightforward to show that the eigenenergies of this single-site spin problem are as given in Fig. 2.2. The excitation energies

$$\begin{aligned} E_1 &= -t_0 - \frac{1}{2}JS & E_3 &= -t_0 + U - \frac{1}{2}J(S+1) \\ E_2 &= -t_0 + \frac{1}{2}J(S+1) & E_4 &= -t_0 + U + \frac{1}{2}JS \end{aligned} \tag{2.40}$$

correspond to adding an electron, which couples parallel or antiparallel to the localized spin, to an empty site (E_1, E_2), and to adding an electron to a site which is already occupied by an electron of opposite spin (E_3, E_4). In the latter case a parallel or antiparallel spin configuration is destroyed.

The excitation spectrum of (2.38) can be obtained e.g. by means of an equation-of-motion approach for the single-electron Green function [104]. The result is

$$G_\sigma(E) = \sum_{i=1}^{4} \frac{\alpha_{i\sigma}}{E + \mathrm{i}0^+ + \mu + t_0 - E_i} \tag{2.41}$$

with the spin- and temperature-dependent spectral weigths

$$\begin{aligned}
\alpha_{1\sigma} &= \frac{1}{2S+1}\left\{S + 1 + z_\sigma\langle S^z\rangle + \Delta_{-\sigma} - (S+1)\langle n_{-\sigma}\rangle\right\} \,, \\
\alpha_{2\sigma} &= \frac{1}{2S+1}\left\{S - z_\sigma\langle S^z\rangle - \Delta_{-\sigma} - S\langle n_{-\sigma}\rangle\right\} \,, \\
\alpha_{3\sigma} &= \frac{1}{2S+1}\left\{S\langle n_{-\sigma}\rangle - \Delta_{-\sigma}\right\} \,, \\
\alpha_{4\sigma} &= \frac{1}{2S+1}\left\{(S+1)\langle n_{-\sigma}\rangle + \Delta_{-\sigma}\right\} \,.
\end{aligned} \tag{2.42}$$

$\Delta_\sigma = \langle S^\sigma c^\dagger_{-\sigma} c_\sigma\rangle + z_\sigma\langle S_z n_\sigma\rangle$ is a mixed expectation value that can be calculated using the equation of motion and the spectral theorem (2.14). The spin expectation value $\langle S^z\rangle$ must be seen as an external parameter because there is no exchange interaction between the localized moments of the single-site Hamiltonian (2.38).

Sometimes it may be useful to recast the Green function (2.41) into a sum of two terms,

$$\begin{aligned}
G_\sigma(E) &= G^{(1)}_\sigma(E) + G^{(2)}_\sigma(E) \\
&= \frac{1 - \langle n_\sigma\rangle}{E + \mathrm{i}0^+ + \mu + t_0 - M^{(1)}_\sigma(E)} + \frac{\langle n_\sigma\rangle}{E + \mathrm{i}0^+ + \mu + t_0 - U - M^{(2)}_\sigma(E)} \,,
\end{aligned} \tag{2.43}$$

where

$$\begin{aligned}
M^{(1)}_\sigma(E) &= \frac{1}{2}J\,\frac{\frac{1}{2}JS(S+1) - X_{-\sigma}(E + \mu + t_0)}{E + \mathrm{i}0^+ + \mu + t_0 - \frac{1}{2}J(1 + X_{-\sigma})} \,, \\
M^{(2)}_\sigma(E) &= \frac{1}{2}J\,\frac{\frac{1}{2}JS(S+1) + Y_{-\sigma}(E + \mu + t_0 - U)}{E + \mathrm{i}0^+ + \mu + t_0 - U + \frac{1}{2}J(1 + Y_{-\sigma})} \,.
\end{aligned} \tag{2.44}$$

The abbreviations

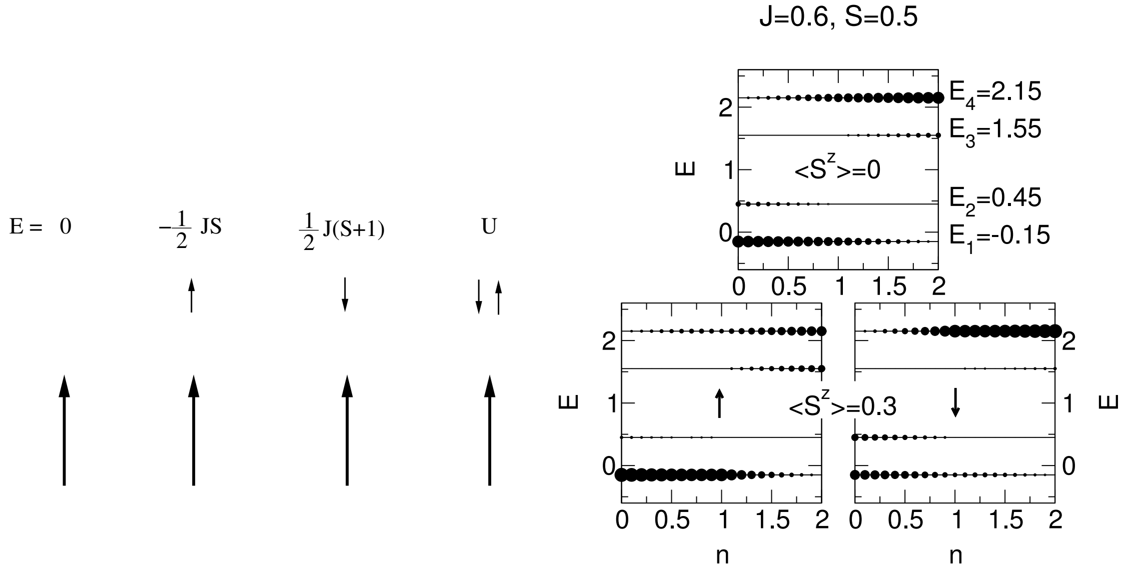

Figure 2.2: Left: spin configurations of the single-site problem and their energies. The eigenenergy $E = -\frac{1}{2}JS$ is twofold degenerate. Right: spectral weigths of the excitation energies in the atomic limit for $J = 0.6$ eV, $U = 2$ eV, $S = 1/2$ (from Ref. [207]). Top panel: paramagnetic case, bottom panel: finite magnetization. The diameter of the points is a measure for the spectral weight.

$$X_\sigma = \frac{\Delta_\sigma - m_\sigma}{1 - \langle n_\sigma \rangle}, \quad Y_\sigma = \frac{\Delta_\sigma}{\langle n_\sigma \rangle}, \quad m_\sigma = z_\sigma \langle S_z \rangle \tag{2.45}$$

have been used. (2.43) corresponds to a separation of the excitations associated with single occupancies ($G_\sigma^{(1)}$) and double occupancies ($G_\sigma^{(2)}$) as is readily verified by U appearing in the denominator of $G_\sigma^{(2)}$.

Fig. 2.2 shows the dependence of the weigths on the band filling n and on $\langle S_z \rangle$ for $S = 1/2$. Particle-hole symmetry

$$\alpha_{1\sigma}(n) = \alpha_{4-\sigma}(2-n), \quad \alpha_{2\sigma}(n) = \alpha_{3-\sigma}(2-n) \tag{2.46}$$

is obviously fulfilled. One observes a strong dependence on the charge carrier density. For most n only two poles have significant spectral weight.

It is worthwhile noting that with respect to the pole E_4, the parameter U has the same effect as (a positive) J. Both energetically punish the double occupancy on a given lattice site. As concerns the Hubbard interaction this is due to the Coulomb repulsion between two electrons on the same site, regarding the spin exchange interaction J it is related to the destruction of a favorable parallel spin orientation of the localized and the itinerant spin.

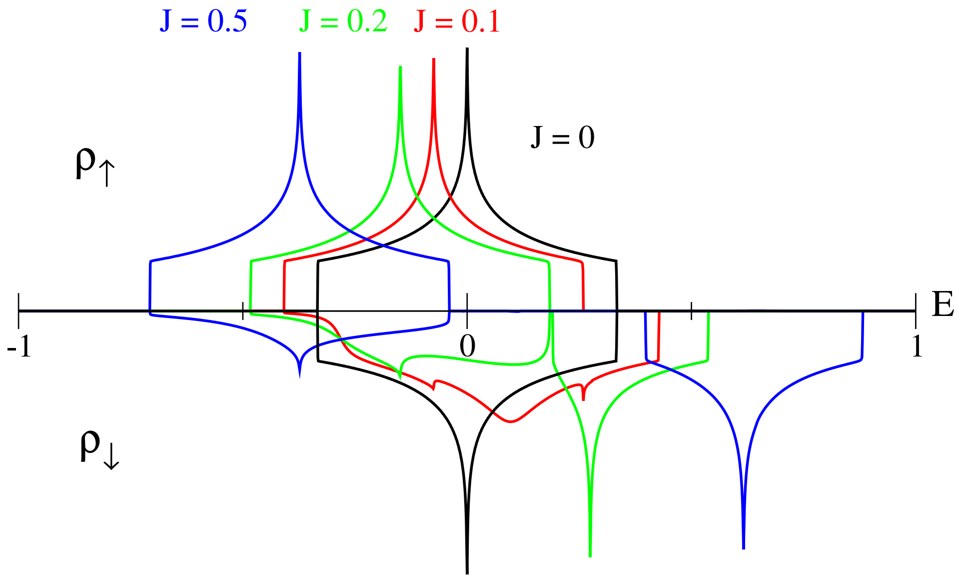

Figure 2.3: Ferromagnetically saturated semiconductor. LDOS of the square lattice (monolayer). The energy unit is eV. Parameters: $n = 0$, $T = 0$, $S = 3/2$.

In the atomic-limit solution (2.40)-(2.42), inconsistencies may arise for certain parameter constellations. For ferromagnetic saturation, $\langle S^z \rangle \to S$, and $J > 0$, a negative spectral weight ($\alpha_{2\uparrow} < 0$) if $n \neq 0$ is possible [206].

2.5 Ferromagnetically saturated semiconductor

Assuming a saturated ferromagnetic state for $T = 0$, $n = 0$ [132, 208, 209, 210], an added ↑-electron cannot exchange its spin with the local-moment subsystem. Therefore the poles of the ↑-Green function are just rigidly shifted Bloch energies:

$$G_{\mathbf{k}\uparrow}(E) = \frac{1}{E + \mathrm{i}0^+ - \epsilon(\mathbf{k}) + \frac{1}{2}JS} \,. \tag{2.47}$$

Hence the ↑-self-energy is rather simple:

$$M_{\mathbf{k}\uparrow}(E) = M_\uparrow = -\frac{1}{2}JS \,. \tag{2.48}$$

The ↓-self-energy is more complicated due to the spinflip interaction with the localized spins. One finds [104]

$$G_{\mathbf{k}\downarrow}(E) = \frac{1}{E + \mathrm{i}0^+ - \epsilon(\mathbf{k}) - M_\downarrow(E)} \tag{2.49}$$

with the local self-energy

$$\begin{aligned} M_{\downarrow}(E) &= \frac{1}{2} JS \left(1 + \frac{JB(E)}{1 - \frac{1}{2} JB(E)} \right) , \\ B(E) &= \frac{1}{N} \sum_{\mathbf{k}} G_{\mathbf{k}\uparrow}(E) \, . \end{aligned} \tag{2.50}$$

The further analysis of the ↓-self-energy reveals two kinds of states in the excitation spectrum. $M_{\downarrow}$ has a finite imaginary part at energies where the ↑-LDOS is finite. These scattering states reflect the finite probability for an added ↓-electron to flip its spin by emitting a magnon. Secondly, there are states outside the ↑-band with a vanishing imaginary part of the self-energy. These states correspond to a ↓-quasiparticle of infinite lifetime which propagates through the lattice while perpetually emitting and re-absorbing virtual magnons ('magnetic polaron'). Fig. 2.3 shows the LDOS of the square lattice. For large enough J, the ↓-polaron band lies outside the energy region of the ↑-band. The ↓-scattering states at energies where $\rho_{\uparrow} \neq 0$ are clearly visible.

Chapter 3

Film geometry

3.1 Notation and transformations

The characteristic feature of film geometry is the broken translational symmetry in the direction of the surface normal, which is conveniently taken as the z-axis of a 3-dimensional (3D) Cartesian coordinate system. Without translational invariance the perpendicular component of the wave vector k_z is no longer a good quantum number and Fourier transformation between real and reciprocal space can only be exploited in the x-y-plane. Generally the observables exhibit a z-dependence. Furthermore the number of nearest neighbors (coordination number) in the surface layer is reduced.

For the formal description of film structures consisting of crystal lattice planes, two real space indices are introduced, a Greek layer index and a latin index to denote the in-plane position of an atom. Any lattice site (i, α) is then unambiguously characterized by a position vector

$$\mathbf{R}_{i\alpha} = \mathbf{r}_\alpha + \mathbf{R}_i \tag{3.1}$$

where $\mathbf{r}_\alpha$ designates the position of the α-th layer and $\mathbf{R}_i$ denotes the position in the x-y-plane (see Fig. 3.1). A slab (= film of finite thickness) is a piece of a bulk crystal cut out along some crystallographic direction. It is thus uniquely defined by a 2D surface lattice ('basal plane') whose sites are referred to by $\mathbf{R}_i$ and a supercell containing the sites denoted by the N_L vectors $\mathbf{r}_\alpha$. A slab is built by N_L monolayers (ML), each consisting of $N_\parallel$ sites in the basal plane. Hence the total number of lattice sites is $N_\mathrm{L} N_\parallel$. If $N_\mathrm{L} \to \infty$ and a surface is present one speaks of a semi-infinite crystal.

A remark should be made about the meaning of the words 'layer' and 'monolayer'. It appears to be common language use that a 'layer' consists of one or more 'monolayers' where a monolayer denotes a plane of atoms. In this work these

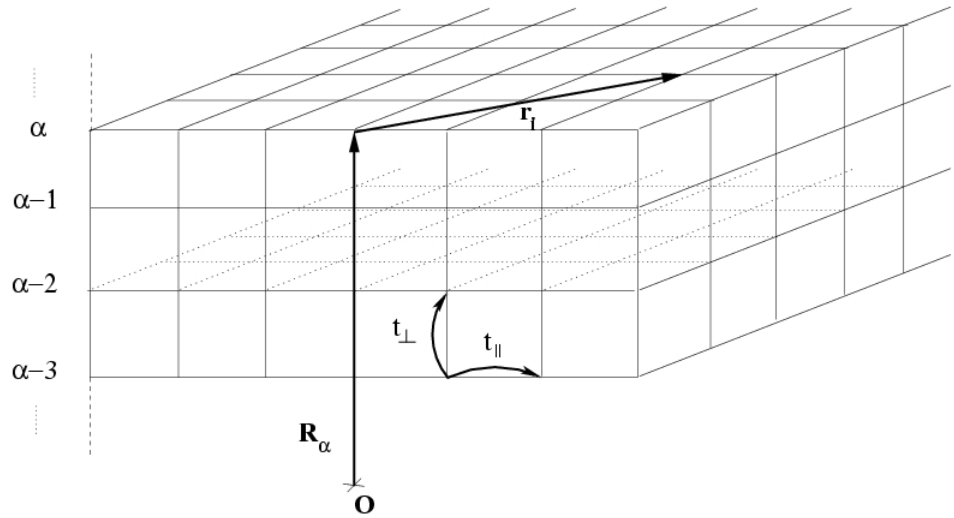

Figure 3.1: Sketch of the first four layers of a simple-cubic(100) Kondo lattice film.

expressions are used in a slightly different manner: 'monolayer' usually denotes the truly 2D-film ($N_{\mathrm{L}} = 1$), and the atomic planes within a film of finite thickness are sometimes called 'layers'.

The operators and the other quantities characterizing the many-body problem now carry layer indices. In formal analogy to the bulk formulas (2.22) and (2.24), an electron annihilation (creation) operator transforms between the 2D real space and the reciprocal space according to

$$c^{(\dagger)}_{i\alpha\sigma} = \frac{1}{\sqrt{N_{\|}}} \sum_{\mathbf{k}_{\|}} c^{(\dagger)}_{\mathbf{k}_{\|}\alpha\sigma} e^{(-)i\mathbf{k}_{\|}\mathbf{R}_i} \tag{3.2}$$

and the hopping integrals transform as

$$\epsilon_{\alpha\beta}(\mathbf{k}_{\|}) = -\frac{1}{N_{\|}} \sum_{ij} t^{\alpha\beta}_{ij} e^{i\mathbf{k}_{\|}(\mathbf{R}_i - \mathbf{R}_j)} \,. \tag{3.3}$$

Wave vector summations are carried out in the first 2D surface Brillouin zone. The latter depends on the type of crystal lattice and on the film orientation given in terms of the Miller indices (l,m,n) [105]. Another distinguishing feature of the different film geometries is the ratio of the coordination number z_α at the surface and in the bulk. For the simple-cubic (sc) bulk crystal ($z_{bulk} = 6$), the intralayer and interlayer coordination numbers at the surface are summarized in Tab. 3.1. The present work mainly considers the sc(100)-configuration, which is sketched in Fig. 3.1. The simple-cubic lattice structure is, e.g., formed by the magnetic Mn-ions of the manganites.

	z_{surf}^{intra}	z_{surf}^{inter}	z_{surf}	$z_{surf}/z_{\mathrm{bulk}}$
sc(100)	4	1	5	5/6
sc(110)	2	2	4	4/6
sc(111)	0	3	3	3/6

Table 3.1: Surface coordination numbers for low-index simple-cubic film geometries. The sc(100)-surface is more 'closed' than the rather 'open' sc(111)-surface.

For low-index film geometry and using the tight-binding approximation, hopping occurs only between sites within the same layer (intralayer or in-plane hopping) or between sites belonging to adjacent layers (interlayer or perpendicular hopping). This means for the dispersion

$$\epsilon_{\alpha\beta}(\mathbf{k}_{\|}) = \begin{cases} \epsilon_{\|}^{\alpha}(\mathbf{k}_{\|})\, if\; \alpha = \beta \\ \epsilon_{\perp}^{\alpha}(\mathbf{k}_{\|})\, if\; \beta = \alpha + 1 \end{cases} \tag{3.4}$$

Using $\epsilon_{\alpha\beta}(\mathbf{k}_{\|}) = \epsilon_{\beta\alpha}^{*}(\mathbf{k}_{\|})$ the energy dispersion can be represented by an N_{L}-dimensional, tridiagonal matrix:

$$\underline{\epsilon}(\mathbf{k}_{\|}) = \begin{pmatrix} \epsilon_{\|}^{1}(\mathbf{k}_{\|}) & \epsilon_{\perp}^{1}(\mathbf{k}_{\|}) & 0 & ... & ... & 0 \\ \epsilon_{\perp}^{1*}(\mathbf{k}_{\|}) & \epsilon_{\|}^{2}(\mathbf{k}_{\|}) & \epsilon_{\perp}^{2}(\mathbf{k}_{\|}) & 0 & ... & ... \\ 0 & \epsilon_{\perp}^{2*}(\mathbf{k}_{\|}) & ... & ... & ... & ... \\ ... & 0 & ... & ... & ... & 0 \\ ... & ... & ... & ... & \epsilon_{\|}^{N_{\mathrm{L}}-1}(\mathbf{k}_{\|}) & \epsilon_{\perp}^{N_{\mathrm{L}}-1}(\mathbf{k}_{\|}) \\ 0 & ... & ... & 0 & \epsilon_{\perp}^{N_{\mathrm{L}}-1*}(\mathbf{k}_{\|}) & \epsilon_{\|}^{N_{\mathrm{L}}}(\mathbf{k}_{\|}) \end{pmatrix} . \tag{3.5}$$

The dispersion matrix corresponds to the non-interacting Hamiltonian matrix in the layer Bloch basis states $\{|\mathbf{k}_{\|}\alpha\sigma\rangle\}$. It can be diagonalized by a similarity transformation

$$\hat{\underline{\epsilon}}(\mathbf{k}_{\|}) = \underline{U}^{\dagger}(\mathbf{k}_{\|})\underline{\epsilon}(\mathbf{k}_{\|})\underline{U}(\mathbf{k}_{\|})\,. \tag{3.6}$$

The eigenvectors $\mathbf{u}_n(\mathbf{k}_{\|})$ $(n = 1, .., N_{\mathrm{L}})$ of (3.5) build the unitary matrix $\underline{U}$:

$$\underline{U}(\mathbf{k}_{\|}) = \begin{pmatrix} \vdots & \vdots & \vdots & \vdots \\ \mathbf{u}_1(\mathbf{k}_{\|}) & \mathbf{u}_2(\mathbf{k}_{\|}) & .. & \mathbf{u}_{N_{\mathrm{L}}}(\mathbf{k}_{\|}) \\ \vdots & \vdots & \vdots & \vdots \end{pmatrix} . \tag{3.7}$$

The elements of $\underline{U}(\mathbf{k}_{\|})$ are scalar products of the layer Bloch states and the eigenstates of the non-interacting film Hamiltonian:

$$U_{\alpha n}(\mathbf{k}_{\|}) = u_n^{\alpha}(\mathbf{k}_{\|}) = \langle \mathbf{k}_{\|}\alpha\sigma|\mathbf{k}_{\|}n\sigma\rangle\,. \tag{3.8}$$

Diagonalization of (3.5) yields N_{L} energy bands:

$$\underline{\hat{\epsilon}}(\mathbf{k}_{\|}) = \begin{pmatrix} \hat{\epsilon}_1(\mathbf{k}_{\|}) & 0 & .. & 0 \\ 0 & \hat{\epsilon}_2(\mathbf{k}_{\|}) & .. & .. \\ .. & .. & .. & 0 \\ 0 & .. & 0 & \hat{\epsilon}_{N_{\mathrm{L}}}(\mathbf{k}_{\|}) \end{pmatrix} . \tag{3.9}$$

The diagonal elements are the eigenvalues of $\underline{\epsilon}(\mathbf{k}_{\|})$, i.e. the solutions of the characteristic equation

$$\mathrm{d}et\left[\underline{\epsilon}(\mathbf{k}_{\|}) - \hat{\epsilon}(\mathbf{k}_{\|})\underline{I}\right] = 0 \tag{3.10}$$

where $\underline{I}$ denotes the identity matrix with $(\underline{I})_{\alpha\beta} \equiv \delta_{\alpha\beta}$. For $N_{\mathrm{L}} \to \infty$ the discrete set of energies for a given $\mathbf{k}_{\|}$ becomes an energy continuum.

In a real crystal there are usually surface or interface relaxations. A modified distance between atoms affects the overlap integrals of the atomic orbitals and thereby leads to a modified hopping. Specifically, in Chap. 6 the consequences of a modified hopping $\epsilon_{\perp}^{1}(\mathbf{k}_{\|})$ between the surface and the subsurface layer on the ferromagnetic stability will be studied. In most other cases, intra- and interlayer dispersion are assumed to be layer-independent, $\epsilon_{\|}^{\alpha}(\mathbf{k}_{\|}) = \epsilon_{\|}(\mathbf{k}_{\|})$ and $\epsilon_{\perp}^{\alpha}(\mathbf{k}_{\|}) = \epsilon_{\perp}(\mathbf{k}_{\|})$ for $\alpha = 1, .., N_{\mathrm{L}}$. For the low-index simple-cubic film structures, the in-plane and perpendicular dispersions for uniform nearest-neighbor hopping ($t \equiv t_{ij}^{\alpha\beta}$ if $\mathbf{R}_{i\alpha}$ and $\mathbf{R}_{j\beta}$ denote nearest neighbors) and zero band centers of gravity ($t_0^{\alpha} \equiv t_{ii}^{\alpha\alpha} = 0$) are given by [211]:

$$\begin{aligned} \epsilon_{\|}(\mathbf{k}_{\|}) &\overset{(100)}{=} -2t\left[cos(k_{\|}^{x}a) + cos(k_{\|}^{y}a)\right] \\ &\overset{(110)}{=} -2tcos(k_{\|}^{x}a) \\ &\overset{(111)}{=} 0 \end{aligned} \tag{3.11}$$

$$\begin{aligned} \left|\epsilon_{\perp}(\mathbf{k}_{\|})\right|^2 &\overset{(100)}{=} t^2 \\ &\overset{(110)}{=} 2t^2 + 2t^2cos(\sqrt{2}k_{\|}^{y}a) \\ &\overset{(111)}{=} 3t^2 + 2t^2cos(\sqrt{2}k_{\|}^{y}a) \\ &\quad + 4t^2cos(\sqrt{3/2}k_{\|}^{x}a)cos(\sqrt{1/2}k_{\|}^{y}a) \end{aligned} \tag{3.12}$$

Note that for all relevant purposes only the absolute square of the interlayer dispersion enters the calculations. For the sc(100)-geometry, the interlayer hopping is dispersionless, that is **k**-independent.

In certain situations it may be necessary to consider layer-dependent band centers of gravity, for example to enforce charge neutrality (i.e. a uniform charge density). They are incorporated as Lagrange parameters and varied self-consistently to fulfill the boundary condition, namely the same band filling n in all layers of the film. Charge transfer is discussed in Chap. 4.5 in terms of the layer-dependent local density of states. Its influence on the magnetic properties like the magnetization and the ferromagnetic transition temperature is addressed in Chap. 6.

In realistic cases, e.g. due to lattice relaxation, the exchange coupling J may acquire a layer-dependence, too ($J \to J_\alpha$). In all of the following considerations, however, J has the same value in all layers of the film.

To avoid cluttered notation the index '$\|$' is mostly dropped from now on:

$$\begin{aligned} \mathbf{k}_{\|} &\to \mathbf{k}\,, \\ N_{\|} &\to N\,. \end{aligned} \tag{3.13}$$

Unless otherwise stated the dispersions and wave vectors refer to the 2D surface lattice of the considered geometry and to the corresponding first surface Brillouin zone.

3.2 Kondo lattice films

Using the notation introduced in the last section the Hamiltonian for Kondo lattice films reads

$$\begin{aligned} H &= H_0 + H_I \\ &= -\sum_{ij\sigma}\sum_{\alpha\beta}(t_{ij}^{\alpha\beta} + \mu\delta_{ij}\delta_{\alpha\beta})c_{i\alpha\sigma}^{\dagger}c_{j\beta\sigma} - \frac{1}{2}J\sum_{i\alpha\sigma}\left(z_\sigma S_{i\alpha}^z n_{i\alpha\sigma} + S_{i\alpha}^{-\sigma}c_{i\alpha\sigma}^{\dagger}c_{i\alpha-\sigma}\right)\,. \end{aligned} \tag{3.14}$$

Latin letters are basal-plane indices and Greek indices refer to the layers of the film. With respect to the fermionic part of the many-body problem (3.14), the single-electron Green function matrix $\underline{G}_{\mathbf{k}\sigma}$ will be the central quantity of interest. The matrix indices refer to the layers:

$$\left[\underline{G}_{\mathbf{k}\sigma}\right]_{\alpha\beta}(E) \equiv G_{\mathbf{k}\sigma}^{\alpha\beta}(E) = \langle\langle c_{\mathbf{k}\alpha\sigma}; c_{\mathbf{k}\beta\sigma}^{\dagger}\rangle\rangle_E\,. \tag{3.15}$$

The formal solution can be written analogously to the bulk case (2.28):

$$G_{\mathbf{k}\sigma}^{\alpha\beta}(E) = \left[\frac{1}{(E + \mathrm{i}0^+ + \mu)\underline{I} - \underline{\epsilon}(\mathbf{k}) - \underline{M}_{\mathbf{k}\sigma}(E)}\right]_{\alpha\beta}\,. \tag{3.16}$$

$\underline{M}_{\mathbf{k}\sigma}$ denotes the self-energy matrix. Concerning the matrix inversion connected with the solution for the single-electron Green function, recursion formulas have proved to be efficient (Appendix E).

The exactly solvable limits presented in Secs. 2.4 and 2.5, namely the zero-bandwidth limit and the ferromagnetically saturated semiconductor, also hold for film geometry. In the case of the atomic limit, being a single-site problem, this is immediately clear. As regards the second limit, translational invariance is no prerequisite for the solution of the problem [212]. In fact the Green function approach, which was briefly outlined for the bulk in Chap. 2.5, is only more cumbersome to write down for film geometry. The solution (3.16) is formally analogous to the bulk Green functions of the FM-saturated semiconductor and corresponds to matrix versions of (2.47) and (2.49). The local self-energy and the Green function in (2.50) are replaced by the respective diagonal matrix elements:

$$M_{\downarrow}(E) \rightarrow M_{\downarrow}^{\alpha}(E) \qquad B(E) \rightarrow B_{\alpha}(E) = \frac{1}{N}\sum_{\mathbf{k}} G_{\mathbf{k}\uparrow}^{\alpha\alpha}(E)\,. \tag{3.17}$$

The restricted translational invariance generally implies a layer-dependence of a physical observable $\mathcal{O}_{i\alpha}$. Lateral translational symmetry within a layer can still be exploited:

$$\langle \mathcal{O}_{i\alpha} \rangle = \langle \mathcal{O}_{\alpha} \rangle\,. \tag{3.18}$$

Two important examples of (3.18) are the charge carrier density

$$\langle n_{\alpha} \rangle \equiv n_{\alpha} = n_{\alpha\uparrow} + n_{\alpha\downarrow} \tag{3.19}$$

and the local-moment magnetization, the latter being proportional to the thermal average of the localized-spin operator $\langle \mathbf{S}_{\alpha} \rangle$. The layer-dependence of both the carrier density and the magnetization will be discussed in more detail in Secs. 4.5 and 6.2.

Another quantity of interest is the layer-dependent density of states:

$$\rho_{ij\sigma}^{\alpha\beta}(E) = \frac{1}{N}\sum_{\mathbf{k}} \mathrm{e}^{\mathrm{i}\mathbf{k}(\mathbf{R}_i - \mathbf{R}_j)} S_{\mathbf{k}\sigma}^{\alpha\beta}(E-\mu)\,. \tag{3.20}$$

The spectral density matrix is related to the Green function matrix as

$$S_{\mathbf{k}\sigma}^{\alpha\beta}(E) = -\frac{1}{\pi}\mathrm{Im} G_{\mathbf{k}\sigma}^{\alpha\beta}(E)\,. \tag{3.21}$$

Actually (3.21) holds only for a real spectral density. This can, however, always be ensured by choosing a set of real one-particle basis states [211]. From the local density of states (LDOS) one can calculate the spin-dependent charge carrier density:

$$n_{\alpha\sigma} = \int\limits_{-\infty}^{+\infty} dE f_{-}(E) \rho_{ii\sigma}^{\alpha\alpha}(E) \,. \tag{3.22}$$

As concerns the density of states (DOS) near the surface of a film one expects, besides the layer-dependence of the LDOS $\rho_{ii\sigma}^{\alpha\alpha}$, an anisotropy of the off-diagonal nearest-neighbor DOS:

$$\rho_{\langle ij\rangle\sigma}^{\alpha\alpha} \neq \rho_{ii\sigma}^{\alpha\alpha\pm1} \,. \tag{3.23}$$

On some occasions it will be instructive to consider the internal energy. It is defined as the expectation value of the Hamiltonian (3.14) and can be separated into a kinetic and a potential part. Hence the internal energy per lattice site is

$$\begin{aligned} U &= \frac{1}{N_{\mathrm{L}}N}\langle H\rangle \\ &= \frac{1}{N_{\mathrm{L}}N}\left(\langle H_0\rangle + \langle H_I\rangle\right) \\ &= U_{\mathrm{k}in} + U_{\mathrm{pot}} \,. \end{aligned} \tag{3.24}$$

The expectation values $\langle H_0\rangle\, and\, \langle H_I\rangle$ may be computed 'directly' using the spectral theorem (2.14). In order to do this the single-electron Green function $G_{ij\sigma}^{\alpha\beta}$ and two higher-order GFs corresponding to the expectation values $\langle S_\alpha^z n_{\alpha\sigma}\rangle$ and $\langle S_\alpha^{-\sigma} c_{\alpha\sigma}^\dagger c_{\alpha-\sigma}\rangle$ are required. These two Green functions will be introduced in Chap. 4.3.

Alternatively, after simple manipulations based on the equation of motion for the one-electron Green function $G_{ij\sigma}^{\alpha\beta}$, the internal energy of Kondo lattice films can be expressed in terms of the LDOS:

$$\begin{aligned} U &= \frac{1}{N_{\mathrm{L}}}\sum_{\alpha\sigma}\int\limits_{-\infty}^{+\infty} dE f_{-}(E) E \rho_{ii\sigma}^{\alpha\alpha}(E) \\ &= -\frac{1}{\pi N N_{\mathrm{L}}}\sum_{\alpha\sigma}\sum_{\mathbf{k}}\int\limits_{-\infty}^{+\infty} dE f_{-}(E) E \mathrm{Im} G_{\mathbf{k}\sigma}^{\alpha\alpha}(E-\mu) \,. \end{aligned} \tag{3.25}$$

Thus the kinetic energy is determined by local expectation values:

$$\begin{aligned} U_{\mathrm{k}in} &= U - U_{\mathrm{pot}} \\ &= U + \frac{J}{2N_{\mathrm{L}}}\sum_{\alpha\sigma}\left(z_\sigma\langle S_\alpha^z n_{\alpha\sigma}\rangle + \langle S_\alpha^{-\sigma} c_{\alpha\sigma}^\dagger c_{\alpha-\sigma}\rangle\right) \,. \end{aligned} \tag{3.26}$$

3.3 Non-interacting limit

Important effects which result from the reduced translational symmetry can already be observed for $J = 0$. It is therefore instructive to consider non-interacting electrons described by

$$H_0 = -\sum_{ij\sigma}\sum_{\alpha\beta}(t_{ij}^{\alpha\beta} + \mu\delta_{ij}\delta_{\alpha\beta})c_{i\alpha\sigma}^{\dagger}c_{j\beta\sigma} \tag{3.27}$$

$$= \sum_{\mathbf{k}\sigma}\sum_{\alpha\beta}(\epsilon_{\alpha\beta}(\mathbf{k}) - \mu\delta_{\alpha\beta})c_{\mathbf{k}\alpha\sigma}^{\dagger}c_{\mathbf{k}\beta\sigma} \,. \tag{3.28}$$

Using (3.6) and (3.7) the inversion in (3.16) can be readily performed. The non-interacting single-electron Green function matrix elements are

$$G_{\mathbf{k}}^{\alpha\beta(0)}(E) = \sum_{n}\frac{u_n^{\alpha}(\mathbf{k})u_n^{*\beta}(\mathbf{k})}{E + \mu - \hat{\epsilon}_n(\mathbf{k}) + \mathrm{i}0^{+}} \,. \tag{3.29}$$

The weights $u_n^{\alpha}(\mathbf{k})$ are given by (3.8).

The further discussion is conveniently done in terms of the layer-dependent free density of states $\rho_{ij}^{\alpha\beta(0)}$. It is furthermore useful to consider the spectral moments

$$m_{\alpha}^{(n,0)} = \int_{-\infty}^{+\infty} dE(E + t_0^{\alpha})^n\rho_{ii}^{\alpha\alpha(0)}(E) \quad (n = 0,\, 1,\, 2, ..) \,. \tag{3.30}$$

For uniform band centers of gravity ($t_0^{\alpha} = 0$), the second moment or variance reads

$$m_{\alpha}^{(2,0)} = z_{\alpha}t^2 \,. \tag{3.31}$$

z_{α} denotes the coordination number in layer α. (3.31) is obtained by evaluating (3.30) with (3.20) and (2.26). The variance is a measure for the effective bandwidth of the LDOS $\rho_{ii}^{\alpha\alpha(0)}$. Due to the reduced coordination number in the surface layer ($\alpha = 1$) the corresponding LDOS is narrower as compared to the LDOS of the subsurface layers (see Tab. 3.1). For the discussion of the subsurface ($\alpha = 2$) and deeper layers, higher moments must be considered. For the simple-cubic film geometry all odd moments vanish, i.e. the LDOS is a symmetric function.

Fig. 3.2 shows the local and nearest-neighbor DOS of the surface, subsurface, and center layer for sc(100)-films of different thickness for uniform *nn* hopping t and zero band centers of gravity ($t_0^{\alpha} = 0$). The bandwidth ranges from $W \equiv W_{mono} = 8t$ for the monolayer to $W_{\mathrm{bulk}} = 12t = 1$ eV for the bulk crystal.

The monolayer LDOS is characterized by van-Hove singularities at the band edges and at the band center. These singularities are also present in the multilayer LDOS but become less pronounced with increasing film thickness. The two

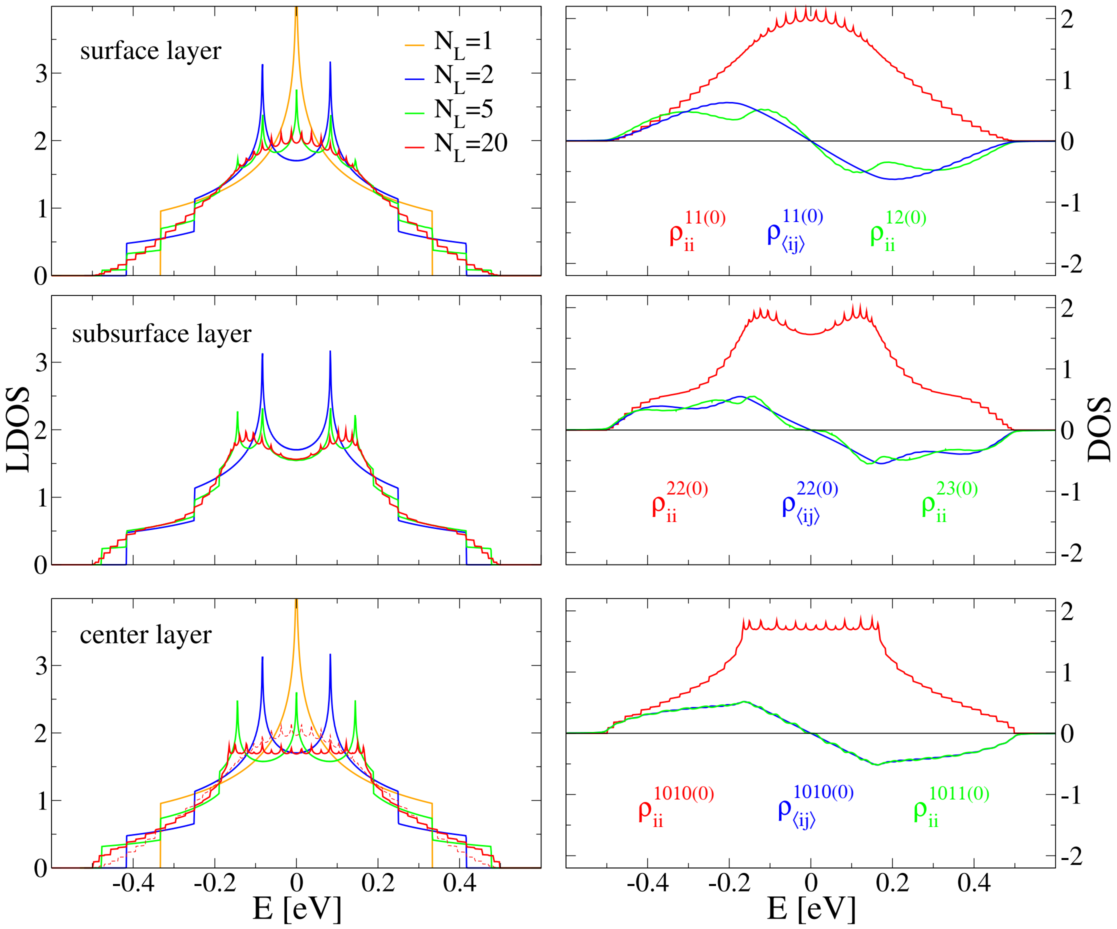

(a) (b)

Figure 3.2: (a) Non-interacting LDOS $\rho_{ii}^{\alpha\alpha(0)}$ of the surface ($\alpha = 1,\ N_{\mathrm{L}}$), subsurface ($\alpha = 2,\ N_{\mathrm{L}} - 1$), and center layer(s) for sc(100)-films of different thickness. For comparison the surface layer LDOS for the 20ML-film is also shown in the bottom panel (dashed line). (b) Non-interacting off-diagonal DOS $\rho_{ij}^{\alpha\beta(0)}$ for an sc(100)-film ($N_{\mathrm{L}} = 20$). The LDOS is also shown for comparison. The off-diagonal DOS refers to nearest neighbors situated in the same layer (blue lines) or in adjacent layers (green lines). Parameter: $t = 1/12$ eV.

broad peaks lying around the center of the subsurface LDOS are a consequence of surface Friedel oscillations [213]. These are charge density oscillations due to the perturbation of the infinite, ideal bulk crystal by the surfaces. They are damped towards the center of the films. Furthermore, one clearly sees the reduced effective bandwidth of the elliptic-shape surface-layer LDOS of the 20ML-film. For the latter, the center-layer LDOS essentially corresponds to the bulk-crystal LDOS. For a given film thickness, the LDOS of all layers share common band edges.

The antisymmetric off-diagonal densities of states refer to various pairs of nearest neighbors in the 20ML-film. Contrary to the LDOS they exhibit hardly any marks of the van-Hove singularities, but there are qualitatively similar footprints of the Friedel oscillations. As expected, the anisotropy (3.23) is most pronounced at the film surface.

Chapter 4

One-particle excitations

The many-body problem (3.14) cannot be solved exactly except for very restricted parameter constellations as discussed in Chap. 2. In this chapter some approximative solutions for the one-electron Green function $\underline{G}_{\mathbf{k}\sigma}(E)$, or equivalently the electronic self-energy $\underline{M}_{\mathbf{k}\sigma}(E)$, in the ferromagnetic and paramagnetic phase are presented. Apart from mean-field theory these approaches are non-perturbative and can therefore be used to study the full parameter range of the model.

From the single-electron Green function, the one-particle excitations are obtained in terms of the spectral density (3.21) or of the local density of states (LDOS):

$$\rho_{\alpha\sigma}(E) \equiv \rho_{ii\sigma}^{\alpha\alpha}(E) = \frac{1}{N}\sum_{\mathbf{k}} S_{\mathbf{k}\sigma}^{\alpha\alpha}(E-\mu) = -\frac{1}{\pi N}\sum_{\mathbf{k}} \mathrm{Im} G_{\mathbf{k}\sigma}^{\alpha\alpha}(E-\mu)\,. \tag{4.1}$$

Both will be referred to as the 'electronic structure' of Kondo lattice films in the following. Physical quantities of interest like the exchange splitting can be read off from them. In addition they yield other relevant information like the spin-dependent band filling. Furthermore, the single-electron spectral density is an experimental observable as it represents the bare line shape of a photoemission measurement.

4.1 Mean-field theory

Mean-field (MF) theory is usually the first approach to solve a many-body problem. It treats the interaction as an effective one-particle or one-spin potential which must be calculated self-consistently. Besides yielding a rough estimate of physical quantities of interest it may serve as the starting point, guide, and reference frame for more elaborate approaches that take correlation effects into account.

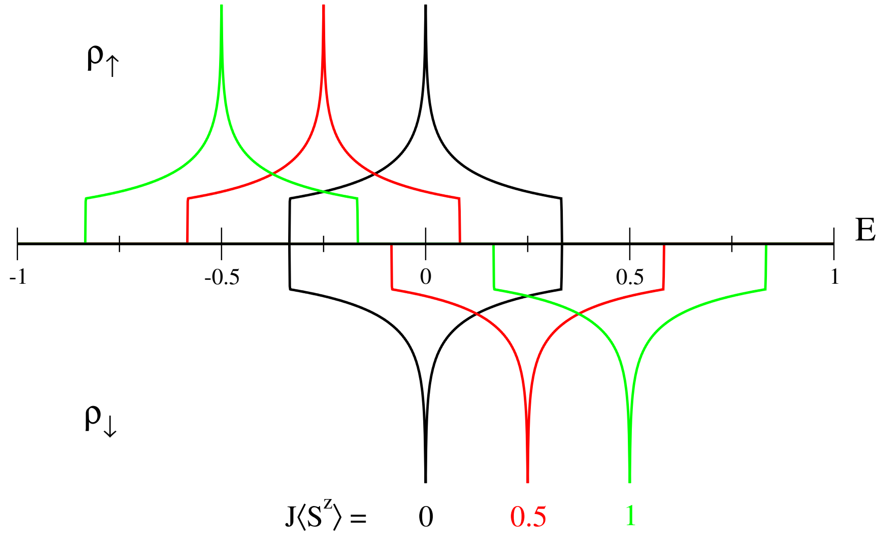

Figure 4.1: LDOS of the sc(100)-monolayer for different values of the effective mean-field coupling $J\langle S^z\rangle$ (in eV). With decreasing temperature (increasing $\langle S^z\rangle$) the majority-spin conduction band shifts to lower energies ('red-shift effect').

Well-known examples of simple mean-field theories are the Weiss theory for a local-moment ferromagnet [214] and the Stoner model for ferromagnetism in the Hubbard model [215]. More sophisticated and widely used mean-field approaches are the Density Functional Theory for band structure and total energy calculations, and the Dynamical Mean-Field Theory for strongly correlated systems [124, 125]. The mean-field treatment of the Kondo lattice model already provides a qualitative explanation of the famous red-shift of the optical absorption edge with decreasing temperature in ferromagnetic semiconductors like EuO and EuS [9, 10].

In order to obtain the MF one-electron excitation spectrum for Kondo lattice films described by (3.14), the spinflip terms are neglected and the z-component of the localized spins is replaced by the thermal average $\langle S^z_\alpha\rangle$. This yields

$$H_I^{\mathrm{MF}} = -\frac{1}{2}J\sum_{i\alpha\sigma} z_\sigma\langle S^z_\alpha\rangle n_{i\alpha\sigma}\,. \tag{4.2}$$

The total MF-Hamiltonian can be written in terms of spin-dependent one-particle energies:

$$\begin{aligned} H^{\mathrm{MF}} &= -\sum_{ij\sigma}\sum_{\alpha\beta}(t_{ij}^{\alpha\beta} + (\mu + \frac{1}{2}z_\sigma J\langle S^z_\alpha\rangle)\delta_{ij}\delta_{\alpha\beta})c^\dagger_{i\alpha\sigma}c_{j\beta\sigma} \\ &= \sum_{\mathbf{k}\sigma}\sum_{\alpha\beta}(\epsilon_{\alpha\beta}(\mathbf{k}) - (\mu + \frac{1}{2}z_\sigma J\langle S^z_\alpha\rangle)\delta_{\alpha\beta})c^\dagger_{\mathbf{k}\alpha\sigma}c_{\mathbf{k}\beta\sigma}\,. \end{aligned} \tag{4.3}$$

Alternatively the same Hamiltonian is obtained using perturbation theory [210]. The matrix elements of the MF one-electron Green function (3.16) read

$$G^{\alpha\beta}_{\mathbf{k}\sigma,\mathrm{MF}}(E) = \left(\frac{1}{(E+\mu+\mathrm{i}0^+)\underline{I} + \frac{1}{2} z_\sigma J \langle \underline{S}^z \rangle - \underline{\epsilon}(\mathbf{k})} \right)_{\alpha\beta} . \tag{4.4}$$

$\langle \underline{S}^z \rangle$ denotes a diagonal matrix with elements $(\langle \underline{S}^z \rangle)_{\alpha\beta} = \langle S^z_\alpha \rangle \delta_{\alpha\beta}$. The mean-field approximation yields independent electrons in an effective spin- and layer-dependent field exerted by the thermal average of the localized spins.

Fig. 4.1 shows the mean-field LDOS of the square lattice. It consists of two energy bands, one for the (majority-)↑-spin and one for the (minority-)↓-spin projection at higher energies. The two bands are separated by the exchange splitting $J\langle S^z \rangle$. Thus mean-field theory does not reproduce the atomic-limit band structure. On the other hand the center of gravity of the ↑-band for $T = 0$ ($\langle S_z \rangle = S$) is in accordance with the atomic limit pole (2.40) and the ↑-band of the ferromagnetically saturated semiconductor (2.47). This suggests that for low temperatures, for a high conduction-band polarization and in case that details of the band structure are unimportant, the MF result for the one-electron Green function may be an acceptable approximation.

However, it should be added that the neglect of spinflip processes also leads to obvious shortcomings in the electronic excitation spectrum. A finite ↓-spectral weight below the chemical potential is only possible up to a critical value of the exchange splitting, contrary to what the zero-bandwidth limit yields and the FM-saturated semiconductor suggests. There is no band-narrowing effect due to the increased spin scattering of ↑-electrons which reduces the effective hopping of the charge carriers with increasing temperature. At the ferromagnetic transition temperature the MF self-energy vanishes and the theory reduces the Kondo lattice to a non-interacting electron lattice gas. This is surely a crude approximation for strong coupling ($JS \gg W$).

The next two sections present self-energy approaches which recover the mean-field result for small coupling but avoid its shortcomings by taking spin-scattering effects into account.

4.2 Interpolating Self-energy Ansatz

The Interpolating Self-energy Ansatz (ISA) fulfills the known limits discussed in Secs. (2.4) and (2.5). It comprises an ansatz for the structure of the self-energy which contains parameters that are fitted by the high-energy expansion of the Green function (2.37). The ISA has been used in the low-density limit $n \to 0$ of the Kondo lattice model [126] and applied in connection with an effective-medium approach to the correlated Kondo lattice model [127]. Below an improved version of

Ref. [126] is discussed which formally corresponds to the ansatz for the correlated KLM but is here evaluated for $U = 0$.

The atomic limit (2.43) and Eqs. (2.47) and (2.49) for the FM-saturated semiconductor are reproduced by the following Green function:

$$\begin{aligned} G_{\mathbf{k}\sigma}(E) &= G^{(1)}_{\mathbf{k}\sigma}(E) + G^{(2)}_{\mathbf{k}\sigma}(E) \\ &= \frac{1-\langle n_\sigma\rangle}{E+\mathrm{i}0^+ +\mu-\epsilon(\mathbf{k})-M^{(1)}_\sigma(E)} + \frac{\langle n_\sigma\rangle}{E+\mathrm{i}0^+ +\mu-\epsilon(\mathbf{k})-M^{(2)}_\sigma(E)} \,. \end{aligned} \tag{4.5}$$

$M^{(1)}_\sigma$ and $M^{(2)}_\sigma$ contain several parameters:

$$\begin{aligned} M^{(1)}_\sigma(E) &= -\frac{1}{2}JX_{-\sigma} + \frac{1}{4}J^2 \frac{a_{-\sigma}G^{(0)}_{-\sigma}(E-\frac{1}{2}JX_{-\sigma})}{1-b_{-\sigma}G^{(0)}_{-\sigma}(E-\frac{1}{2}JX_{-\sigma})} \,, \\ M^{(2)}_\sigma(E) &= \frac{1}{2}JY_{-\sigma} + \frac{1}{4}J^2 \frac{c_{-\sigma}G^{(0)}_{-\sigma}(E+\frac{1}{2}JY_{-\sigma})}{1+d_{-\sigma}G^{(0)}_{-\sigma}(E+\frac{1}{2}JY_{-\sigma})} \,. \end{aligned} \tag{4.6}$$

In addition to the limit of an empty conduction band this ansatz includes the solution for the ferromagnetically saturated semiconductor for a full conduction band ($n = 2$). In that case only the second term in (4.5) contributes. Furthermore, the $n \to 0$-limit of second-order perturbation theory [126, 127] is fulfilled. X_σ and Y_σ are given by (2.44). The propagator $G^{(0)}_\sigma$ is defined as

$$G^{(0)}_\sigma(E-h_\sigma) = \frac{1}{N}\sum_{\mathbf{k}} \frac{1}{E+\mathrm{i}0^+ +\mu-\epsilon(\mathbf{k})-h_\sigma} \,. \tag{4.7}$$

In the next step the parameters in (4.6) are fixed by writing down the high-energy expansion of the Green function (4.5) at $n = 0$ and $n = 2$ and by comparing it with the general form (2.37) in terms of correlation functions obtained from (2.36). They explicitly read:

$$a_\sigma = S(S+1) - X_\sigma(X_\sigma+1), \quad b_\sigma = \frac{1}{2}J = d_\sigma, \quad c_\sigma = S(S+1) - Y_\sigma(Y_\sigma+1) \,. \tag{4.8}$$

The temperature dependence of the ISA self-energy is governed by the expectation values n_σ, Δ_σ and $\langle S^z\rangle$. With the one-electron Green function and its equation of motion the first two can be computed using the spectral theorem. The spin expectation value $\langle S^z\rangle$ requires the evaluation of the transversal spin Green function (Chap. 5) or must be considered as a parameter.

For film geometry the corresponding ansatz for the one-electron Green function matrix reads [205]

$$\begin{aligned}
&\underline{G}_{\mathbf{k}\sigma}(E) = \underline{G}^{(1)}_{\mathbf{k}\sigma}(E) + \underline{G}^{(2)}_{\mathbf{k}\sigma}(E) \\
&= \frac{1-\langle\bar{n}_\sigma\rangle}{(E+\mathrm{i}0^+ +\mu)\underline{I} - \underline{\epsilon}(\mathbf{k}) - \underline{M}^{(1)}_\sigma(E)} + \frac{\langle\bar{n}_\sigma\rangle}{(E+\mathrm{i}0^+ +\mu)\underline{I} - \underline{\epsilon}(\mathbf{k}) - \underline{M}^{(2)}_\sigma(E)} . \qquad (4.9)
\end{aligned}$$

The elements of the diagonal matrices $\underline{M}^{(1)}_\sigma$ and $\underline{M}^{(2)}_\sigma$ are as follows:

$$\begin{aligned}
M^{(1)}_{\alpha\sigma}(E) &= -\frac{1}{2}JX^\alpha_{-\sigma} + \frac{1}{4}J^2\frac{a^\alpha_{-\sigma}G^{\alpha(0)}_{-\sigma}(E-\frac{1}{2}JX^\alpha_{-\sigma})}{1-b^\alpha_{-\sigma}G^{\alpha(0)}_{-\sigma}(E-\frac{1}{2}JX^\alpha_{-\sigma})} , \\
M^{(2)}_{\alpha\sigma}(E) &= \frac{1}{2}JY^\alpha_{-\sigma} + \frac{1}{4}J^2\frac{c^\alpha_{-\sigma}G^{\alpha(0)}_{-\sigma}(E+\frac{1}{2}JY^\alpha_{-\sigma})}{1+d^\alpha_{-\sigma}G^{\alpha(0)}_{-\sigma}(E+\frac{1}{2}JY^\alpha_{-\sigma})} . \qquad (4.10)
\end{aligned}$$

All expectation values in the expressions for the parameters (4.8) now carry a layer index. In the numerator of (4.9) the layer-averaged occupation number $\langle\bar{n}_\sigma\rangle = \sum_\alpha\langle n_{\alpha\sigma}\rangle$ appears. The averaging is necessary to avoid inconsistencies concerning the Green function matrix $\underline{G}_{\mathbf{k}\sigma}$. However, this additional approximation also causes a drawback: the scheme becomes questionable if the charge carrier density of a given spin projection differs significantly in the individual layers. This is for example the case for an antiparallel alignment of two coupled ferromagnetic layers (Chap. 7). In the paramagnetic phase, variations in the carrier density are only due to charge transfer effects (Chap. 4.5) and the averaging is usually not a serious approximation.

4.3 Moment-conserving Decoupling Approach

The Moment-conserving Decoupling Approach (MCDA) to the one-electron Green function is an equation-of-motion (EOM) approach which makes use of exact limits and spectral-moment relations in order to decouple the EOM hierarchy. It has been applied by Nolting and co-workers to the bulk Kondo lattice ferromagnet [184, 186] and to semiconducting local-moment films ($n = 0$) [11, 216, 217]. In what follows, the approach is generalized to ferromagnetic Kondo lattice films with an arbitrary charge carrier density. For better readability the following presentation gives only a brief outline of the approximation scheme, focussing on the general philosophy and taking the reduced translational symmetry into account. Details on the MCDA can be found in Appendix A.

The starting point is the equation of motion (2.26) for the film matrix elements of the one-electron Green function in real-space representation:

$$EG_{ij\sigma}^{\alpha\beta}(E) = \delta_{ij}^{\alpha\beta} + \langle\langle [c_{i\alpha\sigma}, H_0 + H_I]_- ; c_{j\beta\sigma}^{\dagger}\rangle\rangle_E \tag{4.11}$$

The shorthand notation $\delta_{ij}^{\alpha\beta} = \delta_{\alpha\beta}\delta_{ij}$ has been used. Evaluating the commutator with the Hamiltonian (3.14) yields

$$\sum_{l\gamma} \left((E+\mu)\delta_{il}^{\alpha\gamma} + \frac{1}{2} z_\sigma J \langle S_\alpha^z \rangle + t_{il}^{\alpha\gamma} \right) G_{lj\sigma}^{\gamma\beta}(E) = \delta_{ij}^{\alpha\beta} - \frac{1}{2} J \left(z_\sigma I_{iij\sigma}^{\alpha\beta}(E) + F_{iij\sigma}^{\alpha\beta}(E) \right) \tag{4.12}$$

The two higher-order Green functions on the right-hand side,

$$I_{ijk\sigma}^{\alpha\beta}(E) = \langle\langle \delta S_{i\alpha}^z c_{i\alpha\sigma} ; c_{j\beta\sigma}^{\dagger} \rangle\rangle_E \, , \tag{4.13}$$

$$F_{ijk\sigma}^{\alpha\beta}(E) = \langle\langle S_{i\alpha}^{-\sigma} c_{i\alpha-\sigma} ; c_{j\beta\sigma}^{\dagger} \rangle\rangle_E \, , \tag{4.14}$$

describe an Ising-like interaction between the localized and the conduction electron spin and spinflip interactions between the two subsystems, respectively, and are hence named 'Ising' and 'spinflip' Green function. In (4.13) the abbreviation

$$\delta S_{i\alpha}^z = S_{i\alpha}^z - \langle S_\alpha^z \rangle \tag{4.15}$$

was introduced in order to separate the mean-field contribution to the self-energy from the rest. Then the equations of motion for the Ising and spinflip Green function are written down:

$$\begin{aligned} \sum_{l\gamma} \left((E+\mu)\delta_{kl}\delta_{\delta\gamma} + t_{kl}^{\delta\gamma} \right) I_{ilj\sigma}^{\alpha\gamma\beta}(E) &= \langle\langle [\delta S_{i\alpha}^z c_{k\delta\sigma}, H_I]_- ; c_{j\beta\sigma}^{\dagger} \rangle\rangle_E \\ &= \langle\langle \delta S_{i\alpha}^z \, [c_{k\delta\sigma}, H_I]_- ; c_{j\beta\sigma}^{\dagger} \rangle\rangle_E \\ &+ \langle\langle [\delta S_{i\alpha}^z, H_I]_- \, c_{k\delta\sigma} ; c_{j\beta\sigma}^{\dagger} \rangle\rangle_E \, , \end{aligned} \tag{4.16}$$

$$\begin{aligned} \sum_{l\gamma} \left((E+\mu)\delta_{kl}\delta_{\delta\gamma} + t_{kl}^{\delta\gamma} \right) F_{ilj\sigma}^{\alpha\gamma\beta}(E) &= \langle\langle \left[S_{i\alpha}^{-\sigma} c_{k\delta-\sigma}, H_I \right]_- ; c_{j\beta\sigma}^{\dagger} \rangle\rangle_E \\ &= \langle\langle S_{i\alpha}^{-\sigma} \, [c_{k\delta-\sigma}, H_I]_- ; c_{j\beta\sigma}^{\dagger} \rangle\rangle_E \\ &+ \langle\langle \left[S_{i\alpha}^{-\sigma}, H_I \right]_- \, c_{k\delta-\sigma} ; c_{j\beta\sigma}^{\dagger} \rangle\rangle_E \, . \end{aligned} \tag{4.17}$$

In the following step the higher-order Green functions on the right-hand sides are decoupled. The final result for the MCDA one-electron self-energy matrix for Kondo lattice films,

$$\underline{M}_\sigma(E) = -\frac{1}{2}Jz_\sigma\langle\underline{S}^z\rangle + \underline{M}^{\mathrm{c}}_\sigma(E, J)\,, \tag{4.18}$$

contains a local contribution $\underline{M}^{\mathrm{c}}_\sigma(E,\,J)$ which accounts for electronic correlation effects. They make the self-energy dynamic (energy-dependent) and complex, implying quasiparticle damping. Contrary to the mean-field contribution, $\underline{M}^{\mathrm{c}}_\sigma(E,\,J)$ does not vanish in the paramagnetic phase. Details on the MCDA decoupling procedure and the structure of (4.18) are given in Appendix A.

As regards the analytically known limits, the MCDA approach reproduces the ferromagnetically saturated semiconductor (Chap. 2.5). The atomic limit (Chap. 2.4) is recovered for an empty and for a fully occupied conduction band.

The self-energy (4.18) contains several expectation values which can only partly be calculated from MCDA Green functions using the spectral theorem (2.14). The localized-spin expectation values must be determined with the help of a suitably defined spin Green function. This problem will be treated separately in Chap. 5.

A noteworthy property of the MCDA self-energy is that there is no restriction on the quantum character of the localized spins. The approach can be used for any spin quantum number S. This issue is of great importance because the assumption of classical spins usually simplifies the treatment of the model considerably [189].

From now on the MCDA self-energy is used if not otherwise stated. The large number of fermionic, mixed, and localized-spin expectation values entering the self-energy (see Appendix A) suggests that the MCDA accounts better for electronic correlation effects in the Kondo lattice model than mean-field theory and the ISA approach.

4.4 Single-electron excitation spectrum

In this section the electronic structure of Kondo lattice model films is discussed in terms of the temperature-dependent spectral density and local density of states (4.1) calculated in the MCDA approximation. The influence of the model parameters, namely of

- the local exchange interaction J
- the charge carrier density n
- the spin quantum number S
- the number of monolayers N_{L}

on the excitation spectrum shall be studied. All numerical evaluations in this section were carried out for symmetric sc(100)-films. A uniform nearest-neighbor hopping $t = 1/12$ eV which corresponds to a monolayer bandwidth $W \equiv W_{\mathrm{m}ono} = 2/3$ eV and a bulk bandwidth $W_{\mathrm{b}ulk} = 1$ eV was used. The latter is taken as the energy unit, i.e. all energies are given in eV. First, the effects of the model parameters are investigated for the monolayer film (square lattice). Then the electronic structure of films consisting of more than one monolayer is analyzed.

A remark should be made about the spin polarization in the ferromagnetic phase. It was already pointed out in Chap. 2.1 that it is debated under what conditions the Kondo lattice has a fully saturated ferromagnetic ground state. In the combined approach used in this work the two subsystems of the conduction band electrons and the localized spins are treated separately. The effective spin Hamiltonian presented in Chap. 5 imposes a full saturation of the localized magnetic moments at $T = 0$ (being most probably an artefact of the method) even within a self-consistent treatment of the whole model.

Because the low-energy $\downarrow$-states are scattering states associated with magnon emission, a fully saturated spin system is obviously in conflict with a finite $\downarrow$-band occupation. Nonetheless, a fully aligned spin system is assumed for $T = 0$ in the following discussion of the electronic structure. This allows to check if a completely polarized ground state is possible, which requires the conduction band to be fully polarized, too. If there is some finite $\downarrow$-spectral weight below the chemical potential this hints at a reduced $\langle S^z \rangle < S$ at $T = 0$.

Fig. 4.2 shows the temperature dependence of the monolayer LDOS. There are two quasiparticle bands of comparable width for each spin projection. For $T = 0$ the spectrum resembles that of the ferromagnetically saturated semiconductor (cf. Fig. 2.3). The $\uparrow$-LDOS is essentially the non-interacting Bloch density of states shifted by $\approx -\frac{1}{2}JS$ and corresponds to $\uparrow$-quasiparticle states associated with a parallel coupling to the localized spins. The $\downarrow$-spectrum consists of two parts: most of the spectral weight constitutes a band of $\downarrow$-quasiparticle states associated with an antiparallel coupling to the local moments. A second band lies in the energy range of the $\uparrow$-LDOS. These states correspond to the finite scattering probability of an added $\downarrow$-electron into $\uparrow$-states. If there is a finite $\downarrow$-weight below the chemical potential the conduction band is not fully polarized. At $T = 0$ the $\uparrow$-spectral density shown in Fig. 4.3 consists of δ-peaks located at the rigidly shifted Bloch energies. The similarly sharply defined $\downarrow$-spectral density of the upper band stands much in contrast to the smeared out spectral density representing the scattering states.

With increasing temperature spin symmetry is gradually established. The δ-peaks of the $\uparrow$-spectrum broaden and a scattering $\uparrow$-quasiparticle band evolves at higher energies because now an $\uparrow$-electron, too, can flip its spin while *absorbing* a

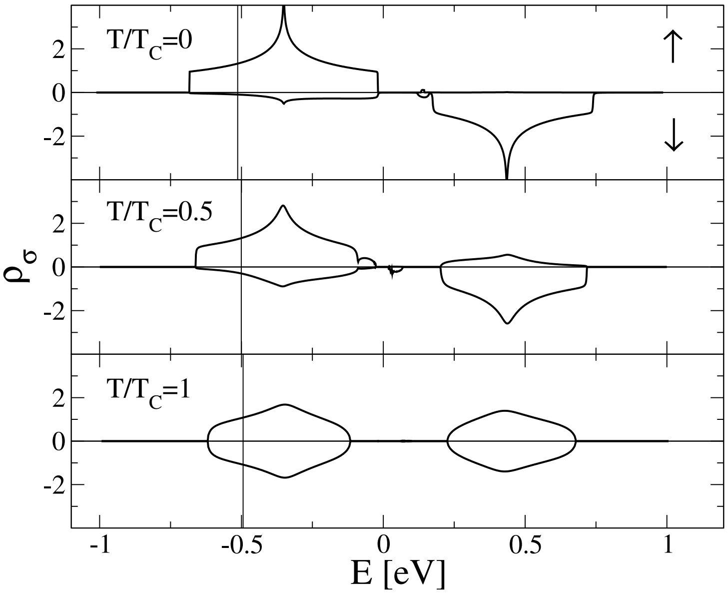

Figure 4.2: Square-lattice LDOS for different reduced temperatures T/T_{C}. The vertical lines indicate the chemical potential. Curie temperature: $T_{\mathrm{C}} = 100$ K. Self-consistently calculated magnetization (Chap. 5). $T/T_{\mathrm{C}} = 0.5$ corresponds to $\langle S^z \rangle = 2.52$. Parameters: $n = 0.2$, $J = 0.2$, $S = 7/2$.

magnon. The spectral weight of the ↓-states associated with a parallel coupling to the local moments increases with the depolarisation of the spin system. At $T = T_{\mathrm{C}}$ the gap between the quasiparticle bands is larger than for T=0 because the bandwidths are smaller as a consequence of the reduced effective hopping due to the thermal disorder in the local moment subsystem. The centers of gravity of the subbands are separated by $\Delta E \approx J\left(S + \frac{1}{2}\right)$ and agree with the atomic limit results (2.40).

Fig. 4.4 demonstrates how the LDOS depends on the local exchange coupling J. In the saturated ferromagnetic phase the dependence is essentially the same as for the FM saturated semiconductor (Chap. 2.5). With increasing J a mean-field-like shift is followed by a 'polaron band' splitting off the ↓-scattering band. In the paramagnetic phase one observes a similar behavior. Once two distinct bands have evolved they are rigidly shifted apart when J is increased. However, due to the reduced bandwidth the gap between the quasiparticle bands opens at a lower value of J than in the ferromagnetic phase.

Fig. 4.5 shows the effects of varying the charge carrier density in the ferromagnetic and in the paramagnetic phase for rather strong coupling ($JS = 1 = 1.5W$). As regards the lower quasiparticle band one observes a decrease of spectral weight with increasing n. In the FM phase the loss affects only the ↓-part. The be-

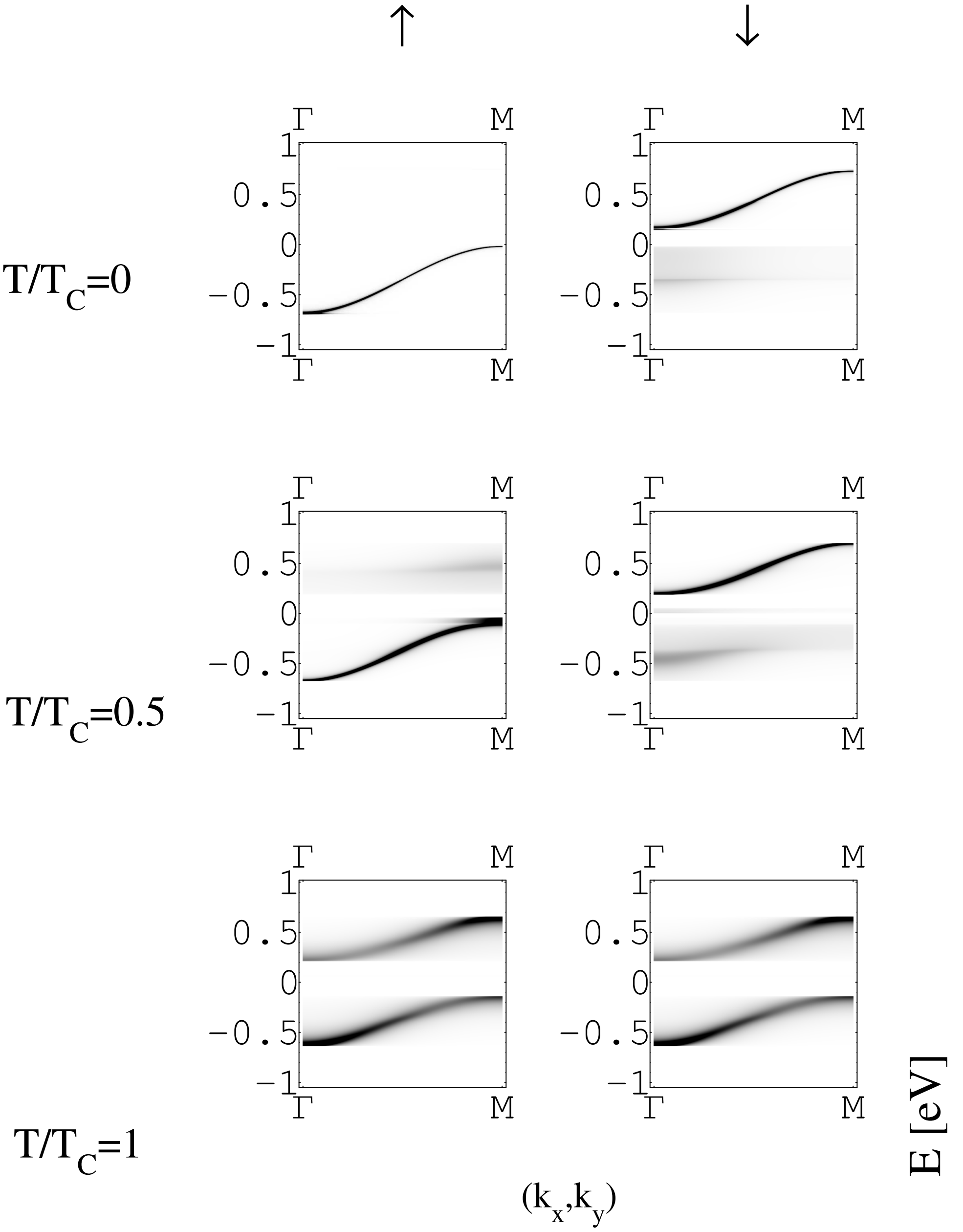

Figure 4.3: Temperature dependence of the spectral density $S_{\mathbf{k}\sigma}(E)$ for the monolayer from the Γ-point (k_x, k_y)=(0,0) to the M-point (π, π). Parameters as in Fig. 4.2.

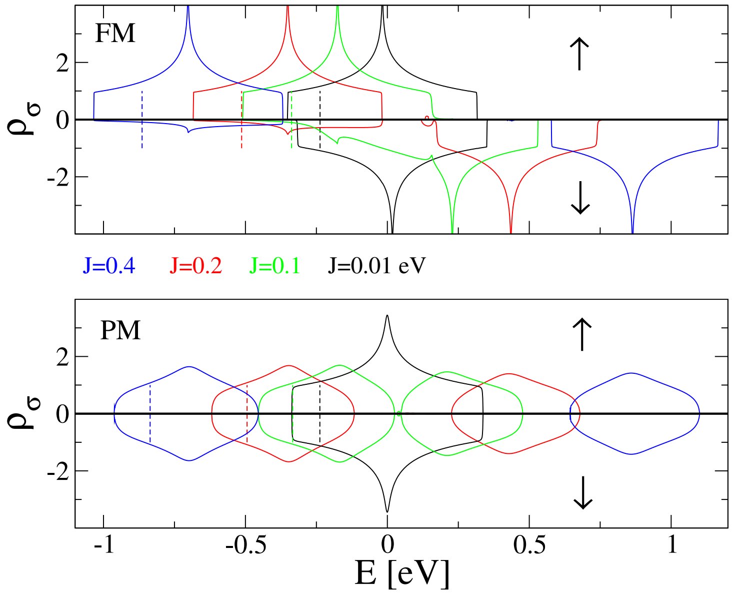

Figure 4.4: Ferromagnetic (FM) and paramagnetic (PM) square-lattice LDOS for different values of the intra-atomic exchange coupling J. The local-moment system is assumed to be saturated in the ferromagnetic phase ($\langle S_z \rangle = S$). Vertical lines indicate the chemical potential. Parameters: $T = 0$, $n = 0.2$, $S = 7/2$.

havior of the ↓-spectral weight below the Fermi energy leads to a charge carrier polarization

$$P = \frac{n_\uparrow - n_\downarrow}{n_\uparrow + n_\downarrow} \tag{4.19}$$

that depends on the band filling as shown in the inset. One observes an increasingly high though not complete conduction band polarization for $JS = 1$ as n rises. For very strong coupling ($JS = 4$) there is a quasi-complete polarization above $n \approx 0.5$. On the contrary for weak coupling ($JS = 0.111 = W/6$), the polarization is maximal if the charge carrier density is low and then rapidly decreases before saturating on a moderate level with $P \approx 0.25$. This reflects the fact that in the mean-field regime the ↑- and ↓-band are essentially rigidly separated by a small exchange splitting.

Another significant feature in both the FM and the PM phase is the shift of the upper band towards lower energies when n is increased. Both trends are in accordance with the behavior of the spectral weight in the atomic limit (cf. Fig. 2.2). As concerns the transfer of spectral weight, in the zero-bandwidth limit the FM and PM spectral weight of the excitation energy E_1 decreases towards half-filling. The shift of the upper band in Fig. 4.5 can be interpreted as the change

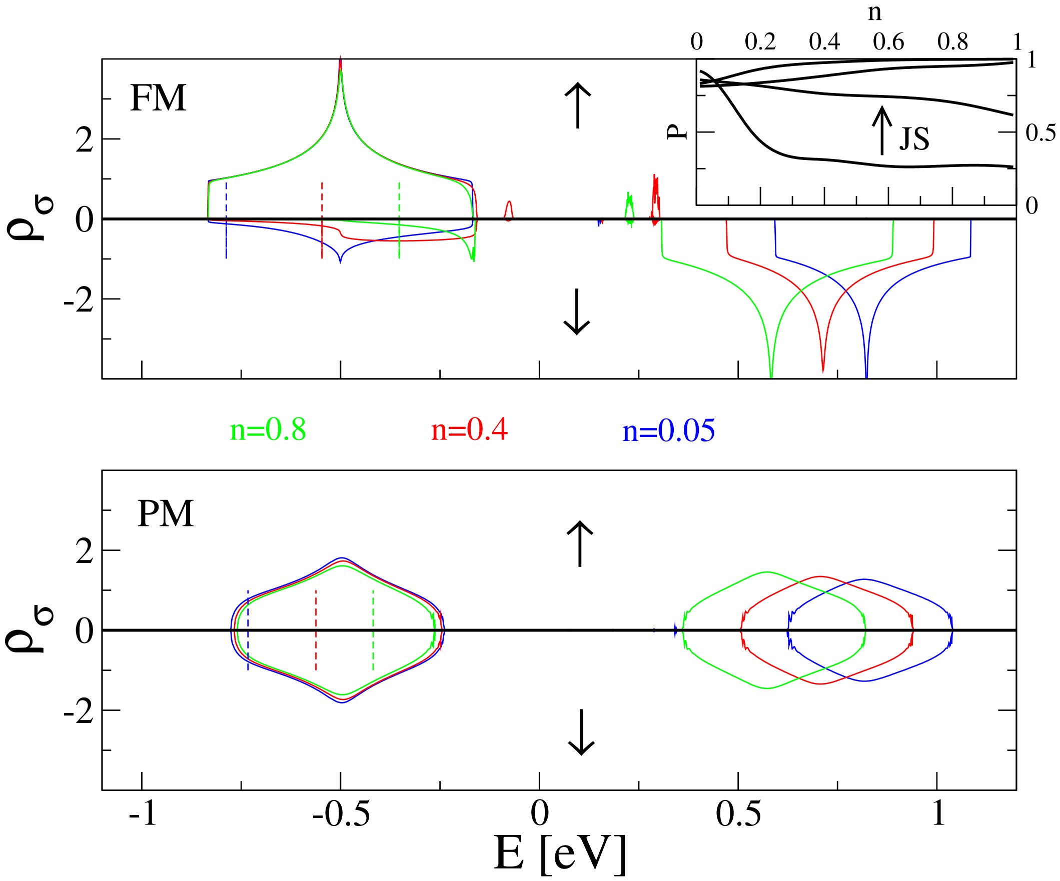

Figure 4.5: Ferromagnetic and paramagnetic square lattice LDOS for different values of the charge carrier density n. Parameters: T=0, $JS = 1$, $S = 3/2$. Inset: Polarization of the conduction band for different values of the effective coupling JS. From bottom to top: $JS = 0.111$, 0.333, 1, and 4.

from a ’polaron-like character’ associated predominantly with single-occupancies of the lattice sites to a quasiparticle band of states related to double-occupancies with a band center $\approx \frac{1}{2}JS$ for a carrier density near $n = 1$. In the atomic limit one observes a similar behavior: a decrease of spectral weight of the pole E_2 is accompanied by an increase of the weight of $E_4 = \frac{1}{2}JS$, both for a finite magnetization and in the PM phase. The Stoner-like transition between the two quasiparticle bands is likely to be a shortcoming of the MCDA approximation. On the other hand this only concerns energies well-above the chemical potential and is thus only a minor drawback of the method.

Fig. 4.6 presents the monolayer LDOS for some spin magnitudes from $S = 1/2$ to $S = 10$, the latter practically representing a classical spin ($S \to \infty$). The effective coupling is the same in all cases. Note that the band centers of gravity scale differently, the lower one $\sim JS$ and the upper one $\sim J(S+1)$. One observes that the $\uparrow$-band in the FM state is practically unaltered, i.e. it scales with JS, a behavior which resembles the analytically known behavior for $n = 0$. On the other hand there is a shift of spectral weight in the PM and in the FM phase (for the $\downarrow$-band) when the spin quantum number is varied: the lower the spin quantum number S, the larger the spectral weight of the lower quasiparticle band.

This variation of the spectral weight with S can be traced back to the different spin configurations associated with the quasiparticle bands in the LDOS. The lower and upper band correspond to states connected with a parallel and an antiparallel alignment, repectively, of the itinerant and the localized spin. In an atomic picture this coupling results in a total spin $S^{\uparrow\uparrow}_{tot} = S + \frac{1}{2}$ for the parallel alignment and $S^{\uparrow\downarrow}_{tot} = S - \frac{1}{2}$ for the antiparallel alignment. Obviously the parallel alignment offers more spin states (labelled by $m_{S_{tot}} = -S_{\text{tot}}, .., S_{tot}$) than the antiparallel coupling. For $S = 1/2$ the ratio of the parallel spin states and the antiparallel spin states is 3:1 (’triplet’ vs. ’singlet’), as opposed to an equal number of both kinds of spin states for $S \to \infty$. The larger relative fraction of parallel spin states for a lower spin quantum number leads to an increase of the relative spectral weight in the many-body problem via the matrix elements in the Lehmann representation (2.17). It is worthwhile mentioning that the instability of the ferromagnetic state with respect to paramagnetism for $S = 1/2$ in the phase diagram shown in Fig. 2.1 can be traced back to this spectral weight effect [189].

The $\downarrow$-spectral weight of the lower band in the FM phase is strongly reduced for $S = 10$, indicating the suppression of scattering processes for classical localized spins ($S \to \infty$). There is, however, a difference concerning the LDOS below and above the Fermi energy: whereas above ϵ_{F} the spectral weight decreases continuously with increasing S, it depends non-monotonously on S below ϵ_{F}. As a consequence the lowest polarization of the conduction band occurs for $S = 3/2$ and not for the quantum spin number $S = 1/2$ as one might naively expect. The

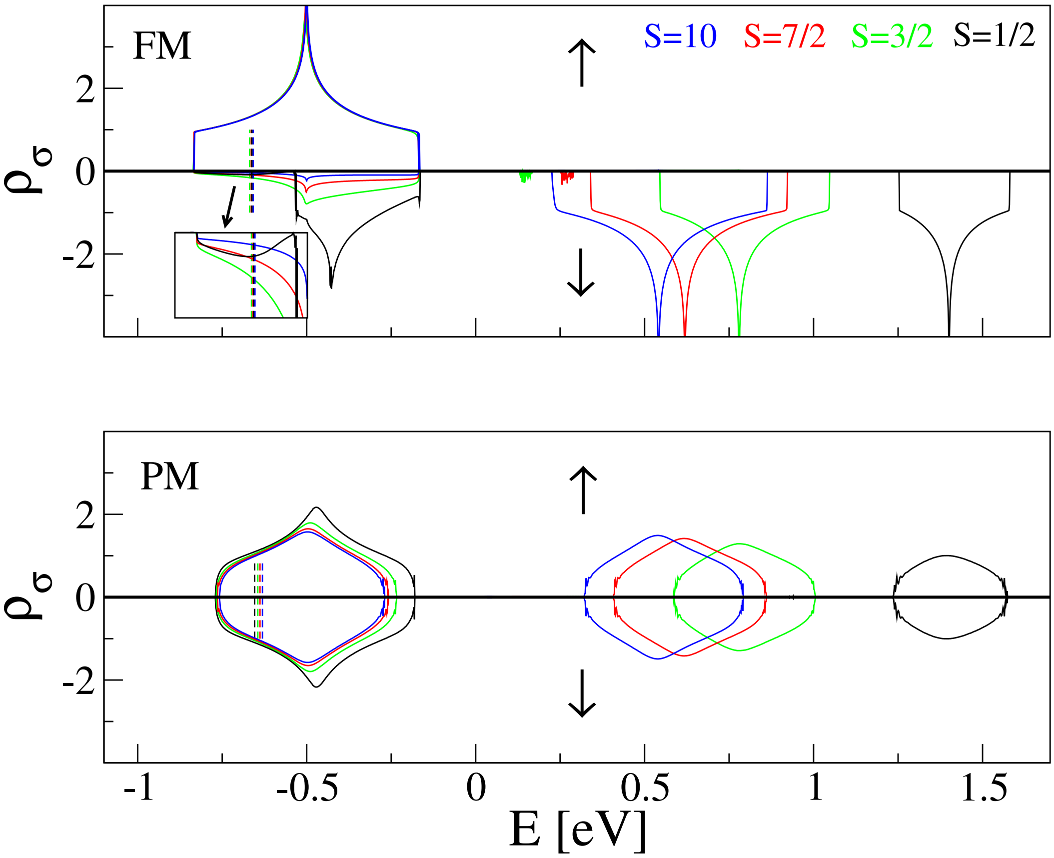

Figure 4.6: Ferromagnetic and paramagnetic square lattice LDOS for different values of the spin quantum number S. The inset in the upper panel shows part of the LDOS on a magnified scale. Parameters: $T = 0$, $JS = 1$, $n = 0.2$.

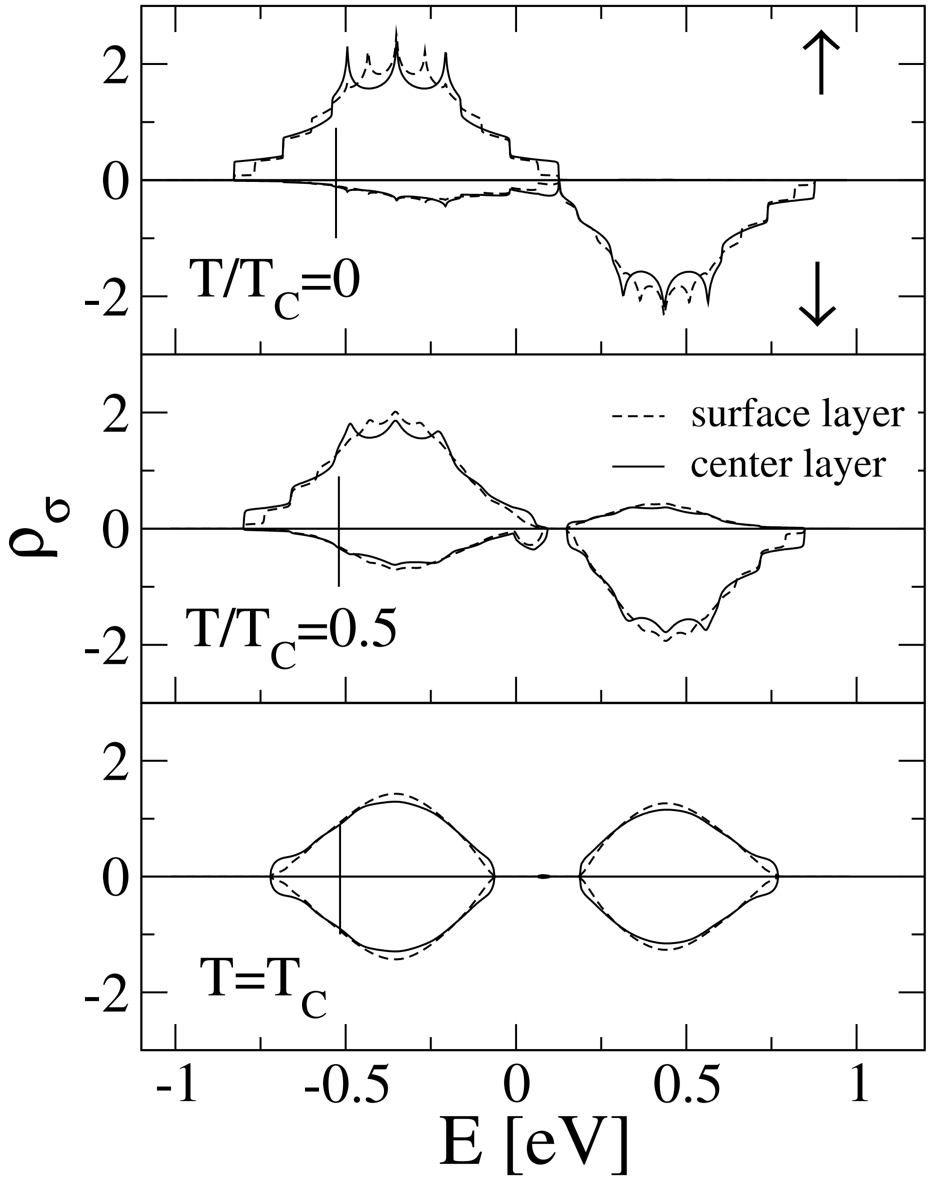

Figure 4.7: Temperature dependence of the LDOS for a 5ML-film. Curie temperature: $T_{\mathrm{C}} = 174$ K. Self-consistently calculated magnetization (Chap. 5). $T/T_{\mathrm{C}} = 0.5$ corresponds to $\langle S_3^z \rangle = 2.62$. Parameters: $n = 0.2$, $J = 0.2$, $S = 7/2$.

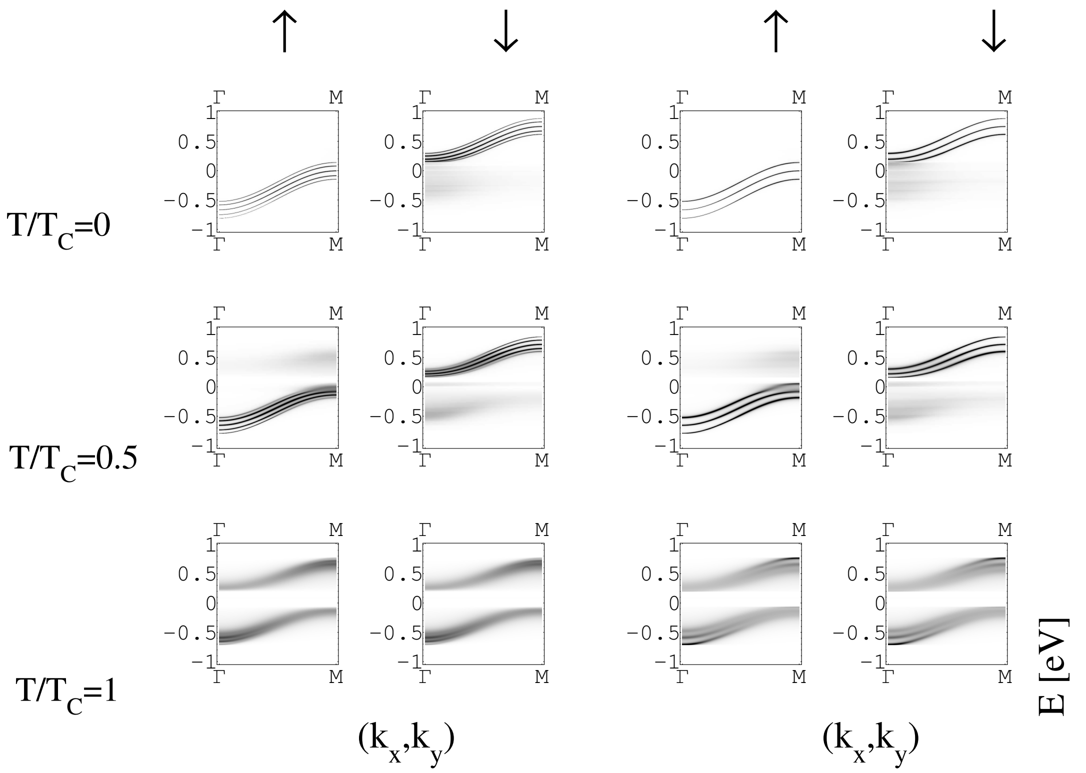

Figure 4.8: Spectral density corresponding to the temperature scan of the LDOS for the 5ML-film in Fig. 4.7. Left: surface layers $S^{11}_{\mathbf{k}\sigma}(E) = S^{55}_{\mathbf{k}\sigma}(E)$, right: center layer $S^{33}_{\mathbf{k}\sigma}(E)$.

inset in the upper panel of Fig. 4.6 shows the low-energy part of the ↓-LDOS in greater detail.

The T-dependent LDOS and spectral density for a 5ML-film and otherwise the same parameters as in Fig. 4.2 are shown in Figs. 4.7 and 4.8, respectively. At low temperatures the LDOS exhibits more van-Hove singularities than the monolayer LDOS as the electronic structure is composed of five subbands shifted with respect to each other. In general, the excitation spectrum of an N_{L}-layer film consists of N_{L} subbands (Chap. 3.1). The multiband structure is clearly visible in the spectral density in Fig. 4.8.

Apart from these multiband features the overall characteristics of the temperature dependence of the interacting LDOS is the same as for the monolayer (Figs. 4.2 and 4.3) and is interpreted within the quasiparticle picture in the same way. The band-splitting occurs at a higher critical value of J due to the larger bandwidth caused by the interlayer hopping. Differences to the square lattice

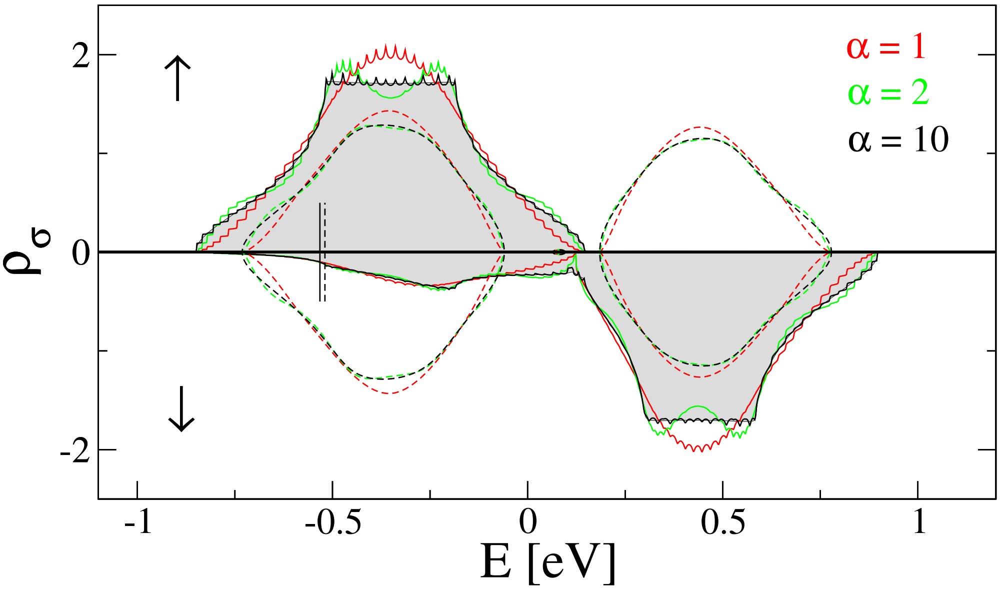

Figure 4.9: Surface- (α=1), subsurface- (α=2), and center-layer (α=10) LDOS of a 20ML-film in the ferromagnetic (full lines) and paramagnetic phase (dashed lines). The parameters are the same as in Fig. 4.2 and 4.7. The shaded area is the ferromagnetic bulk LDOS.

are related to the reduced translational symmetry and are the same as discussed in Chap. 3.3 for non-interacting films: the LDOS becomes layer-dependent and the surface LDOS has a lower coordination number and hence a reduced effective bandwidth compared to the center layer.

Fig. 4.9 finally shows the LDOS of a 20ML-film. Whereas the elliptic-shaped surface-layer LDOS and the subsurface-layer LDOS show clear deviations from the shape of the bulk LDOS, the center-layer LDOS is practically identical to the latter apart from small van-Hove peaks. Provided the film is thick enough, it is thus justified to speak of the 'bulk' part or properties of a film when referring to the center layer(s). Conversely, the surface properties of a semi-infinite lattice may be studied in good approximation by considering a film consisting of a sufficiently large number of layers. This will be exploited in Chap. 6.5 where ferromagnetism at the surface of KLM films will be discussed.

As a consequence of the layer-dependence of the LDOS the charge carrier density becomes generally layer-dependent, too. Deviations from a homogeneous charge distribution are referred to as charge transfer and will be discussed in the next section.

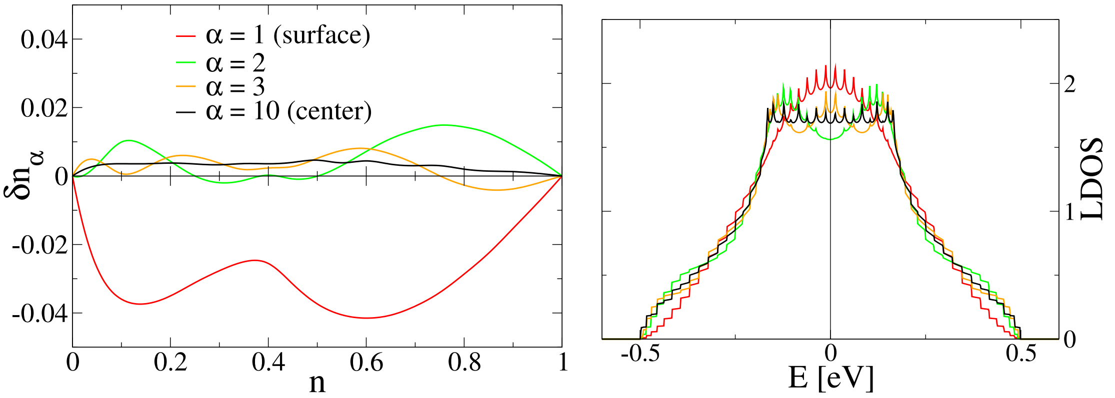

Figure 4.10: Left: charge transfer in a 20ML-sc(100)-film in the non-interacting limit ($J = 0$). Right: corresponding layer-dependent Bloch-LDOS.

4.5 Charge transfer

As a measure for the charge transfer in a film one may take the difference between the charge density in a given layer and the layer-averaged band filling:

$$\delta n_\alpha \equiv n_\alpha - n = \sum_\sigma (n_{\alpha\sigma} - \frac{1}{N_L} \sum_\gamma n_{\gamma\sigma}) . \tag{4.20}$$

Charge transfer already occurs in the non-interacting limit $J = 0$ (Chap. 3.3). The effect can be qualitatively illustrated by means of the layer-dependent LDOS (right panel of Fig. 4.10). Thermodynamical equilibrium means a common chemical potential in all layers. With respect to the smaller effective bandwidth of the surface layer this implies a reduced charge density in the surface layer, $\delta n_{\alpha=1} < 0$ for $n < 1$ (i.e. for μ lying in the lower half of the Bloch-LDOS). Due to the same reason the reverse effect occurs above half-filling ($\delta n_{\alpha=1} > 0$ if $n > 1$). For a bipartite lattice, like e.g. the simple cubic structure and nearest-neighbor hopping, the charge distribution at half-filling is homogeneous because of particle-hole symmetry. The left panel of Fig. 4.10 shows the charge transfer as a function of the average band filling in a non-interacting 20ML-film. Charge transfer is most significant in the surface layer. The relative effect is most pronounced for small charge densities $n \lesssim 0.1$ where the reduction in the surface layer can amount to ≈50% of the layer-averaged carrier density.

Of course any charge transfer in a real system will evoke counterbalancing Coulomb potentials which are not considered in the present case. However, as already pointed out in the discussion of the atomic limit (Chap. 2.4), the local spin-exchange interaction $J > 0$ has a similar effect as the on-site repulsive Coulomb matrix element U because both interactions punish energetically unfa-

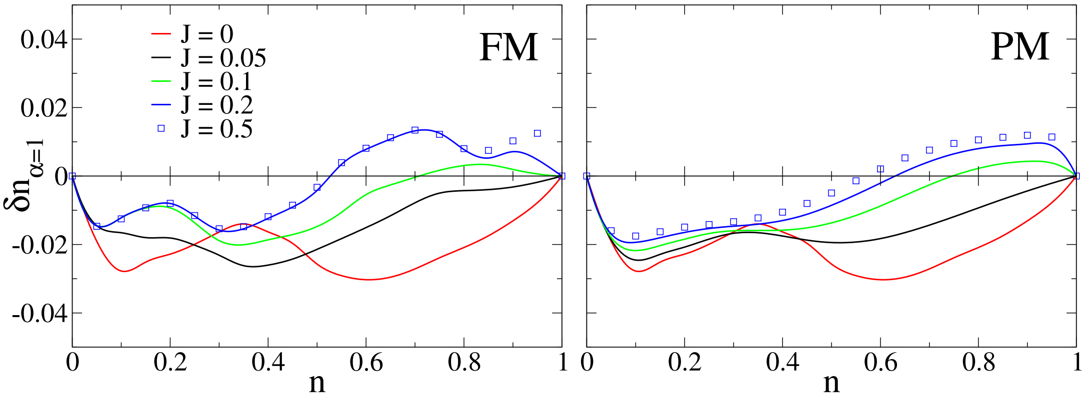

Figure 4.11: Charge transfer in the surface layer of an interacting 5ML-sc(100)-film (MCDA). Left: ferromagnetic phase, right: paramagnetic phase. The red line represents the non-interacting limit. Parameters: $T = 0$, $S = 7/2$.

vorable double-occupancies. Hence by switching on J the consequences of a short-range Coulomb repulsion are accounted for to some degree. It can be expected that this effective repulsion suppresses charge transfer.

As already pointed out in Chap. 3.1 a simple way to take counterbalancing Coulomb potentials effectively into account is to determine the centers of gravity of the Bloch bands in (3.14) self-consistently such that charge neutrality is ensured. The effect of charge transfer vs. charge neutrality on the magnetization and the Curie temperature will be discussed in Chap. 6.

Fig. 4.11 demonstrates the charge transfer at the surface of an interacting film. Contrary to the non-interacting case the variation of $\delta n_{\alpha=1}$ with the average density includes a change of sign below half-filling which is governed by the size of J. This difference is due to the correlation effects producing two quasiparticle bands for each spin projection. The same argument as above regarding the position of μ and the layer-dependent occupation applies: $\delta n_{\alpha=1}$ changes sign when the chemical potential reaches about the middle of the lower majority-spin quasiparticle band, however due to the distribution of spectral weight this occurs for $n < 1$. The value of n where the change of sign takes place decreases monotonously with increasing J and finally saturates, reflecting the evolution of the two quasiparticle bands out of one Bloch band. Once there are two separate bands their shape remains largely unaltered when J is further increased, and so does charge transfer.

Being a geometrical effect it does not come as a surprise that the charge transfer is essentially the same in the ferromagnetic and the paramagnetic phase. The main difference is the smoother dependence on n in the PM phase because the paramagnetic LDOS lacks the van-Hove singularities of the ferromagnetic LDOS.

Fig. 4.12 shows how the charge distribution varies with increasing J. For the

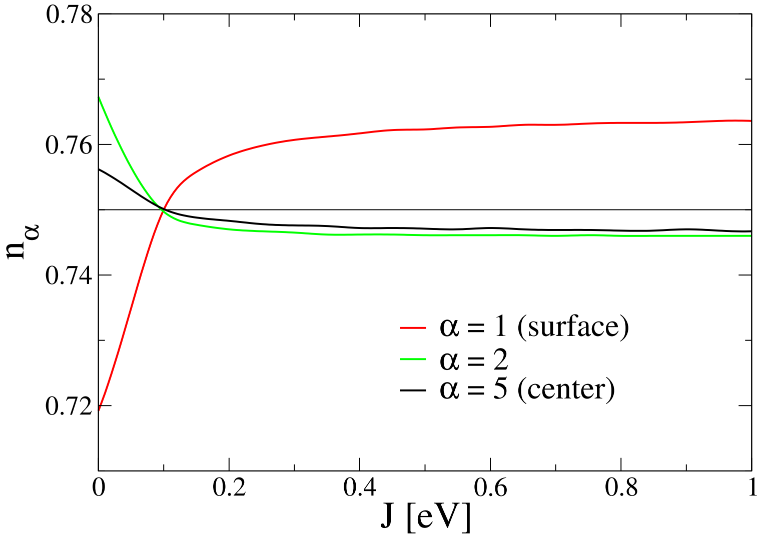

Figure 4.12: Charge transfer in different layers of a 10ML-sc(100)-film in the paramagnetic phase. Parameters: $n = 0.75$, $T = 0$, $S = 7/2$.

chosen average band filling the chemical potential lies in the lower half of the Bloch bands at $J = 0$ and consequently the surface charge carrier density is reduced. With increasing interaction strength spectral weight is redistributed and μ moves to the upper half of the majority quasiparticle band and hence $\delta n_{\alpha=1} > 0$. This is accompanied by a reverse change of sign of the charge transfer in the subsurface layers. One observes that even a quite large J does not lead to complete charge neutrality in the film. For strong coupling the charge transfer effect saturates resulting in a higher occupation of the surface layer while the charge distribution is almost homogeneous in the other layers. To summarize one can state that charge transfer is most pronounced in the weak-coupling regime and for low average charge carrier density n.

The above discussion on charge transfer served to get a quantitative and qualitative estimate of the effect in KLM films. Being restricted to the sc(100)-film geometry it is by no means exhaustive. Charge transfer effects are stronger in open surface geometries with a higher relative reduction of the coordination number at the surface. For instance, it was shown for the Hubbard model that charge transfer is about 3-4 times larger at the surface of an sc(111)-film with a coordination number ratio of $(z_{surf}/z_{\text{bulk}})_{\text{sc}(111)}$=1/2 compared to $(z_{surf}/z_{bulk})_{\text{sc}(100)}$=5/6 in the present case [211]. For comparison the ratio for the Gd-hcp(0001) lattice structure is $(z_{surf}/z_{\text{bulk}})_{\text{hcp}(0001)}$=2/3 and thus lies between the values for sc(100)- and sc(111)-geometry.

Chapter 5

Local-moment interaction

The carrier-mediated magnetism of the Kondo lattice is a result of the indirect interaction among the spins $\mathbf{S}_{i\alpha}$. In order to treat spontaneous magnetic order the transversal spin Green function is introduced:

$$P_{ij}^{\alpha\beta}(E) = \langle\langle S_{i\alpha}^{+}; S_{j\beta}^{-}\rangle\rangle_{E} \,. \tag{5.1}$$

The poles of the Green function matrix $\underline{P}_{\mathbf{q}}$ correspond to the excitations of the localized-spin subsystem. The low-energy modes are collective excitations called spin waves [112, 218]. By means of the transversal spin Green function one can calculate the layer-dependent magnetization $\propto \langle S_{\alpha}^{z}\rangle$ of the local moments as well as higher-order expectation values like $\langle (S_{\alpha}^{z})^{2}\rangle$, $\langle S_{\alpha}^{+}S_{\alpha}^{-}\rangle$ etc. which enter the electronic self-energy discussed in Chap. 4.

One possibility is to evaluate this Green function directly in connection with the Hamiltonian (3.14) using the Random Phase Approximation (RPA) [91, 133, 219] or the Mori (projection operator) formalism [146, 147]. Another ansatz is to map the intra-atomic interaction H_I onto a bilinear localized-spin Hamiltonian [184, 185, 186]. This is the strategy followed in this work. The next two sections deal with approaches which yield such effective Heisenberg Hamiltonians. An approximate solution for the spin Green function (5.1) is obtained using the Tyablikov (RPA) approach to the Heisenberg model.

5.1 Ruderman-Kittel-Kasuya-Yosida interaction

The Ruderman-Kittel-Kasuya-Yosida (RKKY) theory treats the intra-atomic interaction H_I perturbatively. Originally, it was proposed to describe the interaction between two nuclear spins [150, 220], and later applied to the case of two magnetic moments which are exchange-coupled to conduction electrons [6, 7].

Second-order perturbation theory for two magnetic moments situated at 0 and $\mathbf{r}$, each interacting with a non-magnetic electron gas via (2.3), yields the following effective bilinear spin Hamiltonian:

$$H_{\mathrm{R}KKY} = -J^{\mathrm{R}KKY}(\mathbf{r})\mathbf{S}(\mathbf{0})\mathbf{S}(\mathbf{r})\,. \tag{5.2}$$

The exchange integral or range function $J^{\mathrm{R}KKY}(\mathbf{r})$ is given by the Fourier transform of the non-uniform static susceptibility (Lindhard function) $\chi(\mathbf{q})$:

$$J^{\mathrm{R}KKY}(\mathbf{r}) = \frac{1}{2}J^2\chi(\mathbf{r})\,. \tag{5.3}$$

$\chi(\mathbf{r})$ can be expressed in terms of the Matsubara Green function [213]:

$$\chi(\mathbf{r}) = -\frac{1}{\beta}\sum_n \left(G(i\omega_n, \mathbf{r})\right)^2\,. \tag{5.4}$$

$\omega_n = \frac{(2n+1)\pi}{\beta}$ are fermionic Matsubara frequencies and the thermal Green function $G(i\omega_n, \mathbf{r})$ is the Fourier transform of $G(i\omega_n, \mathbf{k}) = (i\omega_n - \epsilon(\mathbf{k}))^{-1}$.

For the 3D free electron gas the asymptotic behavior of the exchange integral ($k_{\mathrm{F}}r \gg 1$) is [152, 214]

$$J^{\mathrm{R}KKY}_{\mathrm{3D}}(r) = -\frac{1}{\pi}J^2\rho_0(\epsilon_{\mathrm{F}})k_{\mathrm{F}}^3\frac{cos(2k_{\mathrm{F}}r)}{(2k_{\mathrm{F}}r)^3}\,. \tag{5.5}$$

k_{F} is the Fermi wave vector and $\rho_0(\epsilon_{\mathrm{F}})$ is the density of states at the Fermi level. Characteristic features of the RKKY interaction are its long range and oscillating sign. The effective exchange is quadratic in the intra-atomic coupling and thus does not depend on the sign of J. The RKKY range function has also been obtained in 1D [153, 155] and 2D [154]. An analytic expression for arbitrary dimension is presented in Ref. [152].

The RKKY interaction shall now be formulated in terms of the retarded Green function for film geometry. Using a mixed Wannier-Bloch representation the intra-atomic interaction term in (3.14) reads

$$H_I = -\frac{J}{2N}\sum_{i\alpha\sigma\sigma'}\sum_{\mathbf{k}q} e^{-\mathrm{i}\mathbf{q}\mathbf{R}_i}\left(\mathbf{S}_{i\alpha}\cdot\boldsymbol{\sigma}\right)_{\sigma\sigma'} c^\dagger_{\mathbf{k}+\mathbf{q}\alpha\sigma}c_{\mathbf{k}\alpha\sigma'}\,. \tag{5.6}$$

$\boldsymbol{\sigma} = (\sigma_x, \sigma_y, \sigma_z)$ are the Pauli matrices. The mapping of H_I onto an effective localized spin Hamiltonian of the form (5.2) is achieved by integrating out the fermionic degrees of freedom:

$$H_{\mathrm{eff}} \equiv \langle H_I\rangle^{(c)} = -\frac{J}{2N}\sum_{i\alpha\sigma\sigma'}\sum_{\mathbf{k}q} e^{-\mathrm{i}\mathbf{q}\mathbf{R}_i}\left(\mathbf{S}_{i\alpha}\cdot\boldsymbol{\sigma}\right)_{\sigma\sigma'} \langle c^\dagger_{\mathbf{k}+\mathbf{q}\alpha\sigma}c_{\mathbf{k}\alpha\sigma'}\rangle^{(c)}\,. \tag{5.7}$$

The superscript 'c' indicates that the statistical average $\langle..\rangle = \frac{1}{\Xi}\mathrm{T}r(\mathrm{e}^{\beta H}..)$ is carried out with states of the fermionic Hilbert subspace only. This holds also for the 'restricted' Green function

$$G^{(c)\sigma'\sigma}_{\mathbf{k},\mathbf{k}+\mathbf{q}\alpha\beta}(E) = \langle\langle c_{\mathbf{k}\alpha\sigma'}; c^{\dagger}_{\mathbf{k}+\mathbf{q}\beta\sigma}\rangle\rangle^{(c)}_{E} \,. \tag{5.8}$$

In order to obtain an approximate solution for the restricted Green function consider its equation of motion (2.19):

$$\begin{aligned}\sum_{\gamma}\left((E+\mu)\delta_{\gamma\alpha} - \epsilon_{\alpha\gamma}(\mathbf{k})\right) G^{(c)\sigma'\sigma}_{\mathbf{k},\mathbf{k}+\mathbf{q}\gamma\beta}(E) &= \delta_{\mathbf{q}\mathbf{0}}\delta_{\sigma\sigma'}\delta_{\alpha\beta} \\ &- \frac{J}{2N}\sum_{i\mathbf{p}\sigma''} e^{i(\mathbf{k}-\mathbf{p})\mathbf{R}_i}\left(\mathbf{S}_{i\alpha}\cdot\boldsymbol{\sigma}\right)_{\sigma'\sigma''} G^{(c)\sigma''\sigma}_{\mathbf{p},\mathbf{k}+\mathbf{q}\alpha\beta}(E)\,.\end{aligned} \tag{5.9}$$

Using the unperturbed one-electron Bloch states in conventional RKKY theory corresponds to solving (5.9) to lowest order. Hence the restricted propagator on the right-hand side is replaced by the free propagator:

$$G^{(c)\sigma''\sigma}_{\mathbf{p},\mathbf{k}+\mathbf{q}\alpha\beta}(E) \rightarrow \delta_{\mathbf{p},\mathbf{k}+\mathbf{q}} G^{\alpha\beta(0)}_{\mathbf{k}+\mathbf{q}}(E)\,. \tag{5.10}$$

The expectation value in (5.7) can be calculated by exploiting the spectral theorem (2.14). This finally yields

$$H^{\mathrm{RKKY}}_{\mathrm{eff}} = -\sum_{ij}\sum_{\alpha\beta} J^{\mathrm{RKKY}}_{i\alpha j\beta}\mathbf{S}_{i\alpha}\mathbf{S}_{j\beta}\,. \tag{5.11}$$

The RKKY exchange integrals for film geometry are given by

$$\begin{aligned}J^{\mathrm{RKKY}}_{\alpha\beta}(\mathbf{q}) &= \frac{1}{N}\sum_{ij}\mathrm{e}^{\mathbf{i}\mathbf{q}(\mathbf{R}_i-\mathbf{R}_j)}J^{\mathrm{RKKY}}_{i\alpha j\beta} \\ &= \frac{J^2}{2\pi N}\sum_{\mathbf{k}}\mathrm{Im}\int\limits_{-\infty}^{+\infty} dE f_{-}(E) G^{\alpha\beta(0)}_{\mathbf{k}}(E-\mu) G^{\beta\alpha(0)}_{\mathbf{k}+\mathbf{q}}(E-\mu)\,.\end{aligned} \tag{5.12}$$

In case of translational invariance in all spatial direction the greek layer indices can be dropped. The energy integration in (5.12) yields

$$J^{\mathrm{RKKY}}(\mathbf{q}) = -\frac{J^2}{2N}\sum_{\mathbf{k}}\frac{f_{-}(\epsilon(\mathbf{k}+\mathbf{q})) - f_{-}(\epsilon(\mathbf{k}))}{\epsilon(\mathbf{k}+\mathbf{q}) - \epsilon(\mathbf{k})}\,. \tag{5.13}$$

The result (5.5) is obtained from the Fourier transform of this expression after carrying out the **k**-sum in 3D using a parabolic effective-mass dispersion. The long-wavelength limit ($\mathbf{q} \to \mathbf{0}$) of (5.13) is equivalent to the sum over all exchange integrals and can be expressed in terms of the density of states at the Fermi energy:

$$\sum_j J_{ij}^{\mathrm{R}KKY} = J^{\mathrm{R}KKY}(\mathbf{q}=0) = \frac{1}{2} J^2 \rho(\epsilon_{\mathrm{F}}) \,. \tag{5.14}$$

5.2 Modified RKKY interaction

The perturbational RKKY theory is valid in the weak-coupling regime. The restriction to a small polarization of the charge carriers is lifted in an extention of the conventional RKKY approach. This modified version was originally devised for a local-moment bulk ferromagnet [184, 186] and later applied to film geometry [185, 205].

In the MRKKY approach one writes down the equation of motion additionaly in the alternative form (2.20). The restricted Green functions on the right-hand side of the equations of motion are then approximated by the full spin-dependent, one-particle propagator:

$$G^{(c)\sigma''\sigma}_{\mathbf{p},\mathbf{k}+\mathbf{q}\alpha\beta}(E) \to \delta_{\sigma''\sigma}\delta_{\mathbf{p},\mathbf{k}+\mathbf{q}} G^{\alpha\beta}_{\mathbf{k}+\mathbf{q}\sigma}(E) \,, \tag{5.15}$$

$$G^{(c)\sigma'\sigma''}_{\mathbf{k},\mathbf{p}\alpha\beta}(E) \to \delta_{\sigma'\sigma''}\delta_{\mathbf{kp}} G^{\alpha\beta}_{\mathbf{k}\sigma'}(E) \,. \tag{5.16}$$

Contrary to the lowest-order RKKY approach (5.10), which is recovered for $J \to 0$, there is no strict justification for this replacement. The *ad-hoc*-approximations (5.15) and (5.16) amount to a renormalization of the one-particle energies in order to take into account the effect of polarized conduction electrons on the interaction between localized spins. The approximation will get some justification *a posteriori* by reproducing properties in the strong-coupling limit to be discussed later.

Postulating the validity of the spectral theorem in the fermionic subspace and using (2.18) one obtains

$$\langle c^\dagger_{\mathbf{k}+\mathbf{q}\alpha\sigma} c_{\mathbf{k}\alpha\sigma'} \rangle^{(c)} = -\frac{1}{\pi} \int\limits_{-\infty}^{+\infty} dE f_-(E) \mathrm{Im} G^{(c)\sigma'\sigma}_{\mathbf{k},\mathbf{k}+\mathbf{q}\alpha\beta}(E-\mu) \,. \tag{5.17}$$

The combination of the two approximate solutions of the equations of motion for the restricted Green function $G^{(c)\sigma'\sigma}_{\mathbf{k},\mathbf{k}+\mathbf{q}\alpha\beta}(E)$ and insertion of (5.17) into (5.7) yields the MRKKY Heisenberg Hamiltonian for film geometry:

$$H^{\mathrm{M}RKKY}_{eff} = -\sum_{ij}\sum_{\alpha\beta} J^{\mathrm{M}RKKY}_{i\alpha j\beta} \mathbf{S}_{i\alpha}\mathbf{S}_{j\beta} \,. \tag{5.18}$$

The MRKKY exchange integrals read

$$J_{\alpha\beta}^{\mathrm{M}RKKY}(\mathbf{q}) = -\frac{J^2}{8}\sum_{\sigma} D_{\mathbf{q}\sigma\sigma}^{\alpha\beta}\,, \tag{5.19}$$

$$D_{\mathbf{q}\sigma\sigma'}^{\alpha\beta} = -\frac{1}{\pi N}\mathrm{I}m\sum_{\mathbf{k}}\int\limits_{-\infty}^{+\infty} dE f_{-}(E) A_{\mathbf{k},\mathbf{k}+\mathbf{q}\sigma\sigma'}^{\alpha\beta}(E-\mu)\,. \tag{5.20}$$

They contain the temperature-dependent electronic structure via the full one-particle interacting propagator in

$$A_{\mathbf{k},\mathbf{k}+\mathbf{q}\sigma\sigma'}^{\alpha\beta}(E) = G_{\mathbf{k}}^{\alpha\beta(0)}(E) G_{\mathbf{k}+\mathbf{q}\sigma}^{\beta\alpha}(E) + G_{\mathbf{k}\sigma'}^{\alpha\beta}(E) G_{\mathbf{k}+\mathbf{q}}^{\beta\alpha(0)}(E)\,. \tag{5.21}$$

In order to obtain (5.19) the property

$$D_{\mathbf{q}\uparrow\downarrow}^{\alpha\beta} = D_{\mathbf{q}\downarrow\uparrow}^{\alpha\beta} = \frac{1}{2}\sum_{\sigma} D_{\mathbf{q}\sigma\sigma}^{\alpha\beta} \tag{5.22}$$

has been used. The first equality in (5.22) follows from inversion symmetry ($\mathbf{k} \leftrightarrow -\mathbf{k}$) and the second directly from the definition (5.21).

The transversal spin Green function (5.1) can be calculated for the effective model (5.18) in order to get the thermal expectation values needed for the electronic self-energy. As the latter enters the effective exchange integrals (5.19) one has a closed system of equations which can be solved self-consistently, in particular, for the magnetization. Before presenting an approximate solution for the spin Green function, some properties of the MRKKY result shall be discussed.

According to the Goldstone theorem [109, 145], there are gapless excitations from the ground state ('Goldstone modes') in a system exhibiting spin-rotational invariance as described by the Hamiltonian (3.14). For this kind of continuous symmetry, the gapless excitations are spin waves. The mapping onto the isotropic MRKKY spin Hamiltonian recovers this type of excitations in the subsystem of the localized spins. The fact that spin wave contributions by the itinerant charge carriers inherent to (3.14) do not explicitly appear in the Hamiltonian (5.18) stresses its effective character. Spin wave damping due to electron-hole excitations is neglected in the MRKKY approach.

In a strict sense, the strong-coupling regime is characterized by $JS/W \gg 1$ and is to be distinguished from the double-exchange regime where $J \to \infty$ and the spin quantum number S is finite (e.g. $S = 3/2$ for manganites). However, it was shown in Ref. [189] that for large J, and apart from $S = 1/2$, the magnetic ground state of the Kondo lattice model at $T = 0$ is obtained to good approximation using classical spins. Moreover, in the modified RKKY approach, the localized spins are essentially treated classically by neglecting their operator character in the full Hilbert space.[1] For these reasons the expressions 'strong coupling' and 'double exchange' are used synonymously in the following.

In the strong-coupling regime, the interaction among localized spins is essentially restricted to the nearest-neighbor exchange integral (see Chap. 6.1). Furthermore the latter is closely connected to the kinetic energy. Assuming a fully-polarized conduction band and isotropic hopping one obtains for the bulk (see Appendix C):

$$J_1^{MRKKY} = -\frac{1}{zS^2} U_{\mathrm{k}in} \,. \tag{5.23}$$

The nearest-neighbor exchange interaction does not depend on the intra-atomic coupling J and is proportional to the kinetic energy. (5.23) relates a ferromagnetic exchange interaction among localized spins to the charge carriers minimizing their kinetic energy in a ferromagnetic background ($U_{\mathrm{k}in} < 0$). This result corresponds to the 'double exchange'[2] considered first by Zener in the framework of a semi-classical two-site model [22] and further discussed by Anderson and Hasegawa [23] and deGennes [221]. It is also obtained for the infinite lattice using an $1/S$-expansion for the spin wave self-energy [144, 166, 167] and with the effective-spin Hamiltonian proposed in Ref. [222].

From a microscopic point of view, the saturation of J_1^{MRKKY} with increasing J appears reasonable. For strong coupling and $J > 0$, the spin of a conduction electron is essentially oriented parallel to the localized spin in the local frame. A further increase of the coupling strength J does not change the configuration. This is reflected by the rigid shift of the lower band $\sim \frac{1}{2}JS$ of the one-electron excitation spectrum obtained by a variety of methods like mean-field, ISA, MCDA (see Fig. 4.4), or DMFT [143, 166].

Spin wave excitation spectrum

In order to compare the MRKKY effective-spin Hamiltonian with other approaches it is instructive to consider the explicit solution of (5.1). Details of the Tyablikov theory for the local-moment interaction are discussed in Chap. 5.4.1. The spin wave excitations $E(\mathbf{q})$ for the translationally invariant Heisenberg model are given by the poles of

---

[1] Note that the effective exchange integrals depend on S via the electronic self-energy. For finite temperatures they may be influenced to a greater extent by the quantum character of the localized spins than for T=0.

[2] The name refers to the simultaneous hopping of two e_g-electrons which leads to the coupling between localized Mn-ions in MnO_3-compounds.

$$P_{\mathbf{q}}(E) = \frac{2\langle S^z\rangle}{E - E(\mathbf{q}) + \mathrm{i}0^+}\,. \tag{5.24}$$

$P_{\mathbf{q}}$ is the Fourier transform of (5.1) in the bulk. The magnon energies read

$$E(\mathbf{q}) = 2\langle S^z\rangle(J(\mathbf{0}) - J(\mathbf{q}))\,. \tag{5.25}$$

Note that the non-local exchange integrals $J(\mathbf{q})$ refer to the interaction among the localized spins. Using the double-exchange MRKKY exchange integrals with a mean-field electronic self-energy (see Appendix C) in (5.25), one obtains for the fully spin-polarized case:

$$E_{\mathrm{DE}}^{\mathrm{MR}KKY}(\mathbf{q}) = \frac{2}{N\langle S^z\rangle}\sum_{\mathbf{k}}\langle n_{\mathbf{k}+\mathbf{q}\uparrow}\rangle(\epsilon(\mathbf{k}) - \epsilon(\mathbf{k}+\mathbf{q}))\,. \tag{5.26}$$

Apart from the factor $1/\langle S^z\rangle$, the spin wave excitation spectrum is determined by electronic quantities only. This result corresponds, up to a numerical factor, to the strong-coupling limit of an equation-of-motion approach for the transversal spin Green function where the mixed higher Green functions are RPA-decoupled [133, 219].[3]

The full spin wave spectrum of the RPA approach to the Kondo lattice comprises the Stoner continuum of spin-flip electron-hole excitations which may cause a damping of the magnons. Essentially the same result is obtained for $\langle S^z\rangle = S$ within a functional integral approach using non-interacting Holstein-Primakov bosons [223]. It bears also a close similarity to the diagramatic RPA approach (summation of all particle-hole bubble diagrams) proposed in Ref. [224]. There, the fermion mean-field propagators in the symmetry-broken phase at $T = 0$ were used to evaluate the magnon Green function. The double-exchange limit of the spin wave spectrum in these approaches is equivalent to the static limit where only the Goldstone modes in the spectrum are retained. For $T = 0$, $\langle S^z\rangle = S$ this corresponds to the leading order of the $1/S$-expansion for $J \to \infty$ [142, 143, 225]. In the double-exchange/static limit, the spin wave spectrum is Heisenberg-like with effective exchange integrals given by

$$J_{\mathrm{DE}}^{\mathrm{RPA}}(\mathbf{q}) = \frac{J^2}{4\pi N}\sum_{\mathbf{k}}\mathrm{I}m\int\limits_{-\infty}^{+\infty} dE f_-(E) G_{\mathbf{k}\uparrow}^{\mathrm{M}F}(E-\mu) G_{\mathbf{k}+\mathbf{q}\downarrow}^{\mathrm{M}F}(E-\mu) \tag{5.27}$$

with the mean-field propagators

---

[3] This approach is to be distinguished from the RPA/Tyablikov decoupling of the spin Green functions for the Heisenberg model.

$$G^{\mathrm{M}F}_{\mathbf{k}\sigma}(E) = \frac{1}{E + \mathrm{i}0^+ + \mu - \epsilon(\mathbf{k}) + \frac{1}{2} z_\sigma J \langle S^z \rangle} \,. \tag{5.28}$$

For reduced translational symmetry, the Green functions in (5.27) are to be replaced by the corresponding mean-field film matrix elements. The RPA Green function method for the Kondo lattice can also be employed in real space [226]. Together with a mean-field electronic self-energy it was used to obtain the T-dependent magnetization of ferromagnetic semiconducting thin films in Ref. [91].

The Stoner continuum complicates the calculation of the magnetization up to the Curie temperature considerably [227]. On the other hand, the electron-hole damping is not important in the strong-coupling limit, and can also be neglected near T_C [133, 227]. Therefore the magnetic properties are often evaluated without the Stoner continuum [133, 224]. This amounts to treating the exchange splitting in the fermionic subsystem in mean-field as demonstrated by (5.27). The corresponding structure of the spin wave spectrum is corroborated by a variety of different approaches as outlined above but is restricted to the low-temperature limit. Obviously, this is problematic for higher temperatures and, in particular, in the vicinity of the Curie temperature where the mean-field self-energy vanishes.

In order to resolve this problem one might be tempted to replace the propagators in (5.27) by Green functions containing a more sophisticated electronic self-energy beyond the mean-field level (cf. Ref. [228] for such an approach applied to the disordered Kondo lattice). This was checked and found to produce rather questionable results in the strong-coupling limit where the effective exchange does not saturate with the intra-atomic coupling J, in contrast to the double-exchange behavior discussed above (see also Chap. 6.3).

It must certainly be considered advantageous that no restrictions are imposed on the electronic self-energy in the modified RKKY treatment, which enables one to use more elaborate self-energies like the MCDA. Furthermore, this combined treatment reproduces the weak-coupling conventional RKKY interaction on the one hand and the double-exchange limit on the other. The approach appears to be a suitable approximation for studying the magnetic properties over the full temperature range and in all coupling regimes.

5.3 Magnetic anisotropy

The easy axis of a magnetic system is the direction of the magnetization which minimizes the free energy without external field. Magnetic anisotropy energies are energies needed to rotate the magnetization away from the easy axis to another ('hard') direction. In thin films, they can be orders of magnitudes larger than in the corresponding bulk systems and significantly influence the magnetic properties [229, 230].

Reorientation transitions of thin films are of great physical and practical interest. They are closely associated with the magnetic anisotropy. A reorientation transition may be caused by varying the film thickness [231], temperature [232, 233], or an external magnetic field [234]. The thickness-driven reorientation transition can be understood as the result of the interplay between a surface and a bulk contribution to the anisotropy with both preferring different easy directions. A temperature-driven reorientation transition may be due to different temperature dependences of physically distinct magnetic anisotropies. It can even occur in a monolayer as was shown by Körmann et al. [233].

Microscopically, two sources of magnetic anisotropy can be distinguished. First, the electrons in the atomic orbitals are subject to the Coulomb potential of the other atoms ('crystal field') in a solid. Via the spin-orbit interaction this transfers to localized magnetic moments if present and thus the latter are coupled to the crystal lattice. This lattice or magneto-crystalline anisotropy can favor any crystallographic direction, depending sensitively on the electronic structure and on spatial restrictions like strain or the presence of a surface. The second source of magnetic anisotropy is the dipolar interaction between magnetic moments (shape anisotropy). It is long-ranged and favors an in-plane orientation of the magnetization.

Apart from the physical origin, different anisotropy contributions can be classified according to their symmetry [230, 235]. Expanding the free energy in terms of the cosine of the angle between the magnetization and the film normal, uneven powers do not appear because these are not invariant with respect to a magnetization reversal. Neglecting azimuthal anisotropy, and up to fourth order, the expansion reads

$$F(\theta) = F_0 - K_2 cos^2\theta - K_4 cos^4\theta \,. \tag{5.29}$$

In this phenomenological picture, the uniaxial anisotropy coefficients K_2 and K_4 are thickness- and temperature-dependent. The second-order anisotropy is often much larger than the fourth-order contribution, $|K_2| \gg |K_4|$. The easy axis of the system is then determined by the sign of K_2: if $K_2 > 0$, the easy direction of the magnetization is out-of-plane, for $K_2 < 0$ it is in-plane.

In this work, a uniaxial second-order anisotropy is considered exclusively. Furthermore, only the local part of the magneto-crystalline contribution is taken into account. This is also known as single-ion anisotropy and reads in terms of spin operators [110]

$$H_A = -\sum_{i\alpha} K_2^{\alpha} (S_{i\alpha}^z)^2 \,. \tag{5.30}$$

An approximate treatment of this term in connection with the Green function approach of the next section is discussed in Chap. (5.4.2). The microscopic layer-dependent coupling constant K_2^α is to be distinguished from the macroscopic coefficient K_2 in (5.29). (5.30) will be shown to lead to an effective temperature-dependent anisotropy field.

It should be noted that - besides making the model approach to thin film magnetism more realistic - the introduction of the single-ion anisotropy satisfies a *necessary* condition for the effective Heisenberg Hamiltonian (5.18) to describe magnetic ordering. The RPA approximation for the spin wave Green function presented in the next section fulfills the Mermin-Wagner theorem [94]. The generalization of this theorem to film geometry states that magnetic long-range order is impossible for non-zero temperatures in spin-isotropic Heisenberg films [95].

5.4 Spin Green function for Heisenberg films

This section presents a solution for the spin Green function (5.1) applied to the effective spin Hamiltonian (5.18) supplemented with the single-ion anisotropy (5.30). First, the RPA/Tyablikov solution for Heisenberg films and the Anderson-Callen theory for the single-ion anisotropy are discussed for a uniform alignment of the magnetization of all monolayers in the direction of the easy axis. In a second step, arbitrary orientations of the layer-dependent magnetizations are considered. Such configurations are relevant for the treatment of reorientation transitions and interlayer exchange coupling (Chap. 7).

5.4.1 RPA/Tyablikov solution

The Heisenberg Hamiltonian for a layered geometry which is considered in the following reads

$$H = -\sum_{ij}\sum_{\alpha\beta} J_{ij}^{\alpha\beta}\mathbf{S}_{i\alpha}\mathbf{S}_{j\beta} - \sum_{i\alpha} K_2^\alpha (S_{i\alpha}^z)^2 - B\sum_{i\alpha} S_{i\alpha}^z\,. \tag{5.31}$$

$J_{ij}^{\alpha\beta}$ is the exchange interaction between the localized spins, K_2^α is the layer-dependent single-ion anisotropy strength, and B is a magnetic field coupling to the same spin (z-)component that defines the uniaxial anisotropy. The g-factor and the Bohr magneton μ_B have been absorbed into B. As usual i, j denote the in-plane x-y-coordinates and α, β are monolayer indices.

After transformation to spin raising and lowering operators, the exchange term in (5.31) reads

$$H_{\mathrm{ex}} = -\sum_{ij}\sum_{\alpha\beta} J_{ij}^{\alpha\beta}\left(S_{i\alpha}^{+}S_{j\beta}^{-} + S_{i\alpha}^{z}S_{j\beta}^{z}\right) . \tag{5.32}$$

The aim is to obtain an approximate solution for the transversal spin Green function 5.1. In order to write down the equation of motion (2.19) for $P_{ij}^{\alpha\beta}$ the following commutator is needed:

$$\left[S_{i\alpha}^{+}, H_{\mathrm{ex}} + H_{\mathrm{B}}\right]_{-} = -2\sum_{l\gamma} J_{il}^{\alpha\gamma}\left(S_{i\alpha}^{z}S_{l\gamma}^{+} - S_{l\gamma}^{z}S_{i\alpha}^{+}\right) + BS_{i\alpha}^{+} . \tag{5.33}$$

The anisotropy Green function is approximated using the Anderson-Callen (AC) decoupling approach [234, 236] which will be discussed in more detail in Chap. 5.4.2. The result is

$$\begin{aligned}\langle\langle\left[S_{i\alpha}^{+}, H_{A}\right]_{-} ; S_{j\beta}^{-}\rangle\rangle_{E} &= K_{2}^{\alpha}\langle\langle S_{i\alpha}^{+}S_{i\alpha}^{z} + S_{i\alpha}^{z}S_{i\alpha}^{+}; S_{j\beta}^{-}\rangle\rangle_{E} \\ &\overset{\mathrm{A}C}{\approx} K_{2}^{\alpha}\Phi_{\alpha}(T)\langle\langle S_{i\alpha}^{+}; S_{j\beta}^{-}\rangle\rangle_{E} ,\end{aligned} \tag{5.34}$$

with Φ_{α} given by (5.55). One sees in (5.34) that the single-ion anisotropy acts as an effective, temperature-dependent field $K_{2}^{\alpha}\Phi_{\alpha}(T)$ which couples to S_{α}^{z}. With (5.33) and (5.34) one obtains the following equation of motion for $P_{ij}^{\alpha\beta}$:

$$\begin{aligned}&\left(E - B - K_{2}^{\alpha}\Phi_{\alpha}(T)\right) P_{ij}^{\alpha\beta}(E) = \\ &\qquad 2\delta_{\alpha\beta}\langle S_{\alpha}^{z}\rangle + 2\sum_{l\gamma} J_{il}^{\alpha\gamma}\left(\langle\langle S_{l\gamma}^{z}S_{i\alpha}^{+}; S_{j\beta}^{-}\rangle\rangle_{E} - \langle\langle S_{i\alpha}^{z}S_{l\gamma}^{+}; S_{j\beta}^{-}\rangle\rangle_{E}\right) .\end{aligned} \tag{5.35}$$

The RPA/Tyablikov decoupling [110, 237] replaces the z-components of the spin operators in the higher-order Green functions by their thermal expectation values:

$$\begin{aligned}\langle\langle S_{l\gamma}^{z}S_{i\alpha}^{+}; S_{j\beta}^{-}\rangle\rangle_{E} &\rightarrow \langle S_{\gamma}^{z}\rangle\langle\langle S_{i\alpha}^{+}; S_{j\beta}^{-}\rangle\rangle_{E} , \\ \langle\langle S_{i\alpha}^{z}S_{l\gamma}^{+}; S_{j\beta}^{-}\rangle\rangle_{E} &\rightarrow \langle S_{\alpha}^{z}\rangle\langle\langle S_{l\gamma}^{+}; S_{j\beta}^{-}\rangle\rangle_{E} .\end{aligned} \tag{5.36}$$

With this approximation and exploiting Fourier transformation, Eq. (5.35) can be solved. Using

$$J_{\mathbf{q}}^{\alpha\beta} = \frac{1}{N}\sum_{ij} J_{ij}^{\alpha\beta} \mathrm{e}^{\mathrm{i}\mathbf{q}(\mathbf{R}_{i}-\mathbf{R}_{j})} \tag{5.37}$$

and

$$S_{\mathbf{q}\alpha}^{\nu} = \sum_{i} S_{i\alpha}^{\nu}\mathrm{e}^{-\mathrm{i}\mathbf{q}\mathbf{R}_{i}} \qquad S_{i\alpha}^{\nu} = \frac{1}{N}\sum_{i} S_{\mathbf{q}\alpha}^{\nu}\mathrm{e}^{\mathrm{i}\mathbf{q}\mathbf{R}_{i}} \qquad (\nu = x, y, z, +, -) \tag{5.38}$$

one obtains in matrix form

$$\underline{\mathrm{P}}_{\mathbf{q}}(E) = \frac{2\langle \underline{\mathrm{S}}^z \rangle}{(E + \mathrm{i}0^+)\underline{\mathrm{I}} - \underline{\mathrm{M}}_{\mathbf{q}}} \,. \tag{5.39}$$

$\langle \underline{\mathrm{S}}^z \rangle$ denotes a diagonal matrix with $\langle \underline{\mathrm{S}}^z \rangle_{\alpha\beta} = \langle S^z_\alpha \rangle \delta_{\alpha\beta}$, $\underline{\mathrm{I}}$ is the $(N_\mathrm{L} \times N_\mathrm{L})$ identity matrix, and the elements of the self-energy matrix $\underline{\mathrm{M}}_{\mathbf{q}}$ are

$$\left[\underline{\mathrm{M}}_{\mathbf{q}}\right]_{\alpha\beta} = \left(B + K_2^\alpha \Phi_\alpha(T) + 2\sum_\gamma J_{\mathbf{0}}^{\alpha\gamma} \langle S^z_\gamma \rangle \right) \delta_{\alpha\beta} - 2 J_{\mathbf{q}}^{\alpha\beta} \langle S^z_\beta \rangle \,. \tag{5.40}$$

The first three terms in (5.40) are local and represent an effective field: the first term is due to the external field, the second stems from the single-ion anisotropy, and the third term originates from the coupling to the other localized spins and corresponds to a mean-field treatment of H_{ex} (cf. Chap. 6.6). The fourth term is non-local and describes spin wave excitations in ferromagnetic Heisenberg films.

Performing a similarity transformation (Eq. (3.6)), the inversion in (5.39) can be transformed to the diagonalization of $\underline{\mathrm{M}}_{\mathbf{q}}$ and one obtains for the diagonal elements of the spectral density of $\underline{\mathrm{P}}_{\mathbf{q}}$:

$$-\frac{1}{\pi}\mathrm{Im} P^\alpha_{\mathbf{q}}(E) = 2\langle S^z_\alpha \rangle \sum_\gamma w_{\mathbf{q}}^{\alpha\gamma} \delta(E - E_\gamma(\mathbf{q})) \,. \tag{5.41}$$

The spin wave energies $E_\gamma(\mathbf{q})$ are the eigenvalues of $\underline{\mathrm{M}}_{\mathbf{q}}$ and the weights $w_{\mathbf{q}}^{\alpha\gamma}$ can be obtained from the eigenvectors building the unitary matrix that diagonalizes $\underline{\mathrm{M}}_{\mathbf{q}}$. The eigenproblem can be solved numerically using standard routines.

In order to evaluate the magnetization self-consistently for arbitrary S one has to establish a further relation between the spin Green function $\langle\langle S^+_{i\alpha}; S^-_{j\beta} \rangle\rangle_E$ and $\langle S^z_\alpha \rangle$. From the operator identity

$$S^\sigma_\alpha S^{-\sigma}_\alpha = S(S+1) + z_\sigma S^z_\alpha - (S^z_\alpha)^2 \qquad (\sigma = +, -) \tag{5.42}$$

one sees that this amounts to finding a relation between S^z_α and $(S^z_\alpha)^2$. There are various possibilities to define suitable higher Green functions to achieve this [110, 237, 238, 239]. For example, following the proposal by Tyablikov [237] extended to film geometry [217], one can introduce the parametrized Green function $\langle\langle S^+_{i\alpha}; \mathrm{e}^{aS^z_{j\beta}} S^-_{j\beta} \rangle\rangle_E$ and carry out the decoupling procedure exactly as above. In addition it is possible to derive a differential equation for the quantity $\langle \mathrm{e}^{aS^z_{j\beta}} \rangle$ which yields, after differentiation with respect to a and setting $a = 0$, an expression for the layer-dependent spin expectation value:

$$\langle S^z_\alpha \rangle = \frac{(1 + \varphi_\alpha + S)\varphi_\alpha^{2S+1} + (S - \varphi_\alpha)(1 + \varphi_\alpha)^{2S+1}}{(1 + \varphi_\alpha)^{2S+1} - \varphi_\alpha^{2S+1}} \,. \tag{5.43}$$

The Bose spin wave distribution function $\varphi_\alpha(T)$ in (5.43) depends on the spin wave energies and weights contained in (5.41):

$$\varphi_\alpha(T) = \sum_{\mathbf{q}} \sum_{\gamma} \frac{w_{\mathbf{q}}^{\alpha\gamma}}{\mathrm{e}^{\beta E_\gamma(\mathbf{q})} - 1} \,. \tag{5.44}$$

Eqs. (5.40), (5.43), and (5.44) can be solved iteratively for any S. The procedure leading to (5.43) also yields the following higher-order spin expectation values:

$$\begin{aligned} \langle S_\alpha^- S_\alpha^+ \rangle &= 2\langle S_\alpha^z \rangle \varphi_\alpha \,, \\ \langle (S_\alpha^z)^2 \rangle &= S(S+1) - \langle S_\alpha^z \rangle (1 + 2\varphi_\alpha) \,, \\ \langle (S_\alpha^z)^3 \rangle &= S(S+1)\varphi_\alpha + \langle S_\alpha^z \rangle (S(S+1) + \varphi_\alpha) - \langle (S_\alpha^z)^2 \rangle (1 + 3\varphi_\alpha) \,. \end{aligned} \tag{5.45}$$

From (5.43), the layer-dependent magnetization of the localized-spin subsystem can be obtained. The total magnetization consists of a local-moment and a conduction-band contribution:

$$M_\alpha = M_\alpha^{loc} + M_\alpha^{cb} = -\mu_{\mathrm{B}} \left(g \langle S_\alpha^z \rangle + 2 \langle \sigma_\alpha^z \rangle \right) n_{2\mathrm{D}} \,. \tag{5.46}$$

g is the Landé factor for the local magnetic moments and $n_{2\mathrm{D}}$ is their density. The second term contains the thermal average of the electron spin (2.5).

Curie temperature

It is possible to obtain a simple formula for the Curie temperature T_{C} of the translationally invariant crystal ($\alpha = 1$). From (5.25) it follows that near the critical temperature the spin wave energy $E(\mathbf{q}) \to 0$, and hence the magnon number (5.44) diverges ($w_{\mathbf{q}}^{\alpha\alpha} \equiv 1$). Expanding (5.43) in $1/\varphi$ yields

$$\langle S_\alpha^z \rangle = \frac{S(S+1)}{3\varphi} + \mathcal{O}(\varphi^{-2}) \,. \tag{5.47}$$

Furthermore expanding the exponential in (5.44), one ends up with

$$\frac{3 k_{\mathrm{B}} T_{\mathrm{C}}}{S(S+1)N} = \left(\sum_{\mathbf{q}} \frac{1}{(K_2 \gamma + 2\left[J(\mathbf{0}) - J(\mathbf{q}) \right])} \right)^{-1}_{T=T_{\mathrm{C}}} \,. \tag{5.48}$$

The constant γ depends on the approximative treatment of the anisotropy. The Anderson-Callen approach yields

$$\gamma = \lim_{T \to T_{\mathrm{C}}} \frac{\Phi(T)}{\langle S^z \rangle} = \frac{2(2S-1)}{3S} \,. \tag{5.49}$$

Expression (5.48) indicates that the RPA treatment of the Heisenberg model fulfills the Mermin-Wagner theorem [94]. Without the anisotropy term $K_2\gamma$, the divergence at $\mathbf{q} = \mathbf{0}$ is not integrable for $D < 3$ and no finite critical temperature is possible.

5.4.2 Anderson-Callen theory of the single-ion anisotropy

The approximate solution for the anisotropy Green function in (5.34),

$$\langle\langle S^+_{i\alpha} S^z_{i\alpha} + S^z_{i\alpha} S^+_{i\alpha}; S^-_{j\beta}\rangle\rangle_E \,, \tag{5.50}$$

shall be discussed in more detail. The heuristic decoupling scheme for the anisotropy terms proposed by Anderson and Callen [236] goes back to the treatment of the (bulk) exchange term (5.32) [239] and is based upon the following exact representation of the operator S^z:

$$S^z = \lambda S(S+1) + \frac{1}{2}(1-\lambda)S^+S^- - \frac{1}{2}(1+\lambda)S^-S^+ - \lambda(S^z)^2 \,. \tag{5.51}$$

The site indices have been dropped because all terms of interest are local. The parameter λ is chosen such that the error associated with the decoupling of higher-order Green functions is minimized. An approximate treatment of the deviations of S^z for ferromagnetic saturation ($\langle S^z\rangle = S$) and in the paramagnetic phase ($\langle S^z\rangle = 0$) is ensured by [110]

$$\lambda = \frac{\langle S^z\rangle}{2S^2} \,. \tag{5.52}$$

After inserting (5.51) and (5.52) into the anisotropy Green function (5.50), the resulting Green functions are decoupled under the condition of spin conservation according to the replacements of the following operator combinations:

$$\begin{aligned}
S^+S^-S^+ &\overset{\mathrm{AC}}{\rightarrow} \langle S^+S^-\rangle S^+ + \langle S^-S^+\rangle S^+ \,, \\
S^+S^+S^- &\overset{\mathrm{AC}}{\rightarrow} 2\langle S^+S^-\rangle S^+ \,, \\
S^-S^+S^+ &\overset{\mathrm{AC}}{\rightarrow} 2\langle S^-S^+\rangle S^+ \,, \\
S^+(S^z)^2,\ (S^z)^2S^+ &\overset{\mathrm{AC}}{\rightarrow} \langle (S^z)^2\rangle S^+ \,.
\end{aligned} \tag{5.53}$$

This leads to the following expression for the anisotropy Green function:

$$\langle\langle S^+_{i\alpha} S^z_{i\alpha} + S^z_{i\alpha} S^+_{i\alpha}; S^-_{j\beta}\rangle\rangle_E \overset{\mathrm{AC}}{\rightarrow} \Phi_\alpha(T)\langle\langle S^+_{i\alpha}; S^-_{j\beta}\rangle\rangle_E \,. \tag{5.54}$$

The temperature-dependent coefficient Φ_α reads

$$\Phi_\alpha(T) = 2\langle S^z_\alpha\rangle \left(1 - \frac{1}{2S^2}\left[S(S+1) - \langle (S^z_\alpha)^2\rangle\right]\right) . \tag{5.55}$$

The Anderson-Callen approximation for the single-ion anisotropy is supported by the following facts:

- For $S = \frac{1}{2}$ one has $(S^z_\alpha)^2 \equiv \frac{1}{4}$ and AC correctly yields $\Phi_\alpha^{S=\frac{1}{2}}(T) \equiv 0$
- The choice of λ can be traced back to the application of Wick's theorem [139] to the bosonic spin wave operators associated with S^+ and S^- in linear spin wave theory [112, 236]
- Correct power law for the effective anisotropy coefficient for low T [236, 240]
- Good agreement with Quantum Monte Carlo results for the field-induced reorientation transition of a Heisenberg monolayer (see Fig. 5.1)

It should be mentioned that the Anderson-Callen approximation for the single-ion anisotropy gives significantly better results than an RPA decoupling (the latter formally corresponding to the case $\lambda = 0$, cf. Fig. 5.1). The situation is somewhat different regarding the exchange terms. Although the Callen decoupling of those yields an improved low-temperature behavior of the magnetization for $S > 1/2$ compared to RPA, Curie temperatures do not differ much in both approaches [110]. The RPA equations, however, are numerically much less expensive - a great advantage given the numerical cost of calculating the effective exchange integrals self-consistently for the film structures considered in this work. Apart from the practical argument this suggests that an RPA treatment of localized-spin Green functions is an acceptable approximation if the decoupling is carried out for non-local operator products. The (Anderson-)Callen approach appears to be particularly superior to RPA if local operator terms are concerned.

5.4.3 Layer-dependent rotated frame

In order to treat non-uniform orientations of the layer-dependent magnetization in a Heisenberg film, the layer-dependent frame is rotated such that the z'-axis coincides with the direction of the magnetization [234, 241]. Then RPA and Anderson-Callen decouplings of the exchange and anisotropy Green functions, respectively, are carried out in exactly the same manner as done in the 'parallel limit' treated in Secs. 5.4.1 and 5.4.2.

For the magnetic configuration considered in this work, the rotation of the layer-dependent frame is restricted to the x-z-plane. This implies that only one polar angle θ_α per monolayer is required to determine the rotation unambiguously. A generalization to an additional azimuthal angle is straightforward [242]. The layer-dependent transformation matrix between the fixed and the rotated frame reads

$$\underline{\mathbf{R}}_\alpha = \begin{pmatrix} \cos\theta_\alpha & 0 & -\sin\theta_\alpha \\ 0 & 1 & 0 \\ \sin\theta_\alpha & 0 & \cos\theta_\alpha \end{pmatrix} . \tag{5.56}$$

The relation between the representation of a vector in the old and in the new frame is given by

$$\begin{aligned} \mathbf{x'}_\alpha &= \underline{\mathbf{R}}_\alpha \mathbf{x}_\alpha \, , \\ \mathbf{x}_\alpha &= \underline{\mathbf{R}}_\alpha^{-1} \mathbf{x'}_\alpha \, , \end{aligned} \tag{5.57}$$

where the primed vectors refer to the rotated coordinate system. The components of the expectation values of the spin operators $\mathbf{S}_{i\alpha}, \mathbf{S'}_{i\alpha}$ are then related via

$$\begin{aligned} \langle S^x_\alpha \rangle &= \sin\theta_\alpha \langle S^{z'}_\alpha \rangle \, , \\ \langle S^z_\alpha \rangle &= \cos\theta_\alpha \langle S^{z'}_\alpha \rangle \, , \end{aligned} \tag{5.58}$$

assuming in-plane translational invariance. It holds $\langle S^{x'}_\alpha \rangle = \langle S^{y'}_\alpha \rangle \equiv 0$ by definition of the rotation. The angle θ_α is determined in a self-consistent fashion. With the external field given by $\mathbf{B} = (B^x, 0, B^z)$, the Hamiltonian (5.31) is transformed into a representation H' in the rotated frame using (5.57). Decoupling the exchange and anisotropy operator terms according to the Tyablikov and the Anderson-Callen approach, respectively, one obtains for the commutator of the z'-component of the total spin with the Hamiltonian:

$$\begin{aligned} \left[\sum_{i\alpha} S^{z'}_{i\alpha}, H' \right]_- \xrightarrow{\mathrm{R}PA+AC} \sum_{i\alpha} \Bigg(& \sum_{m\gamma} 2J^{\alpha\gamma}_{im} sin(\theta_\alpha - \theta_\gamma) \langle S^{z'}_\gamma \rangle + \sin\theta_\alpha B^z - \cos\theta_\alpha B^x \\ & + 2K^\alpha_2 \sin\theta_\alpha \cos\theta_\alpha \langle S^{z'}_\alpha \rangle \left[1 - \frac{\langle (S^{y'}_\alpha)^2 \rangle}{S^2} \right] \Bigg) i S^{y'}_{i\alpha} \, . \end{aligned} \tag{5.59}$$

The Anderson-Callen decouplings used to obtain (5.59) were carried out directly for the spatial components of the spin operators rather than for the raising and lowering operators as in Chap. 5.4.2. In this (equivalent) way the decoupling yields for the relevant operator products:

$$S^{x'}S^{y'} + S^{y'}S^{x'} \xrightarrow{\mathrm{AC}} 0\,,$$
$$S^{x',y'}S^{z'} + S^{z'}S^{x',y'} \xrightarrow{\mathrm{AC}} 2\langle S^{z'}\rangle\left(1 - \frac{\langle (S^{x',y'})^2\rangle}{S^2}\right)S^{x',y'}\,. \tag{5.60}$$

Note that the spin components now refer to the rotated frame.

From (5.59) the rotation angles θ_α can be approximately determined. In order for the total spin to commute with H' and thus to be a conserved quantity,

$$\left[\sum_{i\alpha} S^{z'}_{i\alpha}, H'\right]_- = 0\,, \tag{5.61}$$

the following equation must be fulfilled:

$$\sum_{m\gamma} 2J^{\alpha\gamma}_{im} sin(\theta_\alpha - \theta_\gamma)\langle S^{z'}_\gamma\rangle + \sin\theta_\alpha B^z - \cos\theta_\alpha B^x$$
$$+ 2K^\alpha_2 \sin\theta_\alpha\cos\theta_\alpha\langle S^{z'}_\alpha\rangle\left(1 - \frac{1}{2S^2}\left(S(S+1) - \langle (S^{z'}_\alpha)^2\rangle\right)\right) = 0\,. \tag{5.62}$$

The rotation angles are the self-consistent solutions of these N_L equations. One sees that the equilibrium angle of the magnetization of a given monolayer is determined by the competition of three kinds of interaction. The first term corresponds to the interlayer exchange coupling and contributes only if the orientations of the layer-dependent magnetization are different. The second and third term are due to the external magnetic field and the fourth stems from the single-ion anisotropy. They contribute irrespective of the relative orientation of the magnetization.

Having obtained the equations (5.62) to determine the equilibrium angles, the magnetization in the rotated frame must still be calculated. Rather than solving for the Green function (5.1) as in the parallel limit, this is achieved by considering the set of Green functions

$$P^{\mu\nu}_{ij\alpha\beta}(E) = \langle\langle S'^{\mu}_{i\alpha}; S'^{\nu}_{j\beta}\rangle\rangle_E \qquad (\mu,\nu = +,-) \tag{5.63}$$

in the rotated frame. A multiple Green function method of this kind to treat non-uniform orientations of the magnetization is proposed in Ref. [243]. The decoupling procedure for the equations of motion in the rotated frame is exactly the same as presented in 5.4.1 and 5.4.2. After Fourier transformation the RPA+AC solution can be written as a $(2N_L \times 2N_L)$-matrix equation:

$$\begin{pmatrix} \underline{P}^{+-}_{\mathbf{q}}(E) & \underline{P}^{--}_{\mathbf{q}}(E) \\ \underline{P}^{++}_{\mathbf{q}}(E) & \underline{P}^{-+}_{\mathbf{q}}(E) \end{pmatrix} \cdot \left[\underline{E} - \begin{pmatrix} \underline{M}^{+-}_{\mathbf{q}} & \underline{M}^{++}_{\mathbf{q}} \\ \underline{M}^{--}_{\mathbf{q}} & \underline{M}^{-+}_{\mathbf{q}} \end{pmatrix}\right] = \begin{pmatrix} \underline{\eta} & \underline{0} \\ \underline{0} & -\underline{\eta} \end{pmatrix}\,. \tag{5.64}$$

The elements of the submatrix building the inhomogeneity matrix on the right-hand side are given by $\eta_{\alpha\beta} \equiv \delta_{\alpha\beta}\langle S_\alpha^{z'}\rangle$. The submatrices $\underline{M}_{\mathbf{q}}^{\mu\nu}$ explicitly read

$$\begin{aligned}
M_{\mathbf{q}\alpha\beta}^{+-} &= \left(2J_{\mathbf{0}}^{\alpha\alpha}\langle S_\alpha^{z'}\rangle + B_{\mathrm{e}ff}^{\alpha}\right)\delta_{\alpha\beta} - J_{\mathbf{q}}^{\alpha\beta}\left(cos(\theta_\alpha - \theta_\beta) + 1\right)\langle S_\beta^{z'}\rangle \\
&= -M_{\mathbf{q}\alpha\beta}^{-+} \\
M_{\mathbf{q}\alpha\beta}^{--} &= -\frac{1}{2}\mathrm{s}in^2\theta_\alpha K_{2,\mathrm{e}ff}^{\alpha}\delta_{\alpha\beta} - J_{\mathbf{q}}^{\alpha\beta}\left(cos(\theta_\alpha - \theta_\beta) - 1\right)\langle S_\beta^{z'}\rangle \\
&= -M_{\mathbf{q}\alpha\beta}^{++}
\end{aligned} \tag{5.65}$$

with the effective field

$$B_{\mathrm{e}ff}^{\alpha} = 2\sum_{\gamma}^{\alpha\neq\gamma} J_{\mathbf{0}}^{\alpha\gamma}cos(\theta_\alpha - \theta_\gamma)\langle S_\gamma^{z'}\rangle + B^x\mathrm{s}in\theta_\alpha + B^z cos\theta_\alpha + K_{2,\mathrm{e}ff}^{\alpha}(cos^2\theta_\alpha - \frac{1}{2}\mathrm{s}in^2\theta_\alpha) \tag{5.66}$$

and the effective anisotropy

$$\begin{aligned}
K_{2,\mathrm{e}ff}^{\alpha}(T) &= 2K_2^{\alpha}\langle S_\alpha^{z'}\rangle C_\alpha(T)\,, \\
C_\alpha(T) &= 1 - \frac{1}{2S^2}\left[S(S+1) - \langle (S_\alpha^{z'})^2\rangle\right]\,.
\end{aligned} \tag{5.67}$$

Together with (5.43) and (5.44), where the sum now runs over the $2N_L$ eigenvalues of the supermatrix composed of the $\underline{M}_{\mathbf{q}}^{\mu\nu}$ in (5.64) and the $2N_L$ corresponding weights, (5.64)-(5.67) and (5.62) form a closed system of equations which can be solved iteratively.

For the self-consistent determination of the rotation angles it is convenient to evaluate the layer-dependent effective field in the unrotated frame. Combining the expressions for the effective field in the rotated frame (5.66) with the angle equations (5.62) and using (5.57) one obtains:

$$\begin{aligned}
\left(B_{\mathrm{e}ff}^{\alpha}\right)_x &= sin\theta_\alpha B_{\mathrm{e}ff}^{\alpha} \\
&= B^x - K_2^{\alpha}C_\alpha \mathrm{s}in^2\theta_\alpha\langle S_\alpha^x\rangle + 2\sum_{\gamma}^{\alpha\neq\gamma} J_{\mathbf{0}}^{\alpha\gamma}\langle S_\gamma^x\rangle\,,
\end{aligned} \tag{5.68}$$

$$\begin{aligned}
\left(B_{\mathrm{e}ff}^{\alpha}\right)_z &= cos\theta_\alpha B_{\mathrm{e}ff}^{\alpha} \\
&= B^z + 2K_2^{\alpha}C_\alpha(cos^2\theta_\alpha + \frac{1}{2}\mathrm{s}in^2\theta_\alpha)\langle S_\alpha^z\rangle + 2\sum_{\gamma}^{\alpha\neq\gamma} J_{\mathbf{0}}^{\alpha\gamma}\langle S_\gamma^z\rangle\,.
\end{aligned} \tag{5.69}$$

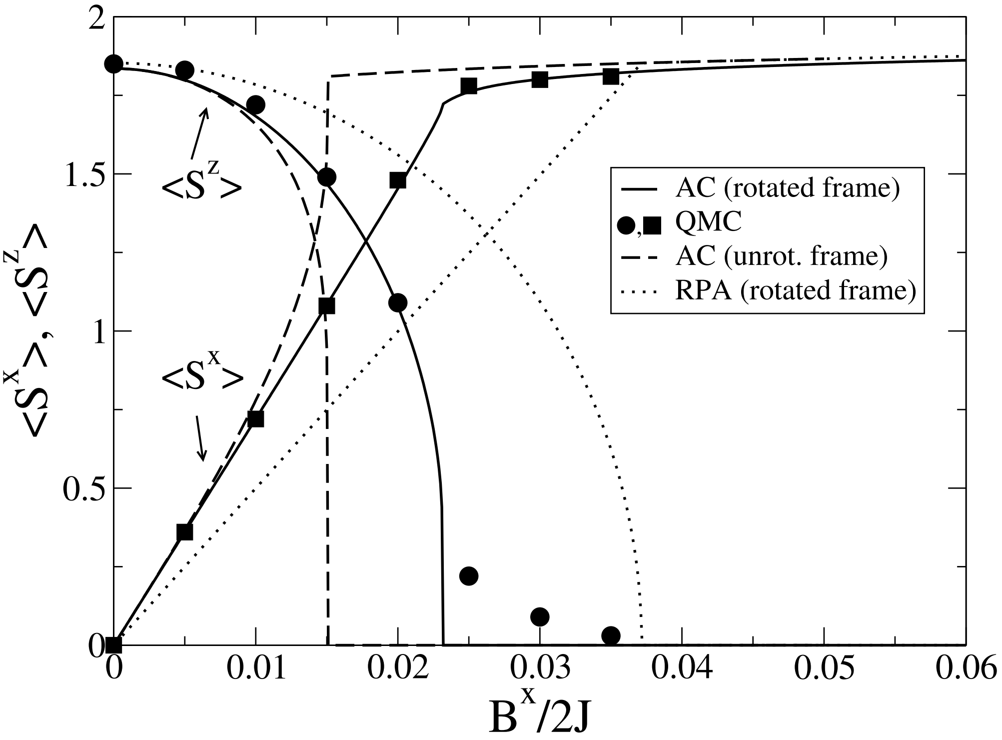

Figure 5.1: x- and the z-component of the spin expectation value in a Heisenberg monolayer with out-of-plane easy axis as a function of the external magnetic field for the approximate treatments of the single-ion anisotropy as indicated. The nearest-neighbor exchange terms are treated in RPA. QMC data are taken from Ref. [245]. Parameters: $K_2 = 0.02J$, $k_\mathrm{B}T = 2J \approx 0.32 k_\mathrm{B}T_\mathrm{C}$, $S = 2$.

Fig. 5.1 shows a field-driven reorientation transition of a Heisenberg monolayer based on the approach presented above and for other treatments of the single-ion anisotropy. More details on this problem can be found in Ref. [234] where the transition is studied using the rotated-frame method but considering only one spin Green function instead of (5.63). The results obtained with the Anderson-Callen theory in the rotated frame are compared with an Anderson-Callen decoupling in the unrotated frame and with an RPA decoupling of the anisotropy Green function (i.e. $\lambda = 0$ in (5.51) in the rotated frame). In addition QMC data are shown. The Anderson-Callen result in the rotated frame is in much better agreement with QMC than the two other approaches. The field-induced reorientation transition of easy-plane Heisenberg films is studied in Ref. [244].

Chapter 6

Ferromagnetism

This chapter treats the ferromagnetism of metallic local-moment sc(100)-films described by the Kondo lattice model. By means of the MCDA+MRKKY approach, the spin Green function (5.1) is calculated using the methods presented in Chap. 5.4 for the effective Hamiltonian (5.18) supplemented with a single-ion anisotropy (5.30).

After discussing the layer- and temperature-dependent magnetization and the Curie temperature, the effective exchange integrals and the ferromagnetic stability at the film surface are considered. A particular point of interest here is the connection between the local-moment interaction and the ferromagnetism on the one hand and the intra-atomic coupling, the carrier density, and the electronic structure on the other. Two effects are studied in more detail, the magnetic instability via charge transfer and the consequences of modified interlayer hopping at the surface.

The last part of this chapter is devoted to the issue of a magnetic surface transition. The considerations of Chap. 6.6 are intended to contribute to the theoretical aspects of the debate about possibly different critical temperatures in the bulk and at the surface of a semi-infinite crystal. They stress the importance of taking spin wave excitations into account in the theoretical treatment of film and surface magnetism.

6.1 Effective monolayer exchange integrals

The carrier-mediated interaction among the localized spins is represented by the effective exchange integrals (5.19). They interpolate between the weak-coupling, long-range RKKY regime and the strong-coupling, short-range double-exchange limit (cf. Chap. 5.2). In order to demonstrate this Fig. 6.1 (a) shows the MRKKY effective exchange integrals of the first 30 shells in a monolayer (for details on the

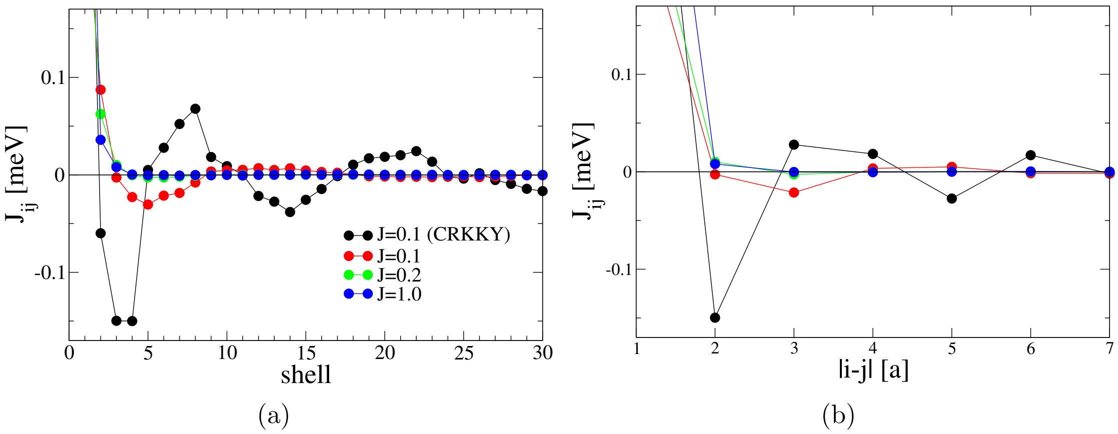

(a) (b)

Figure 6.1: Effective MRKKY exchange integrals for the monolayer (a) as a function of the shell number and (b) along the high-symmetry (x- or y-)direction in units of the lattice constant. Lines are guides to the eye. J is given in units of the bulk Bloch bandwidth $W_{bulk} = 1$ eV. The monolayer bandwidth is $W = 2/3$ eV. Parameters: $T = 0$, $n = 0.2$, $S = 7/2$.

shell picture see Appendix B).

The local exchange interaction J ranges from intermediate coupling ($JS/W \approx 1$) to strong coupling ($JS/W \gg 1$). For comparison the conventional RKKY exchange integrals are also shown. The latter exhibit the well-known long-range oscillatory dependence on the distance r between two localized spins. For the 2D free electron gas, the asymptotic form ($2k_{\mathrm{F}}r \gg 1$) of the exchange integral is given by [154]

$$J_{\mathrm{2D}}^{\mathrm{R}KKY}(r) \sim J^2 \rho_0(\epsilon_{\mathrm{F}}) k_{\mathrm{F}}^2 \frac{sin(2k_{\mathrm{F}}r)}{(2k_{\mathrm{F}}r)^2} \,. \tag{6.1}$$

Note that the decrease is less rapid than for the RKKY interaction in 3D (see Eq. (5.5)). The shell number does not represent an equidistant measure. In Fig. 6.1 (b) the same exchange integrals are shown along the x-direction. With increasing coupling strength, the local-moment interaction is significantly damped so that for $JS/W \approx 1$ only three shells yield notable contributions. Fig. 6.2 demonstrates the behavior of the MRKKY exchange integrals in more detail. For strong coupling, the effective exchange essentially reduces to a nearest-neighbor interaction. This is the double-exchange limit which was already discussed in Chap. 5.2 (see also Appendix C).

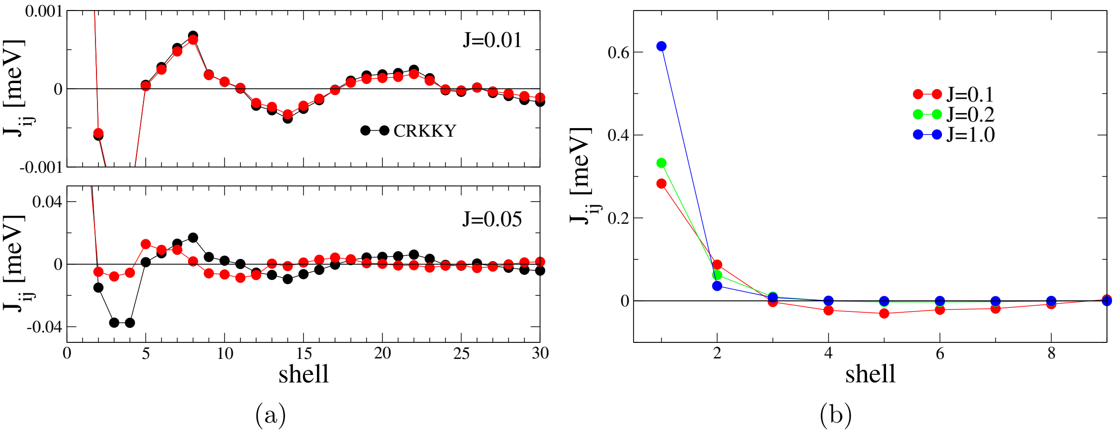

(a) (b)

Figure 6.2: Effective MRKKY exchange integrals for (a) weak and (b) intermediate and strong coupling (double-exchange regime). Note the different scale of the graphs. Parameters as in Fig. 6.1.

6.2 Local-moment magnetization

Fig. 6.3 shows the layer-dependent, normalized spin expectation value $\langle S^z_\alpha \rangle / S$ (in the following called 'magnetization' for simplicity) for different values of J. The curves exhibit a typical Brillouin-like concave shape. A stronger intra-atomic coupling induces a larger effective exchange interaction and thus enhances the ferromagnetism (the dependence of the Curie temperature on J is discussed further below). A characteristic manifestation of the film geometry is the reduced magnetization of the surface layer. This phenomenon has been known for long and can be explained within a mean-field picture [86, 87]: it follows from the smaller number of interaction partners for a localized spin in the surface layer compared to a spin in the inner layers. The difference between the surface magnetization and the 'bulk-like' magnetization ($\alpha = 5$) is most pronounced for intermediate temperatures $T \approx 0.5T_\mathrm{C}$ and vanishes at T_C. A (smaller) relative reduction of the magnetization is also observed for the subsurface layer ($\alpha = 2$).

Figs. 6.3 shows results for both charge-transfer and charge-neutral calculations. There are only small quantitative differences for the chosen moderate carrier density. It is shown in Chap. 6.5.1, however, that the effect of charge transfer on the surface layer magnetization can be rather drastic for lower band filling.

Fig. 6.4 exhibits how the magnetization varies with the film thickness for fixed interaction strength ($JS/W \approx 1$). As in Fig. 6.3 the transitions from the ferromagnetic to the paramagnetic phase are of the second-order, continuous type. With increasing film thickness, the *relative* surface magnetization (i.e. with respect to the center layer magnetization) is found to decrease. This effect is best seen on

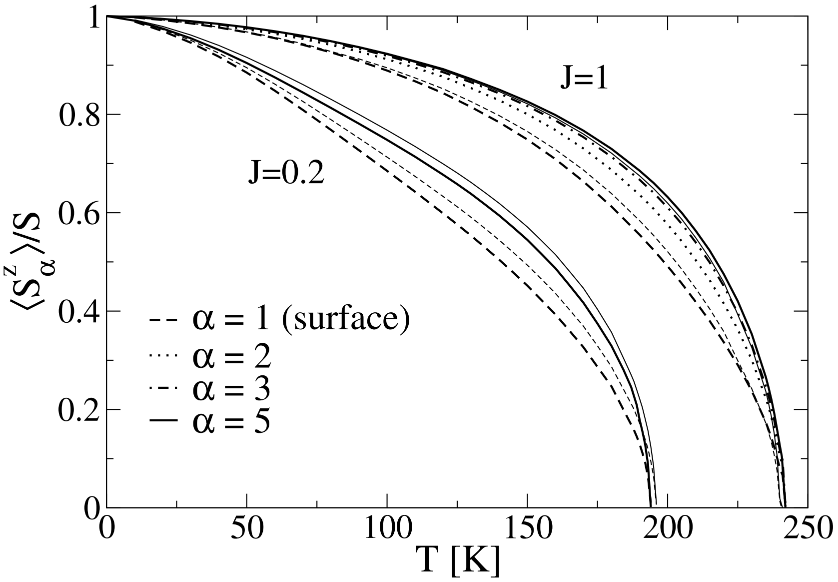

Figure 6.3: Local-moment magnetization as a function of temperature for a 10ML-film (J in eV). Thick lines: charge transfer calculation, thin lines: charge neutral calculation. Parameters: $n = 0.2$, $t = 1/12$, $S = 7/2$, $K_2^\alpha \equiv K_2 = 10^{-6}$.

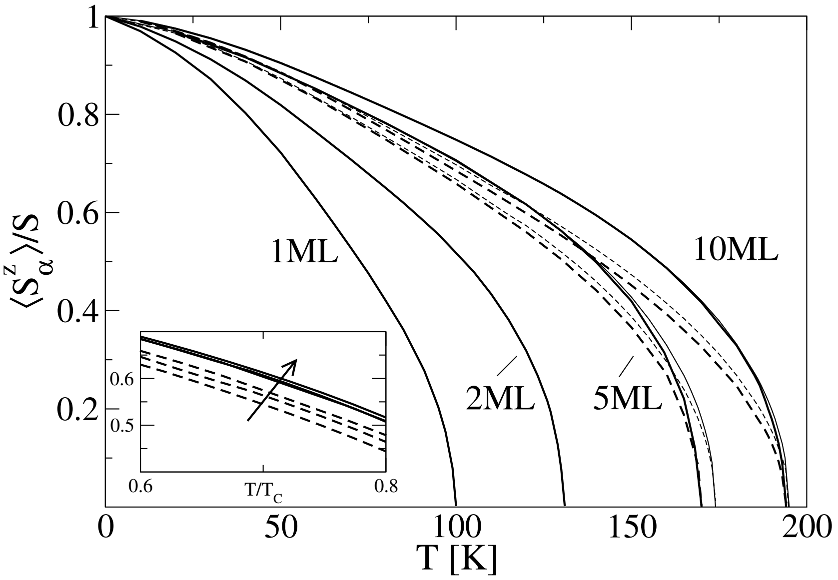

Figure 6.4: Local-moment magnetization as a function of temperature for different film thickness N_L. The dashed lines denote the surface layer magnetization. Thick lines: charge transfer calculation, thin lines: charge neutrality. Inset: magnified part on a reduced temperature scale for $N_\mathrm{L} = 3, 5, 10$ (in the direction of the arrow). Parameters: $J = 0.2$, others as in Fig. 6.3.

a reduced temperature scale as it is shown in the inset. The Curie temperature, however, monotonically increases with the number of layers. This 'conventional' behavior has often been found experimentally and obtained theoretically (see e.g. [50] for Gd-films and [84] for the Heisenberg model). Like the reduced surface layer magnetization, it can be directly linked to the smaller average number of interaction partners in the mean-field picture. It is furthermore known that spin fluctuations become more important in lower dimensions [94, 95]. In addition to these effects, however, there is a strong dependence of the exchange integrals on the local spin-fermion interaction and on the charge carrier density in the KLM. It is shown below that depending on the parameter constellations, deviations from the conventional behavior of an increasing Curie temperature with growing film thickness are possible.

6.3 Curie temperature

The Curie temperature T_{C} separates the ordered (ferromagnetic) from the disordered (paramagnetic) phase. The present section is concerned with the dependence of T_{C} on the charge carrier density n, on the intra-atomic exchange coupling J, and on the film thickness. Where not otherwise stated charge neutrality was enforced.

Fig. 6.5 summarizes the dependence of the Curie temperature on the intra-atomic coupling J. Ferromagnetism is only possible above a critical interaction strength J_{c} which is smaller for thinner films. For stronger coupling, T_{C} saturates as a function of J and increases monotonously with the film thickness (see below). Fig. 6.5 also contains results which were obtained using the ISA electronic self-energy for comparison (see Chap. 4.2). Both J_{c} and $T_{\mathrm{C}}(J \to \infty)$ are larger than the corresponding MCDA results, however the qualitative behavior is the same. It should be noted that the absence of ferromagnetic order below a critical interaction strength is in accordance with analytical results as well as with DMFT results obtained for $D = \infty$ [170].

J_{c} marks the transition from the weak-coupling, long-range RKKY interaction including non-FM correlations to the strong-coupling, double-exchange region favoring a ferromagnetic alignment of the localized spins. Since it is the ratio JS/W which determines the coupling regime, the lower J_{c} for thinner films can be attributed to their reduced bandwidth. What's more, non-FM correlations in the bulk, which are absent in the monolayer for mere topological reasons, may be responsible for the reduced FM stability of the bulk.

From a microscopic point of view, the saturation of T_{C} as a function of J appears reasonable. For strong coupling, the spin of a conduction electron spin is essentially oriented parallel to the localized spin on a given lattice site, with no further effect when J is increased more. The structure of the one-electron

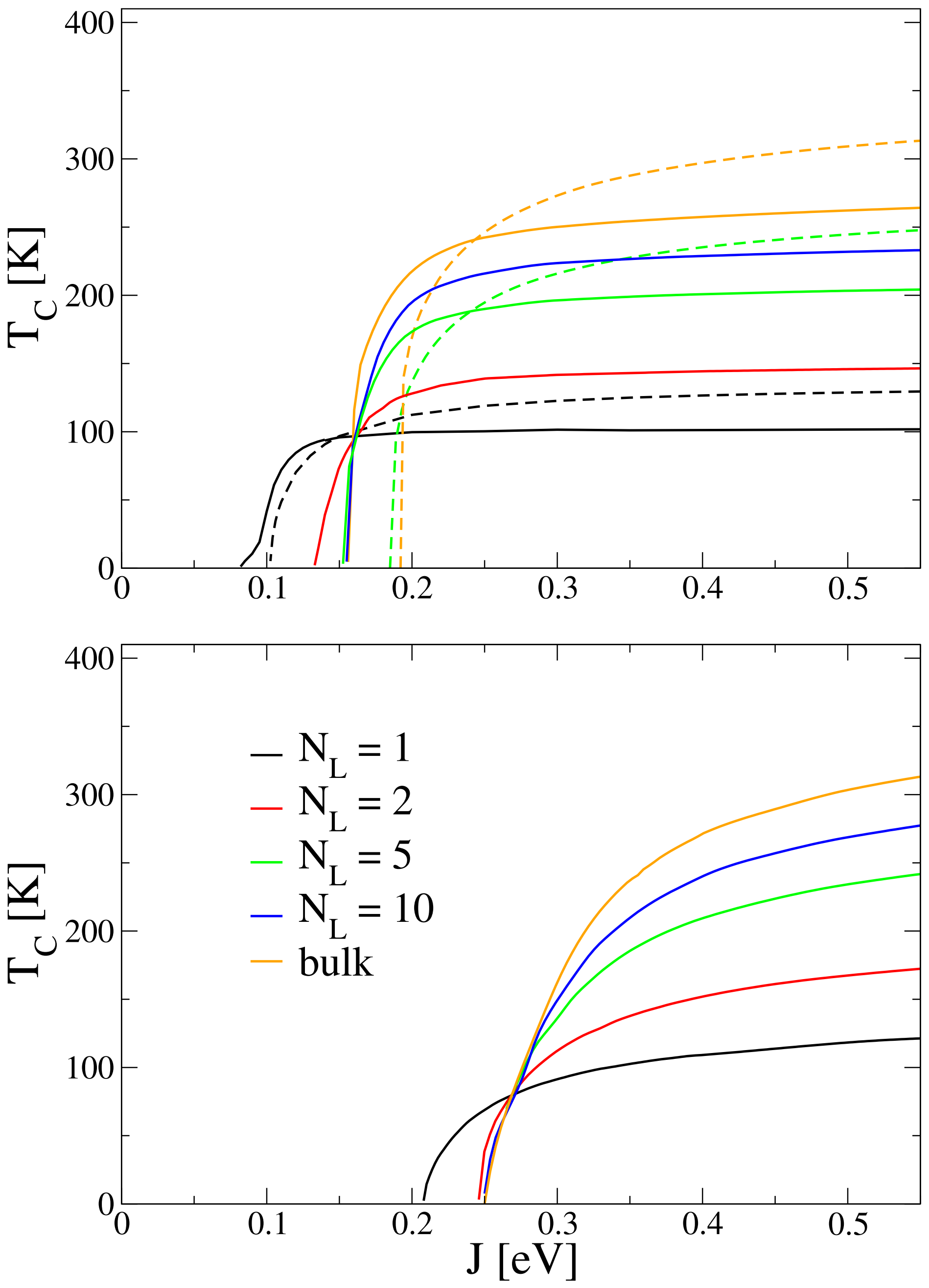

Figure 6.5: Curie temperature as a function of the intra-atomic coupling constant J. Top panel: $n = 0.2$. The dashed lines refer to the ISA electronic self-energy. Bottom panel: $n = 0.6$. Parameters: $S = 7/2$, $K_2 = 10^{-6}$.

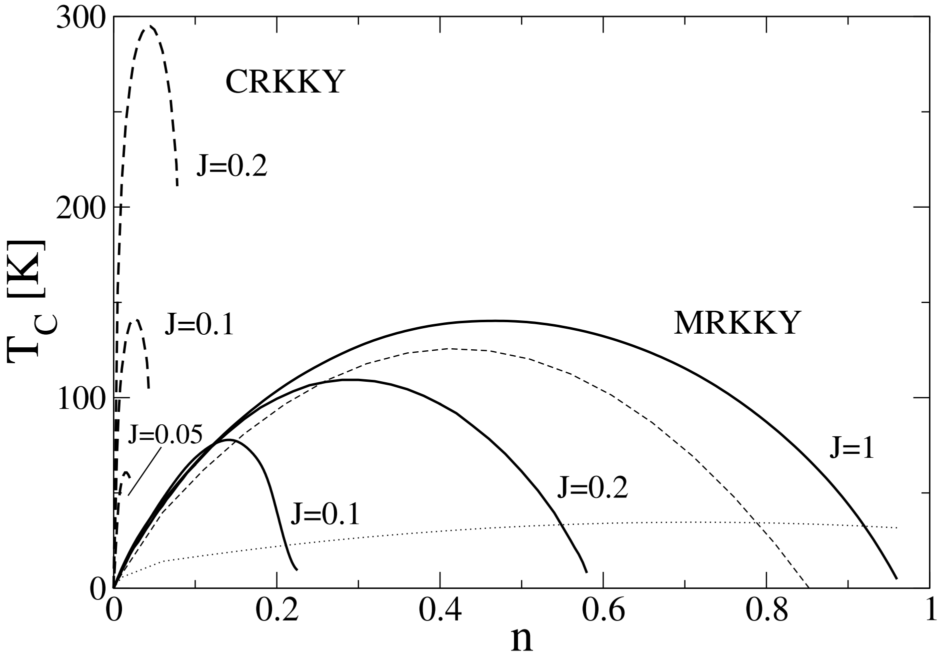

Figure 6.6: Curie temperature of the monolayer as a function of the charge carrier density for different values of J. The dotted line denotes $\Delta U_{\mathrm{pot}}/k_{\mathrm{B}}$, the thin dashed line $\Delta U_{\mathrm{k}in}/k_{\mathrm{B}}$. Parameters: $S = 7/2$, $K_2 = 10^{-6}$.

excitation spectrum remains largely unchanged apart from a rigid shift of the lower band $\sim \frac{1}{2}JS$ (see Fig. 4.4). The exchange interaction among the localized spins, and hence T_{C}, stays constant.

As pointed out in the introduction, the dependence of T_{C} on the charge carrier concentration is of particular interest as regards the manipulation of the ferromagnetic properties by doping or by optical excitations. Comparing the conventional and the modified RKKY interaction (Fig. 6.6), one observes quite a different behavior concerning the maximum value of $T_{\mathrm{C}}(n)$ and the range of FM stability. Since for the conventional RKKY exchange integrals $J_{ij}^{\mathrm{R}KKY} \propto J^2$, the critical temperature goes up rapidly with J. On the other hand ferromagnetism is restricted to small band fillings, indicating that antiferromagnetic correlations are more pronounced in conventional RKKY theory.

In contrast to this, T_{C} is considerably lowered when correlation effects are taken into account using the MCDA+MRKKY approach. The range of FM stability is significantly enlarged: for strong coupling it stretches almost to half-filling, and the maximum lies near quarter-filling. In the double-exchange regime, the dependence of T_{C} on the charge carrier density corresponds to the variation of the kinetic energy difference between the PM state and the FM state with n. The energy

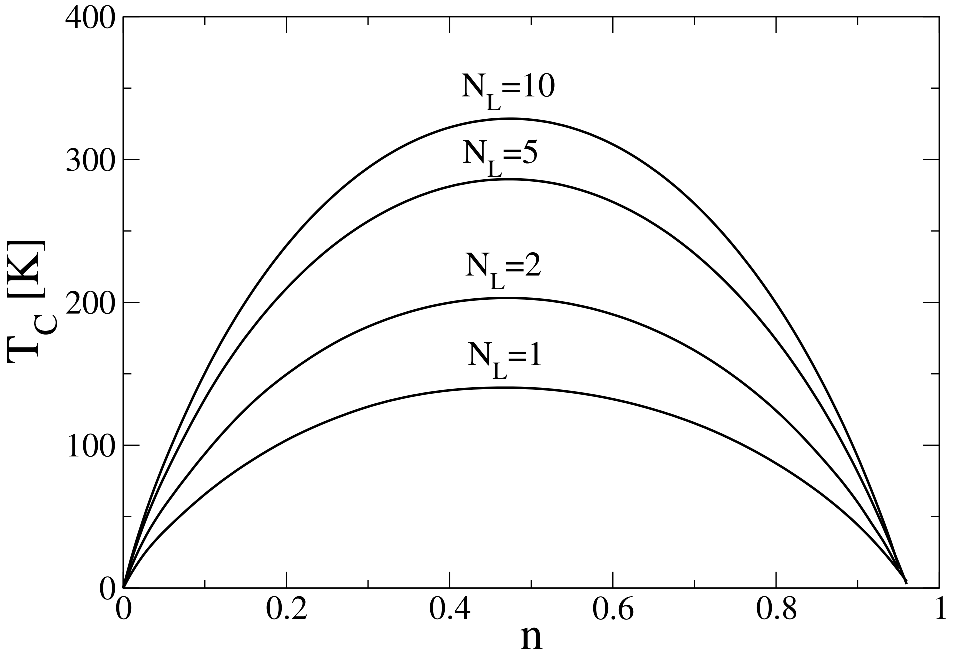

Figure 6.7: Curie temperature as a function of the charge carrier density for strong coupling. Parameters: $J = 1$, $S = 7/2$, $K_2 = 10^{-6}$.

gain in the ordered phase is maximal at quarter filling and then diminishes as the motion of the spin-polarized charge carriers is more and more blocked with increasing carrier density. The Curie temperature can be estimated as

$$k_{\mathrm{B}} T_{\mathrm{C}} \approx \Delta U \approx \Delta U_{\mathrm{k}in} = U_{\mathrm{k}in}(\mathrm{P}M) - U_{\mathrm{k}in}(\mathrm{F}M)\,, \tag{6.2}$$

because the potential energy difference plays only a minor role. Fig. 6.6 demonstrates how the ferromagnetic transition temperature correlates with the kinetic energy difference.

Fig. 6.7 shows $T_{\mathrm{C}}(n)$ in the strong-coupling regime for different film thickness. The qualitative behavior is the same in all cases. A quantitative analysis has to take into account that varying the film thickness affects the Curie temperature in two ways. First, the kinetic energy of the charge carriers is lowered with an increasing number of layers since the hopping is enhanced. Secondly, as already mentioned earlier, the change in T_{C} is partly due to the change in the average number of (nn) localized-spin interaction partners. The proportionality of the Curie temperature to the coordination number is hidden in the **q**-sum over the exchange integrals in Eq. (5.48). At his point it is useful to introduce the effective coordination number

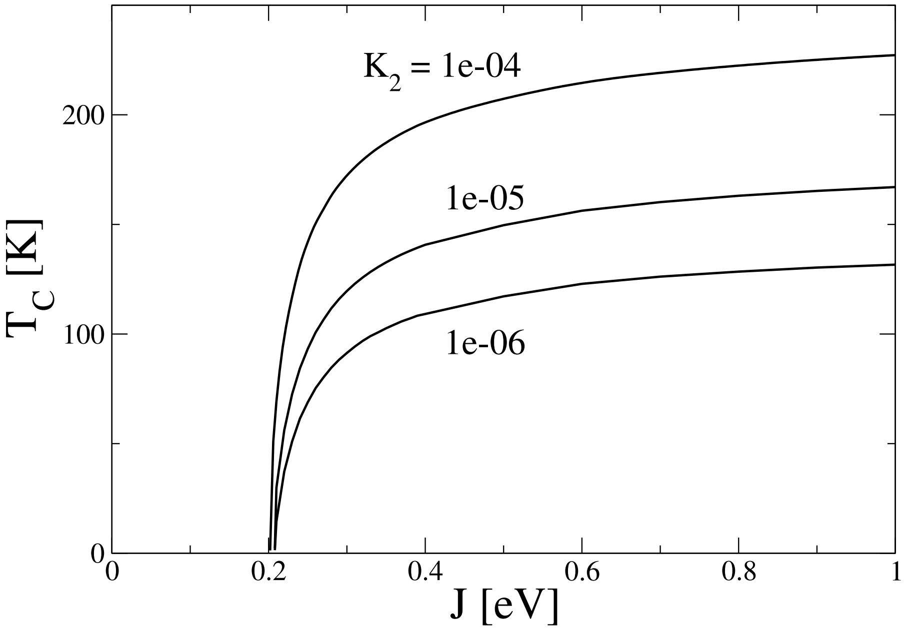

Figure 6.8: Curie temperature of the monolayer as a function of the intra-atomic coupling J for different values of the single-ion anisotropy strength K_2. Parameters: $n = 0.6$, $S = 7/2$.

$$z_{\mathrm{e}ff} = \frac{z_{\mathrm{b}ulk}(N_{\mathrm{L}} - 2) + 2z_{surf}}{N_{\mathrm{L}}} \tag{6.3}$$

which yields the average number of nn-bonds as a function of the thickness for a given film geometry. In case of the sc(100)-symmetry ($z_{surf} = 5$) it ranges from $z_{\mathrm{m}ono} = 4$ for the monolayer to $z_{\mathrm{b}ulk} = 6$ for the bulk crystal. Since the change in kinetic energy is approximately proportional to the effective coordination number, too, one expects the variation of T_{C} with the number of layers to be about quadratic in $z_{\mathrm{e}ff}$, provided that anisotropy effects are not dominant, i.e. the anisotropy is much smaller than the effective exchange as it is the case here. A quadratic dependence on $z_{\mathrm{e}ff}$ is compatible with the results in Fig. 6.7. Spin fluctuations apparently lead to a further suppression of T_{C} for small film thickness.

Fig. 6.8 demonstrates the influence of the single-ion anisotropy on the critical temperature of the monolayer. J_{c} depends rather weakly on the anisotropy strength K_2. In the double-exchange regime, the interaction between localized moments essentially reduces to nearest-neighbor exchange integrals which are determined by the kinetic energy and independent of the local coupling J. Therefore general results concerning the role of a second-order anisotropy in localized-spin models can be drawn upon. In agreement with Monte Carlo simulations of classical *nn* Heisenberg films [246], a renormalization group study of a spin model in the continuum limit with an exchange coupling J_1 and a uniaxial anisotropy K_2 yields for the Curie temperature of a monolayer [247]

$$T_{\mathrm{C}}^{2D} = \frac{2T_{\mathrm{C}}^{3D}}{\ln(\pi J_1/K_2)} \,. \tag{6.4}$$

On the other hand, using the RPA-formula for the Curie temperature (5.48) with the nearest-neighbor effective exchange integral J_1 only, and solving the $\mathbf{q}$-integral approximately by considering only the predominantly contributing small wave vectors, one obtains

$$k_{\mathrm{B}}T_{\mathrm{C}}^{2D} = \frac{\frac{8\pi}{3}S(S+1)J_1}{\ln(1+2\pi^2 J_1/(K_2\gamma))} \,. \tag{6.5}$$

With the RPA expression for the *nn* Heisenberg model $k_{\mathrm{B}}T_{\mathrm{C}}^{3D} \approx \frac{24}{9}S(S+1)J_1$ and with $\gamma \approx 1$, the two expressions for the critical temperature (6.4) and (6.5) are in agreement for $K_2 \ll J_1$.

A quantity of general interest in thin film magnetism is the dependence of the ferromagnetic transition temperature on the film thickness, i.e. on the number of layers N_{L}. The very different characteristics of the conventional RKKY interaction on the one hand - long-range, oscillating exchange integrals with antiferromagnetic and incommensurate correlations - and of the double-exchange interaction - short-range, strong ferromagnetic exchange - on the other may lead to quite different dependences of the Curie temperature on the film thickness. As already mentioned above, a decrease of T_{C} with diminishing film thickness is usually found, both in experiment [50] and in theory [84]. This conventional behavior is found for KLM films in the strong-coupling regime as Fig. 6.9 illustrates. For intermediate coupling near the critical J-region, the dependence changes drastically (cf. Fig. 6.5). Here, the Curie temperature may not vary at all with the film thickness. For an appropriately chosen J, the transition temperature decreases with increasing N_{L} and a finite T_{C} exists only for very thin films. If $J < J_{\mathrm{c}}^{mono}$ no ferromagnetism is possible for any thickness. The same picture is obtained for a higher band filling and using the ISA self-energy (Fig. 6.5). The behavior follows eventually from the reduced J_{c} for smaller thickness and is therefore due to the larger effective coupling JS/W in ultrathin films.

6.4 Effective exchange interaction at the surface

The presence of a surface leads to a reduced magnetization of the surface layer due to the smaller number of interaction partners. In the following, it is investigated how the effective exchange integrals *themselves*, being dependent on the electronic

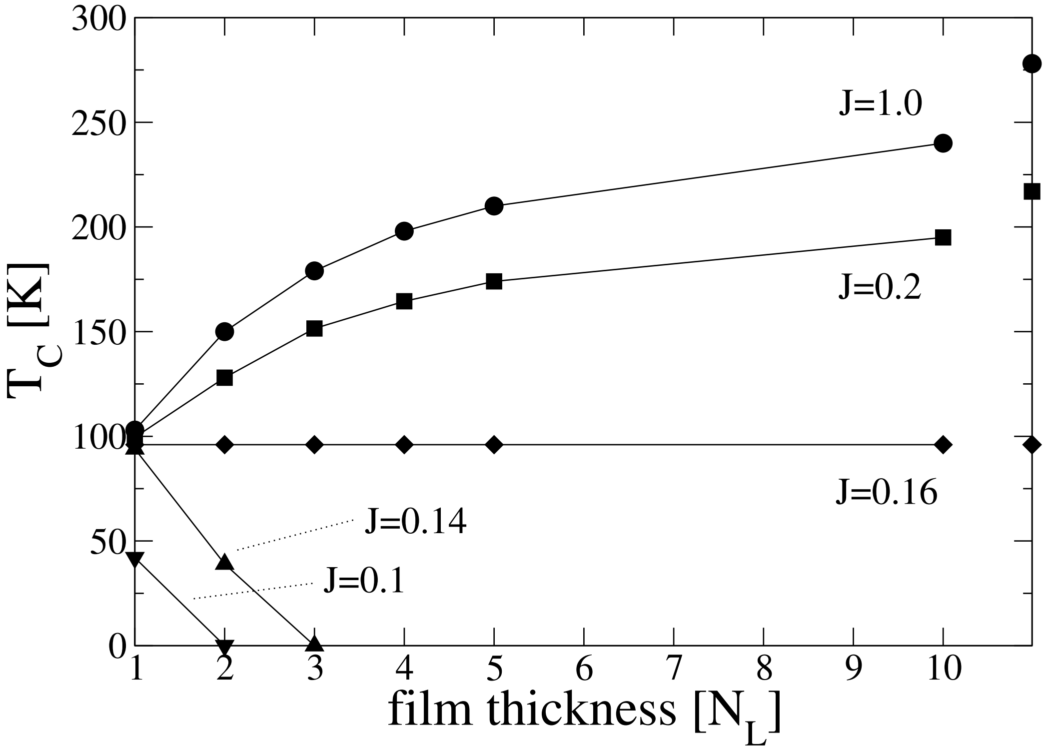

Figure 6.9: Curie temperature as a function of the film thickness for different values of the intra-atomic coupling J. The big dots on the right axis indicate the bulk T_C-values. Lines are guides to the eye. Parameters: $n = 0.2$, $S = 7/2$, $K_2 = 10^{-6}$.

structure, are modified by the reduced translational symmetry. One may name this effect an 'indirect' coordination number effect, in contrast to the conventional 'direct' coordination number effect. In order to distinguish them, the weigthed (or specific) exchange interaction of a spin in the surface layer is introduced:

$$J_{\mathrm{w}}^{surf} = \sum_n \frac{z_{n,\mathrm{bulk}}}{z_{n,surf}} J_n^{\alpha=1} \,.$$

$z_{n,..}$ denotes the number of interaction partners in the nth 3D-shell around a bulk/surface atom. For the concrete numerical evaluation, the first four shells are taken into account. The weigthed exchange in the surface layer of an sc(100)-film then explicitly reads

$$J_{\mathrm{w}}^{surf} = \frac{6}{5}J_1^1 + \frac{12}{8}J_2^1 + \frac{8}{4}J_3^1 + \frac{6}{5}J_4^1 \,. \tag{6.6}$$

Fig. 6.10 displays the different effective exchange interactions in the surface layer and in the center layer for intermediate coupling ($JS/W \approx 1$) and for strong coupling ($JS/W \gg 1$).

The energies of a few meV lie in the typical range for spin waves [248]. The overall temperature dependence is rather weak. One observes an increase with temperature in the intermediate coupling regime, whereas for strong coupling the exchange interaction decreases. The exchange interaction only weakly depends on temperature in the paramagnetic phase.

The modified RKKY interaction interpolates between the weak-coupling limit and the double-exchange regime. Although strictly speaking $J = 0.2$ does not quite belong to the weak-coupling regime (see Chap. 6.1), Fig. 6.10 reveals the contributions from higher shells. The proportionality of the conventional RKKY interaction to the density of states at the Fermi level (5.14) implies an inverse proportionality to the bandwidth: $J_{\mathbf{q}=0}^{\mathrm{R}KKY} \propto 1/W$. In the interacting case, one should rather speak of an *effective* bandwidth W_{eff}. With increasing temperature, the latter is narrowed due to the growing thermal disorder in the spin system. The resulting increase of the spin-integrated LDOS at the chemical potential (see e.g. Fig. 4.9) fits to the increasing total effective exchange interaction. The validity of the RKKY picture is also supported by the stronger thermal variation of the 'bulk-like' exchange interactions ($\alpha = 5$). Since the effective bandwidth of the LDOS is larger for the inner layers, the exchange interaction in the bulk is governed to a greater extent by weak-coupling RKKY physics than at the surface.

On the contrary, for strong coupling ($J = 1$), the exchange interactions decrease with temperature. In the double-exchange regime, one should rather inspect the kinetic energy (see Eq. (5.23) and Appendix C). A higher/lower absolute value of the kinetic energy is associated with a larger/smaller effective bandwidth (provided that the spectral weight transfer is not too large). The fact that the band narrowing

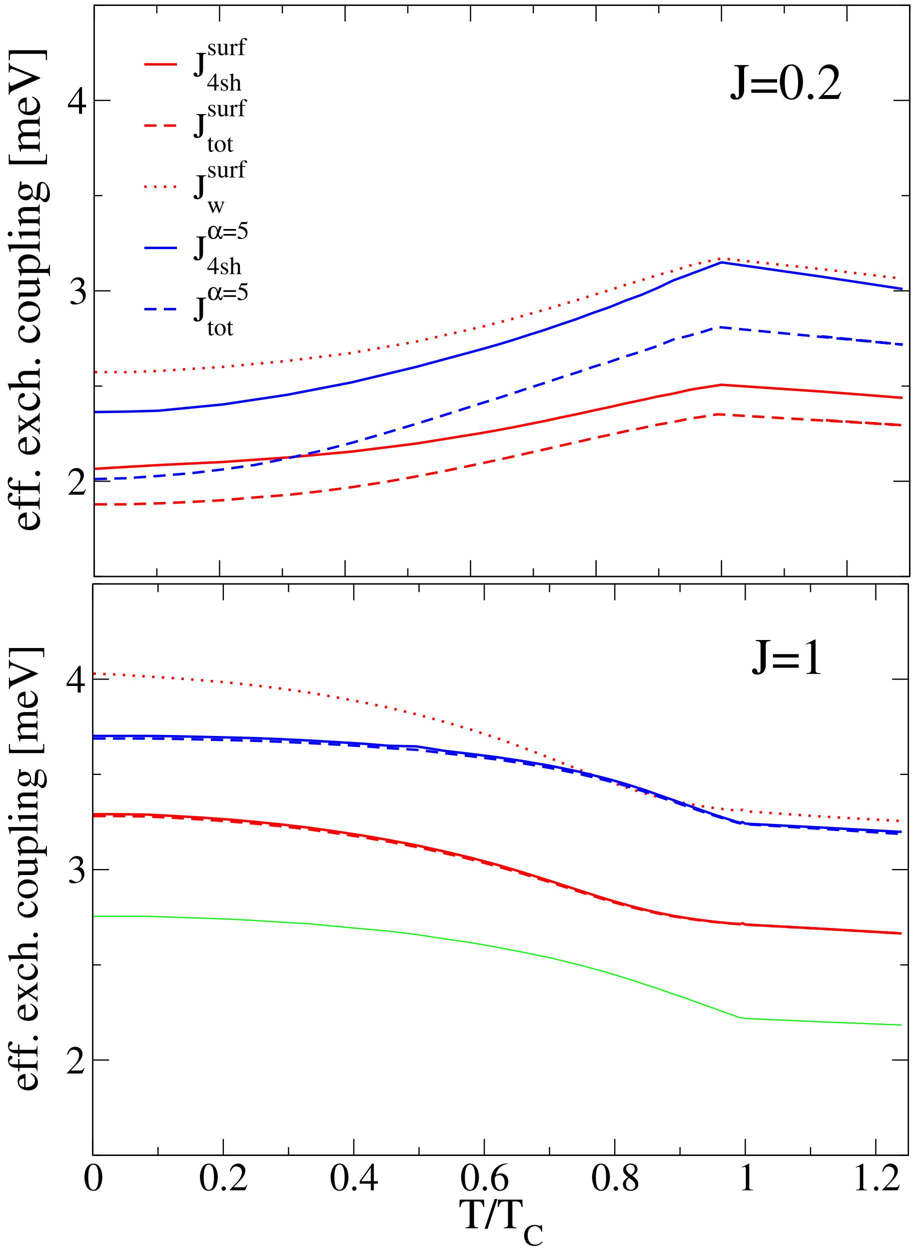

Figure 6.10: Effective exchange coupling in a 10ML-sc(100)-film for intermediate (top panel) and strong coupling (bottom panel). Red lines denote the surface layer, blue lines the center layer. Full lines: exchange interaction due to the first four shells. Dotted line: weighted surface exchange interaction due to the first four shells. Dashed line: total exchange interaction $J_{tot}^{\alpha} = \sum_{j\beta} J_{ij}^{\alpha\beta}$. The green line is proportional to $|U_{\mathrm{kin}}|$. Charge-transfer calculation. Parameters: $n = 0.2$, $S = 7/2$.

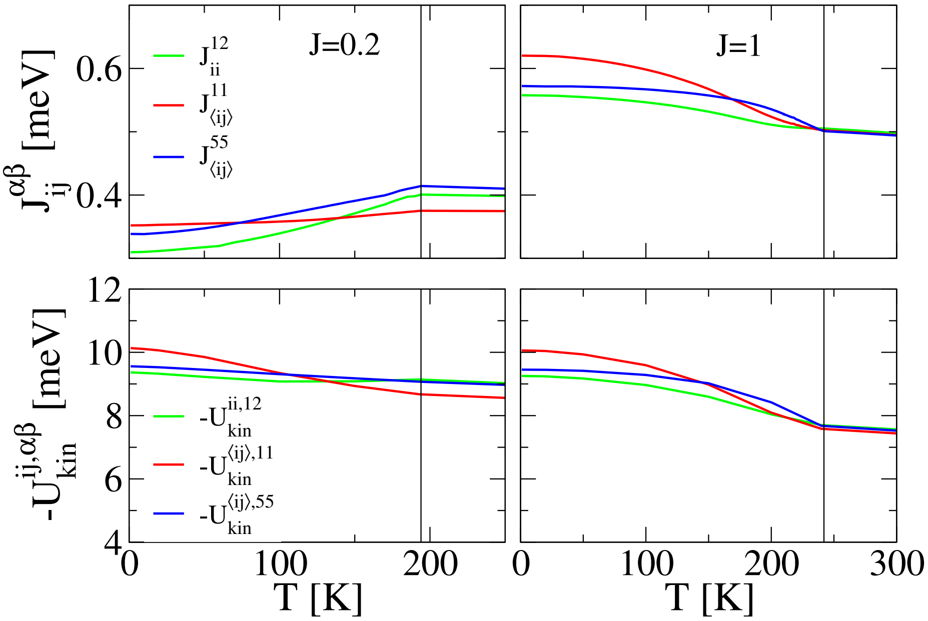

Figure 6.11: Effective nearest-neighbor exchange integrals (top panel) and kinetic energy (bottom panel) for a 10ML-film. The three different contributions to the kinetic energy refer to the hopping from the surface to the subsurface layer (green line), *nn*-hopping within the surface layer (red line), and *nn*-hopping in the center layer (blue line). Vertical lines indicate the Curie temperature. Other parameters as in Fig. 6.10.

with increasing T is accompanied by a reduced effective exchange indicates that the proportionality between the latter and the kinetic energy is not restricted to zero temperature.

One observes that the total exchange and the exchange from the first four shells are weaker at the surface than in the center of the film. This is the trivial consequence of missing neighbors at the surface. The *weighted* exchange, however, is larger up to T_C ($J = 0.2$) and up to $0.7T_\mathrm{C}$ ($J = 1$), revealing that the coupling of a localized spin at the surface is in fact *stronger* than in the bulk part of the film for these temperatures.

Fig. 6.11 displays the nearest-neighbor inter- and intralayer surface exchange integrals $J_{ii}^{1,2}$ and $J_{\langle ij\rangle}^{1,1}$ and the *nn* in-plane exchange integral in the center layer. For comparison, the corresponding contributions to the kinetic energy according to

$$U_{\mathrm{k}in} = \sum_{i\alpha j\beta} U_{\mathrm{k}in}^{ij,\alpha\beta} \tag{6.7}$$

are also shown. They can be calculated using the off-diagonal DOS (3.20):

$$U_{\mathrm{k}in}^{ij,\alpha\beta} = -t_{ij}^{\alpha\beta} \sum_{\sigma} \int_{-\infty}^{+\infty} dE f_{-}(E) \rho_{ij\sigma}^{\alpha\beta}(E) \,. \tag{6.8}$$

For strong coupling, the effective interaction is practically restricted to the *nn*-exchange integrals shown in Fig. 6.11. The enhanced exchange interaction at the surface turns out to be the result of an increased in-plane effective exchange, which overcompensates a slight suppression of the perpendicular coupling. There is a clear proportionality between the exchange integrals and the kinetic energy resulting from the hopping of charge carriers along the corresponding bonds.

For $J = 0.2$, nearest-neighbor contributions do not suffice and more shells have to be considered. The curves in Fig. 6.11 exhibit a remarkable mixture of both weak-coupling and strong-coupling behavior. The overall temperature dependence of the *nn* exchange integrals is, just like the summed exchange integrals, more or less inversely proportional to the kinetic energy as is typical for the conventional RKKY interaction. For fixed temperature, however, the relative magnitude of the surface and bulk exchange integrals is paralleled by a qualitatively similar proportion between the corresponding *nn* kinetic energy contributions, albeit with no such neat proportionality as in the strong-coupling case.

It is to be expected that the absolute value of and the ratio between the different kinds of exchange interaction depends on the band filling. Fig. 6.12 demonstrates how they evolve with increasing n. For low charge carrier density, the specific exchange interaction at the surface is *reduced* as compared to the bulk exchange. This holds for both, $J = 0.2$ and $J = 1$.

The kinetic energy, being the driving mechanism behind the effective spin interaction in the double-exchange regime, is determined by integration over the off-diagonal DOS which is shown in Fig. 6.13. The n-dependence of the exchange in the bulk and at the surface can be inferred from the layer-dependence and the anisotropy of the DOS near the surface on the one hand and from the position of the chemical potential on the other. In particular, the band narrowing of $\rho_{\langle ij \rangle \sigma}^{11}$ explains the reduced exchange for low band fillings.

To summarize, the analysis of the exchange interactions at the film surface demonstrated their close connection to the kinetic energy of the charge carriers in the strong-coupling regime. The modification of the effective exchange integrals near the surface represents an 'indirect' coordination-number effect due to the layer-dependent and anisotropic off-diagonal density of states. The *full* exchange coupling of a spin at the surface is furthermore reduced 'directly' by a smaller number of interaction partners compared to the bulk. Clearly, both effects depend

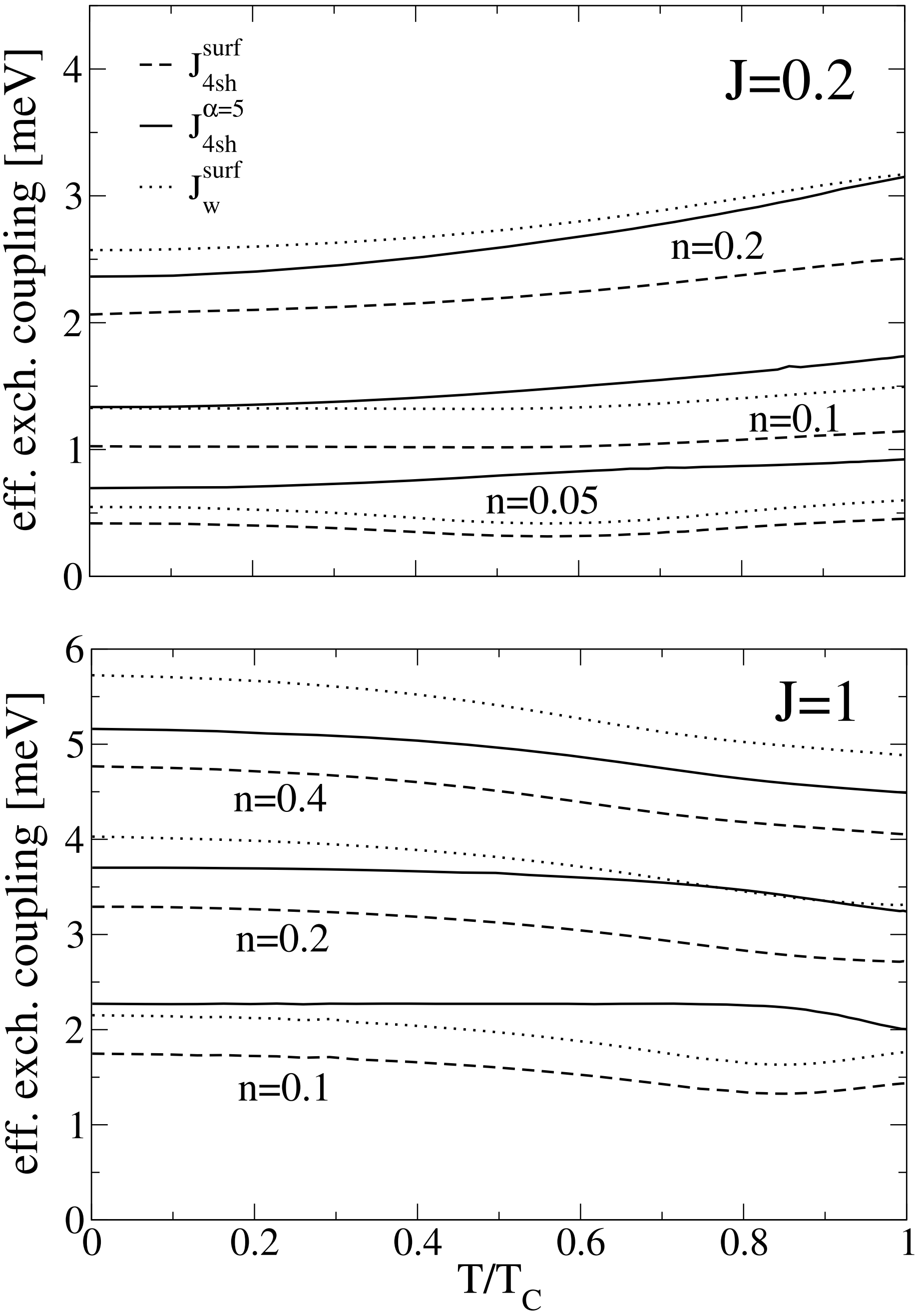

Figure 6.12: Effective exchange coupling for different values of the carrier density.

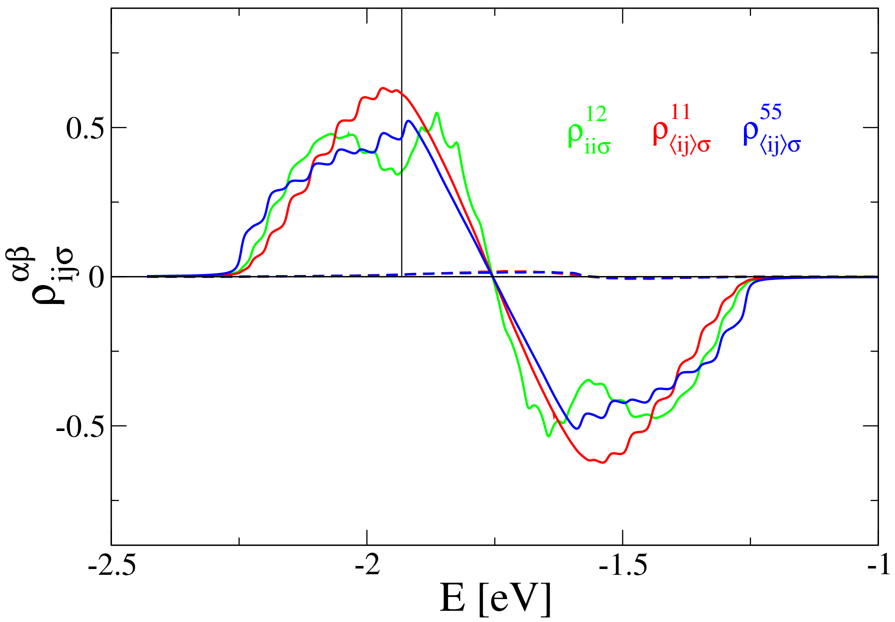

Figure 6.13: Off-diagonal nearest-neighbor DOS in the FM-saturated phase ($T = 0$). Full lines denote the ↑-DOS, dashed lines the ↓-DOS. Parameters: $N_\mathrm{L} = 10$, $J = 1$, $n = 0.2$, $S = 7/2$.

on the lattice structure and the surface geometry. They are stronger for more open configurations like, e.g., the sc(111)-surface.

If the exchange integrals near the film surface are increased or decreased is crucially determined by the band filling. For moderate n, the specific surface exchange interaction is enhanced. This enhancement is relatively weak compared to the absolute size of the exchange interaction. On the other hand, a more pronounced modification of the surface exchange integrals which may influence the surface layer magnetization significantly is more probable for small n. Here, the narrowing of the surface LDOS leads to marked charge transfer (Chap. 4.5).

6.5 Ferromagnetic surface stability

6.5.1 Charge-transfer-induced magnetic surface instability

The consequences of charge transfer on the magnetization profile were found to be marginal for an average band filling of $n = 0.2$ in Chap. 6.2. In the upper panel of Fig. 6.14 (top), the surface, subsurface, and center layer magnetization of a strongly-coupled 10ML-film for different small band fillings is shown. The magnetic stability of the top layer is strongly weakened with decreasing n. This is accompanied by a stronger relative decrease of the surface charge density (bottom panel). The instability is the result of the self-consistent interplay between a reduced surface magnetization and a decreased effective bandwidth of the surface LDOS. The latter enhances charge transfer out of the surface layer and thereby reduces the interaction among the localized spins.

Fig. 6.14 also demonstrates how the effect of charge transfer on the ferromagnetic surface stability varies with the film thickness. The reduction of the top-layer magnetization and of the surface-to-center density ratio is more pronounced if the number of layers is increased. The temperature-dependent LDOS of the surface and center layer of a 20ML-film is shown in Fig. 6.15. One observes that the top-layer LDOS exhibits a rather paramagnetic shape already at $T \approx 0.65T_{\mathrm{C}}$, where the minimum of n_{surf}/n_{center} is reached.

As already pointed out in Chap. 4.5, the two scenarios of charge transfer and charge neutrality are extreme limits. Of course, any quantitative analysis of charge transfer, depending sensitively on the electronic structure, must be based on a realistic band structure. The above results should therefore not be overcharged. However, Fig. 6.14 demonstrates that the magnetic destabilization of the surface layer can be quite significant for small charge carrier densities and for sufficiently thick films. It may therefore be an observable effect in real systems like manganites.

6.5.2 Relaxation of the sc(100)-surface

In any real crystal the surface layers experience some kind of relaxation: the distance between crystal planes close to the surface deviates from the interplanar spacing in the bulk. For Gd, DFT-calculations mostly yield a reduction of the surface-subsurface layer distance of up to $\approx 4\%$ of the bulk interlayer distance [45, 46, 47, 249, 250], in agreement with experimental LEED-investigations [251]. Taking the distance dependence of the hopping integrals for d-electrons, $t \sim r^{-5}$ [252], a reduction of $\approx 4\%$ gives rise to an increase of the surface-to-subsurface hopping $t_{\perp}^{surf}$ by $\approx 20\%$. In the model calculations below, this parameter is changed by up to 80% in order to work out the main effects of a modified surface hopping on the magnetic stability.

Fig. 6.16 shows the layer-dependent magnetization for a 10ML-film in the intermediate ($JS \lesssim W$) and strong coupling ($JS \approx 3.5W$) regime for different values of surface-to-subsurface hopping $t_{\perp}^{surf} \equiv t_{ii}^{12} = t_{ii}^{9,10}$ (called 'surface hopping' in what follows). As regards the overall temperature dependence, one observes a more concave shape for the magnetically stiffer case $J = 1$ compared to a rather linear decrease of the magnetization for $J = 0.2$. A smaller surface hopping leads to a reduced magnetic stability particularly at intermediate temperatures. In the limit $t_{\perp}^{surf} = 0$, the surface layer represents a monolayer film with a smaller Curie temperature than that of a 9ML-film (Fig. 6.9).

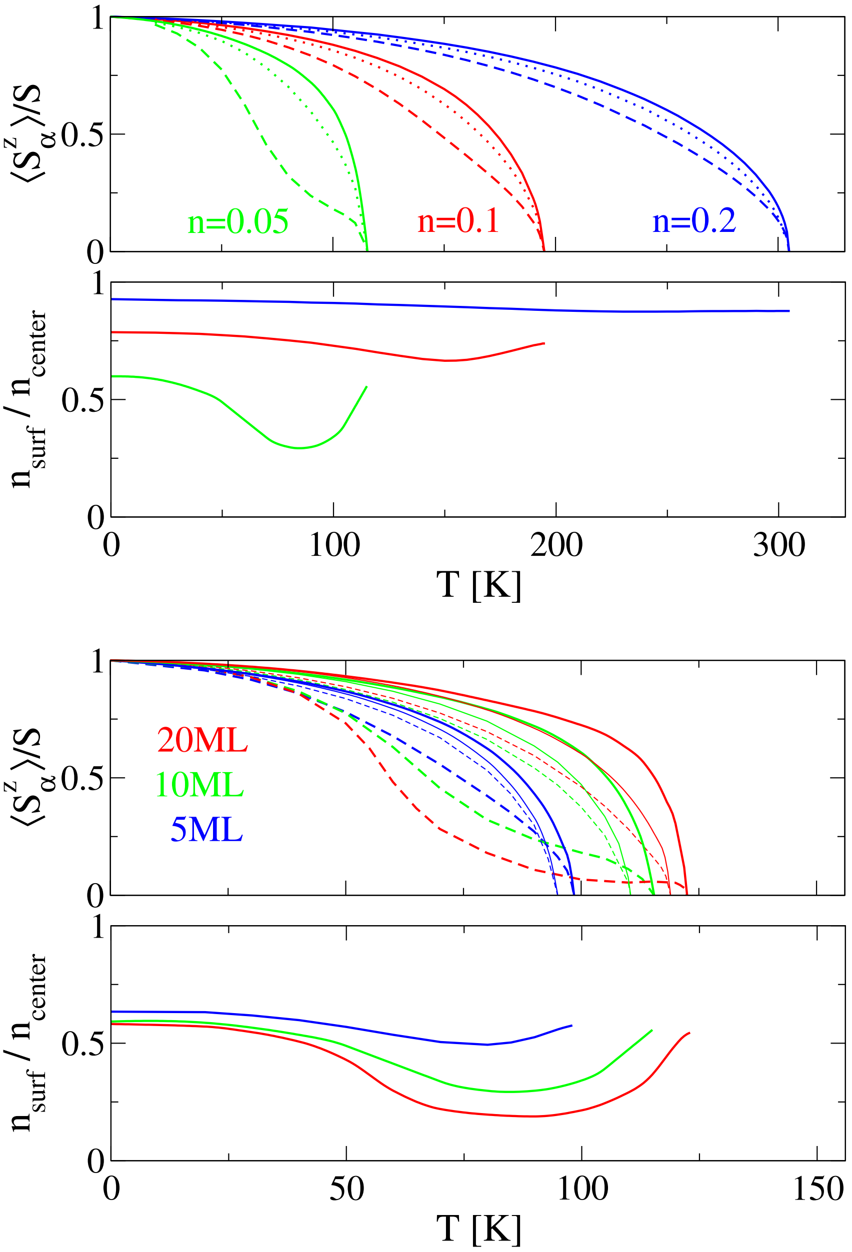

Figure 6.14: Local-moment magnetization of the center layer (full line), subsurface layer (dotted line), and surface layer (dashed line) and surface-to-center layer ratio of the charge density. Top two panels: 10ML-film for different values of the average band filling. Bottom two panels: fixed carrier density $n = 0.05$ and different film thickness. Thin lines indicate enforced charge neutrality. Parameters: $J = 2$, $S = 3/2$.

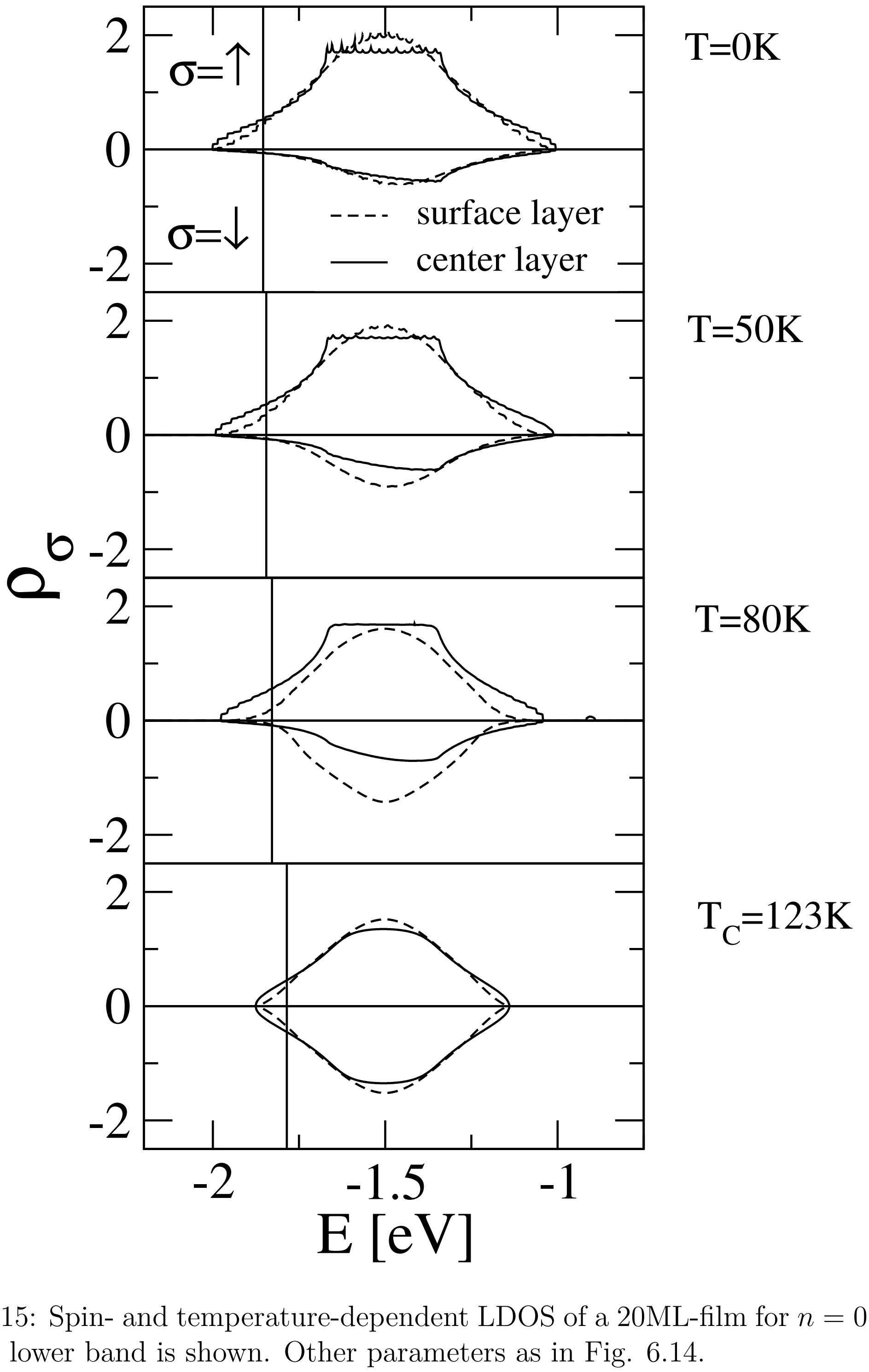

Figure 6.15: Spin- and temperature-dependent LDOS of a 20ML-film for $n = 0.05$. Only the lower band is shown. Other parameters as in Fig. 6.14.

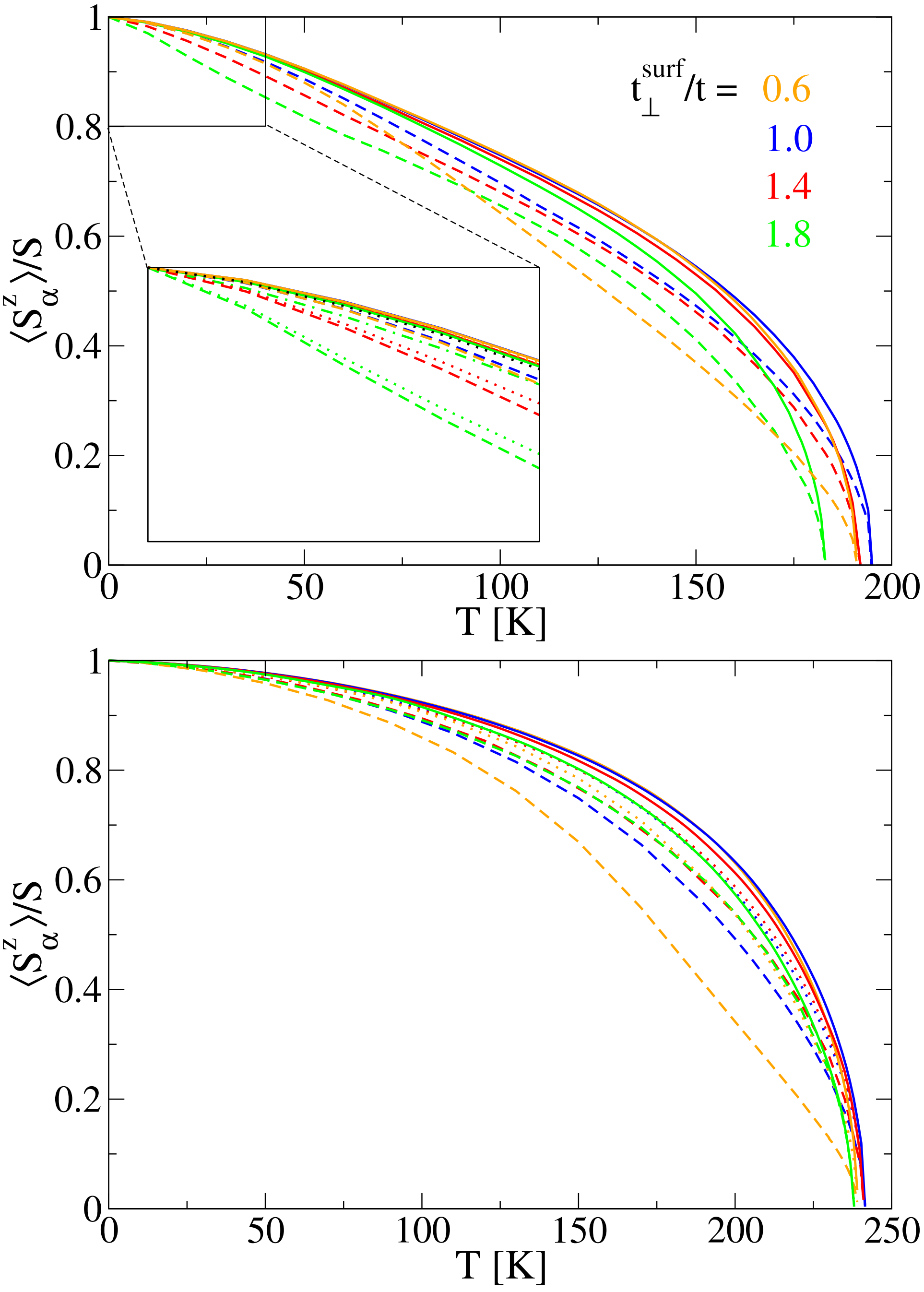

Figure 6.16: Local-moment magnetization of a 10ML-sc(100)-film as a function of temperature for different ratios of the surface-to-subsurface and bulk hopping $t_\perp^{surf}/t$. Top panel: $J = 0.2$. Bottom panel: $J = 1$. Full lines: center layer ($\alpha = 5, 6$), dashed lines: surface layer ($\alpha = 1, 10$), dotted lines: subsurface layer, dash-dotted lines: subsubsurface layer ($\alpha = 3$). Other parameters: $n = 0.2$, $S = 7/2$. Charge-transfer calculation.

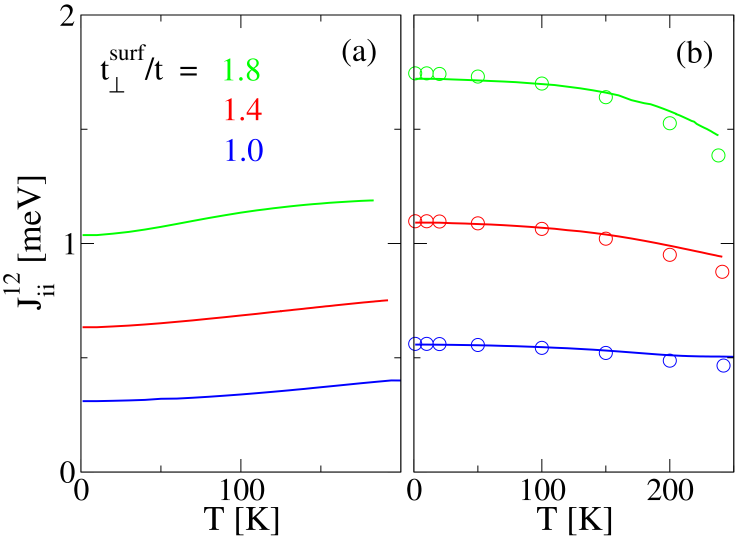

Figure 6.17: Effective exchange integral $J_{ii}^{1,2}$ in a 10ML-film for enhanced hopping between the surface and the subsurface layer. (a) $J = 0.2$, (b) $J = 1$. The open circles indicate the kinetic energy contribution $|U_{kin}^{ii,12}|$ up to a proportionality factor.

For *enhanced* surface hopping ($t_\perp^{surf}/t > 1$) a somewhat unexpected behavior is observed. There is a drastic suppression of the surface and subsurface layer magnetization at low temperatures for $J = 0.2$. This magnetic destabilization amounts to an increase of $\approx 100\%$ in the reduction $\Delta\langle S_\alpha^z\rangle = S - \langle S_\alpha^z\rangle$ ($\alpha = 1, 2$) at $T \approx 0.25T_\mathrm{C}$ if the surface hopping is varied from $t_\perp^{surf}/t = 1$ to 1.8. If one considers the *relative* reduction of the (sub)surface layer magnetization with respect to the center layer magnetization $\langle S_{\alpha=5}^z\rangle - \langle S_{\alpha=1,2}^z\rangle$, the modified surface hopping even leads to a tenfold enhancement of this value. Contrary to this, for strong coupling, there is hardly any change in the magnetic stiffness at low temperatures.

Fig. 6.17 shows the interlayer effective exchange integral $J_{ii}^{1,2}$ for uniform and for enhanced surface hopping. $J_{ii}^{1,2}$ depends quadratically on the interlayer hopping: $J_{ii}^{1,2} \propto (t_\perp^{surf})^2$. The *intra*layer *nn* exchange integral $J_{\langle ij\rangle}^{1,1}$ at low temperatures, on the other hand, *decreases* for larger $t_\perp^{surf}$ on a scale which is an order of magnitude smaller than the change in $J_{ii}^{1,2}$ (Fig. 6.18).

In the double-exchange regime, the effective nn-coupling is proportional to the kinetic energy (see Chap. 5.2). For a translationally invariant situation this means that the exchange integral depends linearly on the hopping parameter t (Appendix C). The quadratic dependence of the interlayer exchange integral on the hopping, $J_{ii}^{1,2} \propto (t_\perp^{surf})^2$, is due to the reflection of the charge carriers at the surface.

A change in the surface-to-subsurface hopping $t_\perp^{surf}$ affects the two top layers

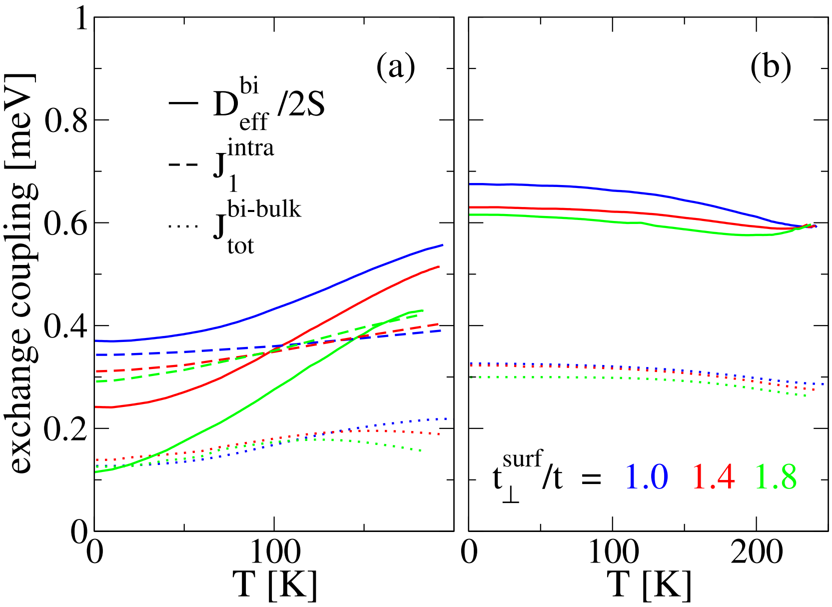

Figure 6.18: Ferromagnetic stiffness of the effective surface bilayer, *nn* in-plane effective exchange integral in the surface layer, and total coupling of a surface bilayer spin to the bulk. (a) $J = 0.2$, (b) $J = 1$.

much more than the inner layers of the film. In order to quantitatively describe the reduced surface magnetic stiffness for enhanced $t_\perp^{surf}$ at low temperatures, one may therefore approximate these two layers by an effective bilayer which is coupled to the other layers of the slab. The total coupling of an average bilayer spin to all spins situated outside the bilayer,

$$J_{tot}^{bi-bulk} = \frac{1}{2} \sum_{j\beta}^{\beta \neq 1,2} (J_{ij}^{1\beta} + J_{ij}^{2\beta}) \,, \tag{6.9}$$

does not change much if $t_\perp^{surf}$ is varied as can be verified in Fig. 6.18.

The crucial point concerning the ferromagnetic bilayer stiffness is that it does not depend on the interlayer coupling if the latter is dispersionsless. However, this is the case for the sc(100)-geometry considered here (see Appendix D). The interlayer coupling J_{ii}^{12}, on the other hand, is the exchange integral which is affected most by the relaxation. Hence, the effect is specific to the sc(100)-geometry. In general, the *nn* interlayer exchange integral may be wave-vector-dependent, and a modification of this coupling (e.g. by lattice relaxation) would influence the stiffness of the acoustical spin wave branch.

Fig. 6.18 illustrates how the ferromagnetic stiffness of the effective surface bilayer is changed by a modified surface hopping. The stiffness is given by

$$D_{\text{eff}}^{\text{bi}} = 2S \sum_{i=1}^{\infty} c_i \left(J_i^{intra} + J_i^{inter} \right)$$

where $J_i^{intra} = \frac{1}{2}\left(J_i^{11} + J_i^{22}\right)$. The coefficients c_i of the first shells are given in Appendix D. With increasing $t_{\perp}^{surf}$ the bilayer stiffness is significantly more reduced for intermediate coupling compared to the strong-coupling case. The strong reduction is only partly due to the decreased in-plane *nn* exchange interaction - the most important contributions which weaken the stiffness stem from higher shells. Thus, the RKKY regime appears to be more favorable for this relaxation-induced magnetic instability. It should be mentioned that a mean-field treatment, in which the enhanced surface exchange $J_{ii}^{1,2}$ *does* enter the coupling between the top two layers, completely fails to describe such an effect.

6.6 Magnetic surface transition vs. spin waves

Having discussed the magnetic surface stability at low temperatures in the last section, the focus is now redirected on the ferromagnetic transition of a local-moment film. More precisely, the interest lies in the role of spin wave excitations concerning the ferromagnetic ordering at the surface and in the bulk of a semi-infinite crystal. The following considerations are motivated by possibly differing transition temperatures of the bulk and the surface of a Gd(0001)-crystal. Enhanced magnetic surface stability in Gd is a longstanding issue and has attracted much attention from the experimental and theoretical side alike. The question if a Gd crystal exhibits a surface phase transition above the bulk ordering temperature has not been unambiguously answered experimentally: while some works claim to have found indications for surface long-range magnetic order above the bulk Curie temperature with T_{C}^{surf} up to 85 K larger than T_{C}^{bulk} [39, 40, 41, 42], others did not [43, 44].

On the theoretical side, several authors have presented results in favor of an enhanced T_{C}^{surf} [45, 46, 47]. Their approach is based on a combination of DFT-LDA (+U) calculations in combination with Ginzburg-Landau mean-field theory for a Heisenberg ferromagnet [86, 87]. Surface and bulk exchange integrals are computed by comparing the energy differences of ferromagnetic and antiferromagnetic configurations of a Gd slab:

$$\frac{J_{surf}}{J_{bulk}} = \frac{E(\text{F}M) - E(\text{F}M \uparrow\downarrow)}{E(\text{F}M) - E(\text{A}FM)} . \tag{6.10}$$

$E(\text{F}M)/E(\text{A}FM)$ means an all-FM/all-AFM configuration and $E(\text{F}M \uparrow\downarrow)$ denotes an FM configuration with the surface layer oriented antiparallel to all other layers. It is assumed that the *nn* intralayer surface exchange integral and the *nn* surface-subsurface exchange integral have the same value, i.e. $J_{ii}^{12} = J_{\langle ij \rangle}^{11} = J_{surf}$ [45]. Application of the continuum mean-field theory proposed by Mills [87] for a semi-infinite crystal adapted to the Gd-hcp lattice geometry yields surface T_{C}-enhancements of 20-60% [45, 46, 47]. These enhancements are obtained with or without taking a surface layer relaxation into account and are the result of an increased J_{surf} which was found to be twice the value of $J_{\mathrm{b}ulk}$ according to the evaluation of (6.10). It should be remarked that this proportion is rather different from what the findings for the bulk and surface exchange interaction in Chap. 6.4 suggest.

In the following, the possible sources of an enhanced exchange interaction at the surface, like e.g. relaxation effects, are disregarded and the exchange integrals are taken as parameters. Classical Landau theory is based on an expansion of the free energy in terms of the magnetic order parameter $M(\mathbf{r})$ [89, 253]. For a semi-infinite crystal, an additional surface contribution to the free energy is considered. In Ref. [86] the phenomenological Landau theory is related to the microscopic mean-field Ising model, which corresponds to the Heisenberg model in the limit of infinite uniaxial anisotropy strength (see also [88]). Three principal results of this work are:

- The transition point in the bulk of a semi-infinite crystal coincides with the Curie temperature of the infinite bulk system.
- For sufficiently enhanced exchange coupling within the surface layer, a ferromagnetically ordered surface exists above the bulk critical temperature: $T_{\mathrm{C}}^{surf} > T_{\mathrm{C}}^{\mathrm{b}ulk}$ ('surface transition').
- The order parameter decays exponentially fast from its maximum value at the surface towards zero in the bulk in the regime $T_{\mathrm{C}}^{\mathrm{b}ulk} < T < T_{\mathrm{C}}^{surf}$.

Essentially the same results were obtained by Mills [87] who derived Landau-Ginzburg equations from the mean-field result of a Heisenberg magnet and suitable boundary condition. Both approaches yield a criterion for the existence of a surface transition in an sc(100)-semi-infinite crystal, namely that the exchange integral J_{surf} has to be enhanced such that the reduced exchange due to the lower coordination number at the surface is compensated: $J_{surf} \geq \frac{5}{4} J_{\mathrm{b}ulk}$. Note that this result refers to the case where J_{surf} denotes the four nearest-neighbor *in-plane* exchange integrals at the surface and is thus slightly different to the case where also the surface-subsurface coupling J_{ii}^{12} is changed.

Mean-field treatments neglect spin waves which are the elementary excitations of a Heisenberg ferromagnet and which determine its low-temperature behavior [112, 113, 218]. Furthermore, taking the spin fluctuations into account usually leads to significantly reduced Curie temperatures compared to the mean-field values. The non-local correlations due to spin wave excitations are expected to be particularly important in dimensionally-reduced systems [95, 97] and should be considered when studying the magnetic surface stability.

The following calculations are based on a Heisenberg model with *nn* interactions for an sc(100)-lattice structure. In-plane and inter-plane surface exchange integrals are taken to be equal, $J_{ii}^{12} = J_{\langle ij\rangle}^{11} \equiv J_{surf}$. All other *nn* exchange integrals are equal to $J_{\mathrm{b}ulk}$. The effect of spin fluctuations are studied by contrasting a microscopic mean-field description similar to the one in the above cited works with the RPA solution, the latter representing an effective spin wave theory (Chap. 5.4.1).

RPA calculations for Heisenberg film systems with modified exchange interactions at the surface have been carried out in Refs. [78, 79]. The focus in these works is on a *reduced* surface exchange. Only moderate enhancement was investigated and considered for temperatures below the critical region. In another work even a very large surface 'pinning' single-ion anisotropy yielded one common critical temperature for surface and bulk, albeit with strong variations of the spontaneous magnetization in the different layers [82]. For a spin-anisotropic surface exchange interaction, a finite surface magnetization was found to persist at $T_{\mathrm{C}}^{\mathrm{b}ulk}$ [80]. An enhanced surface Curie temperature was found, but only for a very large spin anisotropy ($\approx 50\%$) and by modelling the surface as an effective 3ML-slab above the bulk ordering temperature.

The Heisenberg model on a lattice for layered geometry used here reads

$$H = \sum_{ij}\sum_{\alpha\beta} J_{ij}^{\alpha\beta}\mathbf{S}_{i\alpha}\mathbf{S}_{j\beta}\,. \tag{6.11}$$

Within the mean-field theory, fluctuations of a spin operator around its expectation value are neglected:

$$\mathbf{S}_{i\alpha}\mathbf{S}_{j\beta} \rightarrow \langle\mathbf{S}_{i\alpha}\rangle\mathbf{S}_{j\beta} + \mathbf{S}_{i\alpha}\langle\mathbf{S}_{j\beta}\rangle - \langle\mathbf{S}_{i\alpha}\rangle\langle\mathbf{S}_{j\beta}\rangle\,. \tag{6.12}$$

In second-quantized notation, taking the z-direction as the quantization axis, and neglecting the last term which is not important for the present considerations, one obtains an effective one-spin Hamiltonian:

$$H_H^{MF} = 2\sum_{ij}\sum_{\alpha\beta} J_{ij}^{\alpha\beta} S_{i\alpha}^z\langle S_{j\beta}^z\rangle\,. \tag{6.13}$$

The present interest is in the temperature-dependent magnetization $M_\alpha \propto \langle S_\alpha^z\rangle$. Mean-field theory for the bulk crystal leads to the well-known Brillouin-function solution [110]. The corresponding solution for film geometry yields a coupled system of equations for the layer-dependent magnetization [254]:

$$M_\alpha = M_S B_S(\beta S(h_\alpha^{\mathrm{ex}} + h_\alpha^{\mathrm{e}ff}))\,. \tag{6.14}$$

M_S is the saturation magnetization and $B_S(x)$ denotes the Brillouin function. A layer-dependent external field h_α^{ex} has been added, and the effective field is given by

$$h_\alpha^{\mathrm{e}ff} \propto 2 \sum_{j\beta} J_{ij}^{\alpha\beta} M_\beta\,. \tag{6.15}$$

The prefactor $g\mu_{\mathrm{B}}$ has been absorbed into the fields and the proportionality factor is set to unity. Introducing $J_\alpha \equiv J_{\langle ij\rangle}^{\alpha\alpha}$ and $J_{\alpha,\alpha\pm1} \equiv J_{ii}^{\alpha\alpha\pm1}$, (6.15) becomes for an sc(100)-film

$$h_\alpha^{\mathrm{e}ff} = 2(4J_\alpha M_\alpha + J_{\alpha,\alpha-1}M_{\alpha-1} + J_{\alpha,\alpha+1}M_{\alpha+1})\,. \tag{6.16}$$

Eqs. (6.14) and (6.16) can be evaluated self-consistently in order to obtain the magnetization.

Following the procedure for the Ising model by Binder [86], a condition and formula for $T_{\mathrm{C}}^{\mathrm{s}urf}$ can be derived. With a constant external magnetic field h^{ex} in all layers and h_1^{ex} in the first layer only, the Brillouin function can be expanded above $T_{\mathrm{C}}^{\mathrm{b}ulk}$ and for small fields according to $B_S(x) = \frac{S+1}{3S}x + \mathcal{O}(x^3)$. One obtains

$$M_1 = M_S\frac{(S+1)}{3}\beta(h^{\mathrm{ex}} + h_1^{\mathrm{ex}}) + M_S\frac{2(S+1)}{3}\beta(4J_{\mathrm{s}urf}M_1 + J_{\mathrm{s}urf}M_2) \tag{6.17}$$

$$M_2 = M_S\frac{(S+1)}{3}\beta h^{\mathrm{ex}} + M_S\frac{2(S+1)}{3}\beta(4J_{\mathrm{bulk}}M_2 + J_{\mathrm{s}urf}M_1 + J_{\mathrm{bulk}}M_3) \tag{6.18}$$

$$M_\alpha = M_S\frac{(S+1)}{3}\beta h^{\mathrm{ex}} + M_S\frac{2(S+1)}{3}\beta(4J_{\mathrm{bulk}}M_\alpha + J_{\mathrm{bulk}}M_{\alpha-1} + J_{\mathrm{b}ulk}M_{\alpha+1}) \tag{6.19}$$

This coupled system of equations is solved by the ansatz

$$M_\alpha = M_{\mathrm{b}ulk} + \delta \mathrm{e}^{-q(\alpha-1)}\,. \tag{6.20}$$

For the simple-cubic bulk crystal one finds by expanding around $T_{\mathrm{C}}^{\mathrm{b}ulk}$ that $q = \big((T/T_{\mathrm{C}}^{\mathrm{b}ulk} - 1)(9T/T_{\mathrm{C}}^{\mathrm{b}ulk} - 3)\big)^{1/2}$ where $k_{\mathrm{B}}T_{\mathrm{C}}^{\mathrm{b}ulk} = \frac{2}{3}J_0S(S+1)$ and $J_0 = zJ_{\mathrm{b}ulk} = 6J_{\mathrm{b}ulk}$. In order for the local susceptibility

$$\chi_{1,1} = \frac{\partial M_1}{\partial h_1^{\mathrm{ex}}} \tag{6.21}$$

to diverge at $T = T_{\mathrm{C}}^{\mathrm{s}urf}$ the following equation has to be fulfilled:

$$A\left(\frac{T_\mathrm{C}^{surf}}{T_\mathrm{C}^{\mathrm{b}ulk}}\right)^2 + 2\frac{T_\mathrm{C}^{surf}}{T_\mathrm{C}^{\mathrm{b}ulk}} + \frac{\Delta}{6} = \frac{T_\mathrm{C}^{surf}}{T_\mathrm{C}^{\mathrm{b}ulk}} q(T = T_\mathrm{C}^{surf}) \,. \tag{6.22}$$

Δ is defined by $J_{surf} = J_{\mathrm{b}ulk}(1+\Delta)$ and $A = \frac{3\Delta-3}{1+\Delta}$. The further analysis of (6.22) reveals that in case of an sc(100)-crystal, the condition $\Delta > 0.192$ has to be fulfilled in order to obtain an enhanced surface Curie temperature. Hence

$$T_\mathrm{C}^{surf} > T_\mathrm{C}^{\mathrm{b}ulk} \;\Leftrightarrow\; J_{surf}/J_{\mathrm{b}ulk} > 1.192 \,. \tag{6.23}$$

Noting that $\Delta \ll 1$ for not too large exchange enhancements, the term $\Delta/6$ can be neglected in (6.22), and the resulting quadratic equation can be solved for an approximate formula for the surface Curie temperature:

$$\frac{T_\mathrm{C}^{surf}}{T_\mathrm{C}^{\mathrm{b}ulk}} = \sqrt{\frac{3A+15}{(A-3)(A^2-9)}} + \frac{2}{3-A} \,. \tag{6.24}$$

Mean-field theory for the Heisenberg semi-infinite crystal lattice leads to separate bulk and surface transitions for a sufficiently enhanced surface exchange, similar to the continuum Landau-Ginzburg MF theory used in Refs. [45, 87].

Fig. 6.19 demonstrates the existence of two distinct transition temperatures for sufficiently enhanced surface exchange in the mean-field approach. The surface and center layer magnetization as a function of temperature are shown for a 30ML-film which models the semi-infinite crystal. Three different scenarios are considered: uniform exchange in the whole film ($J_{surf} = J_{\mathrm{b}ulk}$), reduced surface exchange ($J_{surf} = 0.5J_{\mathrm{b}ulk}$), and enhanced surface exchange ($J_{surf} = 1.5J_{\mathrm{b}ulk}$ and $J_{surf} = 2J_{\mathrm{b}ulk}$).

For uniform exchange interaction (black), the magnetization of the surface layer is significantly reduced compared to that of the center layer due to the smaller number of interaction partners at the surface. A weaker exchange interaction at the surface supports the tendency of the first layer to order at a lower temperature than the other layers and can lead, if small enough, to a concave magnetization curve. The Curie temperatures for uniform exchange and for reduced surface exchange practically coincide. More important to the present interest, the surface and center layer exhibit a common critical temperature in both scenarios. The latter is less obvious for the case of enhanced surface exchange. Here, the magnetization of the surface layer is always higher than in all other layers. There is a slight softening of the FM/PM-transition of the center layer near $T_\mathrm{C}^{\mathrm{b}ulk}$ due to the finite film thickness. The bulk transition temperature is strictly reached for $N_\mathrm{L} \to \infty$.

The behavior of the MF-magnetization corresponds to what one would intuitively expect to be a consequence of the self-consistent field (6.15). A magnetically softer surface is 'pulled' by the bulk magnetization. This effect can be observed

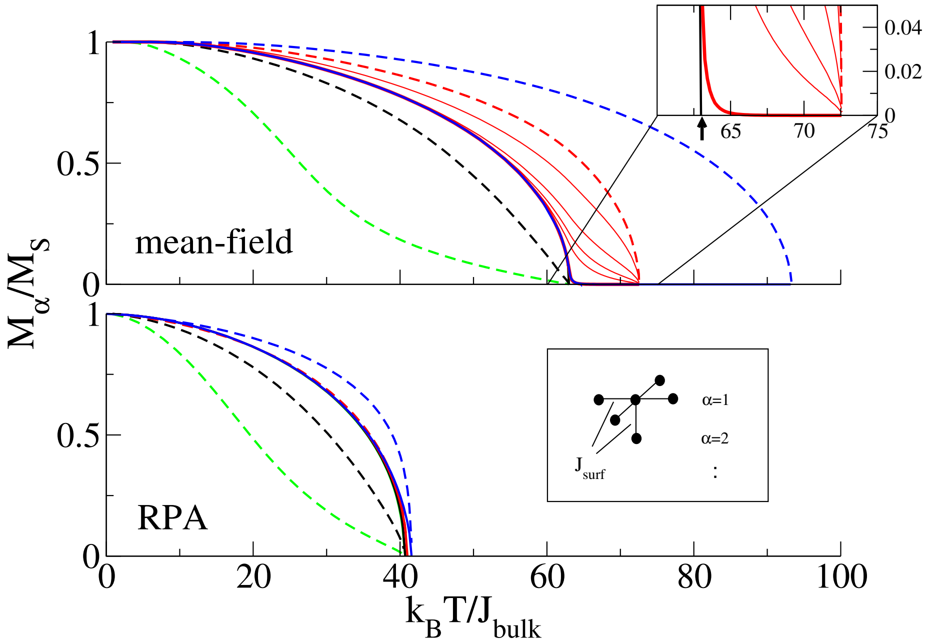

Figure 6.19: Magnetization of a 30ML-sc(100)-film. The dashed/full lines refer the surface/center layers. A single-ion anisotropy $K_2^\alpha \equiv K_2$ is included. Black lines: uniform exchange $J_{surf} = J_{\mathrm{b}ulk}$, green lines: reduced surface exchange $J_{surf} = 0.5J_{\mathrm{b}ulk}$, red lines: enhanced surface exchange $J_{surf} = 1.5J_{\mathrm{b}ulk}$, blue lines: $J_{surf} = 2J_{\mathrm{b}ulk}$. The center layer magnetizations are practically the same in all cases. Thin red lines refer to the layers $\alpha = 2, 3, 4,\ \mathrm{a}nd\,5$ (MF). The black arrow in the inset indicates $T_{\mathrm{C}}^{\mathrm{b}ulk}$. Parameters: $S = 7/2$, $K_2/J = 10^{-3}$.

already for uniform interaction and is a consequence of the reduced coordination number at the surface. Of course in the reversed case, the effective field of a stiffer surface layer affects the magnetization of a layer deeply in the film far less than a stiffer bulk influences the surface layer magnetic ordering.

The RPA evaluation of the layer-dependent magnetization according to (5.43) yields a completely different picture (Fig. 6.19). Due to spin wave excitations, there is a power-law decrease of the magnetization at low temperatures (Bloch's law), in contrast to the mean-field result yielding an exponential decrease because the reduction is associated with single spinflips. As expected, spin wave excitations lower the critical temperature markedly compared to mean-field theory, in the present case $T_{\mathrm{C}}^{\mathrm{R}PA} \approx 2/3T_{\mathrm{C}}^{\mathrm{M}F}$.[1] For uniform interactions and reduced surface

---

[1] Within RPA a finite K_2 is required in order to obtain a non-zero T_{C}. The 30ML-film is sufficiently thick (and the chosen anisotropy sufficiently weak) for the Curie temperature to be practically determined by the exchange interaction J_{bulk} only, both in RPA and mean-field. Contrary to RPA, mean-field theory violates the Mermin-Wagner theorem and does not require

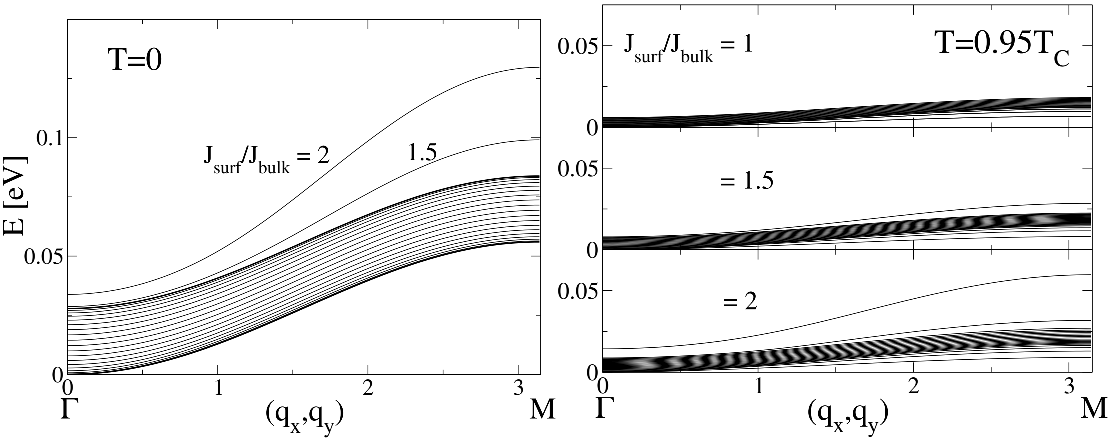

Figure 6.20: Surface-projected spin wave spectrum of a Heisenberg 20ML-sc(100)-film for ferromagnetic saturation (left) and near the Curie temperature (right) from $\Gamma = (0, 0)$ to $M = (\pi, \pi)$. $(q_x, q_y) = \mathbf{q}_{\parallel}$ is a wave vector of the first Brillouin zone of the square lattice. Parameters: J=10^{-3}, $K_2 = 10^{-6}$, $S = 7/2$.

exchange, one observes qualitatively similar features as in the mean-field treatment.

In case of an enhanced J_{surf}, no indications for separate bulk and surface transition temperatures are found. An increased magnetic stiffness of the surface layer can lead to a higher magnetization than in the bulk, but the latter still determines the critical temperature. The bulk magnetization is practically unaffected by a modified interaction at the surface. One notices a slight increase of the Curie temperature for enhanced surface exchange compared to the uniform case, but this effect is due to the finite film thickness and disappears gradually if the number of layers is increased. The RPA results demonstrate that spin wave excitations couple the critical behavior of all layers. Isolated surface magnetism is only possible if these modes are suppressed and solely the mean-field part (6.15) acts (see also Eq. (5.40)). This, however, means to overestimate seriously the influence of an enhanced surface exchange interaction.

In order to illustrate the effect of an increased surface exchange integral on the magnetic excitation spectrum the 2D-projected spin wave dispersion is considered. For the semi-infinite crystal it reads

$$E(\mathbf{q}_{\parallel}) = \frac{1}{N_{\perp}} \sum_{\mathbf{q}_{\perp}} E(\mathbf{q}_{\parallel}, \mathbf{q}_{\perp}) \tag{6.25}$$

with $N_{\perp} \equiv N_{\mathrm{L}} \to \infty$. Fig. 6.20 shows dispersions of a 20ML-film. For enhanced

---

an anisotropy term in order to yield magnetic long-range order.

surface exchange, an optical surface spin wave branch splits off the bulk continuum. A magnon in this mode with an energy that lies outside the bulk continuum represents an excitation which is essentially confined to the surface layer ('surface magnon'). Large $\mathbf{q}_{\|}$ are more favorable for the optical surface modes, which first evolve at the M-point. For temperatures close to the Curie temperature and high enough surface exchange enhancement more optical modes appear above the bulk spectrum, reflecting the increased relative magnetic stiffness of the first layers as compared to the bulk layers. The low-energy acoustical branch, however, which vanishes at the critical temperature, remains unchanged by the modified surface exchange.

Concludingly, in order to study ferromagnetism in the surface layer and in the bulk of a semi-infinite sc(100)-crystal, a sufficiently thick Heisenberg film with uniform single-ion anisotropy was treated on mean-field level and using RPA. Spin wave excitations induce a common transition temperature of the bulk and the surface. This holds, in particular, for an enhanced exchange interaction within the surface layer and between the surface and subsurface layer. The existence of a separate $T_{\mathrm{C}}^{surf} \neq T_{\mathrm{C}}^{bulk}$ in the mean-field description results from disregarding spin wave excitations. Explanations for a possibly enhanced transition temperature of the real Gd(0001)-surface based on this approach [45, 46, 47] should be questioned because there is no reason to assume that spin wave excitations can be neglected in this case. The problem of a realistic mechanism for a ferromagnetic surface transition remains an open and interesting issue for future investigations.

Chapter 7

Interlayer exchange coupling

The interaction of ferromagnetic layers through a non-magnetic spacer layer has evoked considerable research effort by theoreticians and experimentalists alike over the past two decades. The interlayer exchange coupling (IEC) couples the directions of the magnetizations in the magnetic layers and thereby influences the spin-dependent transport properties.

7.1 Introduction

Interlayer exchange coupling has been studied for a variety of combinations of different substances in 3D or in dimensionally reduced systems, with no spacer at all up to large spacer thickness, and for various spatial configurations of layered structures. Usually the term 'multilayer' denotes the fact that more, at least two different magnetic ('M') and non-magnetic ('N') constituents are combined. Often a periodic arrangement of such M/N-supercells is studied so that one can make use of translational invariance also in the normal direction. 'Trilayer' structures are made up by one non-magnetic spacer sandwiched between two ferromagnetic layers ('M/N/M'). The IEC-systems considered in this work are exclusively of this type (Fig. 7.1).

The interlayer exchange coupling is significantly influenced by the charge carrier density. Generally, the variation with the carrier density is of considerable practical interest because it can be manipulated in a controlled manner by doping or optical excitations.

With increasingly refined techniques to fabricate ultrathin films, the temperature dependence of the IEC becomes more and more important. Usually the Curie temperature diminishes with decreasing film thickness (see Fig. 6.9). Thus the magnetic properties at room temperature including the interlayer coupling may differ significantly from their $T = 0$-values due to spin wave excitations.

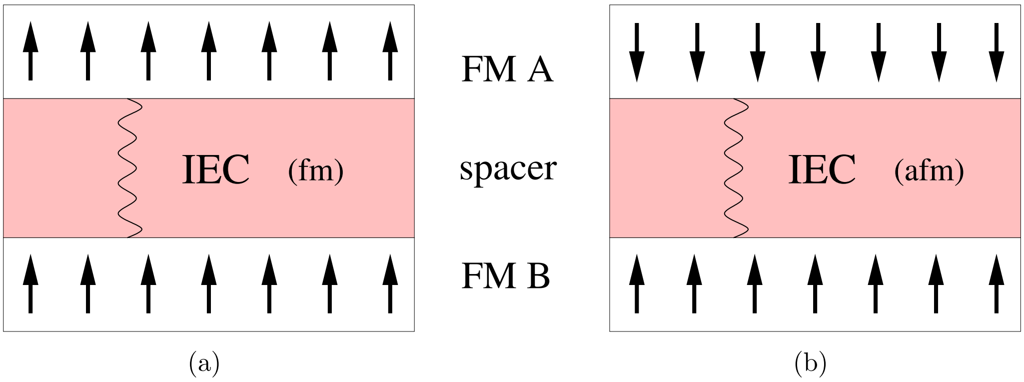

Figure 7.1: Interlayer exchange coupling between two ferromagnetic layers A and B separated by a non-magnetic spacer layer. (a) Parallel alignment of the magnetizations (ferromagnetic IEC), (b) antiparallel alignment of the magnetizations (antiferromagnetic IEC).

Brief survey of IEC

By the middle of the 1980s the coupling between magnetic layers through a non-magnetic metal was confirmed by a number of experiments using various probing techniques [73, 74, 163, 164, 255]. In particular the observation of Grünberg et al. that Fe films separated by a Cr spacer couple antiferromagnetically sparked intense research on the interlayer exchange interaction between ferromagnetic layers [73, 74]. The measurements of Parkin et al. on Fe/Cr/Fe, Co/Ru/Co, and systems with other metallic spacer materials directed the focus on the oscillatory dependence of the interlayer exchange coupling on the spacer thickness [256, 257]. A change of sign of the IEC when varying the spacer thickness had been found before in Gd/Y multilayers [163, 164, 255, 258, 259, 260]. Generally speaking, the interlayer interaction is due to the polarization of the spacer conduction electrons through their interaction with polarized electrons or local moments of the magnetic metals rather than due to magnetostatic forces or pinholes.

Inspired by the oscillatory character of IEC, an RKKY description by Bruno and Chappert was among the first approaches to provide a deeper understanding of the experimental results [261, 262]. The theory makes use of the RKKY interaction for arbitrary Fermi surfaces [263] and thus went beyond earlier RKKY results for the coupling between sheets of constant spin density embedded in a free electron gas by Yafet [153]. Although the ferromagnetic $3d$-transition metals under consideration rather suggest a delocalized description, the RKKY approach could explain key experimental features such as long periods and multiperiodic oscillations of the IEC with varying noble-metal spacer thickness [262]. This success is related to the fact that these oscillation features are determined by extremal properties of the (bulk) Fermi surface of the *spacer* material.

Several theories of interlayer exchange coupling consider the spin-dependent confinement of the electrons in the spacer layer and were brought forward in the form of quantum interference approaches by Bruno [264, 265, 266] and Stiles [267, 268, 269], or in the framework of a quantum-well model by Edwards et al. [270, 271, 272, 273, 274]. These theories include the RKKY interaction as a limit [265, 275, 276, 277]. The most general of the approaches is the formulation in terms of spin-dependent reflection coefficients of the spacer electrons by Bruno [265]. Other (mostly model-dependent) approaches are recovered by an appropriate evaluation of the reflection coefficients. The theory can also be used in combination with *ab-initio* calculations of the electronic band structure and the reflection coefficients [278, 279]. A brief summary of the quantum interference approach is given in Chap. 7.1.2.

The dependence of interlayer exchange coupling on the spacer thickness was also studied in a perovskite-oxide metallic magnetic/non-magnetic trilayer [280]. In a similar system, namely the layered manganite compound $\mathrm{L}a_{2-2x}\mathrm{S}r_{1+2x}\mathrm{M}n_2\mathrm{O}_7$, bilayer slices of $\mathrm{M}n\mathrm{O}_6$-octahedra are separated by insulating $(\mathrm{L}a, Sr)_2\mathrm{O}_2$ layers and are magnetically decoupled from each other. For the IEC within the bilayer a drastic doping dependence with a change from FM to AFM coupling at $x \approx 0.45$ was observed [248] and traced back to a change of the Jahn-Teller splitting of the d-orbital with varying carrier concentration [21, 92, 93].

The IEC was also measured in semiconductor multilayer structures with ferromagnetic (Ga,Mn)As layers [69]. Total energy calculations for such DMS-III/V-systems in order to obtain the variation of the IEC energy with the average charge carrier density and with the spacer thickness have been carried out for [(Ga,Mn)As/(Al)GaAs] multilayers in an approach based on mean-field theory for the carrier induced ferromagnetism and using the Kohn-Luttinger kinetic exchange Hamiltonian in a single-parabolic-band approximation [29, 72], or using a realistic supercell tight-binding Hamiltonian solved by numerical diagonalization [71]. In Ref. [70], a (Ga,Mn)As bilayer embedded in a thin film of GaAs is considered. A confinement-adapted RKKY theory using spin-polarized eigenstates of the hole gas and Monte Carlo simulation of the temperature-dependent magnetization yields a ferromagnetic alignment of the two (Ga,Mn)As layers.

7.1.1 Definition of interlayer exchange coupling

The interlayer exchange coupling is usually defined as the difference between the grand canonical potentials for parallel and antiparallel alignment of the two ferromagnetic layers [265],

$$E_{IEC} \sim \Omega_{\uparrow\uparrow} - \Omega_{\uparrow\downarrow}, \tag{7.1}$$

or similarly, depending on which thermodynamical potential is better suited for the system under consideration, as the difference between the free energies of the two configurations [281, 282],

$$E_{IEC} \sim F_{\uparrow\uparrow} - F_{\uparrow\downarrow} \,. \tag{7.2}$$

Alternatively, the IEC at $T = 0$ may be defined within an (effective) local-moment picture using the Heisenberg interaction (5.32). In order to obtain the IEC between two ferromagnetic slabs A and B, all pair interactions between the $N \cdot N_{\mathrm{L}}^{\mathrm{A}}$ spins in the $N_{\mathrm{L}}^{\mathrm{A}}$ monolayers of A and the $N \cdot N_{\mathrm{L}}^{\mathrm{B}}$ spins in B are summed up:

$$J_{\mathrm{IEC}}^{\mathrm{A}B} = \sum_{\substack{\alpha\in A \\ \beta\in B}} J_{\mathrm{IEC}}^{\alpha\beta} = \frac{1}{N} \sum_{\substack{i,\alpha\in A \\ j,\beta\in B}} J_{ij}^{\alpha\beta} \,. \tag{7.3}$$

Using Fourier transformation the interlayer exchange coupling reads

$$J_{\mathrm{I}EC} \equiv J_{\mathrm{IEC}}^{\mathrm{A}B} = \sum_{\substack{\alpha\in A \\ \beta\in B}} J_{\mathbf{q}=0}^{\alpha\beta} \,. \tag{7.4}$$

The spacer layer consists of N_{L}^{spac} non-magnetic monolayers and separates the magnetic layers by a distance $(N_{\mathrm{L}}^{spac} + 1)a$ where a is the distance between two monatomic layers.

Total energy calculations yield the IEC directly according to (7.1) and (7.2) at $T = 0$. They have been performed using the local-spin-density approximation [72, 283, 284] or various tight-binding models [71, 285, 286, 287]. These numerical computations are usually very demanding due to the tiny energy differences relative to the total energies of the parallel and antiparallel configuration.

For $T = 0$ the two definitions (7.2) and (7.4) are readily connected since $F = U$ and the interlayer contribution to the internal energy U of the Heisenberg model is given by $\pm J_{IEC} S^2$ where $+/-$ stands for the AFM/FM-coupled configuration. The difference between the free energies of the two configurations reads

$$F_{\uparrow\uparrow} - F_{\uparrow\downarrow} = -2 J_{\mathrm{I}EC} S^2 \,. \tag{7.5}$$

The magnetic layers align parallel if $J_{IEC} > 0$ and antiparallel if $J_{IEC} < 0$. For finite temperatures, a relation of the type (7.5) cannot be simply established because the definition (7.2) assumes that both the parallel and the antiparallel configuration exist. In a Heisenberg system, however, the state with higher energy is not stable with respect to spin wave excitations if the exchange coupling is the same in both configurations. Furthermore, the *effective* exchange integrals depend on the electronic structure and thus on the magnetic configuration. Hence the interlayer exchange interaction is temperature-dependent and in general different for a parallel and for an antiparallel alignment of the magnetic layers:

$$J^{\uparrow\uparrow}_{IEC}(T) \neq J^{\uparrow\downarrow}_{IEC}(T) \,. \tag{7.6}$$

This difference can be quite significant for small spacer widths. In Chap. 7.3.2, a criterion based on the magnetic excitation spectrum will be presented in order to evaluate the magnetic stability in the parallel and in the antiparallel configuration as a function of temperature. It should be noted that even if both states exist, the interlayer coupling, being a free energy difference, is no longer merely the sum of the interlayer exchange integrals (7.4). The influence of the different spin excitation spectra of the FM-coupled state and of the AFM-coupled state has to be taken into account.

Physically, the T-dependence of the IEC has three major sources [98, 282] which can be summarized as the broadening of the Fermi edge ('Fermi softening'), the thermal variation of the exchange splitting, and the excitation of spin waves. The first two sources affect mainly the spacer electrons while the latter effect is the result of the exchange interaction within the ferromagnetic layers. In a local-moment picture, the spacer effects are contained in the exchange integrals: within the conventional RKKY theory, the thermal variation is due to the Fermi softening only (Chap. 5.1) [261]; in the modified-RKKY version (Chap. 5.2), the temperature dependence of the spin-dependent band structure is additionally included. Another possible source of the thermal variation of the effective exchange integrals are magnon *interactions* [96, 113, 288]. This kind of temperature dependence is not considered here.

7.1.2 Quantum interference approach

The quantum interference approach starts with the definition (7.1) of IEC. The grand potential difference is evaluated making use of the magnetic force theorem which states that the energy difference between two magnetic configurations is approximately given by the difference in the single-particle energies [265, 266, 268, 289]. For weak confinement of the bulk-like spacer electrons between the two magnet/spacer interfaces A and B, and for large spacer thickness D, the asymptotic interlayer coupling energy reads [265]

$$E_{IEC} = E_{\mathrm{F}M} - E_{\mathrm{A}FM} = \mathrm{I}m \sum_{\alpha} \frac{\hbar v^{\alpha}_{\perp} \kappa_{\alpha}}{4\pi^2 D^2} \Delta r^{\alpha}_{A} \Delta r^{\alpha}_{B} \mathrm{e}^{\mathrm{i} q^{\alpha}_{\perp} D} F(2\pi k_{\mathrm{B}} T D / \hbar v^{\alpha}_{\perp}) \,, \tag{7.7}$$

with $F(x) \equiv \frac{x}{sinh(x)}$. In the above expression, the index α labels spanning vectors of the Fermi surface (FS) with length $q^{\alpha}_{\perp}$ in the direction perpendicular to the film plane. They connect points on the FS which are stationary with respect to the in-plane component of the wave vector. $v_\perp^\alpha$ and κ_α are obtained from the perpendicular component of the Fermi velocities at these points and from the corresponding curvature radii of the Fermi surface, respectively. One sees from (7.7) that an oscillation period of IEC is given by (possibly more than one) $q_\perp^\alpha$; in the simplest case of free electrons with a spherical FS, there is only one such vector with $q_\perp = 2k_\mathrm{F}$. The same selection rule for the oscillation periods had been obtained before by the RKKY approach in Ref. [261]. The decay of the interlayer coupling is proportional to the inverse square of the distance D between the magnetic layers. Amplitude and phase of the coupling depend sensitively on the spin asymmetry of the reflection coefficients

$$\Delta r_{\mathrm{A}(B)} = \frac{r^{\uparrow}_{A(B)} - r^{\downarrow}_{A(B)}}{2} \,. \tag{7.8}$$

The spin index refers to the parallel (↑) or antiparallel (↓) direction of the electron spin with respect to the magnetization direction in the ferromagnet A(B).

The reflection coefficients contain a dependence of the IEC on the magnetic layer thickness L because the reflections of electrons at the surfaces of the ferromagnets give rise to interferences, too. Within a free-electron model including the exchange splitting of the ferromagnets, one obtains for a metallic spacer ($r^\uparrow = 0$) in the asymptotic limit of large D and L:

$$E_{IEC} = \frac{\epsilon_\mathrm{F}^2}{4\pi^2 D^2} \mathrm{Im} \left\{ \frac{r_\infty^{\downarrow 2}}{2} e^{2\mathrm{i}k_\mathrm{F}D} \left[1 - 2\left(1 - r_\infty^{\downarrow 2}\right) \left(1 + \frac{k_\mathrm{F}}{k_\mathrm{F}^{\downarrow}} \frac{L}{D}\right)^{-2} e^{2\mathrm{i}k_\mathrm{F}^{\downarrow}L} \right] \right\} \,. \tag{7.9}$$

The Fermi energy ϵ_F and the Fermi wave vector k_F refer to the spacer, $r_\infty^\downarrow$ is the reflection coefficient at the interface with a semi-infinite ferromagnetic layer, and $k_\mathrm{F}^\downarrow$ is the Fermi wave vector of the minority band of the ferromagnetic layers.

The amplitude of the IEC-oscillations versus magnetic layer thickness have turned out to be much smaller than the oscillations versus spacer thickness. In particular, no change of sign of the IEC has been reported [265, 266]. This was shown experimentally [290, 291] and theoretically [292, 293, 294, 295].

7.1.3 Rare-earth multilayers

Oscillatory dependence on the spacer thickness

Experiments on Gd/Y multilayers yielded clear indications for a long-range coupling of the Gd-slabs across the Y-layers. The sign of the coupling oscillates with a period of about seven monolayers over a range of at least twenty monolayers

[163, 164]. Yafet et al. proposed an *ad-hoc* ansatz for the evaluation of the exchange coupling [161, 162]. It is based on two main assumptions:

1. The IEC can be calculated for two atomic layers of Gd instead of two slabs, embedded in bulk Y, and separated by a number of atomic layers of Y.
2. The intra-atomic (s-f-) exchange interaction J_{sf} for a Gd-ion in bulk Y is the same as in bulk Gd.

With the additional assumption that the wave-vector dependence of the s-f-exchange is

$$J_{\mathrm{s}f}(\mathbf{k},\mathbf{k}') = J_{\mathrm{s}f}(\mathbf{k}-\mathbf{k}') \equiv J_{\mathrm{s}f}(\mathbf{q})\,, \tag{7.10}$$

the RKKY exchange interaction $J(\mathbf{q})$ can be written (up to a numerical factor, cf. (5.3)) in terms of the static susceptibility:

$$J(\mathbf{q}) = |J_{\mathrm{s}f}(\mathbf{q})|^2\,\chi(\mathbf{q})\,. \tag{7.11}$$

For directions of $\mathbf{q}$ normal to the basal plane, the exchange coupling of Gd-ions in an Y-matrix can then be expressed as

$$\begin{aligned} J_{\mathrm{G}d/Y/Gd}(q) &= \left|J_{\mathrm{s}f}^{\mathrm{G}d}(q)\right|^2 \chi_{\mathrm{Y}}(q) \\ &= J_{\mathrm{G}d}(q)\,\frac{\chi_{\mathrm{Y}}(q)}{\chi_{\mathrm{G}d}(q)}\,. \end{aligned} \tag{7.12}$$

The evaluation of (7.12) was carried out using experimental data for the exchange coupling $J_{\mathrm{G}d}(q)$ in Gd [296] and for the susceptibilities $\chi_{\mathrm{G}d}(q)$ and $\chi_{\mathrm{Y}}(q)$ [297, 298]. With respect to the oscillatory character in general and to the parallel or antiparallel alignment of the Gd slabs at specific distances, the interplanar coupling obtained after Fourier transformation of (7.12) agrees with the magnetic measurements and neutron scattering results of Refs. [163] and [164], respectively.

Temperature-induced magnetic reorientation transition

Recently a temperature-induced magnetic reorientation transition in a Tb/Y/Gd-trilayer was detected by MOKE measurements [299, 300]. A change of sign from FM to AFM interlayer exchange coupling was observed at a temperature as low as $T \approx 0.25T_C^{\mathrm{G}d}$. The findings are discussed on the basis of the quantum interference picture with temperature-dependent reflection coefficients assumed to be proportional to the average magnetization of the Gd- and Tb-layers. Additionally, an interface contribution is considered [279, 282].

7.1.4 Effective Heisenberg bilayer

Investigating the sources of the temperature dependence of IEC, Schwieger et al. proposed an effective Heisenberg Hamiltonian [98]. The interlayer exchange coupling is obtained by a one-parameter fit to ferromagnetic resonance (FMR) data [281] from measurements on a $\mathrm{N}i_7/Cu_9/Co_2/Cu(001)$ prototypical trilayer. At first glance this system may appear as a prime candidate for the quantum interference description. However, this approach does not include spin wave excitations in the magnetic layers. In Eq. (7.7) one can rather identify the two sources of the temperature dependence which are related to properties of the charge carriers in the *spacer*:

1. The function $F(x)$ describes the effect of the Fermi surface broadening with increasing T.

2. The spin asymmetry of the reflection amplitudes (7.8) contains the T-dependent exchange splitting in the two ferromagnets A and B.

In contrast, using the Heisenberg model, magnon excitations in the ferromagnetic layers are accounted for explicitly. Spacer effects may be included additionally by using spacer theories like (7.7) or effectively in a fit to experiment. Thus the temperature dependences due to the different spacer-related effects can be separated quantitatively from the thermal variation caused by magnetic excitations.

The effective two-layer Hamiltonian used in Ref. [98] reads

$$
\begin{aligned}
H = &-\sum_{\langle ij\rangle\alpha} J_\alpha \mathbf{S}_{i\alpha}\mathbf{S}_{j\alpha} - \sum_{i\alpha} g_\alpha \mu_\mathrm{B} \mathbf{B}_0 \mathbf{S}_{i\alpha} - \\
&- \sum_{\substack{\alpha\neq\beta \\ \langle ij\rangle\alpha\beta}} J_{\mathrm{I}EC} \mathbf{S}_{i\alpha}\mathbf{S}_{j\beta} - \sum_{i\alpha} K_2^\alpha (S_{i\alpha}^z)^2 + \\
&+ \sum_{ij\alpha} g_0^\alpha \left(\frac{1}{r_{ij}^3} \mathbf{S}_{i\alpha}\mathbf{S}_{j\alpha} - \frac{3}{r_{ij}^5} (\mathbf{S}_{i\alpha}\mathbf{r}_{ij})(\mathbf{S}_{j\alpha}\mathbf{r}_{ij}) \right) . \qquad (7.13)
\end{aligned}
$$

The parameter J_{IEC} contains all spacer contributions to the IEC. The first term describes nearest-neighbor exchange-coupled spin moments $\mathbf{S}_{i\alpha}$ and $\mathbf{S}_{j\alpha}$ at sites i and j within the same layer α (=Ni, Co). Specifically, $S_{\mathrm{N}i} = 1$ and $S_{\mathrm{C}o} = 2.5$ were used. The finite thickness of the Ni- and Co-layers is effectively included in J_α (see below). The second term contains an external magnetic field $\mathbf{B}_0$ in arbitrary direction with the spectroscopic splitting factors $g_{\mathrm{N}i} = g_{\mathrm{C}o} = 2.2$. The fourth and fifth term represent second-order uniaxial and shape anisotropy, respectively. r_{ij} is the distance between the lattice sites i and j in the same layer.

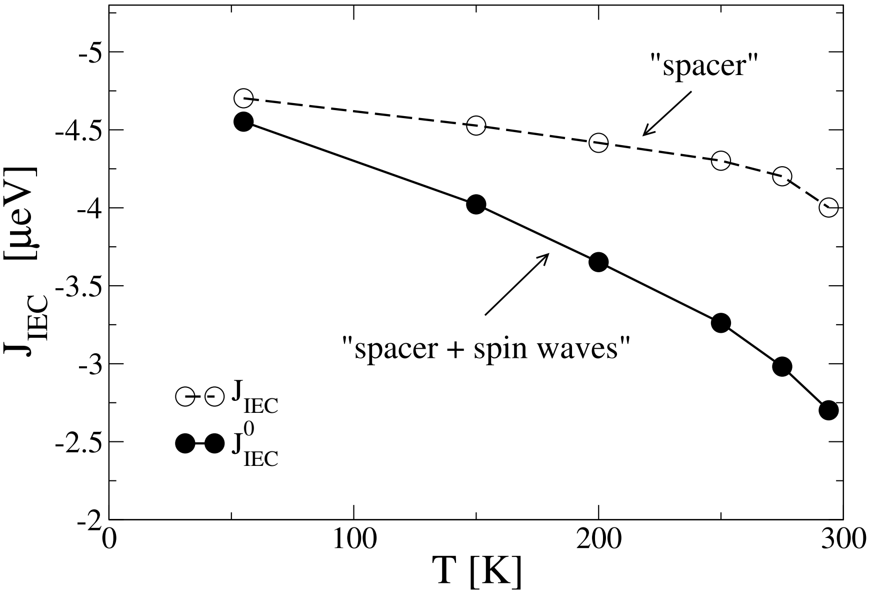

Figure 7.2: Temperature dependence of interlayer exchange coupling in the trilayer $\mathrm{N}i_7/Cu_9/\mathrm{C}o_2/Cu(001)$ (from Ref. [98]). Symbols are from fits of the experimental resonance field at 90° at the given temperatures. Open circles: T-dependent calculation. Filled circles: evaluation at $T = 0$. Lines are guides to the eye.

One may raise the question if the local-moment picture of the Heisenberg model is appropriate for itinerant magnets such as Ni and Co. No definite answer can be given in this respect. However, results like Heisenberg spin wave dispersions of an itinerant band model [301], a high degree of the d-band moment localization ($> 90\%$ for $0 < T < T_{\mathrm{C}}$) in an LDA+many-body approach to bulk Ni [120], and the successful use of the Heisenberg model with *ab-initio* exchange parameters for calculating the Curie temperature of Ni [302] indicate that localized-spin models can be a justified choice also for the description of itinerant-carrier systems. In principle, an effective description like (7.13), combined with spin wave data obtained from FMR or Brillouin light scattering experiments, can be applied to any real IEC-system.

Ferromagnetic resonance [281] probes the uniform spin wave mode $\omega(\mathbf{q} = \mathbf{0})$ of a magnetic sample in an external field $\mathbf{B}_0$ which is tuned for a given probe frequency $\nu_{\mathrm{hf}} = \omega(\mathbf{q} = \mathbf{0})/2\pi$ until resonance occurs for $B_{\mathrm{res}}(T, \theta_{B_0})$. θ_{B_0} is the angle between the magnetic field and the normal to the film plane. For the resonance field $B_{\mathrm{res}}(T, \theta_{B_0})$, uniform ($\mathbf{q} = \mathbf{0}$)-spin wave modes of energy $E^{\mathrm{SW}} = h\nu_{\mathrm{hf}}$ are excited in the magnetic system. It is this quantity which connects experiment and theory [241]. The latter yields an expression for the spin wave energy 'dispersion' $E^{\mathrm{SW}}(\mathbf{q} = \mathbf{0}, \mathbf{B}_0, T)$ from which one can read off the resonance field for a given

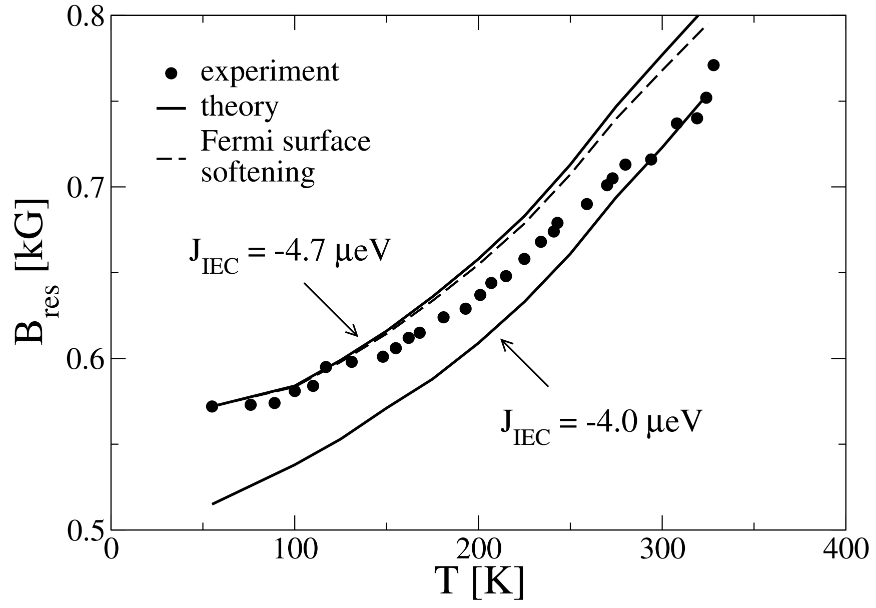

Figure 7.3: Resonance field for $\theta_{\mathrm{B}_0} = 90°$as a function of temperature for $\mathrm{N}i_7/\mathrm{C}u_9/\mathrm{C}o_2/\mathrm{C}u(001)$ (from Ref. [98]). Solid lines: theory considering magnetic contribution only. Dashed line: theory considering magnetic contribution and T-dependence due to the softening of the Cu Fermi surface.

resonance frequency. In Ref. [98] the evaluation of the spin wave spectrum of the Hamiltonian (7.1.4) is carried out using the RPA treatment of the exchange terms and of the dipolar interaction and the Anderson-Callen theory of the single-ion anisotropy in the rotated frame method. The concrete experimental procedure to investigate the IEC in the trilayer system $\mathrm{N}i_7/\mathrm{C}u_9/\mathrm{C}o_2/\mathrm{C}u(001)$ [281] consisted of measuring the angular dependence of the resonance field $B^{\mathrm{Co}}_{\mathrm{res}}(T, \theta_{B_0})$ for the $\mathrm{Cu_9/Co_2/Cu(001)}$ film at two temperatures (55 K and 294 K) as well as the temperature dependence for $T \in [55 \text{ K}, \approx 300 \text{ K}]$ at a fixed angle ($\theta_{B_0} = 90°$). The same was repeated for the coupled system $\mathrm{Ni_7/Cu_9/Co_2/Cu(001)}$ after the deposition of the top Ni-layer and also for a $\mathrm{Ni_7/Cu(001)}$-film.

The anisotropy parameters K^α_2 and g^α_0 were fitted unambiguously to the experimental data from the measurements of the Co and Ni single-films. With the intralayer *nn* exchange integrals J_α chosen such that the two monolayers yield the correct magnetic moments of the $\mathrm{N}i_7$- and $\mathrm{C}o_2$-multilayer films at room temperature, respectively, the interlayer exchange coupling J_{IEC} remains the only fit parameter for the experimental resonance field.

The distinction between the spacer sources and the magnetic sources of the temperature dependence of IEC is achieved by carrying out the fitting procedure in two steps. First, the data are fitted for the temperatures as given by the experimental conditions. The temperature dependence of $J_{\mathrm{I}EC}(T)$ thus includes all spacer contributions to the IEC. Then, an additional fit is performed with the temperature artificially switched-off during the evaluation of the spin wave spectrum, thereby describing *all* sources of the T-dependence of IEC by the effective parameter $J^0_{\mathrm{I}EC}(T = T_{exp})$. The comparison of the two quantities $J_{\mathrm{I}EC}(T)$ and $J^0_{\mathrm{I}EC}(T)$ is shown in Fig. 7.2. The difference between the two curves yields the spin wave contribution to the temperature dependence of IEC and amounts to about 75% in the studied T-interval. Hence spin waves dominate the thermal variation; spacer effects are present but of minor importance. This result suggests that only considering band structure effects in the evaluation of the T-dependence of IEC is not sufficient except for very low temperatures.

A further result of Ref. [98] is the separation of the spacer effects into Fermi surface softening and other electronic sources of the T-dependence, mainly the reflection coefficients (Chap. 7.1.2). Fig. 7.3 demonstrates that the broadening of the Fermi surface due to the function F in Eq. (7.7) has only a small influence on the thermal variation of the IEC.

7.2 RKKY interlayer exchange coupling

In what follows, two aspects regarding the interlayer exchange coupling in thin Kondo lattice model films are considered. First, the IEC between confined monolayers is studied using the conventional RKKY theory. The focus is on the dependence of the IEC on the Fermi energy, i.e. on the charge carrier density. The temperature dependence is addressed in Sec. 7.3.

In a film consisting of N_{L} layers, the charge carriers are confined in the normal direction. Due to the discrete wave vector component $k_z \equiv k_\perp$ the Fermi 'surface' consists of N_{L} 1D-Fermi surfaces. The consequences of this confinement for the IEC are investigated in a comparison to the bulk behavior. It will also turn out to be instructive to contrast the IEC for the free electron gas with the tight-binding approach pursued here.

7.2.1 Green function formulation of RKKY-IEC

The following RKKY description assumes an ideal film structure, an unpolarized electron lattice gas, and a periodic distribution of the localized moments in the magnetic layers. Within the Green function formulation of the RKKY exchange, the interlayer exchange coupling between two monolayers α and β of a Kondo lattice film is given by (5.12) and (7.4):

$$J^{\alpha\beta}_{\mathrm{IEC}} \equiv J^{\alpha\beta}_{\mathbf{q}=0} = \frac{J^2}{2\pi N}\mathrm{I}m\sum_{\mathbf{k}}\int\limits_{-\infty}^{+\infty} dE f_-(E) G^{\alpha\beta(0)}_{\mathbf{k}}(E-\mu) G^{\beta\alpha(0)}_{\mathbf{k}}(E-\mu)\,. \tag{7.14}$$

The non-interacting Green function matrix elements read

$$G^{\alpha\beta(0)}_{\mathbf{k}}(E) = \left[\frac{1}{(E+\mathrm{i}0^+ +\mu)\underline{I} - \underline{\epsilon}(\mathbf{k})}\right]_{\alpha\beta}\,. \tag{7.15}$$

Expression (7.14) can be numerically evaluated for a given Bloch dispersion matrix and film geometry. In particular the band centers of gravity may be chosen differently for the individual monolayers of the slab. The Green function description of RKKY-IEC (7.14) includes the summation over all states up to the Fermi level and no further approximation has to be made like the restriction to some subset of states [61, 62, 277, 303, 304, 305].

Inserting (3.29) into (7.14) and performing the energy integration yields

$$\begin{aligned} J^{\alpha\beta}_{\mathrm{IEC}} &= \frac{J^2}{2\pi N}\mathrm{I}m\sum_{\mathbf{k}}\sum_{m,n}\int\limits_{-\infty}^{+\infty} dE f_-(E)\frac{u^{\alpha}_m(\mathbf{k})u^{*\beta}_m(\mathbf{k})u^{\beta}_n(\mathbf{k})u^{*\alpha}_n(\mathbf{k})}{\left[E+\mathrm{i}0^+ - \hat{\epsilon}_m(\mathbf{k})\right]\left[E+\mathrm{i}0^+ - \hat{\epsilon}_n(\mathbf{k})\right]} \\ &= -\frac{J^2}{2N}\mathrm{I}m\sum_{\mathbf{k}}\sum_{m,n} A^{\alpha\beta}_{mn}(\mathbf{k})\frac{f_-(\hat{\epsilon}_m(\mathbf{k})) - f_-(\hat{\epsilon}_n(\mathbf{k}))}{\hat{\epsilon}_m(\mathbf{k}) - \hat{\epsilon}_n(\mathbf{k})}\,. \end{aligned} \tag{7.16}$$

The factor

$$A^{\alpha\beta}_{mn}(\mathbf{k}) = \mathrm{R}e\left\{u^{\alpha}_m(\mathbf{k})u^{*\beta}_m(\mathbf{k})u^{\beta}_n(\mathbf{k})u^{*\alpha}_n(\mathbf{k})\right\} \tag{7.17}$$

describes intraband ($m = n$) and interband ($m \neq n$) contributions of the eigenstates of $\underline{\epsilon}(\mathbf{k})$ to the interlayer exchange between the monolayers α and β. $u^{\alpha}_m(\mathbf{k})$ denotes the projection of the Bloch state $|\mathbf{k}\alpha\sigma\rangle$ in monolayer α onto the eigenstate $|\mathbf{k}n\sigma\rangle$ of $\underline{\epsilon}(\mathbf{k})$.

In the tight-binding approximation and using layer-independent $\epsilon_{\parallel}(\mathbf{k})$ and $\epsilon_{\perp}(\mathbf{k})$ in (3.5), the eigenvalues $\hat{\epsilon}_n(\mathbf{k})$ occur in pairs. For the simple-cubic crystal, the interlayer hopping is $\mathbf{k}$-independent and the eigenvalues are given by

$$\begin{aligned} \hat{\epsilon}_n(\mathbf{k}) &= \epsilon_{\parallel}(\mathbf{k}) + \hat{\epsilon}_{\perp,n} \\ &= \epsilon_{\parallel}(\mathbf{k}) - 2t_{\perp}cos\left(\frac{n}{N_{\mathrm{L}}+1}\pi\right) \qquad (n = 1, ..., N_{\mathrm{L}})\,. \end{aligned} \tag{7.18}$$

The second term contains the discrete values of $k_\perp$ and $\epsilon_{||}(\mathbf{k})$ is the in-plane dispersion:

$$\epsilon_{||}(\mathbf{k}) = -2t_{||}\left[cos(k_x a) + cos(k_y a)\right] . \tag{7.19}$$

One sees from (7.18) that for a given $\hat{\epsilon}_n(\mathbf{k})$, there is a corresponding $\hat{\epsilon}_{n'}(\mathbf{k}) = \epsilon_{||}(\mathbf{k}) - \hat{\epsilon}_{\perp,n}$.

7.2.2 Dependence on the carrier density

Formula (7.16) shall be further evaluated for specific film geometries and densities of states at $T = 0$. A detailed discussion is given for the bilayer to work out the dependence of the interlayer coupling on the electronic structure. Then multilayers ($N_L > 2$) are considered.

7.2.2.1 Bilayer

The simplest film which can possibly exhibit interlayer exchange coupling is a bilayer ($N_\mathrm{L} = 2$). The general dispersion matrix for a symmetric 2ML-film is

$$\begin{pmatrix} \epsilon_{||}(\mathbf{k}) & \epsilon_\perp(\mathbf{k}) \\ \epsilon_\perp^*(\mathbf{k}) & \epsilon_{||}(\mathbf{k}) \end{pmatrix} . \tag{7.20}$$

One readily obtains

$$\hat{\epsilon}_{1,2}(\mathbf{k}) = \epsilon(\mathbf{k}) \pm |\epsilon_\perp(\mathbf{k})| \quad , \quad A_{11}^{12}(\mathbf{k}) = A_{22}^{12}(\mathbf{k}) = \frac{1}{4} = -A_{12}^{12}(\mathbf{k}) = -A_{21}^{12}(\mathbf{k}) . \tag{7.21}$$

Using[1]

$$\lim_{\mathbf{q}\to\mathbf{0}} \frac{f_-(\hat{\epsilon}_n(\mathbf{k})) - f_-(\hat{\epsilon}_n(\mathbf{k}+\mathbf{q}))}{\hat{\epsilon}_n(\mathbf{k}) - \hat{\epsilon}_n(\mathbf{k}+\mathbf{q})} = -\frac{\beta_T}{4cosh^2\left[\frac{1}{2}\beta_T\left(\hat{\epsilon}_n(\mathbf{k}) - \mu\right)\right]} , \tag{7.22}$$

the IEC reads

$$J_{IEC}^{12} = \frac{J^2}{2N}\sum_{\mathbf{k}}\left\{\frac{1}{4}\sum_{n=1}^{2}\frac{\beta_T}{4cosh^2\left[\frac{1}{2}\beta_T\left(\hat{\epsilon}_n(\mathbf{k}) - \mu\right)\right]} - \frac{f_-(\hat{\epsilon}_2(\mathbf{k})) - f_-(\hat{\epsilon}_1(\mathbf{k}))}{4|\epsilon_\perp(\mathbf{k})|}\right\} . \tag{7.23}$$

The first term corresponds to intraband and the second term to interband contributions.

---

[1] A subscript T is added to the thermal $\beta \to \beta_T = 1/k_\mathrm{B}T$.

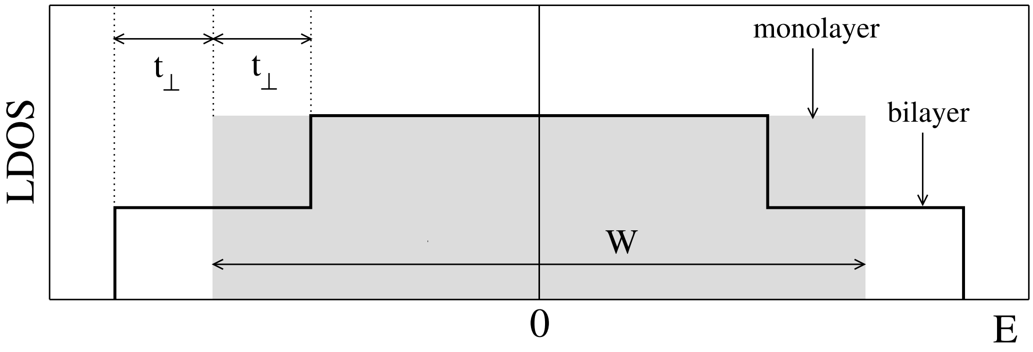

Figure 7.4: LDOS of a monolayer with parabolic electron dispersion and LDOS of a bilayer with parabolic in-plane dispersion and interlayer hopping $t_\perp$. The band cut-off is chosen such that the LDOS is centered around zero.

In the low-temperature limit ($T \rightarrow 0$), the cosh-term is sharply peaked at the Fermi level. With the monolayer LDOS

$$\rho(E) = \frac{1}{N} \sum_{\mathbf{k}} \delta\left(E - \epsilon_{\|}(\mathbf{k})\right) \tag{7.24}$$

one obtains for the diagonal terms in (7.23) for an sc(100)-bilayer:

$$\frac{1}{N} \sum_{\mathbf{k}} \sum_{n=1}^{2} \frac{\beta_T}{4cosh^2\left[\frac{1}{2}\beta_T\left(\hat{\epsilon}_n(\mathbf{k}) - \mu\right)\right]} \overset{T \to 0}{=} \rho(\epsilon_\mathrm{F} + t_\perp) + \rho(\epsilon_\mathrm{F} - t_\perp)\,. \tag{7.25}$$

For the sc(100)-geometry, the non-diagonal terms can be expressed in terms of the shifted monolayer LDOS, too, yielding for (7.23) the equivalent form

$$J^{12}_{IEC}(\epsilon_\mathrm{F}) = \frac{J^2}{2} \left[\frac{1}{4} \left(\rho(\epsilon_\mathrm{F} + t_\perp) + \rho(\epsilon_\mathrm{F} - t_\perp)\right) \right. \\ \left. - \frac{\int_{W_{\mathrm{m}in} - t_\perp}^{\epsilon_\mathrm{F}} dE \rho(E + t_\perp) - \int_{W_{\mathrm{m}in} + t_\perp}^{\epsilon_\mathrm{F}} dE \rho(E - t_\perp)}{4 t_\perp} \right]\,. \tag{7.26}$$

$W_{\mathrm{m}in}$ is the lower edge of the monolayer CB: $W_{\mathrm{m}in} = -\frac{W}{2} = -W_{\mathrm{m}ax}$.

Effective-mass approximation

In a further simplification, the effective free-electron approximation is applied for the in-plane dispersion, i.e. $\epsilon_{\|}(\mathbf{k}) \sim k^2$. This is a good approximation for lattices with a quadratic dispersion at the band bottom, like e.g. the simple cubic lattice, if the charge carrier density is low. The evaluation of (7.24) yields a constant monolayer LDOS:

$$\rho(E) = \rho_0 \,. \tag{7.27}$$

Due to the additional hopping the bilayer bandwidth is increased by $2t_\perp$ compared to the monolayer bandwidth (Fig. 7.4).

Fig. 7.5 shows the interlayer coupling $J_{\mathrm{I}EC} \equiv J_{IEC}^{12}$ as a function of the Fermi energy. The IEC jumps abruptly to a finite positive value as soon as there are free carriers available, i.e. when the Fermi energy enters the bilayer conduction band at $E = W_{\mathrm{m}in} - t_\perp$. With increasing charge carrier density the IEC falls off linearly and changes sign at $\epsilon_{\mathrm{F}} = W_{\mathrm{m}in}$ before it vanishes at a critical value $\epsilon_{\mathrm{F}}^c = W_{\mathrm{m}in} + t_\perp$: when the Fermi energy crosses the lower edge of the second electronic subband, the two monolayers are magnetically decoupled. The IEC is point-symmetric with respect to the lower edge of the monolayer LDOS at $\epsilon_{\mathrm{F}} = W_{\mathrm{m}in}$. For a very high band occupation a corresponding behavior of the IEC due to particle-hole symmetry is observed. The intralayer coupling $J_{\mathbf{q}=0}^{11}$ and the total exchange coupling are always positive. The latter is given by the bilayer LDOS at the Fermi level in analogy to the bulk relation (5.14):

$$\begin{aligned} J_{\mathrm{t}otal} &= J_{\mathrm{i}ntra} + J_{\mathrm{I}EC} && (7.28)\\ &= J_{\mathbf{q}=0}^{11} + J_{\mathbf{q}=0}^{12} && (7.29)\\ &= \frac{J^2}{2}\rho^{11}(\epsilon_{\mathrm{F}}) \,. && (7.30) \end{aligned}$$

Fig. 7.6 shows the intraband and interband contributions to the interlayer coupling. The intraband exchange is always ferromagnetic and the interband part is always antiferromagnetic. The intraband contribution leads to a discontinuous jump of the IEC at the lower band edge. The negative interband exchange, being the result of an integration over electronic states up to the Fermi level, starts at zero and then decreases. This makes the total $J_{\mathrm{I}EC}$ change its sign and decrease until $\epsilon_{\mathrm{F}}^c = W_{\mathrm{m}in} + t_\perp$. At this point, the second subband comes into play with another discontinuous jump of the intraband exchange to a higher constant level. Parallel to this the second interband term in (7.26) exactly compensates the further increase of the first interband term. The full interband part therefore stays constant with increasing ϵ_{F} just like the intraband part, but has a negative sign. Since the two contributions have the same absolute magnitude, they cancel above ϵ_{F}^c.

In order to discuss the antiferromagnetic interband exchange interaction further, a 1D cross section of the parabolic energy dispersion of the sc(100)-bilayer is shown in Fig. 7.7. There are two energy bands separated by $2t_\perp$. The interband exchange interaction in (7.26),

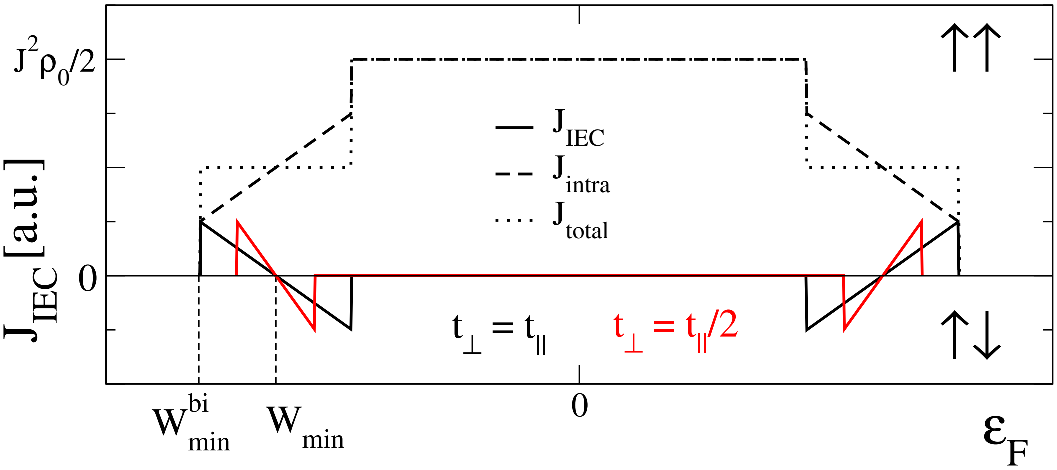

Figure 7.5: Interlayer exchange coupling in the sc(100)-bilayer. A positive/negative J_{IEC} corresponds to ferromagnetic/antiferromagnetic ('↑↑'/'↑↓') coupling. The thin dashed vertical lines indicate the lower band edges of the bilayer LDOS, $W^{bi}_{min} = -4t_{\|} - t_{\perp}$, and of the monolayer LDOS, $W_{min} = -4t_{\|}$.

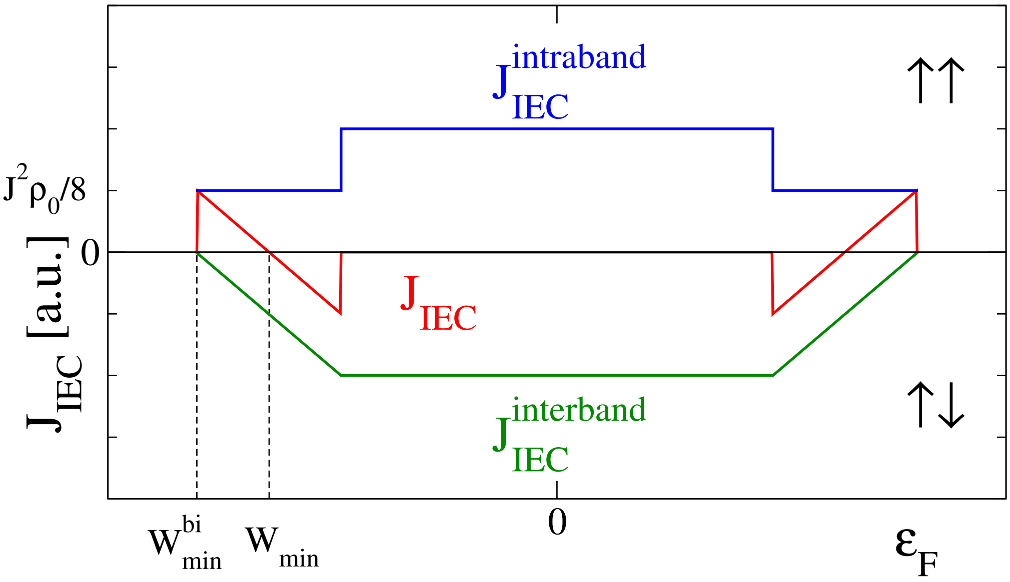

Figure 7.6: Intraband and interband contribution to the interlayer exchange coupling for $t_{\perp} = t_{\|}$. Other parameters as in Fig. 7.5.

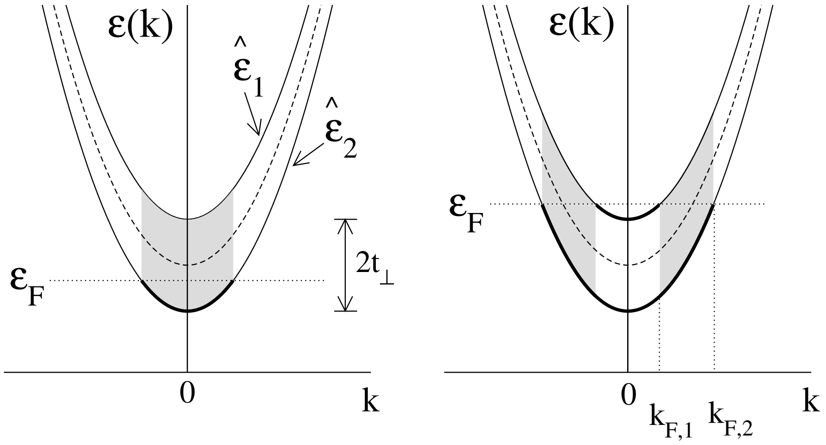

Figure 7.7: 1D cross section of the energy dispersion of the sc(100)-bilayer with parabolic in-plane dispersion for two values of the Fermi energy ϵ_F. An antiferromagnetic exchange interaction results from virtual excitations from the lower to the upper band (shaded areas).

$$J_{\mathrm{IEC}}^{interband} \sim -\frac{J^2}{4} \cdot \frac{1}{2t_\perp}\,, \tag{7.31}$$

results from virtual excitations from the lower band to the upper band which are associated with hopping processes between the two monolayers. For an electron of given spin such hopping can only occur if the electrons in the other monolayer have opposite spin, thus favoring an antiparallel alignment of the localized spins in one monolayer with respect to the other. On increasing ϵ_F, more transitions of this kind add to the AFM coupling as long as there are empty states in the upper band. The situation changes when the Fermi level crosses the bottom of the upper subband. The second band fills up and the number of empty states available for virtual transitions diminishes since these are not possible for wave vectors up to $\mathbf{k}_{\mathrm{F},1}$ where $\hat{\epsilon_1}(\mathbf{k}_{\mathrm{F},1}) = \epsilon_\mathrm{F}$. At the same time, the loss is accompanied by a gain of such processes at $\mathbf{k}_{\mathrm{F},2}$. The increase and decrease of such transitions is represented by the integrals over the density of states in (7.26). For the constant monolayer LDOS, loss and gain balance each other and in total the number of virtual processes and hence the antiferromagnetic interband contribution to the IEC stay the same. The constant interband exchange interaction above $\epsilon_\mathrm{F}^c = W_{\mathrm{m}in} + t_\perp$ is thus a peculiarity of the parabolic dispersion of the effective-mass approximation for the in-plane motion of the charge carriers.

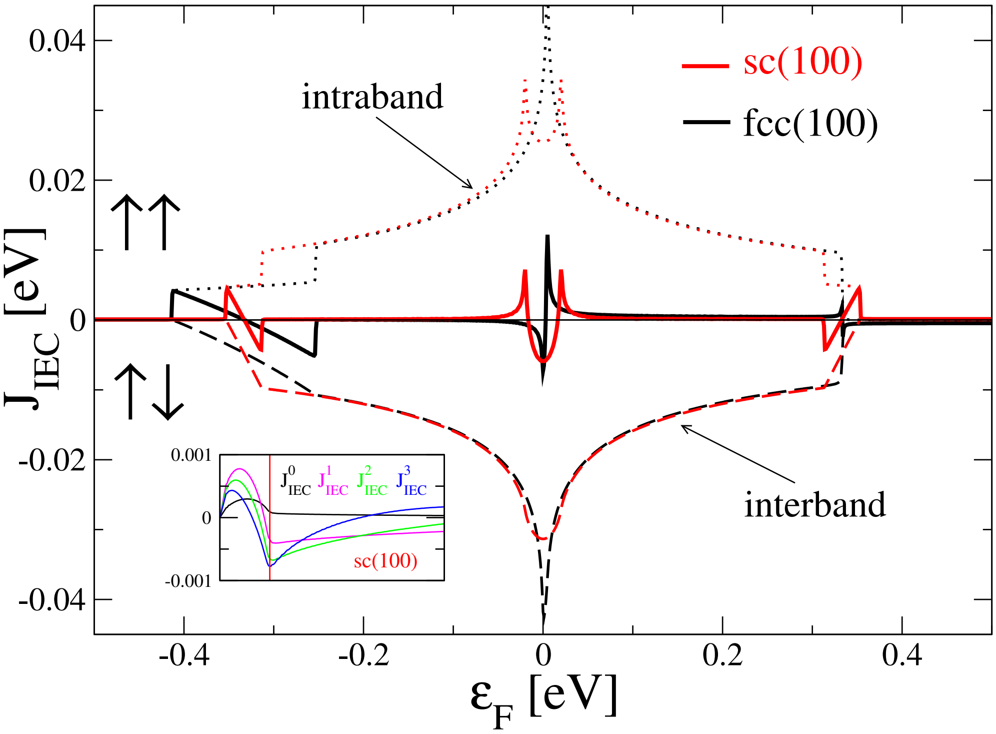

Figure 7.8: Interlayer exchange coupling for the sc(100)- and for the fcc(100)-bilayer. Inset: the first four RKKY exchange integrals in the sc-bilayer, $J^n_{IEC} \equiv J^{12}_{ij}$, with i, j being nth nearest-neighbors in the basal plane. The vertical red line indicates the position of the Fermi energy where the IEC vanishes. Parameters: $t_{\|} = 1/12$, $t_{\perp} = t_{\|}/4$, $J = 0.2$.

Bloch density of states and dispersive interlayer hopping

Fig. 7.8 shows the total IEC and the intraband and interband part as a function of ϵ_{F} for an sc(100)- and an fcc(100)-bilayer. The fcc(100)-bilayer consists of two square-lattice monolayers shifted with respect to each other by $\mathbf{r}_0 = (\frac{a}{2}, 0)$ in the x-y-plane. Fig. 7.9 displays the IEC for the sc-geometry and two different values of the interlayer hopping $t_{\perp}$.

The monolayer LDOS now exhibits a sharp van-Hove-peak at the band center. Furthermore, the fcc(100)-interlayer hopping is $\mathbf{k}$-dependent:

$$\epsilon_{\perp}(\mathbf{k}) = 4t_{\perp} cos\left(\frac{1}{2}k_x a\right) cos\left(\frac{1}{2}k_y a\right) . \tag{7.32}$$

As expected, the behavior of the Bloch-sc-bilayer for low band fillings resembles closely that which was obtained using the effective-mass approximation: upon increasing ϵ_{F} an abrupt jump to a positive initial value of the IEC is followed

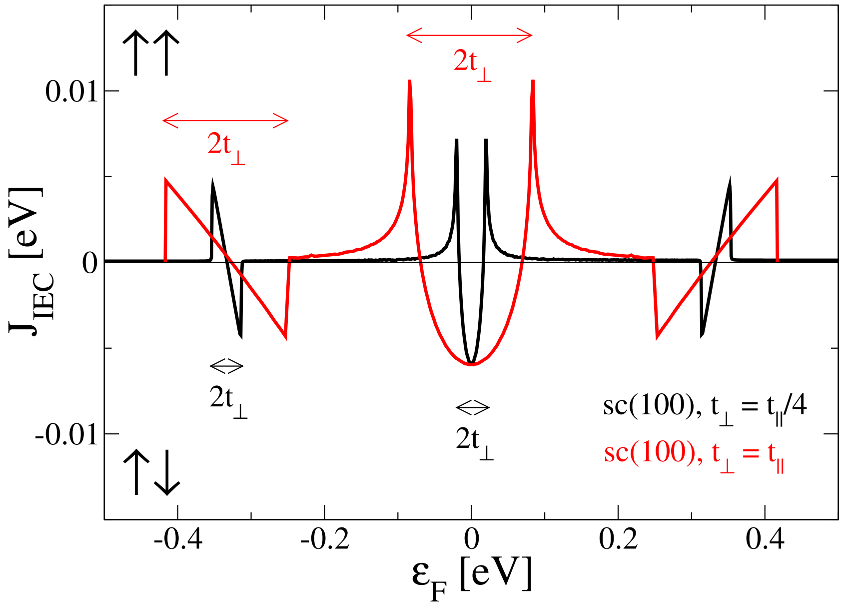

Figure 7.9: Interlayer exchange coupling in the bilayer for different interlayer hopping $t_\perp$. Parameters: $t_\parallel = 1/12$, $J = 0.2$.

by a decrease due to the interband exchange. When the upper subband starts being filled, the IEC is strongly reduced. For the fcc-bilayer the same behavior is observed, but over a larger energy range because the band gap at the Γ-point is four times larger than for the dispersionless interlayer hopping in the sc-bilayer. Apart from this, the **k**-dependence of $\epsilon_\perp$ does not significantly alter the behavior of the IEC as compared to the sc-bilayer.

The intraband and interband exchange interactions nearly cancel each other at $\epsilon_\mathrm{F} = W_\mathrm{min} + max(\epsilon_\perp)$. Besides a rapid variation of the IEC around $\epsilon_\mathrm{F} = 0$, which is of width $\sim 2t_\perp$, the interlayer exchange coupling between the two monolayers practically vanishes over a wide energy range. However, this range depends on $t_\perp$ and becomes smaller for stronger interlayer hopping as demonstrated in Fig. 7.9 for the simple-cubic case.

The considerations of this section were concerned with the IEC mainly in an sc(100)-bilayer using the parabolic in-plane dispersion as well as the full Bloch dispersion. In the former case, the IEC was found to vanish completely above some critical Fermi energy. In fact, it follows from Eq. (7.26) that any monolayer LDOS which depends *linearly* on energy leads to a magnetic decoupling. This condition for a vanishing IEC is slightly more general than the (physically more interesting) constant-LDOS approximation.

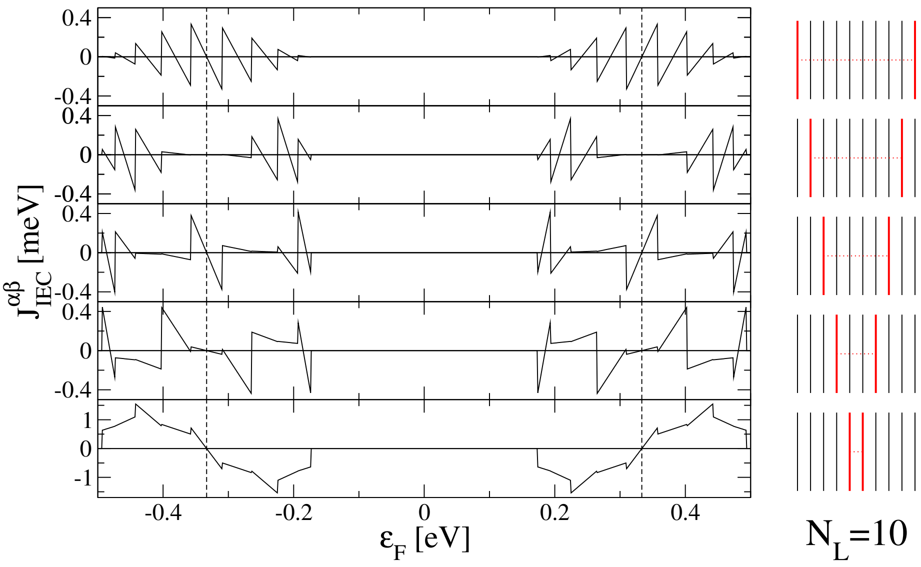

Figure 7.10: Interlayer exchange coupling between two monolayers in a 10ML-film. The positions of the monolayers are indicated by the red vertical lines in the film sketch on the right. The dashed line designates the lower edge of the monolayer LDOS. In-plane effective-mass approximation (constant monolayer LDOS). Parameters: monolayer band width $W = 2/3$, $t_\perp = 1/12$, $J = 0.2$.

7.2.2.2 Multilayer films

It appears natural to investigate if and how the results obtained for the bilayer apply to films consisting of more than two monolayers. Again, for better transparency, the in-plane effective-mass approximation implying a constant monolayer LDOS is first used. All layers have the same band centers of gravity t_0^α and the interlayer hopping $t_\perp$ is the same throughout the sc(100)-films considered in the following.

Fig. 7.10 shows the IEC between different pairs of monolayers in a 10ML-film. Note that the electronic structure is the same in all cases because the film thickness is the same, and thus the dependence of the interlayer coupling on ϵ_{F} is exclusively determined by the spacer width. The sharp features are typical confinement effects. The values of ϵ_{F} where the IEC undergoes abrupt changes correspond to the band edges of the electronic subbands $\hat{\epsilon}_n$. As for the bilayer the IEC exhibits point symmetry with respect to the lower monolayer band edge ($\epsilon_{\mathrm{F}} = W_{min}$). In all cases, the IEC vanishes at the same critical value of the Fermi energy ϵ_{F}^c which is given by the lower band edge of the highest electronic subband. From (7.18) one explicitly obtains for $N_{\mathrm{L}} = 10$:

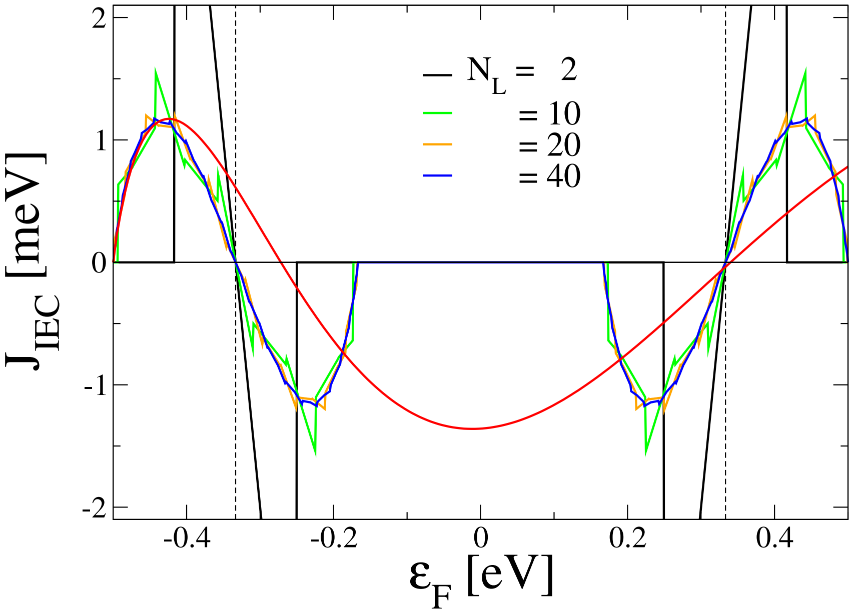

Figure 7.11: Interlayer exchange coupling between the two center layers for different film thickness as indicated. The red line is the RKKY result for the coupling of two spin sheets in a 3D free-electron gas (the amplitude is scaled). Other parameters as in Fig. 7.10.

$$\epsilon_{\mathrm{F}}^{c} = W_{min} + 2t_{\perp}cos\left(\frac{1}{11}\pi\right) . \tag{7.33}$$

The dependence of the IEC on the Fermi energy evolves from a rapidly oscillating, ratched-like behavior to just one, relatively smooth period. This agrees with the bulk results obtained with the quantum interference model [265] (see Chap. 7.7) and the continuum RKKY result in 3D [153]. Both approaches yield an asymptotic periodic behavior

$$\sim sin(2k_{\mathrm{F}}D)/D^2 \tag{7.34}$$

for the coupling of two magnetic planes separated by D. An increasing spacer thickness implies a shorter wavelength of the oscillation with respect to the Fermi energy $\epsilon_{\mathrm{F}} \sim k_{\mathrm{F}}^2$.

It is illustrative to compare the confined RKKY results for the KLM considered here with the free-electron RKKY theory for the bulk in more detail. The full interlayer exchange coupling energy per unit area between two sheets of areal spin density σ_S embedded in a 3D free electron gas is [153, 306]

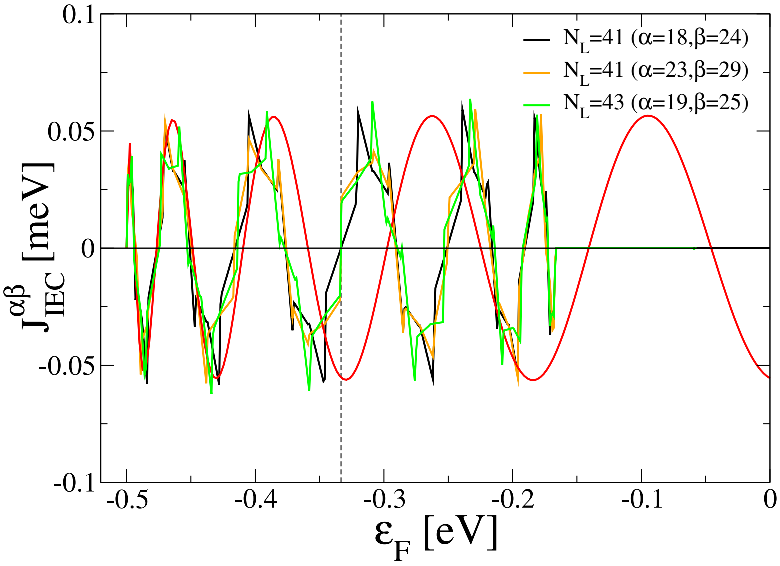

Figure 7.12: Interlayer exchange coupling between two monatomic layers separated by five spacer monolayers. The black line and the green line correspond to symmetrically lying layers, the orange line refers to the same separation but shifted positions of the layers. The red line is the continuum RKKY result (the amplitude is scaled). Other parameters as in Fig. 7.10.

$$J_{IEC}^{3DFEG} = \frac{mJ^2S^2k_{\mathrm{F}}^2}{\sigma_S^2 8\pi^2\hbar^2}\left[\left(\frac{\pi}{2} - \mathrm{S}i(x)\right) - \frac{cos(x)}{x} + \frac{sin(x)}{x^2}\right] . \tag{7.35}$$

$\mathrm{S}i(x) = \int_0^x \frac{sint}{t}dt$ is the sine integral function and the abbreviation $x = 2k_{\mathrm{F}}D$ is used. For the Fermi vector k_{F} in (7.35), the perpendicular wave vector from the energy spectrum (7.18) is taken. For $N_{\mathrm{L}} \rightarrow \infty$, an expansion about the bottom of the conduction band yields:

$$\epsilon_{\mathrm{F}} = W_{\mathrm{min}} - 2t_{\perp}cos\left(k_{\mathrm{F}}^{\perp}a\right) \approx W_{\mathrm{min}} - 2t_{\perp} + t_{\perp}(k_{\mathrm{F}}^{\perp})^2a^2 . \tag{7.36}$$

Hence

$$k_{\mathrm{F}} \rightarrow k_{\mathrm{F}}^{\perp} = \sqrt{\frac{\epsilon_{\mathrm{F}} - W_{\mathrm{min}}^{\mathrm{bulk}}}{t_{\perp}}\frac{1}{a}} , \tag{7.37}$$

where $W_{\mathrm{min}}^{\mathrm{bulk}} = W_{\mathrm{min}} - 2t_{\perp} < \epsilon_{\mathrm{F}}$ is the bottom of the bulk conduction band. (7.37) is a good approximation for small charge carrier densities and is used in (7.35) in the following.

Figs. 7.11 and 7.12 display the interlayer exchange coupling between two neighboring monolayers ($D = a$) and for a spacer thickness of five monolayers ($D = 6a$),

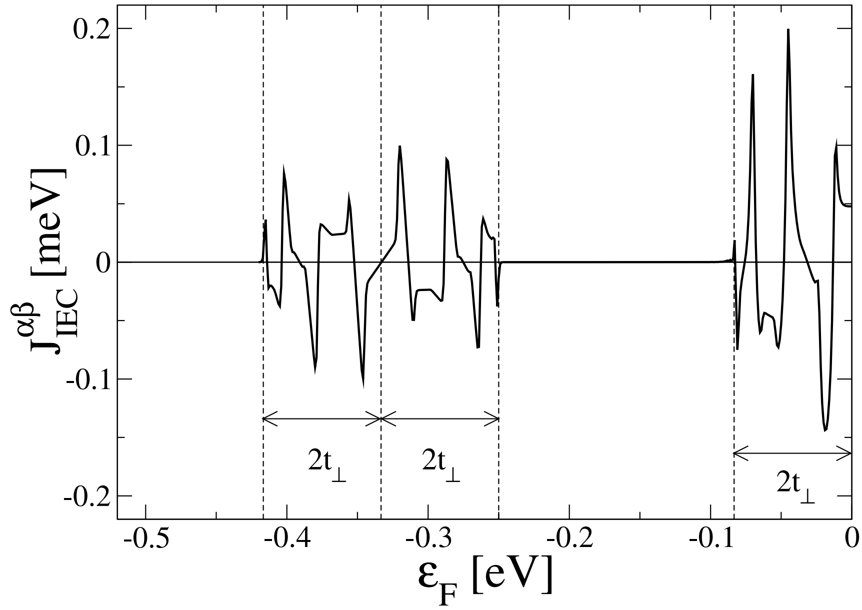

Figure 7.13: Interlayer exchange coupling between two monolayers separated by five spacer monolayers in a 21ML-film using the monolayer Bloch-LDOS. The nearest-neighbor hopping is anisotropic: $t_\perp = t_\|/2$. Parameters: $\alpha = 8, \beta = 14, t_\| = 1/12, J = 0.2$.

respectively. Upon increasing the film thickness, confinement effects become less important in Fig. 7.11, and the result is a smooth variation of the IEC with the charge carrier density. The amplitude is strongly damped and the region of finite IEC becomes larger due to the increased bandwidth. The bulk bandwidth is practically reached for $N_{\mathrm{L}} = 10$; for $N_{\mathrm{L}} \to \infty$, the IEC vanishes at $\epsilon_{\mathrm{F}}^c = W_{\mathrm{m}in} + 2t_\perp = W_{\mathrm{m}in}^{\mathrm{b}ulk} + 4t_\perp$. Regarding the periodic behavior, the continuum RKKY result is qualitatively similar, however with the important difference that the IEC does not vanish above some critical value of ϵ_{F}.

The same holds for larger spacer thickness (Fig. 7.12). Although varying the film thickness modifies the IEC-curves even for quite large N_{L}, the general picture concerning the periodicity and the breakdown of IEC is the same. Similarly, considering the coupling between two monolayers separated by the same distance but at shifted positions within a film of fixed thickness, no major changes are observed. Hence the vanishing IEC in the tight-binding model is not restricted to symmetrically lying monolayers, implying that any two slabs of finite thickness are decoupled above ϵ_{F}^c. A similar observation when using the in-plane effective-mass approximation was made in Ref. [271] where the IEC in the bulk was treated in the framework of a hole-confinement model.

For large film and spacer thickness, the known analytic RKKY results for the IEC in the bulk can be used. The continuum free-electron RKKY-IEC (7.34) in the large-spacer limit is also obtained by the more general RKKY approach for arbitrary Fermi surface [261, 262]. According to this theory, the IEC is governed by perpendicular extremal Fermi surface spanning vectors $\mathbf{q}_\perp^\alpha$ identical to those of the quantum interference approach (Chap. 7.1.2). For the spherical Fermi surface of the 3D free electron gas, there is one such wave vector with $q_\perp^{\mathrm{F}EG} = 2k_\mathrm{F}$. This wave vector connects the two stationary points $(0, 0, k_z)$ and $(0, 0, -k_z)$.

For the isotropic bulk tight-binding dispersion ($t \equiv t_\parallel = t_\perp$),

$$\epsilon(k_x, k_y, k_z) = -2t\left[cos(k_x a) + cos(k_y a) + \cos(k_z a)\right] , \tag{7.38}$$

the Fermi surface is a free-electron-like sphere for small wave vectors. With increasing ϵ_F, it is deformed by the *cos*-terms and develops necks at the boundaries of the first Brillouin zone when these are crossed for $\epsilon_\mathrm{F} > -2t = \epsilon_\mathrm{F}^c$. For $\epsilon_\mathrm{F} < \epsilon_\mathrm{F}^c$ the critical spanning vector is the same as for free electrons; for $\epsilon_\mathrm{F} > \epsilon_\mathrm{F}^c$ it no longer exists due to the necks. However, its disappearance coincides with the emergence of a new critical point at the zone boundaries in the k_x-k_y-plane. The IEC is governed by this extremal point and, in particular, it does not vanish above ϵ_F^c.

The combined model with the tight-binding perpendicular dispersion and with the effective-mass in-plane dispersion shows the same qualitative behavior as the all-tight-binding approach up to ϵ_F^c. However, the necks now appear only at the zone boundaries in k_z-direction for $\epsilon_\mathrm{F} = \epsilon_\mathrm{F}^c$, and the initial critical point breaks down. For a given k_z, the k_x- and k_y-values of the Fermi 'surface' always lie on a circle for a parabolic in-plane dispersion. Hence no new critical spanning vector emerges above ϵ_F^c and the IEC vanishes.

A similar behavior occurs using the all-tight-binding dispersion with anisotropic hopping $t_\perp \neq t_\parallel$, which in practice might arise from tetragonal distortion due to epitaxial growth on a substrate with a different lattice constant. In this case, the necks at the zone boundaries in the k_x-k_y-plane and in k_z-direction evolve at different values of the Fermi energy. If $t_\perp < t_\parallel$, the IEC is finite for $\epsilon_\mathrm{F} < \epsilon_\mathrm{F}^{c,1} = W_{\mathrm{m}in} + 2t_\perp$, but there is no critical wave vector between $\epsilon_\mathrm{F}^{c,1}$ and $\epsilon_\mathrm{F}^{c,2} = -2t_\perp$ where the necks in the k_x- and k_y-direction develop. This 'intermediate' vanishing of the IEC for an anisotropic tight-binding dispersion is demonstrated in Fig. 7.13. It represents the bulk limit of the corresponding bilayer behavior shown in Figs. 7.8 and 7.9. There, the occupation of the highest electronic subband corresponds to the Fermi 'surface' reaching the boundaries of the 'Brillouin zone' in k_z-direction.

7.3 Temperature dependence

The Ni/Cu/Co-trilayer discussed in Sec. 7.1.4 exhibits a negative IEC, i.e. an antiferromagnetic coupling of Ni and Co. The IEC decreases with increasing T mainly due to magnon excitations but does not change sign. In similar systems no T-induced transition between an FM and an AFM interlayer exchange coupling has been found. On the contrary, a temperature-induced reorientation transition from ferromagnetic to antiferromagnetic IEC far below the Curie temperatures of the magnetic layers was reported for a Tb/Y/Gd system [299, 300].

The different thermal behavior of the IEC in such *real* local-moment metallic systems may be qualitatively understood as a consequence of the RKKY interaction. Concerning the magnetic properties, the RKKY picture is surely more appropriate for rare-earth systems than for the 3d-transition metals [12, 13, 14]. This holds, in particular, for the interlayer exchange coupling. In a Kondo lattice system with finite charge carrier density, the intra-atomic interaction can be mapped onto an effective Heisenberg interaction among the localized moments (Chap. 5). The long-range oscillatory character in the weak-coupling limit makes the interlayer coupling inherently prone to reorientation and frustration phenomena. Besides being a generic description for metallic systems containing localized moments, the effective Heisenberg exchange integrals relate the IEC directly to the temperature-dependent electronic structure and are in this respect more fundamental than the interlayer coupling constant J_{IEC} in (7.13).

The following considerations are concerned with the temperature-dependence of the IEC in ultrathin, symmetric Kondo lattice trilayer films.

7.3.1 Model Hamiltonian

The starting point is the single-band, tight-binding Kondo lattice model (3.14). For a trilayer consisting of two ferromagnetic layers A and B separated by a spacer layer it reads

$$H^{tri}_{\mathrm{KLM}} = -\sum_{ij\sigma}\sum_{\alpha\beta}(t^{\alpha\beta}_{ij} + \mu\delta_{ij}\delta_{\alpha\beta})c^{\dagger}_{i\alpha\sigma}c_{j\beta\sigma} - \frac{1}{2}\sum_{i\alpha\sigma} J_{\alpha}\left(z_{\sigma}S^{z}_{i\alpha}n_{i\alpha\sigma} + S^{-\sigma}_{i\alpha}c^{\dagger}_{i\alpha\sigma}c_{i\alpha-\sigma}\right) . \tag{7.39}$$

Symmetric and uniform parameter configurations are considered: $N^{\mathrm{A}}_{\mathrm{L}} = N^{\mathrm{B}}_{\mathrm{L}} = N^{mag}_{\mathrm{L}}$, a uniform hopping $t \equiv t^{\alpha\alpha}_{\langle ij\rangle} = t^{\alpha\alpha\pm 1}_{ii}$, and exchange integrals $J_{\alpha\in\mathrm{A}} = J_{\alpha\in\mathrm{B}} \equiv J \neq 0$. There are no localized magnetic moments in the spacer; this is taken care of by setting $J_{\alpha} = 0$ in the spacer layers.

(7.39) is approximately solved using the MCDA for the electronic self-energy (Chap. 4.3) and the modified RKKY method (Chap. 5.2). The MRKKY exchange integrals account for the influence of the exchange-split electronic band structure on the local-moment interaction and in particular for its T-dependence. The effective Heisenberg film consists of the ferromagnetic layers in (7.39). Together with an additional single-ion anisotropy and with an external field in z-direction it reads

$$\begin{aligned} H_{\mathrm{eff}}^{tri} = &-\sum_{ij}\sum_{\alpha\beta\in\mathrm{A}} J_{ij}^{\alpha\beta}\mathbf{S}_{i\alpha}\mathbf{S}_{j\beta} - \sum_{ij}\sum_{\alpha\beta\in\mathrm{B}} J_{ij}^{\alpha\beta}\mathbf{S}_{i\alpha}\mathbf{S}_{j\beta} - 2\sum_{ij}\sum_{\alpha\in\mathrm{A},\beta\in\mathrm{B}} J_{ij}^{\alpha\beta}\mathbf{S}_{i\alpha}\mathbf{S}_{j\beta} \\ &-\sum_{i}\sum_{\alpha\in\mathrm{A},B} K_2^{\alpha}(S_{i\alpha}^z)^2 - B\sum_{i}\sum_{\alpha\in\mathrm{A},B} S_{i\alpha}^z\,. \end{aligned} \tag{7.40}$$

The first two exchange terms describe the intralayer coupling and the third one represents the interlayer coupling. A positive uniaxial second-order anisotropy is chosen which is the same in both layers, $K_2 \equiv K_2^{\alpha\in\mathrm{A}} = K_2^{\alpha\in\mathrm{B}} > 0$. The factor $g_\alpha\mu_\mathrm{B}$ has been absorbed into the magnetic field B. The coupling of the latter to the itinerant subsystem is neglected.

(7.40) is used for studying the IEC between two metallic, ferromagnetic local-moment layers A and B separated by a metallic spacer. It is solved by means of the Tyablikov and the Anderson-Callen treatment of the exchange and the anisotropy terms, respectively. Using the layer-dependent rotated-frame method, an antiparallel orientation of the magnetizations of A and B can be considered in addition to the parallel alignment.

The chosen type and positive sign of the anisotropy imply an easy-axis direction of the magnetization perpendicular to the film plane (z-direction). With no external field in the x-y-plane, the layer-dependent polar angles θ_α can only be 0 or π. This follows directly from the symmetry of the Hamiltonian and can be readily verified using the effective fields (5.68) and (5.69) for the simple case of a bilayer consisting of two ferromagnetic monolayers. For thicker films, more complex configurations are possible, like e.g. alternating FM and AFM coupling, but the angle between the magnetizations of any two monolayers is always 0 or π. For an interlayer exchange-coupled trilayer, one either has a parallel alignment ('ferromagnetic coupling', '↑↑') or an antiparallel alignment ('antiferromagnetic coupling', '↑↓').

The following considerations apply analogously to in-plane easy axes of the magnetization. In order to describe this case, however, an appropriate additional anisotropy term in (7.40) and an azimuthal angle for the rotation of the layer-dependent frame are required. Note that such a configuration is different from the easy-plane case ($K_2 < 0$) in which no specific direction is preferred in the x-y-plane [244].

It can be inferred from the effective fields (5.68) and (5.69) that the possible magnetic configurations are not only determined by the sign of the summed interlayer exchange integrals $\sum_{\alpha\beta} J_{\mathbf{0}}^{\alpha\beta}$ as (7.4) suggests but also by the external field and the effective anisotropy $K_{2,eff}(T)$. The combined effect of the two latter may lead to a magnetically stable parallel alignment even if the summed exchange integrals are negative. For a *fixed* set of exchange integrals, there are one or two self-consistent solutions depending on the anisotropy strength and on the external field. However, the effective exchange integrals used in (7.40) depend on the electronic structure and are in general different for a parallel and for an antiparallel alignment of the layers. Hence, there may be no self-consistent solution at all, indicating that the assumption of ferromagnetic layers is no longer justified and other magnetic states must be considered like antiferromagnetism within the local-moment layers.

One could use the effective fields (5.68) and (5.69) to determine the possible self-consistent, magnetically stable configurations. This procedure would, however, underestimate the influence of spin wave excitations. The next section presents a criterion for the magnetic stability of an interlayer exchange-coupled film.

7.3.2 Magnetic interlayer stability

For $T = 0$, the interlayer exchange interaction is given by the sum over all interlayer exchange-coupled film planes (Eq. (7.4)). For finite temperatures, the interlayer coupling can no longer be obtained by just summing up the exchange integrals because spin wave excitations have to be taken into account.

The interlayer exchange contributes in two terms of the RPA spin wave self-energy matrix elements $\left[\underline{\mathrm{M}}_{\mathbf{q}}\right]_{\alpha\alpha'}$ (Eq. (5.40)), namely in the mean-field part

$$2\sum_{\beta} J_{\mathbf{0}}^{\alpha\beta}\langle S_{\beta}^{z}\rangle\delta_{\alpha\alpha'} \tag{7.41}$$

and in the **q**-dependent term

$$-2J_{\mathbf{q}}^{\alpha\alpha'}\langle S_{\alpha'}^{z}\rangle\,. \tag{7.42}$$

In principle, (5.40) has to be evaluated self-consistently in order to obtain the magnetic exitation spectrum for a given electronic configuration (charge carrier density, band width, hopping, intra-atomic interaction, number of monolayers). However, this turns out to be a formidable computational task. The intralayer exchange in the ferromagnetic layers can often be computed for a finite interaction range among the localized spins provided the intra-atomic interaction J is not too small. For the IEC, a very large, in fact infinite number of shells would have to be considered in order to obtain the interlayer coupling within sufficient accuracy (see Appendix C for details on the shell picture). This amounts to do the **k**-sum in the exchange integrals (5.19) explicitly in order to get $J_{\mathbf{0}}^{\alpha\beta}$, $2J_{\mathbf{q}}^{\alpha\alpha'}$ in (7.41) and (7.42) for each iteration step during the evaluation.

This enormous numerical effort can be circumvented. The thermal variation of the magnetization of the ferromagnetic layers is determined by the intra-ferromagnetic-layer exchange integrals; the exchange integrals across the spacer are usually much smaller. The magnetization can therefore be obtained to good approximation by carrying out the calculation for an *enforced* FM or AFM configuration with some small, fixed $J_{ii}^{\alpha\beta}$ where $\alpha \in$ A, $\beta \in$ B. Then the interlayer exchange integrals are computed in an additional step *after* the electronic and the magnetic quantities have converged for a given temperature.

It is discussed next how these interlayer exchange integrals are related to the T-dependent magnetic stability of the FM- and the AFM-aligned configuration.

Parallel configuration

The gap between the acoustical and the optical branch in the spin wave spectrum of an FM-aligned Heisenberg bilayer (Fig. 7.14, see also Appendix D) is given by the interlayer exchange interaction only. The intralayer exchange governs the magnetic stiffness of both branches. Whereas the intralayer exchange integrals are thus responsible for the magnetic order in each of the FM layers, it is the interlayer exchange, i.e. the gap between the acoustical and the optical mode, which determines the magnetic stability of the parallel alignment of A and B.

Ferromagnetism within the monolayers becomes unstable if there are negative magnon energy states belonging to the acoustic branch. Similarly, the ferromagnetic coupling of the two layers becomes unstable when there are negative energy modes in the optical branch of the spectrum. Given a sufficiently stiff acoustical branch and no spin wave softening for wave vectors away from the Γ-point, the interlayer exchange integrals are most important for small wave numbers $\mathbf{q} \to \mathbf{0}$. As already remarked, for suitable anisotropy and external field, the parallel configuration is magnetically stable even for *negative* interlayer exchange integrals. In order for the magnon energy to become negative at $\mathbf{q} = 0$, the interlayer coupling has to overcompensate the contributions of the external field and of the anisotropy to the effective field which cause the gap of the acoustical branch at $\mathbf{q} = 0$:

$$-J_{IEC}^{\mathrm{bi}}(T) > B_{\mathrm{e}ff}(T) = B + K_{2,\mathrm{e}ff}(T)\,. \tag{7.43}$$

where $J_{IEC}^{\mathrm{bi}}(T) < 0$ is the (negative) gap between the optical and the acoustical branch for $\mathbf{q} = 0$:

$$J_{IEC}^{\mathrm{bi}}(T) = 4\langle S^z\rangle J_{\mathbf{0}}^{inter}(T)\,. \tag{7.44}$$

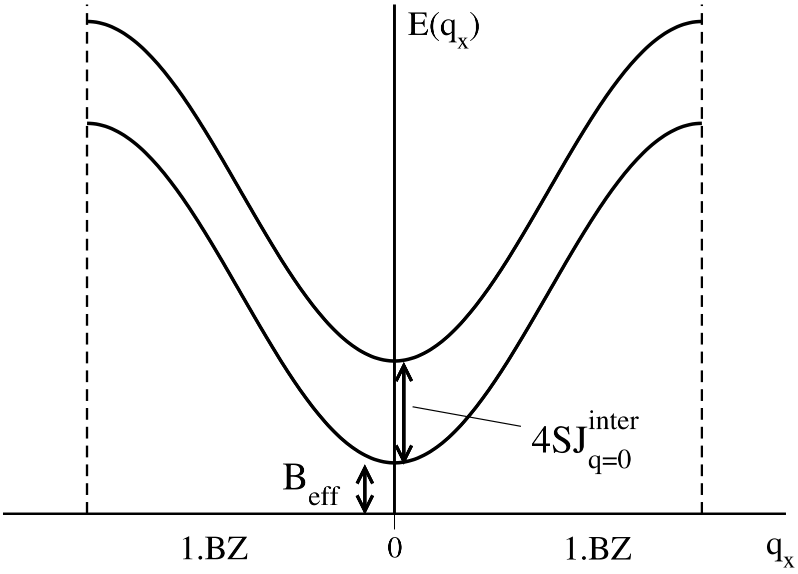

Figure 7.14: Spin wave spectrum of the ferromagnetic sc(100)-Heisenberg bilayer from the Γ-point $(q_x, q_y) = (0, 0)$ to the M-point $(\pi, 0)$ at $T = 0$.

Note that B_{eff} used in (7.43) deviates from the definition (5.66) of the effective field in that it does not contain the interlayer exchange integrals. (7.44) can be generalized to magnetic layers consisting of more than one monolayer. The energy gap between the two lowest-lying $\mathbf{q} = 0$-spin waves modes in a symmetric film consisting of two ferromagnetically coupled slabs A and B, each consisting of N_{L}^{mag} magnetic monolayers, is given by

$$J_{\mathrm{I}EC}(T) = \frac{4}{N_{\mathrm{L}}^{\mathrm{m}ag}} \langle S^z \rangle \sum_{\alpha \in \mathrm{A}, \beta \in \mathrm{B}} J_{\mathbf{0}}^{\alpha\beta}(T) \tag{7.45}$$

if one neglects the layer-dependence of the magnetization $(\langle S^z \rangle \equiv \langle S^z_{\alpha \in \mathrm{A}} \rangle = \langle S^z_{\beta \in \mathrm{B}} \rangle)$. This is surely more justified for larger thickness, however the uniform-magnetization approximation can be expected not to affect much the qualitative behavior of $J_{\mathrm{I}EC}(T)$. In the same spirit, the effective anisotropy $K_{2,\mathrm{e}ff}(T)$ is assumed to be layer-independent in the following.

In order to separate the electronic and the spin wave contributions to $J_{\mathrm{I}EC}(T)$, it is useful to define the quantity

$$J^{el}_{\mathrm{I}EC}(T) = \sum_{\alpha \in \mathrm{A}, \beta \in \mathrm{B}} J_{\mathbf{0}}^{\alpha\beta}(T) \, . \tag{7.46}$$

This expression corresponds to (7.4) and yields the electronic contribution to $J_{\mathrm{I}EC}(T)$. For the numerical evaluation, the layer-averaged magnetization

$$\langle S^z_{\mathrm{av}}\rangle = \frac{1}{N_{\mathrm{L}}^{\mathrm{mag}}}\sum_{\alpha}\langle S^z_{\alpha}\rangle \tag{7.47}$$

is used in (7.45) in order to get the temperature-dependence of the spin wave gap:

$$J_{\mathrm{I}EC}(T) = \frac{4}{N_{\mathrm{L}}^{\mathrm{m}ag}}\langle S^z_{\mathrm{av}}\rangle J^{el}_{\mathrm{I}EC}(T)\,. \tag{7.48}$$

(7.48) is a measure for the magnetic stability of the ferromagnetic alignment in an IEC-film. The parallel configuration is unstable if

$$-\,J_{\mathrm{I}EC}(T) > B_{\mathrm{e}ff}(T)\ \wedge\ J_{\mathrm{I}EC}(T) < 0\,. \tag{7.49}$$

Antiparallel configuration

The quantity (7.45) defined for two FM-aligned layers applies also to an antiparallel alignment. The evaluation of the multiple Green function approach (5.64) yields for the spin wave spectrum of an AFM-aligned bilayer in zero external field[2]

$$E^{\mathrm{b}i}_{\uparrow\downarrow}(\mathbf{q}) = \sqrt{\left(K_{2,\mathrm{e}ff} + 2\langle S^z\rangle(J^{intra}_{\mathbf{0}} - J^{intra}_{\mathbf{q}}) - 2\langle S^z\rangle J^{inter}_{\mathbf{0}}\right)^2 - \left(2\langle S^z\rangle J^{inter}_{\mathbf{q}}\right)^2} \tag{7.50}$$

which is doubly degenerate. It is readily verified that just like in the case of the parallel configuration, the $\mathbf{q} = 0$-mode is most sensitive to the interlayer coupling because the intralayer terms drop out. One obtains for the gap:

$$E^{\mathrm{b}i}_{\uparrow\downarrow}(\mathbf{q} = 0) = \sqrt{K_{2,\mathrm{e}ff}\left(K_{2,\mathrm{e}ff} - 4\langle S^z\rangle J^{inter}_{\mathbf{0}}\right)}\,. \tag{7.51}$$

(7.51) corresponds to the energy gap in the spin wave spectrum of an antiferromagnet in zero external field if $J^{inter}_{\mathbf{0}}$ is replaced by the sum over all antiferromagnetically aligned neighboring spins [110]. The antiferromagnetic configuration becomes unstable if the radicand is negative, i.e. if a (positive) interlayer coupling $J^{inter}_{\mathbf{0}}$ overcompensates the effective anisotropy field. This occurs for

$$K_{2,\mathrm{e}ff}(T) = 4\langle S^z\rangle J^{inter}_{\mathbf{0}}(T) \tag{7.52}$$

which is consistent with the stability criterion (7.43) for the parallel alignment of a bilayer. Similarly, for $N_{\mathrm{L}} > 1$, in the uniform-magnetization limit ($\langle S^z_{\alpha}\rangle \equiv \langle S^z\rangle$) and for vanishing external field, the spin wave gap is given by (7.45) in the AFM-aligned case, too. The degeneracy of the spin wave spectrum is lifted if an external

---

[2] The expectation value $\langle S^z\rangle > 0$ refers to the magnetic layer with $\theta = 0$.

field is switched on. The stability of the antiparallel configuration is reduced and one finds that it is unstable if

$$J_{\mathrm{I}EC}(T) > K_{2,\mathrm{e}ff}(T) - \frac{B^2}{K_{2,\mathrm{e}ff}(T)}\,. \tag{7.53}$$

7.3.3 Temperature-dependent magnetic stability of IEC

In order to facilitate the discussion of the numerical results, the focus is at first on the temperature dependence of $J^{el}_{IEC}(T)$ defined in (7.46). The full interlayer coupling $J_{\mathrm{I}EC}(T)$ including the temperature dependence due to magnon excitations modifies $J^{el}_{\mathrm{I}EC}(T)$ by an additional factor which is essentially proportional to the average magnetization. The magnetic stability of a given configuration is the result of the competition between $J_{\mathrm{I}EC}(T)$, the temperature-dependent effective anisotropy field $K_{2,\mathrm{e}ff}(T)$, and the external magnetic field.

All calculations based on (7.39) and (7.40) were carried out with enforced charge neutrality using the intra-atomic coupling $J = 0.1$, the spin $S = 3.5$, the anisotropy $K_2 = 10^{-6}$ in both ferromagnetic layers, and the uniform hopping $t = 1/12$. The effective coupling ratio $JS/W_{\mathrm{b}ulk} = 0.35$ for the considered one-band model lies in the weak-to-intermediate regime, thus referring to Gd. The shorthand notation $(N_{\mathrm{L}}^{\mathrm{m}ag}/N_{\mathrm{L}}^{spac}/N_{\mathrm{L}}^{\mathrm{m}ag})$ is used to denote the type of exchange-coupled layered system, for example a (2/3/2)-film means that two magnetic monolayers are separated by three spacer monolayers. Note that the total number of magnetic monolayers in the film is $2N_{\mathrm{L}}^{\mathrm{m}ag}$.

Chap. 7.2 treated the dependence of the IEC on the Fermi energy. It is already known from the bulk that this dependence is crucially determined by properties of the uncorrelated spacer electrons and can be rather well described by the conventional RKKY theory. The situation is different regarding the temperature dependence of the IEC. Here, the thermal variation of the exchange splitting is expected to influence the coupling, and the modified RKKY treatment is the more adequate description.

Using the conventional RKKY-IEC with unpolarized conduction electrons, the T-dependence is caused by the Fermi edge softening only. Fig. 7.15 compares this effect and the influence of the temperature- and spin-dependent band structure. The calculations of $J^{el}_{\mathrm{I}EC}$ were carried out with and without Fermi softening. The latter was achieved by using the T=0-Fermi function for the evaluation of the exchange integrals (5.19) while keeping the full temperature dependence of the spin-dependent electronic self-energy. Fig. 7.16 shows the LDOS of the magnetic layers and of the non-magnetic spacer layers. For the carrier density $n = 0.11$ (FM-alignment), the Fermi energy lies in the same electronic subband as for $n = 0.12$

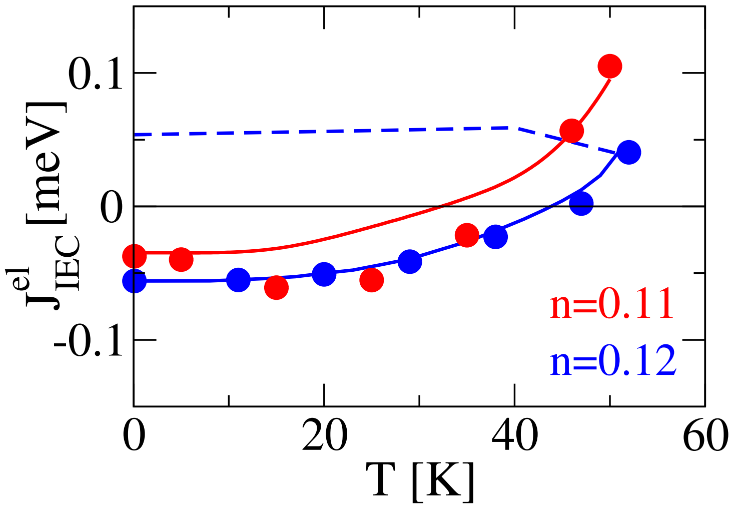

Figure 7.15: Temperature dependence of J^{el}_{IEC} for two magnetic monolayers separated by a 2ML-spacer. The full lines indicate the parallel and the dashed line the antiparallel alignment of the magnetic layers. Dots denote the results of calculations in which the Fermi softening was 'switched off' (see text).

but very close to the subband edges of the LDOS (arrows).

Apparently, a subband edge in the vicinity of the Fermi energy has a marked influence on the temperature dependence. This indicates RKKY-like behavior according to which the IEC between the two surface layers of a slab varies strongly if the Fermi energy crosses such an edge (Chap. 7.2.2). Likewise, the rather flat behavior of $J^{el}_{\mathrm{IEC}}(T)$ in the AFM-coupled film corresponds to a smooth variation of the LDOS. Fig. 7.15 demonstrates that the temperature dependence of the interlayer coupling is largely due to the thermal variation of the exchange-split band structure. The Fermi softening leads to moderate quantitative modifications if the Fermi energy lies very close to a band edge ($n = 0.11$).

The main results of this section are summarized in Fig. 7.17 which shows $J^{el}_{\mathrm{IEC}}(T)$ up to the Curie temperature for an enforced parallel and antiparallel alignment of the magnetic layers. Note once more that this quantity describes the summed interlayer exchange integrals and does not yield immediately the actual configuration. According to (7.49), the magnetic stability of the latter is determined by the competition between J^{el}_{IEC} multiplied by the magnetization on the one hand and the effective anisotropy and the external field on the other. The interplay of these quantities is discussed in more detail in the last part of this section. In the following discussion, the term 'interlayer coupling' refers to J^{el}_{IEC}.

The magnetic and spacer layers consist each of up to four monolayers in Fig. 7.17. The range of charge carrier densities is limited by the instability of the

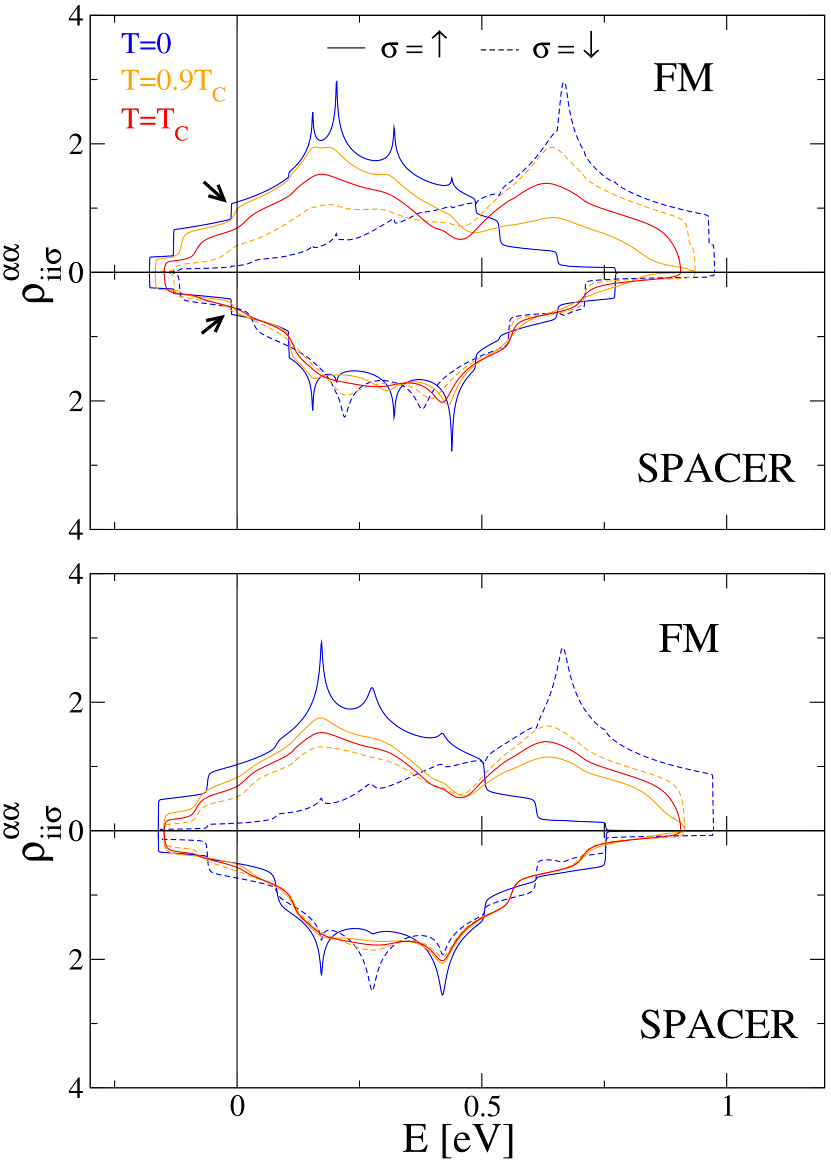

Figure 7.16: LDOS of a 4ML-film consisting of two magnetic monolayers separated by a 2ML-spacer. Top graph: parallel alignment of the magnetic layers, bottom graph: antiparallel alignment. The upper panels show the LDOS of the ferromagnetic monolayers, the lower panels the LDOS of the spacer monolayers. In the AFM configuration, the ↑-LDOS and the ↓-LDOS are interchanged for $\alpha = 3$ and 4 compared to $\alpha = 2$ and 1, respectively. The Curie temperature is 51 K. Parameters: $n = 0.12$, $J = 0.1$, $S = 7/2$.

ferromagnetism with respect to antiferromagnetic correlations *within* the FM layers above a critical density (cf. Chap. 6.3).

As expected the interlayer coupling depends sensitively on variations of the charge carrier density and on the spacer and the magnetic layer thickness. All these quantities are closely connected with the Fermi 'surface' of the system. Whereas the band filling modifies quantitatively but not qualitatively the temperature dependence, there are systematic trends of the thermal variation when changing the spacer and magnetic layer thickness, respectively. In most cases, the interlayer coupling looks similar and in particular $J^{el}_{\mathrm{I}EC}(T)$ has the same sign for the parallel and for the antiparallel configuration. However, there are also important differences. The parallel alignment of the magnetic layers shall be considered first.

With an increasing number of spacer monolayers, the coupling is damped and exhibits an oscillation period of approximately two lattice constants, $\lambda \approx 2a$. This periodic behavior is essentially maintained over the whole temperature range up to T_{C} for most band fillings: the qualitative features of the T-dependent variation are more or less unchanged for a given N_{L}^{mag} when varying N_{L}^{spac}. The oscillation period agrees with that obtained from the continuous IEC for the free electron gas (7.35). Using the relation between the Fermi wave vector and the number of charge carriers per lattice site, $k_{\mathrm{F}}a = (3\pi^2 n)^{1/3}$, a band filling $n = 0.12$ leads to the oscillatory behavior of the interlayer coupling as a function of the spacer thickness as shown in Fig. 7.18. The observed period $\lambda \approx 2a$ is practically independent of the spacer width. The results in Fig. (7.17) show that the RKKY-like periodic dependence of the IEC on the spacer thickness is rather insensitive to the thermal variation of the band structure for all temperatures up to T_{C}. It is furthermore not modified by confinement effects due to the finite thickness of the films.

For increasing magnetic layer thickness, quite a different behavior is observed. One notes a drastic influence on the temperature dependence of the interlayer coupling. For $N_{\mathrm{L}}^{mag} = 2$ a temperature-induced change of sign of $J^{el}_{\mathrm{I}EC}(T)$ becomes a common feature irrespective of the spacer width. Increasing the magnetic layer thickness further leads to a reduced thermal variation. The 'flattening' of the interlayer coupling as a function of temperature with increasing magnetic layer thickness is shown in more detail for a fixed spacer width in Fig. 7.19.

As concerns the variation of $J^{el}_{\mathrm{I}EC}(T)$ with the number of spacer monolayers in the antiparallel configuration, an approximate period of $2a$ is observed just like for the parallel alignment. Compared to the latter, the influence of the magnetic layer thickness is very different. Varying the number of magnetic monolayers has a much smaller effect on the coupling than in the parallel configuration: the thermal variation of $J^{el}_{IEC}(T)$ remains moderate and the tendency to a change of sign is less pronounced. The difference to the FM-aligned case is particularly manifest for $N_{\mathrm{L}}^{mag} = 2$ and becomes smaller for increasing magnetic and spacer layer thickness.

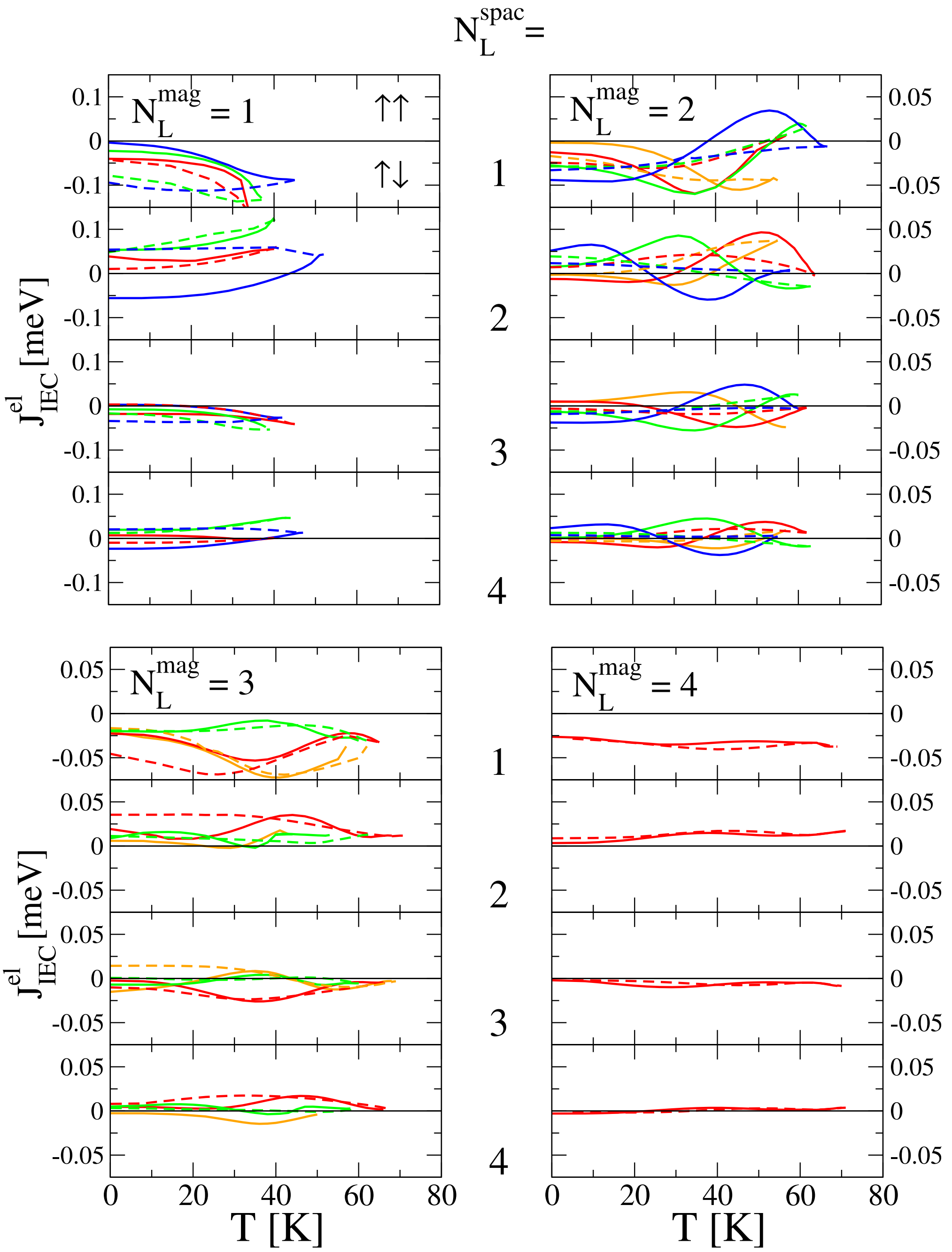

Figure 7.17: Temperature dependence of the summed interlayer exchange integrals $J^{el}_{IEC}(T)$ between two magnetic layers each consisting of N_L^{mag} monolayers and separated by a spacer layer with N_L^{spac} monolayers. Orange lines $n = 0.06$, red $n = 0.08$, green $n = 0.1$, blue $n = 0.12$. Full lines correspond to an enforced parallel alignment of the magnetic layers in the calculations, dashed lines to an enforced antiparallel alignment. Parameters: $J = 0.1$, $t = 1/12$, $S = 7/2$.

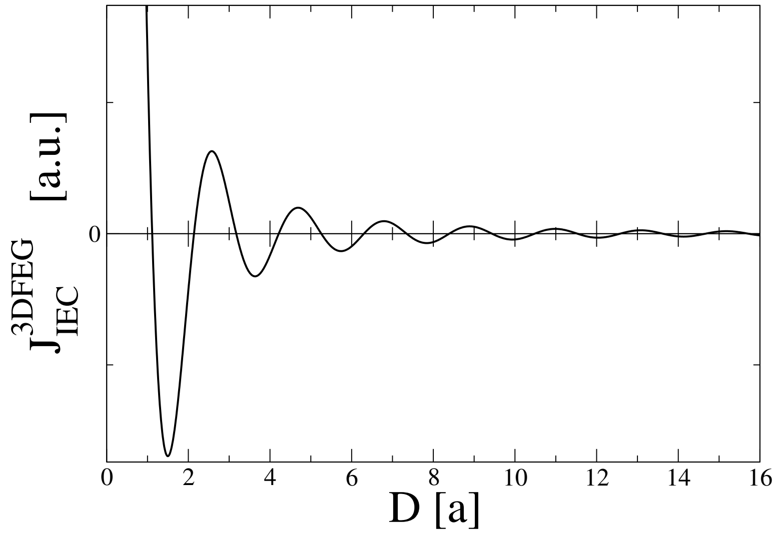

Figure 7.18: Interlayer exchange coupling as a function of the spacer thickness obtained by the RKKY theory for a 3D free electron gas (7.35) for $n = 0.12$.

Fig. 7.19 illustrates how the differing temperature dependences for the parallel and the antiparallel alignment are related to the coupling between single pairs of film planes. The thermal variation of the interlayer coupling between the pairs of monolayers is comparable for both configurations. However, whereas for the parallel configuration the coupling contributions add up constructively, they partly cancel for the antiparallel configuration to yield a rather smooth total interlayer coupling.

The findings for the influence of the magnetic layer thickness on the interlayer coupling can be compared with the asymptotic predictions of the quantum interference approach (Chap. 7.1.2). According to Eq. (7.9), the thickness enters via an oscillatory term which is algebraically damped with increasing magnetic layer thickness L. This is in agreement with the results in Figs. 7.17 and 7.19. Describing the temperature dependence effectively by a T-dependent minority spin Fermi wave vector $k_{\mathrm{F}}^{\downarrow}$ in (7.9), one obtains an oscillatory thermal variation of the IEC. This dependence, however, refers to the definition of the IEC as an energy difference between the parallel and the antiparallel configuration (Eq. (7.1)). In the present treatment, the interlayer coupling $J_{\mathrm{IEC}}^{el}(T)$ *itself* is in general different for the parallel and for the antiparallel alignment of the magnetic layers. The above results demonstrate that the oscillatory dependence on temperature mainly occurs for the *parallel* alignment of the magnetic layers. For small but finite magnetic layer thickness ($N_{\mathrm{L}}^{\mathrm{m}ag} > 1$), the amplitude of these thermal oscillations is most favorable for a change of sign of $J_{\mathrm{IEC}}^{el}(T)$.

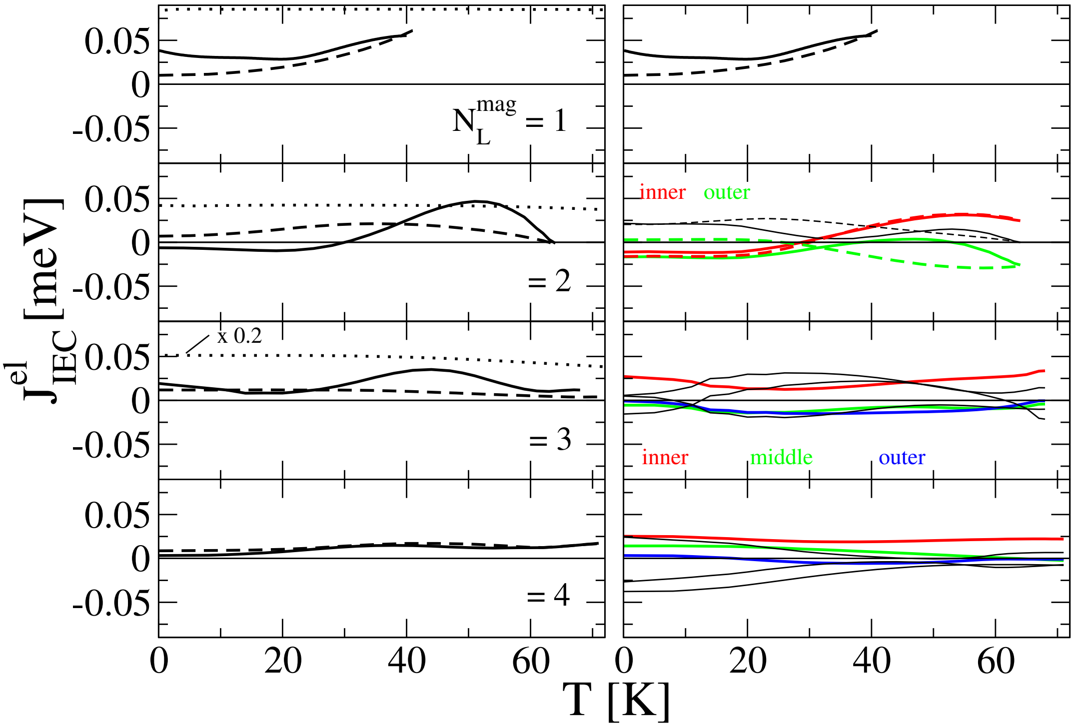

Figure 7.19: Temperature dependence of the summed interlayer exchange integrals for different magnetic layer thickness as indicated. Left: total coupling, right: coupling between the single pairs of monolayers. Full lines for the parallel, dashed lines for the antiparallel configuration. The dotted lines shows the interlayer coupling according to the conventional RKKY-IEC theory. Coloured lines designate symmetric pairs of coupled monolayers: red lines for the two innermost monolayers, green lines for the second and blue lines for the third innermost monolayers. Black lines: non-symmetric pairs of monolayers. Parameters: $N_L^{spac} = 2$, $n = 0.08$.

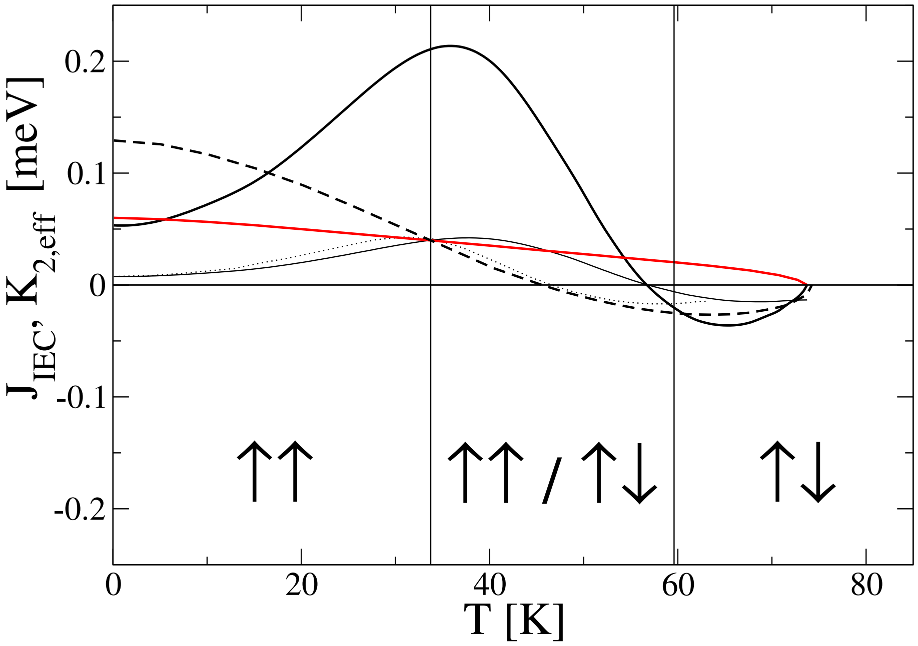

Figure 7.20: Magnetic stability of two ferromagnetic bilayers separated by a non-metallic spacer bilayer. Thick black line: $J_{IEC}(T)$ for the parallel alignment of the magnetic layers. Dashed line: $J_{IEC}(T)$ for the antiparallel alignment. Thin black line: $J^{el}_{\mathrm{IEC}}(T)$ for parallel alignment. The dotted line is $J^{el}_{\mathrm{IEC}}(T)$ in the parallel configuration for a single-ion anisotropy $K_2 = 1\,\mu\mathrm{e}V$ as used in Fig. (7.17). The red line is the effective anisotropy field for the parallel configuration; on the above scale its absolute value is practically identical to that of the antiparallel configuration. The vertical lines indicate the stability boundaries for the FM-aligned and the AFM-aligned configuration. Other parameters: $N^{\mathrm{mag}}_{\mathrm{L}} = 2$, $N^{spac}_{\mathrm{L}} = 2$, $n = 0.1$, $J = 0.1\,\mathrm{e}V$, $K_2 = 10\,\mu\mathrm{e}V$, $B = 0$.

7.3.4 Temperature-induced reorientation transition

The possible magnetic configurations are determined by the interplay between the interlayer exchange integrals, the effective anisotropy, and the external field. For large anisotropies compared to the interlayer exchange ($K_2 \gg J^{el}_{\mathrm{IE}C}$), both a parallel and an antiparallel alignment of the magnetic layers are magnetically stable configurations. In the opposite limit ($K_2 \ll J^{el}_{\mathrm{IE}C}$), the magnetic stability is governed by the thermal variation of $J^{el}_{\mathrm{IE}C}(T)$ shown in Fig. 7.17.

The following discussion considers the intermediate case $K_2 \approx J^{el}_{\mathrm{IE}C} \sim 10^{-5}\,\mathrm{e}V$. This anisotropy constant corresponds to a magnetic anisotropy energy of $\sim 10^{-4}\,\mathrm{e}V$ per atom. A total anisotropy energy of this order of magnitude was measured at low temperatures in ultrathin W/Gd/W and Y/Gd/Y films [52, 53].

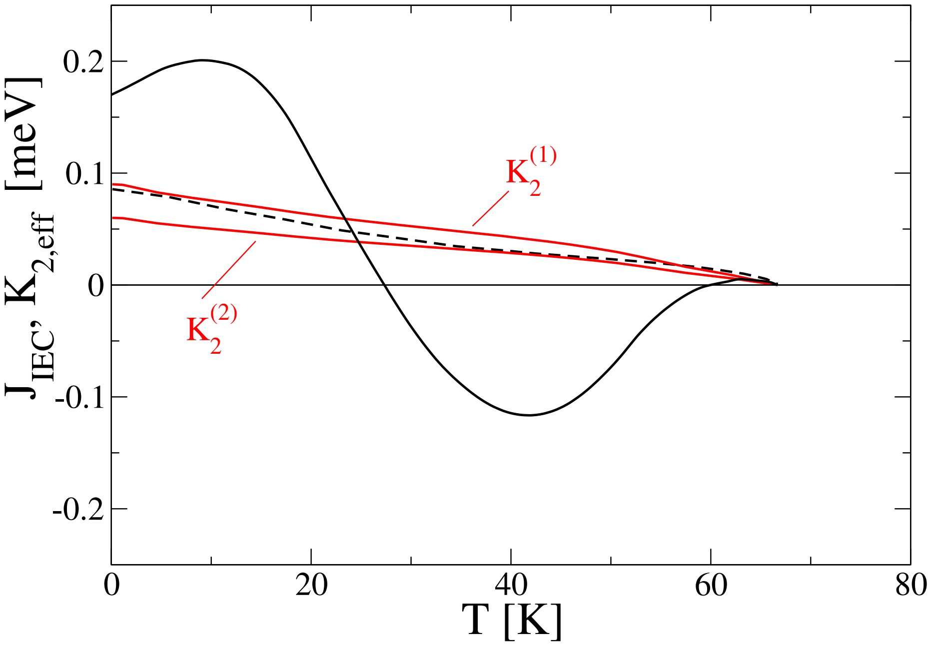

Figure 7.21: Same as Fig. 7.20, but for $K_2^{(1)} = 15\,\mu eV$, $K_2^{(2)} = 10\,\mu eV$ and charge carrier density $n = 0.12$.

Among the various film configurations presented in Fig. 7.17, the case of two coupled bilayers ($N_{\mathrm{L}}^{\mathrm{mag}} = 2$) exhibits the highest thermal fluctuations of the interlayer coupling. The tendency to other than ferromagnetic configurations of the magnetic layers themselves is highest here as can be inferred from the large temperature regions where no self-consistent solution exists neither for the parallel nor for the antiparallel alignment. Fig. 7.20 shows the interlayer coupling and the effective anisotropy for a (2/2/2)-film with a magnetically stable parallel and/or antiparallel configuration over the whole temperature range up to T_{C}. The full interlayer coupling $J_{\mathrm{I}EC}(T)$ given by (7.45) is compared with $K_{2,eff}(T)$ $(B = 0)$. Although the anisotropy strength has been chosen an order of magnitude larger than in Fig. (7.17), there is no significant change in the T-dependence of the interlayer coupling apart from a scaling on the T-axis due to the increased Curie temperature. $J_{\mathrm{I}EC}(T)$ is larger than $J_{\mathrm{I}EC}^{el}(T)$ except for temperatures near T_{C} where the former vanishes. This results from the prefactor in (7.48) which includes the magnetization. The effective anisotropy field decreases monotonically from its T=0-value $(2S-1)K_2$ to zero at T_{C}.

The parallel configuration is the only stable one from $T = 0$ up to $T \approx 0.5T_{\mathrm{C}}$. In this region the interlayer exchange for the antiparallel configuration is strongly ferromagnetic ($J_{\mathrm{I}EC}^{\uparrow\downarrow} > K_{2,eff}$). For higher temperatures, there is a region where both FM and AFM alignment of the layers are possible. Here, the question about the *thermodynamically* stable state would have to be answered by evaluating the free energy of the two *magnetically* stable states. On increasing the temperature further, the parallel orientation becomes unstable and the magnetic layers can only couple antiparallel. Hence Fig. 7.20 shows a temperature-driven reorientation transition from ferromagnetic IEC to antiferromagnetic IEC.

Fig. 7.21 illustrates the important role of the magnetic anisotropy in connection with the weak T-dependence of the interlayer coupling in the antiparallel configuration. The film parameters are the same as in Fig. 7.20 but the carrier density is increased with the consequence that the difference in the T-dependences of $J^{el}_{\mathrm{IE}C}(T)$ for the parallel and for the antiparallel alignment is even more pronounced. Two different values of the single-ion anisotropy are considered. Whereas the decrease from $K_2^{(1)}$ to $K_2^{(2)}$ shifts the magnetically stable region for parallel alignment at $\approx 0.5T_{\mathrm{C}}$ only slightly to a lower temperature, the effect on the antiparallel configuration is much more drastic. For $K_2^{(1)}$ the AFM-state is in concurrence with the FM-alignment at low temperatures and is the only stable state over a large T-range above $\approx 0.5T_{\mathrm{C}}$. On the contrary, for the smaller anisotropy strength $K_2^{(2)}$, the antiparallel configuration is magnetically unstable over the entire temperature range. According to (7.53) a similar effect is obtained by switching on an external field.

Chapter 8

Summary and Outlook

This work treated ferromagnetism and interlayer exchange coupling in thin metallic films described by the Kondo lattice. The Kondo lattice (s-d, s-f) model is the standard model to study many-particle systems in which localized spins are coupled to the spin of mobile charge carriers. It is often employed in the context of (dilute) magnetic semiconductors, manganites, and rare-earths like Gd. Materials that are characterized by such a spin-fermion interaction are considered as promising candidates for the combined manipulation of the charge and spin degrees of freedom in a solid ('spintronics').

The two-dimensional monolayer deviates from the bulk crystal in several respects. In the single-electron excitation spectrum, the reduced coordination number leads to a band narrowing. As regards the magnetism, the Mermin-Wagner theorem which excludes long-range order for isotropic interactions demonstrates the fundamental importance of spin fluctuations and of anisotropies in low-dimensional systems. A film of finite thickness raises interesting questions concerning the behavior of various quantities in the intermediate configuration between the 2D- and the 3D-crystal lattice. Besides strongly influencing the Curie temperature, the reduced translational symmetry leads to a layer-dependence of observables like the spontaneous magnetization or the charge carrier density which becomes particularly pronounced near the film surface. Likewise, the interlayer exchange coupling between thin ferromagnetic layers in a confined environment depends sensitively on geometric parameters.

Methodologically, the coupled spin-fermion problem of the Kondo lattice was treated using a combined approach. The electronic self-energy, giving access to the one-electron properties, was obtained by an equation-of-motion method based on a physically motivated decoupling scheme. In order to calculate the ferromagnetism self-consistently, the fermionic degrees of freedom in the interaction were integrated out. The resulting effective Heisenberg model describes a modified Ruderman-Kittel-Kasuya-Yosida (RKKY) interaction among the localized spins.

Going beyond the conventional, perturbational RKKY interaction, the effective exchange integrals of the modified version depend on the spin- and temperature-dependent electronic structure and, in particular, on the charge carrier density. In the strong-coupling limit, the modified RKKY approximation was shown to exhibit typical double-exchange features like the strongly reduced interaction range, the saturation with the intra-atomic coupling strength J, and the proportionality to the kinetic energy.

The Curie temperatures obtained with the modified RKKY approach show clear differences to the conventional case even for moderate coupling strength. Depending on the band filling, no ferromagnetism was found up to a critical interaction from the monolayer to the bulk. In the double-exchange regime, the qualitative dependence of T_{C} on J, on the charge carrier density, and on the film thickness can be understood in terms of the kinetic energy of the itinerant charge carriers. The latter decreases if the film thickness is increased and thereby the Curie temperature is enhanced. This carrier-induced increase is proportional to the effective coordination number and comes in addition to the usual proportionality of T_{C} to the average number of interaction parameters in a local-moment ferromagnet. The rapid carrier-induced decrease of the transition temperature in the critical interaction region leads to another interesting effect concerning the thickness-dependence of the Curie temperature. Here, contrary to the conventional dependence, a *decrease* of T_{C} with increasing thickness is observed for an appropriate J. This reverse behavior is due to the reduced bandwidth of ultrathin films and the associated greater influence of strong-coupling physics compared to the bulk.

The effective exchange integrals near the film surface deviate from their bulk values. For strong intra-atomic coupling, where the exchange interaction is determined by the non-local density of states, the modifications have the same origin as the charge transfer being related to the local DOS, namely the band narrowing and the (Friedel-)oscillatory features in the DOS. The type of modification depends on the lattice structure, on the film surface geometry, and on the band filling. For low carrier density, charge transfer out of the surface layer and the reduction of the effective exchange at the surface are most pronounced. This can result in a drastic suppression of the top layer magnetization. The importance of spin wave excitations for the surface ferromagnetism was demonstrated in connection with a modified hopping at the surface. Here, a strong *reduction* of the surface and subsurface magnetization at low temperatures was found as a consequence of an *increased* surface-to-subsurface interlayer hopping in the intermediate-coupling regime. Although specifically related to the simple-cubic(100) geometry, this is an interesting effect which might also play a role in more realistic scenarios. Regarding a possible magnetic surface transition above the bulk ordering temperature, discussed extensively in the past for the Gd(0001)-surface, spin wave excitations were also shown to play a decisive role. A simple model study of the layer-dependent magnetization using an effective (Tyablikov) spin wave theory showed no indications that an enhanced magnetic stiffness at the surface may lead to a separate transition temperature. This is in sharp contrast to the commonly used mean-field treatment.

The phenomenon of interlayer exchange coupling (IEC) between two ferromagnetic layers through a non-magnetic spacer is of high interest since the relative orientation of the layer magnetizations influences the electrical transport properties. In this thesis, the IEC was studied in thin metallic Kondo lattice films focussing on two aspects. The conventional RKKY theory of IEC on a lattice was evaluated for the coupling between confined monolayers, concentrating on the dependence on the charge carrier density. The interlayer coupling was discussed in terms of the electronic structure of a bilayer. The main result here is a magnetic decoupling above a critical value of the Fermi energy. If the in-plane dispersion of the charge carriers is described by the effective-mass approximation, the IEC vanishes completely. If the full lattice structure is considered it is strongly damped for not too large interlayer hopping, irrespective of a possible **k**-dependence of the latter. For larger film thickness, it also vanishes above a critical value of the Fermi energy. The comparison with the 3D RKKY-IEC for a free electron gas revealed that confinement effects do not change the qualitative behavior observed in the bulk but rather affect the amplitude and the smoothness of the oscillations with the Fermi energy. In the bulk limit, the different behavior of the IEC for a tight-binding in-plane dispersion on the one hand and for a free-electron-like dispersion on the other can be traced back to the different shapes of the Fermi surface. The tight-binding dispersion perpendicular to the film plane yields a critical spanning vector, associated with a finite IEC, up to a Fermi energy for which necks at the perpendicular boundaries of the Fermi surface emerge. Only if other critical vectors show up, like at the in-plane boundaries in the isotropic tight-binding case, the interlayer coupling remains finite. The strong damping of the IEC for the tight-binding Bloch bilayer with anisotropic hopping represents the corresponding behavior in ultrathin films.

The temperature-dependent magnetic stability of the interlayer exchange coupling was studied using the modified RKKY approach. A criterion for the existence of the parallel and the antiparallel alignment of two ferromagnetic layers with uniaxial anisotropy was derived. The different electronic structures in the two cases imply different interlayer exchange integrals and thus the possibility of one, two, or no stable magnetic solution at all. The magnetic layer thickness influences the interlayer exchange markedly. An important result here is that the thermal variation of the coupling is more pronounced for the parallel alignment of the magnetic layers. For small but finite thickness, the IEC oscillates with temperature and may change its sign. This behavior is robust with respect to the spacer thickness and the charge carrier density. A conventional RKKY-like oscillatory dependence on the spacer thickness was obtained like in the bulk. This property essentially holds for all temperatures up to T_C. Finally, a scenario for a temperature-induced reorientation transition in ultrathin metallic local-moment films was discussed. Apart from the magnetic layer thickness, the magnetic anisotropy is the most important quantity here.

Several extensions and improvements to the present work can be immediately suggested. The discussion of thin films and surfaces is almost exclusively restricted to the simple-cubic(100) geometry, sacrificing a broader range of quantitative results for a focus on the effects related to film geometry in general. For a deeper and broader understanding, to support, disprove, or generalize the results and suggestions presented in this thesis, it is certainly desirable to study other film geometries. Antiferromagnetic phases may be considered which are particularly expected in the RKKY limit. The multi-orbital structure of any real material should be taken into account. Including configurational or Coulomb disorder would represent an important extension. Finally, one can expect interesting contributions to the discussion about Gd(0001)-surface states from the combination of many-body theory with DFT-LDA band structure calculations for real materials like Gd.

Regarding the interlayer exchange coupling, one might speculate about the possible experimental relevance of the findings presented in this work for real nanostructures. Generally, the suppression of the RKKY interlayer coupling is most pronounced in thin films which are only weakly hybridized and for which the tight-binding interlayer hopping yields an adequate description in the first place. Furthermore, the charge carrier density should be low so that the in-plane effective-mass approximation is valid. For a more realistic description, however, the conventional RKKY approach must certainly be improved. Above all, this concerns the simple, single-orbital electronic structure used in this work. A phenomenological damping of the interaction could be introduced. The inclusion of typical interfacial disorder effects due to dislocations or interdiffusion would also be a relevant extension. Referring to a possible experimental context, the IEC between layers down to monatomic thickness in a confined environment may be investigated for δ-doped Mn-layers in quantum wells.

The investigation of the temperature-dependent interlayer coupling in this thesis concentrated on the magnetic rather than on the thermodynamic stability. The latter would have to be determined by an evaluation of the free energy if more than one configuration is magnetically stable. Furthermore, the assumption of enforced charge neutrality may not always apply. The consequences of relaxing this boundary condition should be studied in order to improve the results towards more realistic scenarios. It would also be worthwhile exploring the temperature regions with no self-consistent solution in the parallel or in the antiparallel configuration. Antiferromagnetic intralayer order or phase-separation between FM- and AFM-coupled islands may be considered. The role of asymmetry with respect to the thickness of the magnetic layers, to the intra-atomic exchange interaction, or to the anisotropy strength is another relevant point. For anisotropies favoring different easy directions of the magnetization, canted configurations have to be considered. The model may finally be supplemented with a shape anisotropy term and/or with higher-order anisotropy or exchange terms. These would further increase the number of possible magnetic configurations.

The dependence of the interlayer exchange integrals on the magnetic configuration has implications for ferromagnetic resonance measurements. The evaluation of experimental FMR-data is usually based on the macroscopic Landau-Lifshitz equations including an appropriate expansion of the free energy. The contribution of the interlayer coupling is accounted for by an additional term with a phenomenological parameter which essentially corresponds to the quantity $J^{el}_{\mathrm{IEC}}(T)$, but which is assumed to be the same for the parallel and for the antiparallel configuration. In an experiment, the parallel alignment of the magnetic layers is enforced by an external field. The latter is needed to adjust the resonant excitation of uniform spin wave modes. Hence, the measured temperature dependence of the IEC refers to the parallel configuration and may be quite different from that in zero external field if the system is actually in another, e.g. in the AFM-coupled state.

The considerations on the interplay between interlayer exchange coupling, magnetic anisotropy, and external field in connection with a temperature-driven magnetic reorientation transition may be relevant for ultrathin IEC-systems composed of Gd/W or Gd/Y. These films can be prepared with a thickness of a few monolayers, and the measured magnetic anisotropy energy lies in an appropriate range according to the model calculations in this work.

Appendix A

MCDA electronic self-energy

The non-diagonal terms ($i \neq k$ or $\alpha \neq \delta$) of the higher-order Green functions in (4.16) and (4.17) are considered first.

The spectral representation of the two Green functions in the definition of the self-energy

$$\langle\langle [c_{k\delta\sigma}, H_I]_- \, ; c^\dagger_{j\beta\sigma} \rangle\rangle_E = \sum_{l\gamma} M^{\delta\gamma}_{kl\sigma}(E) \langle\langle c_{l\gamma\sigma}; c^\dagger_{j\beta\sigma} \rangle\rangle_E \tag{A.1}$$

reveals that they have the same one-particle pole structure, i.e. the self-energy ensures the correct distribution of spectral weight. The two higher Green functions

$$\langle\langle \delta S^z_{i\alpha} \, [c_{k\delta\sigma}, H_I]_- \, ; c^\dagger_{j\beta\sigma} \rangle\rangle_E, \quad \langle\langle S^{-\sigma}_{i\alpha} \, [c_{k\delta-\sigma}, H_I]_- \, ; c^\dagger_{j\beta\sigma} \rangle\rangle_E \tag{A.2}$$

in (4.16) and (4.17) differ from the GF on the LHS of (A.1) in that the additional spin operator selects a subset of the poles of this GF. This holds also for the GF on the RHS of (A.1) if the same spin operator is added there. One may therefore approximate (A.2) as

$$\langle\langle \delta S^z_{i\alpha} \, [c_{k\delta\sigma}, H_I]_- \, ; c^\dagger_{j\beta\sigma} \rangle\rangle_E \approx \sum_{l\gamma} M^{\delta\gamma}_{kl\sigma}(E) \langle\langle \delta S^z_{i\alpha} c_{l\gamma\sigma}; c^\dagger_{j\beta\sigma} \rangle\rangle_E \, , \tag{A.3}$$

$$\langle\langle S^{-\sigma}_{i\alpha} \, [c_{k\delta-\sigma}, H_I]_- \, ; c^\dagger_{j\beta\sigma} \rangle\rangle_E \approx \sum_{l\gamma} M^{\delta\gamma}_{kl-\sigma}(E) \langle\langle S^{-\sigma}_{i\alpha} c_{l\gamma-\sigma}; c^\dagger_{j\beta\sigma} \rangle\rangle_E \, , \tag{A.4}$$

assuming that the correct distribution of spectral weight occurs in a similar fashion as in the exact relation (A.1).

For the non-diagonal Green functions

$$\langle\langle [\delta S^z_{i\alpha}, H_I]_- \, c_{k\delta\sigma}; c^\dagger_{j\beta\sigma} \rangle\rangle_E \, , \tag{A.5}$$

$$\langle\langle \left[S^{-\sigma}_{i\alpha}, H_I \right]_- \, c_{k\delta-\sigma}; c^\dagger_{j\beta\sigma} \rangle\rangle_E \tag{A.6}$$

the commutators are evaluated using the effective Heisenberg Hamiltonian (5.18). One obtains

$$\left[\delta S^z_{i\alpha}, H^{\mathrm{MRKKY}}_{eff}\right]_- = \sum_{l\gamma} J^{\alpha\gamma}_{il}(S^+_{i\alpha}S^-_{l\gamma} - S^-_{i\alpha}S^+_{l\gamma})\,, \tag{A.7}$$

$$\left[S^{-\sigma}_{i\alpha}, H^{\mathrm{MRKKY}}_{eff}\right]_- = 2z_\sigma \sum_{l\gamma} J^{\alpha\gamma}_{il}(S^z_{l\gamma}S^{-\sigma}_{i\alpha} - S^z_{i\alpha}S^{-\sigma}_{l\gamma})\,. \tag{A.8}$$

The Green functions (A.5) and (A.6) could be decoupled in a further approximation by replacing the spin operators by their thermal expectation values. However, it follows from (A.7) and (A.8) that these terms are of the order of spin wave energies. As the latter are usually much smaller (typically by a factor of $\sim 10^{-3}$) than the bandwidth W and the intra-atomic exchange J, the Green functions (A.5) and (A.6) can be safely neglected.

The diagonal terms ($i = k$ and $\alpha = \delta$) in (4.16) and (4.17) must be treated more carefully in order to take into account the local correlations. Higher Green function are approximated by lower Green functions exploiting exactly solvable limits and spectral-moment relations.

The commutators in (4.16) and (4.17) yield the following Green functions:

$${}^{(1)}F^{\alpha\beta}_{iij\sigma}(E) = \langle\langle S^{-\sigma}_{i\alpha}S^z_{i\alpha}c_{i\alpha-\sigma}; c^\dagger_{j\beta\sigma}\rangle\rangle_E\,, \tag{A.9}$$

$${}^{(2)}F^{\alpha\beta}_{iij\sigma}(E) = \langle\langle S^{-\sigma}_{i\alpha}S^\sigma_{i\alpha}c_{i\alpha\sigma}; c^\dagger_{j\beta\sigma}\rangle\rangle_E\,, \tag{A.10}$$

$${}^{(3)}F^{\alpha\beta}_{iij\sigma}(E) = \langle\langle S^{-\sigma}_{i\alpha}n_{i\alpha\sigma}c_{i\alpha-\sigma}; c^\dagger_{j\beta\sigma}\rangle\rangle_E\,, \tag{A.11}$$

$${}^{(4)}F^{\alpha\beta}_{iij\sigma}(E) = \langle\langle S^z_{i\alpha}n_{i\alpha\sigma}c_{i\alpha\sigma}; c^\dagger_{j\beta\sigma}\rangle\rangle_E\,. \tag{A.12}$$

In order to motivate ansatzes for approximating (A.9)-(A.12) several exact relations are considered which follow from the spectral representation (2.17):

1. Ferromagnetic saturation ($T = 0$, $\langle S^z_\alpha\rangle = S$):

$${}^{(1)}F^{\alpha\beta}_{iij\sigma}(E) = \left(\left(S - \frac{1}{2}\right) + \frac{1}{2}z_\sigma\right) F^{\alpha\beta}_{iij\sigma}(E) \tag{A.13}$$

$${}^{(2)}F^{\alpha\beta}_{iij\sigma}(E) = SG^{\alpha\beta}_{ij\sigma}(E) - z_\sigma I^{\alpha\beta}_{iij\sigma}(E) \tag{A.14}$$

2. $S = \frac{1}{2}$:

$${}^{(1)}F^{\alpha\beta}_{iij\sigma}(E) = \frac{1}{2}z_\sigma F^{\alpha\beta}_{iij\sigma}(E) \tag{A.15}$$

$${}^{(2)}F^{\alpha\beta}_{iij\sigma}(E) = \frac{1}{2}G^{\alpha\beta}_{ij\sigma}(E) - z_\sigma I^{\alpha\beta}_{iij\sigma}(E) \tag{A.16}$$

3. Full conduction band ($n = 2$):

$$^{(3)}F^{\alpha\beta}_{iij\sigma}(E) = F^{\alpha\beta}_{iij\sigma}(E) \tag{A.17}$$

$$^{(4)}F^{\alpha\beta}_{iij\sigma}(E) = I^{\alpha\beta}_{iij\sigma}(E) \tag{A.18}$$

These relations suggest the following ansatzes:

$$^{(1)}F^{\alpha\beta}_{iij\sigma}(E) = a^{\alpha}_{1\sigma}G^{\alpha\beta}_{ij\sigma}(E) + b^{\alpha}_{1\sigma}F^{\alpha\beta}_{iij\sigma}(E) \tag{A.19}$$

$$^{(2)}F^{\alpha\beta}_{iij\sigma}(E) = a^{\alpha}_{2\sigma}G^{\alpha\beta}_{ij\sigma}(E) + b^{\alpha}_{2\sigma}I^{\alpha\beta}_{iij\sigma}(E) \tag{A.20}$$

$$^{(3)}F^{\alpha\beta}_{iij\sigma}(E) = a^{\alpha}_{3\sigma}G^{\alpha\beta}_{ij\sigma}(E) + b^{\alpha}_{3\sigma}F^{\alpha\beta}_{iij\sigma}(E) \tag{A.21}$$

$$^{(4)}F^{\alpha\beta}_{iij\sigma}(E) = a^{\alpha}_{4\sigma}G^{\alpha\beta}_{ij\sigma}(E) + b^{\alpha}_{4\sigma}I^{\alpha\beta}_{iij\sigma}(E) \tag{A.22}$$

The coefficients $a^{\alpha}_{i\sigma}$, $b^{\alpha}_{i\sigma}$ are fixed by evaluating the first two spectral moments of the Green functions (see below).

With (A.3), (A.4) and (A.19)-(A.22), the equation of motion for the Ising and spinflip Green function reads

$$\begin{aligned}\sum_{l\gamma}\Big((E+\mu)\delta^{\delta\gamma}_{kl} + t^{\delta\gamma}_{kl} - M^{\delta\gamma}_{kl\pm\sigma}(E)\Big)X^{\alpha\gamma\beta}_{ilj\sigma}(E) &= -\delta^{\alpha\delta}_{ik}\sum_{l\gamma}M^{\delta\gamma}_{kl\pm\sigma}(E)X^{\alpha\gamma\beta}_{ilj\sigma}(E)\\ &\quad -\frac{1}{2}J\delta^{\alpha\delta}_{ik}\Big(A^{\alpha}_{X\sigma}G^{\alpha\beta}_{ij\sigma}(E) + B^{\alpha}_{X\sigma}I^{\alpha\beta}_{iij\sigma}(E) + C^{\alpha}_{X\sigma}F^{\alpha\beta}_{iij\sigma}(E)\Big)\,.\end{aligned} \tag{A.23}$$

$X = I$ and the plus sign in $M^{\delta\gamma}_{kl\pm\sigma}$ refer to the Ising Green function, $X = F$ and the minus sign in $M^{\delta\gamma}_{kl\pm\sigma}$ refer to the spinflip Green function. Together with the equation of motion for the one-electron Green function (4.12) one has a closed system of equations which can be solved after Fourier transformation using (3.2), (3.3), and (5.38). The neglect of magnon energies associated with (A.5) and (A.6) leads to a **k**-independent self-energy for the bulk crystal [184, 209]. Transferring this to film geometry one can therefore set

$$M^{\alpha\beta}_{ij\sigma} \rightarrow \delta_{\alpha\beta}\delta_{ij}M^{\alpha}_{\sigma}\,. \tag{A.24}$$

After Fourier transformation the equation of motion for the one-electron Green function yields the following relation between the self-energy and the Ising and spinflip Green functions:

$$\underline{M}_\sigma(E)\underline{G}_{\mathbf{k}\sigma}(E) = -\frac{1}{2}J\left[z_\sigma\langle\underline{S}^z\rangle\underline{G}_{\mathbf{k}\sigma}(E) + \frac{1}{\sqrt{N}}\sum_{\mathbf{q}} z_\sigma\underline{I}_{\mathbf{k}q\sigma}(E) + \underline{F}_{\mathbf{k}q\sigma}(E)\right]. \tag{A.25}$$

The matrix elements of the Ising and spinflip Green function are $\left[\underline{X}_{\mathbf{k}q\sigma}\right]_{\alpha\beta} \equiv X^{\alpha\alpha\beta}_{\mathbf{k}q\sigma}$ $(X = I,\, F)$. Combining (A.25) with (A.23) yields formula (4.18):

$$\underline{M}_\sigma(E) = -\frac{1}{2}Jz_\sigma\langle\underline{S}^z\rangle + \underline{M}^{\mathrm{c}}_\sigma(E, J)\,. \tag{A.26}$$

$\underline{M}^{\mathrm{c}}_\sigma$ is diagonal with the following elements:

$$\left[\underline{M}^{\mathrm{c}}_\sigma\right]_{\alpha\alpha}(E, J) = \frac{1}{4}J^2\frac{z_\sigma\hat{I}^\alpha_\sigma(E, J) + \hat{F}^\alpha_\sigma(E, J)}{N^\alpha_\sigma(E, J)}\,. \tag{A.27}$$

Explicitly one has:

$$\hat{I}^\alpha_\sigma(E, J) = A^\alpha_{I\sigma}\left[G^\alpha_{-\sigma}(E)\right]^{-1} + A^\alpha_{I\sigma}M^\alpha_{-\sigma}(E) + \frac{1}{2}JA^\alpha_{I\sigma}C^\alpha_{F\sigma} - \frac{1}{2}JC^\alpha_{I\sigma}A^\alpha_{F\sigma} \tag{A.28}$$

$$\hat{F}^\alpha_\sigma(E, J) = A^\alpha_{F\sigma}\left[G^\alpha_\sigma(E)\right]^{-1} + A^\alpha_{F\sigma}M^\alpha_\sigma(E) + \frac{1}{2}JA^\alpha_{F\sigma}B^\alpha_{I\sigma} - \frac{1}{2}JB^\alpha_{F\sigma}A^\alpha_{I\sigma} \tag{A.29}$$

$$N^\alpha_\sigma(E, J) = N^\alpha_{1\sigma}(E, J)N^\alpha_{2\sigma}(E, J) - \frac{1}{4}J^2B^\alpha_{F\sigma}C^\alpha_{I\sigma} \tag{A.30}$$

$$N^\alpha_{1\sigma}(E, J) = \left(\left[G^\alpha_{-\sigma}(E)\right]^{-1} + M^\alpha_{-\sigma}(E) + \frac{1}{2}JC^\alpha_{F\sigma}\right) \tag{A.31}$$

$$N^\alpha_{2\sigma}(E, J) = \left(\left[G^\alpha_\sigma(E)\right]^{-1} + M^\alpha_\sigma(E) + \frac{1}{2}JB^\alpha_{I\sigma}\right) \tag{A.32}$$

The local propagator reads

$$G^\alpha_\sigma(E) = \frac{1}{N}\sum_{\mathbf{k}}\left[\left\{(E+\mu)\underline{I} - \underline{\epsilon}(\mathbf{k}) - \underline{M}_\sigma(E)\right\}^{-1}\right]_{\alpha\alpha}\,. \tag{A.33}$$

The coefficients $A^\alpha_{X\sigma}$, $B^\alpha_{X\sigma}$, $C^\alpha_{X\sigma}$ in (A.23) and (A.28)-(A.32) are:

Ising Green function:

$$A^\alpha_{I\sigma} = z_\sigma\left[\langle(\delta S^z_\alpha)^2\rangle + \langle S^{-\sigma}_\alpha S^\sigma_\alpha\rangle\right] + a^\alpha_{1\sigma} - z_\sigma a^\alpha_{2\sigma} + z_\sigma a^\alpha_{3\sigma} - z_\sigma b^\alpha_{2\sigma}\langle S^z_\alpha\rangle \tag{A.34}$$

$$B^\alpha_{I\sigma} = -z_\sigma\langle S^z_\alpha\rangle - z_\sigma b^\alpha_{2\sigma} - 1 \tag{A.35}$$

$$C^\alpha_{I\sigma} = -z_\sigma - \langle S^z_\alpha\rangle + b^\alpha_{1\sigma} + z_\sigma b^\alpha_{3\sigma} \tag{A.36}$$

Spinflip Green function:

$$A^{\alpha}_{F\sigma} = -z_\sigma a^{\alpha}_{1\sigma} + a^{\alpha}_{2\sigma} + a^{\alpha}_{3\sigma} + 2z_\sigma a^{\alpha}_{4\sigma} + b^{\alpha}_{2\sigma}\langle S^z_\alpha\rangle + 2z_\sigma b^{\alpha}_{4\sigma}\langle S^z_\alpha\rangle \tag{A.37}$$

$$B^{\alpha}_{F\sigma} = b^{\alpha}_{2\sigma} + 2z_\sigma b^{\alpha}_{4\sigma} \tag{A.38}$$

$$C^{\alpha}_{F\sigma} = -z_\sigma b^{\alpha}_{1\sigma} + b^{\alpha}_{3\sigma} \tag{A.39}$$

The coefficients $a^{\alpha}_{i\sigma}$, $b^{\alpha}_{i\sigma}$ $(i = 1, .., 4)$ in (A.19)-(A.22) and (A.34)-(A.39) are obtained from the spectral moments of the Green functions in (A.19)-(A.22) using (2.36):

$$\begin{aligned}
a^{\alpha}_{1\sigma} &= 0\\
b^{\alpha}_{1\sigma} &= \frac{K^{\alpha}_{1\sigma} + 4\Delta_{\alpha-\sigma} - 3z_\sigma\mu_{\alpha-\sigma} - \eta_{\alpha\sigma}}{\langle S^{-\sigma}_\alpha S^{\sigma}_\alpha\rangle + 2z_\sigma\Delta_{\alpha-\sigma} - \gamma_{\alpha\sigma}}
\end{aligned}$$

$$\begin{aligned}
a^{\alpha}_{2\sigma} &= \langle S^{-\sigma}_\alpha S^{\sigma}_\alpha\rangle - b^{\alpha}_{2\sigma}\langle S^z_\alpha\rangle\\
b^{\alpha}_{2\sigma} &= \frac{K^{\alpha}_{2\sigma} + 2\eta_{\alpha\sigma}}{\langle (S^z_\alpha)^2\rangle - \langle S^z_\alpha\rangle^2 - \gamma_{\alpha\sigma}}
\end{aligned}$$

$$\begin{aligned}
a^{\alpha}_{3\sigma} &= -\gamma_{\alpha\sigma}\\
b^{\alpha}_{3\sigma} &= \frac{\mu_{\alpha\sigma} - z_\sigma\eta_{\alpha\sigma} + 2z_\sigma\vartheta_\alpha + z_\sigma\gamma_{\alpha\sigma}\langle S^z_\alpha\rangle}{\langle S^{-\sigma}_\alpha S^{\sigma}_\alpha\rangle + 2z_\sigma\Delta_{\alpha-\sigma} - \gamma_{\alpha\sigma}}
\end{aligned}$$

$$\begin{aligned}
a^{\alpha}_{4\sigma} &= \Delta_{\alpha-\sigma} - b^{\alpha}_{4\sigma}\langle S^z_\alpha\rangle\\
b^{\alpha}_{4\sigma} &= \frac{z_\sigma K^{\alpha}_{3\sigma} - \mu_{\alpha-\sigma} - z_\sigma\eta_{\alpha\sigma}}{\langle (S^z_\alpha)^2\rangle - \langle S^z_\alpha\rangle^2 - \gamma_{\alpha\sigma}}
\end{aligned}$$

$$\begin{aligned}
K^{\alpha}_{1\sigma} &= 3z_\sigma\langle S^{\sigma}_\alpha S^{-\sigma}_\alpha\rangle + (S(S+1) - 4)\langle S^z_\alpha\rangle + z_\sigma\langle (S^z_\alpha)^2\rangle\\
&\quad - 2z_\sigma S(S+1)(1 - \langle n_{\alpha-\sigma}\rangle) - \langle (S^z_\alpha)^3\rangle
\end{aligned}$$

$$K^{\alpha}_{2\sigma} = \left(S(S+1) - \langle S^{-\sigma}_\alpha S^{\sigma}_\alpha\rangle\right)\langle S^z_\alpha\rangle - z_\sigma\langle (S^z_\alpha)^2\rangle - \langle (S^z_\alpha)^3\rangle$$

$$K^{\alpha}_{3\sigma} = z_\sigma S(S+1)\langle n_{\alpha-\sigma}\rangle + \Delta_{\alpha-\sigma}(1 - z_\sigma\langle S^z_\alpha\rangle)$$

The following abbreviations for mixed expectation values have been used:

$$\begin{aligned}
\gamma_{\alpha\sigma} &= \langle S_\alpha^{-\sigma} c_{\alpha\sigma}^\dagger c_{\alpha-\sigma} \rangle \\
\Delta_{\alpha\sigma} &= \langle S_\alpha^z n_{\alpha\sigma} \rangle \\
\mu_{\alpha\sigma} &= \langle S_\alpha^{-\sigma} S_\alpha^{\sigma} n_{\alpha\sigma} \rangle \\
\eta_{\alpha\sigma} &= \langle S_\alpha^{-\sigma} S_\alpha^z c_{\alpha\sigma}^\dagger c_{\alpha-\sigma} \rangle \\
\vartheta_\alpha &= \langle S_\alpha^z n_{\alpha\sigma} n_{\alpha-\sigma} \rangle
\end{aligned}$$

The spin expectation values are calculated using (5.43) and (5.45), the mixed expectation values by applying the spectral theorem to the Green functions (A.9)-(A.12).

Appendix B

Effective exchange integrals

It is often convenient to consider the effective exchange integrals (5.12) or (5.19) in real space. Depending on the parameter constellation and desired accuracy, a finite number of them might be sufficient for convergence of the quantities of interest like the magnetization or the Curie temperature. Usually this facilitates the computational effort considerably because a nested $\mathbf{k}, \mathbf{q}$-summation in (5.44) is avoided. Generally speaking, the stronger the coupling J the fewer exchange integrals are needed for the numerical evaluation. In the double-exchange regime only a small number of exchange integrals yields the essential physics while in the RKKY regime the interaction is long-ranged and a summation over a large number of $J_{ij}^{\mathrm{R}KKY}$ is necessary. This is particularly important for the evaluation of the interlayer exchange coupling (Chap. 7).

The explicit form of the real-space MRKKY exchange integrals in (5.18) reads

$$J_{i\alpha j\beta}^{\mathrm{MR}KKY} = \frac{J^2}{4\pi} \sum_{\sigma} \mathrm{Im} \int_{-\infty}^{+\infty} dE f_-(E) G_{ij}^{\alpha\beta(0)}(E-\mu) G_{ji\sigma}^{\beta\alpha}(E-\mu)\,. \tag{B.1}$$

It can be alternatively written

$$J_{n\alpha\beta}^{\mathrm{MR}KKY} = \frac{J^2}{4\pi} \sum_{\sigma} \mathrm{Im} \int_{-\infty}^{+\infty} dE f_-(E) G_{n}^{\alpha\beta(0)}(E-\mu) G_{n\sigma}^{\beta\alpha}(E-\mu) \tag{B.2}$$

provided that the hopping and thus the exchange are invariant with respect to rotations around the axis perpendicular to the basal plane. The index n here defines the nth 2D 'shell' within the monolayer α around the atom at $\mathbf{R}_{i\alpha}$, and the projection of the atom at $\mathbf{R}_{j\beta}$ onto the plane α sits in this nth shell. Note that a shell according to this definition refers to a 2D-projected distance between the interacting atoms. It is thus to be distinguished from a 'real' shell in 3D.

For the further evaluation of (B.2) consider the Fourier-transformed propagator

$$G_{n\sigma}^{\alpha\beta}(E) = \frac{1}{N}\sum_{\mathbf{k}} \mathrm{e}^{\mathrm{i}\mathbf{k}\mathbf{R}_n} G_{\mathbf{k}\sigma}^{\alpha\beta}(E)\,. \tag{B.3}$$

$\mathbf{R}_n$ is a vector connecting $\mathbf{R}_{i\alpha}$ and one of the atoms belonging to the nth shell. For a wave vector-independent self-energy, the $\mathbf{k}$-dependence of $G_{\mathbf{k}\sigma}^{\alpha\beta}$ is exclusively due to the dispersion matrix (3.5) and may thus be associated with different functional expressions containing k_x and k_y (cf. (3.11) and (3.12)). In the simplest case, the whole $\mathbf{k}$-dependence is via just one such expression. This holds, e.g., for the sc(100)-film structure with uniform intralayer hopping where $G_{\mathbf{k}\sigma}^{\alpha\beta}$ depends on $\mathbf{k}$ solely via $\epsilon_{\|}(k_x, k_y)$. One can then accelerate the numerical evaluation of (B.3) by exploiting

$$\begin{aligned} G_{n\sigma}^{\alpha\beta}(E) &= \frac{1}{N}\sum_{\mathbf{k}} \mathrm{e}^{\mathrm{i}\mathbf{k}\mathbf{R}_n} G_{\mathbf{k}\sigma}^{\alpha\beta}(E) \\ &= \frac{1}{N}\sum_{\mathbf{k}} \mathrm{e}^{\mathrm{i}\mathbf{k}\mathbf{R}_n} G_{\epsilon_{\|}(\mathbf{k})\sigma}^{\alpha\beta}(E) \\ &= \int dx \frac{1}{N}\sum_{\mathbf{k}} \delta(x-\epsilon_{\|}(\mathbf{k}))\mathrm{e}^{\mathrm{i}\mathbf{k}\mathbf{R}_n} G_{x\sigma}^{\alpha\beta}(E) \\ &= \int dx \rho_n(x) G_{x\sigma}^{\alpha\beta}(E) \end{aligned} \tag{B.4}$$

where the integral is over the (monolayer) bandwidth. The modified density of states

$$\rho_n(x) = \frac{1}{N}\sum_{\mathbf{k}} \delta(x-\epsilon_{\|}(\mathbf{k}))\mathrm{e}^{\mathrm{i}\mathbf{k}\mathbf{R}_n} \tag{B.5}$$

has to be computed just once for a given intralayer dispersion $\epsilon_{\|}(\mathbf{k})$.

In case of film structures with more complicated $\mathbf{k}$-dependences one must extend (B.4) and introduce more densities of states in order to get rid of the wave vectors. The number of integrations increases accordingly.

Integration in the complex plane

The numerical evaluation of (B.2) may be facilitated by performing the energy integration in the complex plane rather than on the real axis. The effective exchange integrals are of the form

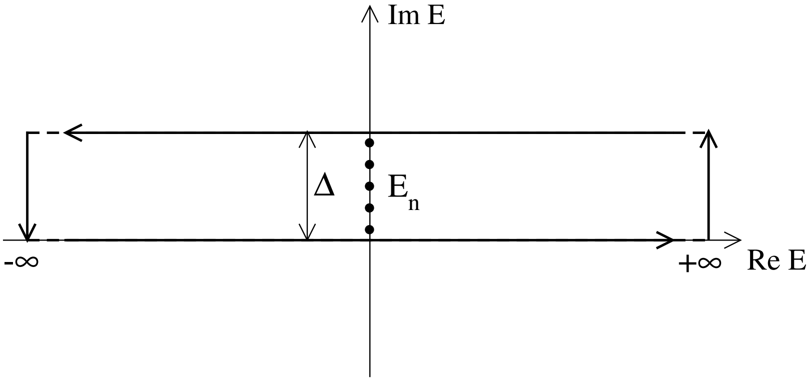

Figure B.1: Integration contour C in the complex plane.

$$I = \mathrm{I}m \int\limits_{-\infty}^{+\infty} dE f_{-}(E+\mu) g(E) \tag{B.6}$$

with the asymptotic behavior

$$g(E) \overset{E\to\infty}{\to} \mathcal{O}(E^{-2}) \, . \tag{B.7}$$

Assuming g to be analytic in the upper half-plane, the poles of the integrand in (B.6) lie at the Matsubara energies

$$E_n = \pi \frac{2n+1}{\beta}, \quad (n \in \mathbb{Z})$$

and the residues are

$$\mathrm{R}es(g) = \frac{2}{\beta} \mathrm{Re}\left[g(\mathrm{i}E_n)\right] \, . \tag{B.8}$$

According to the residue theorem the integration along the contour C shown in Fig. B.1 yields

$$-\frac{1}{\pi} \mathrm{I}m \oint\limits_{C} dE f_{-}(E+\mu) g(E) = \frac{2}{\beta} \mathrm{R}e \sum_{n=0}^{n_{\max}} g(\mathrm{i}E_n) \tag{B.9}$$

where n_{max} labels the largest residue which lies within the contour C. On the other hand, since the contributions to the integral in (B.9) vanish at $\mathrm{R}eE = \pm\infty$ due to (B.7), one has

$$\oint\limits_C dE f_-(E+\mu)g(E) = \int\limits_{-\infty}^{+\infty} dE f_-(E+\mu)g(E) + \int\limits_{+\infty+\mathrm{i}\Delta}^{-\infty+\mathrm{i}\Delta} dE f_-(E+\mu)g(E)\,. \quad \text{(B.10)}$$

Combining (B.9) and (B.10) yields

$$\frac{1}{\pi}\mathrm{Im}\int\limits_{-\infty}^{+\infty} dE f_-(E+\mu)g(E) = -\frac{2}{\beta}\mathrm{Re}\sum_{n=0}^{n_{\max}} g(\mathrm{i}E_n) + \frac{1}{\pi}\mathrm{Im}\int\limits_{-\infty+\mathrm{i}\Delta}^{+\infty+\mathrm{i}\Delta} dE f_-(E+\mu)g(E)\,. \quad \text{(B.11)}$$

The integration on the real axis is replaced by a sum over Matsubara energies and by an energy integration in the complex plane. The imaginary shift is conveniently chosen as $\Delta = \pi\frac{2n}{\beta}$ $(n \in \mathbb{Z})$ so that the imaginary part of the Fermi function vanishes. Note that the higher Δ the larger has to be the energy mesh for the numerical integration.

Appendix C

Strong-coupling limit

The relation between the nearest-neighbor effective exchange integral and the kinetic energy in the strong-coupling limit ($JS \gg W$) is demonstrated for a fully polarized conduction band subject to a mean-field shift of $-\frac{1}{2}JS$. For convenience a bulk crystal with isotropic nearest-neighbor hopping t is considered.

Using Dirac's identity

$$\frac{1}{x-a+i0^+} = -i\pi\delta(x-a) + \mathcal{P}\frac{1}{x-a} \tag{C.1}$$

the energy integral in (5.19) yields for $JS \gg W$

$$\begin{aligned} J^{MRKKY}(\mathbf{q}) &= \frac{1}{4N}J^2 \sum_{\mathbf{k}} \frac{\langle n_{\mathbf{k}+\mathbf{q}\uparrow}\rangle}{\epsilon(\mathbf{k}) - \epsilon(\mathbf{k}+\mathbf{q}) + \frac{1}{2}JS} \\ &\simeq \frac{1}{2N}\frac{J}{S}\sum_{\mathbf{k}} \langle n_{\mathbf{k}+\mathbf{q}\uparrow}\rangle \left(1 - \frac{2(\epsilon(\mathbf{k}) - \epsilon(\mathbf{k}+\mathbf{q}))}{JS}\right) . \end{aligned} \tag{C.2}$$

The nearest-neighbor exchange integral is obtained from this expression via:

$$\begin{aligned} J_1^{MRKKY} &= \frac{1}{N}\sum_{\mathbf{q}} \mathrm{e}^{-i\mathbf{q}\boldsymbol{\Delta}} J^{MRKKY}(\mathbf{q}) \\ &= -\frac{1}{zt}\frac{1}{N}\sum_{\mathbf{q}} \epsilon(\mathbf{q}) J^{MRKKY}(\mathbf{q}) \end{aligned} \tag{C.3}$$

with $\boldsymbol{\Delta} = \mathbf{R}_i - \mathbf{R}_j$ and i, j are nearest neighbors. Inserting (C.2) into (C.3), only the term $\propto \epsilon(\mathbf{k})$ survives:

$$
\begin{aligned}
J_1^{MRKKY} &= \frac{1}{ztS^2N^2}\sum_{\mathbf{k}}\sum_{\mathbf{q}}\epsilon(\mathbf{k})\epsilon(\mathbf{q})\langle n_{\mathbf{k}+\mathbf{q}\uparrow}\rangle \\
&= \frac{1}{ztS^2N^2}\sum_{\mathbf{k}}\sum_{\mathbf{q}}\epsilon(\mathbf{k})\epsilon(\mathbf{q})\frac{1}{N}\sum_{\langle ij\rangle}\mathrm{e}^{\mathrm{i}(\mathbf{k}+\mathbf{q})(\mathbf{R}_i-\mathbf{R}_j)}\langle c^\dagger_{i\uparrow}c_{j\uparrow}\rangle \\
&= \frac{1}{ztS^2N}\sum_{\langle ij\rangle}\left(\frac{1}{N}\sum_{\mathbf{k}}\mathrm{e}^{\mathrm{i}\mathbf{k}(\mathbf{R}_i-\mathbf{R}_j)}\epsilon(\mathbf{k})\right)\left(\frac{1}{N}\sum_{\mathbf{q}}\mathrm{e}^{\mathrm{i}\mathbf{q}(\mathbf{R}_i-\mathbf{R}_j)}\epsilon(\mathbf{q})\right)\langle c^\dagger_{i\uparrow}c_{j\uparrow}\rangle \\
&= \frac{1}{ztS^2N}\sum_{\langle ij\rangle}t^2_{ij}\langle c^\dagger_{i\uparrow}c_{j\uparrow}\rangle \\
&= \frac{t}{S^2}\langle c^\dagger_{i\uparrow}c_{j\uparrow}\rangle \\
&= -\frac{1}{S^2}U^{ij}_{\mathrm{k}in} \\
&= -\frac{1}{zS^2}U_{\mathrm{k}in}
\end{aligned}
\tag{C.4}
$$

A ferromagnetic coupling between the localized spins is favored if $\langle c^\dagger_{i\uparrow}c_{j\uparrow}\rangle > 0$ and $t > 0$. This always holds for a rigidly shifted majority band up to half-filling because the expectation value is given by the (positive) integral over the free off-diagonal density of states (see Fig. 3.2). Next it is shown that $U_{\mathrm{k}in}$ is proportional to t and does not depend on J.

Hopping integral and kinetic energy

The kinetic energy for a translationally invariant lattice and isotropic nearest-neighbor hopping reads:

$$
\begin{aligned}
U_{\mathrm{k}in} &= \sum_{\langle ij\rangle}U^{ij}_{\mathrm{k}in} \\
&= -t\sum_{\langle ij\rangle\sigma}\langle c^\dagger_{i\sigma}c_{j\sigma}\rangle\,.
\end{aligned}
\tag{C.5}
$$

The correlation function can be evaluated using the spectral theorem ($T = 0$):

$$\begin{aligned}\langle c^{\dagger}_{i\sigma}c_{j\sigma}\rangle &= -\frac{1}{\pi}\int\limits_{-\infty}^{\epsilon_{\mathrm{F}}} dE \mathrm{Im} G_{ij\sigma}(E-\mu) \\ &= \int\limits_{-\infty}^{\epsilon_{\mathrm{F}}} dE \rho_{ij\sigma}(E)\,. \end{aligned} \tag{C.6}$$

Consider first the non-interacting case:

$$\rho^{(0)}_{ij}(x) = \frac{1}{N}\sum_{\mathbf{k}} \delta(x-\epsilon(\mathbf{k}))\mathrm{e}^{-\mathrm{i}\mathbf{k}(\mathbf{R}_i-\mathbf{R}_j)}\,. \tag{C.7}$$

Introducing a scaling factor γ for the hopping integral, $t \to \gamma t$, one has ($\epsilon(\mathbf{k}) \propto t$):

$$\begin{aligned}\rho^{(0)\gamma}_{ij}(x) &= \frac{1}{N}\sum_{\mathbf{k}} \delta(x-\gamma\epsilon(\mathbf{k}))\mathrm{e}^{-\mathrm{i}\mathbf{k}(\mathbf{R}_i-\mathbf{R}_j)} \\ &= \frac{1}{N}\sum_{\mathbf{k}} \frac{1}{\gamma}\delta(\frac{x}{\gamma}-\epsilon(\mathbf{k}))\mathrm{e}^{-\mathrm{i}\mathbf{k}(\mathbf{R}_i-\mathbf{R}_j)} \\ &= \frac{1}{\gamma}\rho^{(0)}_{ij}(\frac{x}{\gamma})\,. \end{aligned} \tag{C.8}$$

On the other hand, using the substitution $E \to \frac{E}{\gamma}$, one can write for the correlation function

$$\begin{aligned}\langle c^{\dagger}_{i\sigma}c_{j\sigma}\rangle^{(0)} &= \int\limits_{-\infty}^{\epsilon_{\mathrm{F}}} dE \rho^{(0)}_{ij}(E) \\ &= \int\limits_{-\infty}^{\gamma\epsilon_{\mathrm{F}}} dE \frac{1}{\gamma}\rho^{(0)}_{ij}(\frac{E}{\gamma}) \\ &= \int\limits_{-\infty}^{\gamma\epsilon_{\mathrm{F}}} dE \rho^{(0)\gamma}_{ij}(E)\,. \end{aligned} \tag{C.9}$$

For a given band occupation $n = 2\langle c^{\dagger}_{i\sigma}c_{i\sigma}\rangle^{(0)}$, the Fermi energy is shifted ($\epsilon_{\mathrm{F}} \to \gamma\epsilon_{\mathrm{F}}$) if the hopping is modified. It follows from (C.9) that the off-diagonal expectation value $\langle c^{\dagger}_{i\sigma}c_{j\sigma}\rangle^{(0)}$ ($i \neq j$) remains unaffected by this shift. With (C.5) the kinetic energy is thus proportional to the hopping integral:

$$U_{\mathrm{k}in} \propto t\,. \tag{C.10}$$

The above considerations hold also for the interacting case with a completely polarized conduction band if the Fermi energy lies in the rigidly shifted majority-spin band. Since (C.6) does not depend on the band center of gravity, this means, in particular, that $U_{\mathrm{k}in}$ does not depend on J.

Appendix D

Ferromagnetic Heisenberg bilayer

For a symmetric, ferromagnetic bilayer with

$$J_{\mathbf{q}}^{11} = J_{\mathbf{q}}^{22} \equiv J_{\mathbf{q}}^{intra} \qquad J_{\mathbf{q}}^{12} \equiv J_{\mathbf{q}}^{inter} \qquad K_2^1 = K_2^2 \equiv K_2 \tag{D.1}$$

it holds $\langle S_1^z \rangle = \langle S_2^z \rangle \equiv \langle S^z \rangle$. The self-energy matrix elements (5.40) are

$$\begin{aligned} (\underline{\mathrm{M}}_{\mathbf{q}})_{11} &= B_{\mathrm{eff}} + 2\left(J_{\mathbf{q}=0}^{intra} - J_{\mathbf{q}}^{intra} + J_{\mathbf{q}=0}^{inter}\right)\langle S^z \rangle = (\underline{\mathrm{M}}_{\mathbf{q}})_{22}\,, \\ (\underline{\mathrm{M}}_{\mathbf{q}})_{12} &= -2J_{\mathbf{q}}^{inter}\langle S^z \rangle = (\underline{\mathrm{M}}_{\mathbf{q}})_{21}\,, \end{aligned} \tag{D.2}$$

with the effective field $B_{\mathrm{eff}} \equiv B + K_2\Phi$. The eigenvalues of $\underline{\mathrm{M}}_{\mathbf{q}}$ are the spin wave excitation energies of the Heisenberg bilayer and read

$$\begin{aligned} E^{\mathrm{ac}}(\mathbf{q}) &= B_{\mathrm{eff}} + 2\langle S^z \rangle \left(J_{\mathbf{q}=0}^{intra} - J_{\mathbf{q}}^{intra} + J_{\mathbf{q}=0}^{inter} - J_{\mathbf{q}}^{inter}\right) \\ E^{\mathrm{op}}(\mathbf{q}) &= B_{\mathrm{eff}} + 2\langle S^z \rangle \left(J_{\mathbf{q}=0}^{intra} - J_{\mathbf{q}}^{intra} + J_{\mathbf{q}=0}^{inter} + J_{\mathbf{q}}^{inter}\right) \\ &= E^{\mathrm{ac}}(\mathbf{q}) + 4\langle S^z \rangle J_{\mathbf{q}}^{inter} \end{aligned} \tag{D.3}$$

where the superscripts stand for 'acoustical' and 'optical' to denote the character of the spin excitation. The wave vectors refer to the first Brillouin zone of the underlying 2D-lattice. In a semi-classical spin picture and analogous to a mechanical system of coupled oscillators, the acoustical (optical) spin wave branch represents a collective in-phase (anti-phase) rotation of the spins. For the isotropic case $B_{\mathrm{eff}} = 0$ one immediately gets

$$\lim_{\mathbf{q}\to\mathbf{0}} E_{\mathrm{iso}}^{\mathrm{ac}}(\mathbf{q}) = 0$$

in accordance with Goldstone's theorem which states that the energy of Goldstone modes (in this case magnons) must vanish at the characteristic wave vector of the ground state ($\mathbf{q} = \mathbf{0}$ for a ferromagnet).

Using Fourier transformation, the **q**-dependent exchange integrals can be written in terms of contributions from real-space shells:

$$J^{\alpha}_{\mathbf{q}} = \frac{1}{N}\sum_{ij} J^{\alpha}_{ij} \mathrm{e}^{\mathrm{i}\mathbf{q}(\mathbf{R}_i-\mathbf{R}_j)} = J^{\alpha}_0 + J^{\alpha}_1 f^{\alpha}_1(\mathbf{q}) + J^{\alpha}_2 f^{\alpha}_2(\mathbf{q}) + J^{\alpha}_3 f^{\alpha}_3(\mathbf{q}) + .. \tag{D.4}$$

J^{α}_i denotes the exchange integral of a given spin at $\mathbf{R}_0$ with one of the z^{α}_i constituents of the ith shell in the same layer ($\alpha = intra$) or in the other layer ($\alpha = inter$) and $f^{\alpha}_i(\mathbf{q}) = \sum_{\Delta=1}^{z^{\alpha}_i} \mathrm{e}^{\mathrm{i}\mathbf{q}(\mathbf{R}_0-\mathbf{R}_{i\Delta})}$. The real-space self-interaction term $J^{\alpha}_0 \equiv J^{\alpha}_{ii}$ is to be distinguished from the uniform **q**-space term $J^{\alpha}_{\mathbf{q}=0} = J^{\alpha}_0 + \sum_{i=1}^{\infty} z^{\alpha}_i J^{\alpha}_i$. Note that the shell numbering is done within each single layer here, rather than referring to the projection onto the basal plane as discussed in Appendix B.

Inserting (D.4) into (D.3), one can write for the acoustical and for the optical spin wave mode

$$\begin{aligned} E^{\mathrm{ac}}(\mathbf{q}) &= B_{\mathrm{e}ff} + 2\langle S^z\rangle \sum_{i=1}^{\infty} \left[J^{intra}_i \left(z^{intra}_i - f^{intra}_i(\mathbf{q})\right) + J^{inter}_i \left(z^{inter}_i - f^{inter}_i(\mathbf{q})\right)\right] \\ E^{\mathrm{op}}(\mathbf{q}) &= E^{\mathrm{ac}}(\mathbf{q}) + 4\langle S^z\rangle \left(J^{inter}_0 + \sum_{i=1}^{\infty} J^{inter}_i f^{inter}_i(\mathbf{q}) \right). \end{aligned} \tag{D.5}$$

The interlayer coupling J^{inter}_0 does not appear in the acoustical spin wave dispersion. The optical branch of the spin wave spectrum is separated from the acoustical branch by the **q**-dependent shift $\Delta^{SW}_{\mathbf{q}} = 4\langle S^z\rangle J^{inter}_{\mathbf{q}}$.

For nearest-neighbor exchange coupling and sc(100)-film geometry, the splitting is **q**-independent, $\Delta^{SW} = 4\langle S^z\rangle J^{inter}_0$ (Fig. 7.14). The low-temperature magnetic behavior is determined by the acoustical spin wave branch (Fig. D.1).

Spin wave stiffness

The ferromagnetic stiffness D is a measure for the thermal stability of long-range order at low temperatures. It is defined as ($B_{\mathrm{e}ff} = 0$)

$$E^{\mathrm{SW}}(\mathbf{q}) \simeq D\mathbf{q}^2 \quad (\mathbf{q} \to \mathbf{0})\,. \tag{D.6}$$

Within linear spin wave theory (which the RPA approach reproduces for $T \to 0$, $\langle S^z\rangle \to S$), and in shell notation, an expansion of the spinwave dispersion about $\mathbf{q} = \mathbf{0}$ yields for the translationally invariant system:

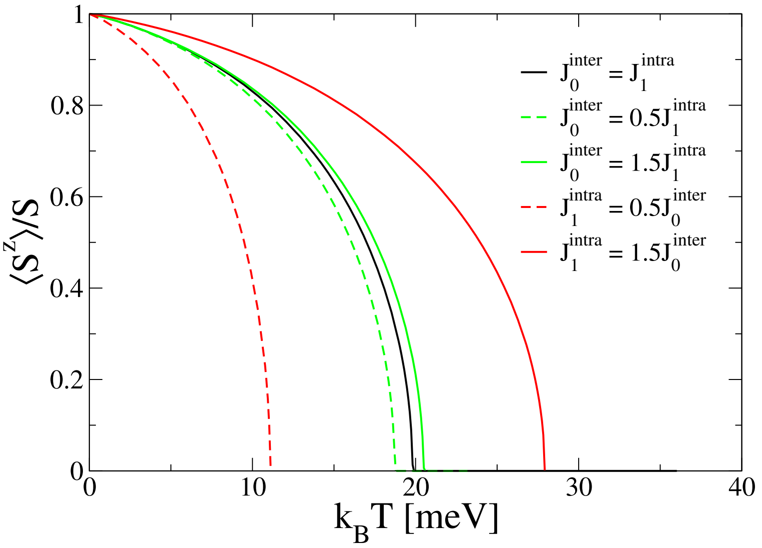

Figure D.1: Magnetization of the sc(100)-bilayer as a function of temperature for uniform exchange interaction $J_0^{inter} = J_1^{intra} = 1\,\mathrm{me}V$, $S = 7/2$ (black curve) and for reduced/enhanced interlayer/intralayer exchange interaction as indicated. Green curves: $J_1^{intra} = 1\,\mathrm{me}V$, red curves: $J_0^{inter} = 1\,\mathrm{me}V$. External field $B = 0$, anisotropy strength $K_2 = 1\,\mu\mathrm{e}V$.

$$
\begin{aligned}
E^{\mathrm{L}SW}(\mathbf{q}) &= 2S\left(J(\mathbf{0}) - J(\mathbf{q})\right) \\
&= 2S \sum_{i=1}^{\infty} J_i (z_i - f_i(\mathbf{q})) \\
&= 2S \sum_{i=1}^{\infty} c_i J_i \mathbf{q}^2 \quad (\mathbf{q} \to \mathbf{0})
\end{aligned}
\tag{D.7}
$$

and thus $D = 2S \sum_{i=1}^{\infty} c_i J_i$ with the shell-dependent coefficients c_i. As an example, for the square lattice one gets for the first shells

$$
D^{\mathrm{mono}} = 2S\left(J_1 + 2J_2 + 4J_3 + 10J_4 + ..\right) . \tag{D.8}
$$

For the sc(100)-bilayer one obtains from (D.5):

$$
\begin{aligned}
D^{\mathrm{bi}} = 2S \Big[& J_1^{intra} + J_1^{inter} + 2\left(J_2^{intra} + J_2^{inter}\right) \\
& + 4\left(J_3^{intra} + J_3^{inter}\right) + 10\left(J_4^{intra} + J_4^{inter}\right) + \ldots \Big] .
\end{aligned}
\tag{D.9}
$$

Appendix E

Recursion formulae for matrix inversion

In order to compute the film matrix elements of the one-electron Green function it is numerically efficient to use recursion formulae. These are given below for the inversion of a complex $n \times n$ tridiagonal matrix of the form

$$\underline{A} = \begin{pmatrix} b_1 & c_1 & 0 & .. & .. & 0 \\ a_1 & b_2 & c_2 & .. & .. & .. \\ 0 & a_2 & .. & .. & .. & .. \\ .. & .. & .. & .. & c_{n-2} & 0 \\ .. & .. & .. & a_{n-2} & b_{n-1} & c_{n-1} \\ 0 & .. & .. & 0 & a_{n-1} & b_n \end{pmatrix}. \tag{E.1}$$

In all cases treated in this work $a_i = c_i^\dagger$. The submatrix $\underline{A}_i$ ($\underline{A}_{i'}$) is obtained by dropping the last (first) $n-i$ rows and columns of $\underline{A}$. The determinants of $\underline{A}_i$ and $\underline{A}_{i'}$ can be computed using the following recursion formulae:

$$\begin{aligned} det\underline{A}_0 &= 1 \\ det\underline{A}_1 &= b_1 \\ det\underline{A}_i &= b_i det\underline{A}_{i-1} - a_{i-1}c_{i-1} det\underline{A}_{i-2} \\ det\underline{A}_n &= det\underline{A} \end{aligned} \tag{E.2}$$

$$\begin{aligned} det\underline{A}_{0'} &= 1 \\ det\underline{A}_{1'} &= b_n \\ det\underline{A}_{i'} &= b_{n-i+1} det\underline{A}_{(i-1)'} - a_{n-i+1}c_{n-i+1} det\underline{A}_{(i-2)'} \\ det\underline{A}_{n'} &= det\underline{A} \end{aligned} \tag{E.3}$$

The diagonal matrix elements of $\underline{A}^{-1}$ are given by

$$\left(\underline{A}^{-1}\right)_{ii} = \frac{\mathrm{det}\underline{A}_{i-1}\mathrm{det}\underline{A}_{(n-i)'}}{\mathrm{det}\underline{A}} \,. \tag{E.4}$$

For a symmetric film it holds

$$b_i = b_{n-i+1} \qquad a_i = a_{n-i} \qquad c_i = c_{n-i} \,.$$

In this case one can speed up the calculation further by exploiting

$$\mathrm{det}\underline{A}_i = \mathrm{det}\underline{A}_{i'} \,. \tag{E.5}$$

The non-diagonal matrix elements are obtained from (E.2), (E.3), and (E.4) as follows [307]:

$$\begin{aligned}
\left(\underline{A}^{-1}\right)_{ij} &= (-1)^{j-i}\left(\prod_{k=1}^{j-i} c_{j-k}\right)\frac{\mathrm{det}\underline{A}_{i-1}}{\mathrm{det}\underline{A}_{j-1}}\left(\underline{A}^{-1}\right)_{jj} \qquad (i<j)\\
\left(\underline{A}^{-1}\right)_{ij} &= (-1)^{i-j}\left(\prod_{k=1}^{i-j} a_{j+k-1}\right)\frac{\mathrm{det}\underline{A}_{(n-i)'}}{\mathrm{det}\underline{A}_{(n-j)'}}\left(\underline{A}^{-1}\right)_{jj} \qquad (i>j)
\end{aligned} \tag{E.6}$$

Bibliography

[1] J.A.C. Bland and B. Heinrich, editors. *Ultrathin Magnetic Structures I-IV.* Springer, Berlin Heidelberg, 2005.

[2] I. Zutic J. Fabian and S. Das Sarma. *Rev. Mod. Phys.*, 76:323, 2004.

[3] E. Ising. *Z. Phys.*, 31:253, 1925.

[4] W. Heisenberg. *Z. Phys.*, 38:441, 1926.

[5] C. Zener. *Phys. Rev.*, 81:440, 1951.

[6] T. Kasuya. *Prog. Theor. Phys.*, 16:45, 1956.

[7] K. Yosida. *Phys. Rev.*, 106:893, 1957.

[8] S.V. Vonsovskii and Y.A. Izyumov. *Sov. Phys. Usp.*, 5:547, 1963.

[9] P. Wachter. *Helv. Phys. Acta*, 37:637, 1964.

[10] G. Busch J. Junod and P. Wachter. *Phys. Lett.*, 12:11, 1964.

[11] R. Schiller and W. Nolting. *Phys. Rev. Lett.*, 86:3847, 2001.

[12] A.J. Freeman. *Magnetic Properties of Rare Earth Metals.* Plenum, New York, 1972.

[13] B. Coqblin. *The Electronic Structure of Rare-Earth Metals and Alloys: the Magnetic Heavy Rare-Earths.* Academic Press, New York, 1977.

[14] A.T. Hindmarch and B.J. Hickey. *Phys. Rev. Lett.*, 91:116601, 2003.

[15] A.P. Ramirez. *J. Phys. C.*, 9:8171, 1997.

[16] E. Dagotto, editor. *Nanoscale Phase Separation and Colossal Magnetoresistance, The Physics of Manganites and Related Compounds.* Springer, New York, 2003.

[17] A.J. Millis P.B. Littlewood and B.I. Shraiman. *Phys. Rev. Lett.*, 74:5144, 1995.

[18] D.M. Edwards. *Adv. Phys.*, 51:1259, 2002.

[19] R. Kilian and G. Khaliullin. *Phys. Rev. B*, 58:R11841, 1998.

[20] L.F. Feiner and A.M. Oles. *Phys. Rev. B*, 71:144422, 2005.

[21] M. Daghofer A.M. Oles D.R. Neuber and W. v. d. Linden. *Phys. Rev. B*, 73:104451, 2006.

[22] C. Zener. *Phys. Rev.*, 82:403, 1951.

[23] P.W. Anderson and H. Hasegawa. *Phys. Rev.*, 100:675, 1955.

[24] T. Jungwirth J. Sinova J. Masek J. Kucera and A.H. MacDonald. *Rev. Mod. Phys.*, 78:809, 2006.

[25] H. Ohno. *Science*, 281:951, 1998.

[26] T. Dietl A. Haury and Y.M. d'Aubigne. *Phys. Rev. B*, 55:R3347, 1997.

[27] T. Dietl. *Semicond. Sci. Technol.*, 17:377, 2002.

[28] F. Matsukura H. Ohno A. Shen and Y. Sugawara. *Phys. Rev. B*, 57:R2037, 1998.

[29] T. Jungwirth W.A. Atkinson B.H. Lee and A.H. MacDonald. *Phys. Rev. B*, 59:9818, 1999.

[30] T. Dietl H. Ohno F. Matsukura J. Cibert and D. Ferrand. *Science*, 287:1019, 2000.

[31] D.J. Priour Jr. E.H. Hwang and S. Das Sarma. *Phys. Rev. Lett.*, 92:117201, 2004.

[32] D.J. Priour Jr. E.H. Hwang and S. Das Sarma. *Phys. Rev. Lett.*, 95:037201, 2005.

[33] D.J. Priour Jr. and S. Das Sarma. *Phys. Rev. Lett.*, 97:127201, 2006.

[34] C. Timm. *J. Phys.: Condens. Matter*, 15:R1865, 2003.

[35] S. Hilbert and W. Nolting. *Phys. Rev. B*, 71:113204, 2005.

[36] G. Tang and W. Nolting. *phys. stat. sol. (b)*, 244:735, 2007.

[37] G. Tang and W. Nolting. *Phys. Rev. B*, 75:024426, 2007.

[38] A.C. Hewson. *The Kondo Problem to Heavy Fermions*. Cambridge University Press, Cambridge, 1993.

[39] D. Weller S. Alvarado W. Gudat K. Schroder and M. Campagna. *Phys. Rev. Lett.*, 54:1555, 1985.

[40] C. Rau and S. Eichner. *Phys. Rev. B*, 34:6347, 1986.

[41] H. Tang D. Weller T.G. Walker J.C. Scott C. Chappert H. Hopster A.W. Pang D.S. Dessau and D.P. Pappas. *Phys. Rev. Lett.*, 71:444, 1993.

[42] E.D. Tober F.J. Palomares R.X. Ynzunza R. Denecke J. Morais Z. Wang G. Bino J. Liesegang Z. Hussain and C.S. Fadley. *Phys. Rev. Lett.*, 81:2360, 1998.

[43] M. Donath B. Gubanka and F. Passek. *Phys. Rev. Lett.*, 77:5138, 1996.

[44] C.S. Arnold and D.P. Pappas. *Phys. Rev. Lett.*, 85:5202, 2000.

[45] A.B. Shick W.E. Pickett and C.S. Fadley. *Phys. Rev. B*, 61:R9213–R9216, 2000.

[46] Ph. Kurz G. Bihlmayer and S. Blügel. *J. Phys.: Condens. Matter*, 14:6353–6371, 2002.

[47] M. Petersen J. Hafner and M. Marsman. *J. Phys.: Condens. Matter*, 18: 7021–7043, 2006.

[48] J.S. Jiang and C.L. Chien. *J. Appl. Phys.*, 79:5615, 1996.

[49] J.S. Jiang D. Davidovic D.H. Reich and C.L. Chien. *Phys. Rev. Lett.*, 74: 314, 1995.

[50] M. Farle K. Baberschke U. Stetter A. Aspelmeier and F. Gerhardter. *Phys. Rev. B*, 47:11571, 1993.

[51] M. Farle and K. Baberschke. *Magnetism and Electronic Correlations in Local-moment Systems*. World Scientific, Singapore, 1998.

[52] M. Farle W. Platow A.N. Anisimov B. Schulz and K. Baberschke. *J. Magn. Magn. Mater.*, 165:74, 1997.

[53] R. Kalinowski C. Meyer A. Wawro and L.T. Baczewski. *Thin Solid Films*, 367:189, 2000.

[54] R. Zhang and R.F. Willis. *Phys. Rev. Lett.*, 86:2665, 2001.

[55] D. Kechrakos N. Papanikolaou K.N. Trohidou and T. Dietl. *Phys. Rev. Lett.*, 94:127201, 2005.

[56] D. Frustaglia J. Koenig and A.H. MacDonald. *Phys. Rev. B*, 70:045205, 2004.

[57] J. Koenig and A.H. MacDonald. *Phys. Rev. Lett.*, 91:077202, 2003.

[58] B. Lee T. Jungwirth and A.H. MacDonald. *Phys. Rev. B*, 65:193311, 2002.

[59] B. Lee T. Jungwirth and A.H. MacDonald. *Phys. Rev. B*, 61:15606, 2000.

[60] L. Brey and F. Guinea. *Phys. Rev. Lett.*, 85:2384, 2000.

[61] U. Gummich and I.C. da Cunha Lima. *Solid State Commun.*, 76:831, 1990.

[62] L.G. Ferreira Filho I.C. da Cunha Lima and A. Troper. *Semicond. Sci. Technol.*, 12:1592, 1997.

[63] R.K. Kawakami E. Johnston-Halperin L.F. Chen M. Hanson N. Guebels J.S. Speck A.C. Gossard and D.D. Awschalom. *Appl. Phys. Lett.*, 77:2379, 2000.

[64] J. Fernandez-Rossier and L.J. Sham. *Phys. Rev. B*, 64:235323, 2001.

[65] A.M. Nazmul T. Amemiya Y. Shuto S. Sugahara and M. Tanaka. *Phys. Rev. Lett.*, 95:017201, 2005.

[66] B. Lv J. Wang J. Yu H. Mao Y. Shen Z. Zhu and H. Xing. *Appl. Phys. Lett.*, 90:142513, 2007.

[67] R.G. Melko R.S. Fishman and F.A. Reboredo. *Phys. Rev. B*, 75:115316, 2007.

[68] N.P. Stern R.C. Myers M. Poggio A.C. Gossard and D.D. Awschalom. *Phys. Rev. B*, 75:045329, 2007.

[69] N. Akiba F. Matsukura A. Shen Y. Ohno H. Ohno A. Oiwa S. Katsumoto and Y. Iye. *Appl. Phys. Lett.*, 73:2122, 1998.

[70] M.A. Boselli I.C. da Cunha Lima. *Phys. Rev. B*, 68:085319, 2003.

[71] P. Sankowski and P. Kacman. *Phys. Rev. B*, 71:201303, 2005.

[72] A.D. Giddings T. Jungwirth and B.L. Gallagher. *cond-mat/0610696*, 2006.

[73] P. Grünberg R. Schreiber Y. Pang M. B. Brodsky and C.H. Sowers. *Phys. Rev. Lett.*, 57:2442, 1986.

[74] C. Carbone and S.F. Alvarado. *Phys. Rev. B*, 36:2433, 1987.

[75] M.N. Baibich J.M. Broto A. Fert F. Nguyen Van Dau F. Petroff P. Eitenne G. Creuzet A. Friederich and J. Chazelas. *Phys. Rev. Lett.*, 61:2472, 1988.

[76] G. Binasch P. Grünberg F. Saurenbach and W. Zinn. *Phys. Rev. B*, 39:4828, 1989.

[77] W.H. Butler and X.-G. Zhang. *Ultrathin Magnetic Structures III - Fundamentals of Nanomagnetism.* Springer, Berlin, 2005.

[78] S. Selzer and N. Majlis. *J. Magn. Magn. Mater.*, 15-18:1095, 1980.

[79] S. Selzer and N. Majlis. *Phys. Rev. B*, 26:404, 1982.

[80] S. Selzer and N. Majlis. *Phys. Rev. B*, 27:544, 1983.

[81] Q. Hong. *Phys. Rev. B*, 41:9621, 1990.

[82] L.-P. Shi and W.-G. Yang. *J. Phys.: Condens. Matter*, 4:7997, 1992.

[83] P. Schilbe S. Siebentritt and K.-H. Rieder. *Phys. Lett. A*, 216:20, 1996.

[84] R. Schiller and W. Nolting. *Solid State Commun.*, 110:121, 1999.

[85] W.-Z. Shen and Z.-Y. Li. *J. Phys.: Condens. Matter*, 4:5873, 1992.

[86] K. Binder. *Phase Transitions and Critical Phenomena.* Academic Press, London, 1983.

[87] D.L. Mills. *Phys. Rev. B*, 3:3887, 1971.

[88] K. Binder and P.C. Hohenberg. *Phys. Rev. B*, 9:2194, 1974.

[89] L.D. Landau and E.M. Lifshitz. *Statistical Physics.* Pergamon Press, London, 1959.

[90] A. Urbaniak-Kucharczyk. *phys. stat. sol. (b)*, 186:263, 1994.

[91] J.M. Wesselinowa L.L. Iliev and W. Nolting. *phys. stat. sol. (b)*, 214:165, 1999.

[92] G. Jackeli and N.B. Perkins. *Phys. Rev. B*, 65:212402, 2002.

[93] A.M. Oles and L.F. Feiner. *Phys. Rev. B*, 67:092407, 2003.

[94] N.D. Mermin and H. Wagner. *Phys. Rev. Lett.*, 17:1133, 1966.

[95] A. Gelfert and W. Nolting. *J. Phys.: Condens. Matter*, 13:R505, 2001.

[96] N.S. Almeida D.L. Mills and M. Teitelman. *Phys. Rev. Lett.*, 75:733, 1995.

[97] P.J. Jensen K.H. Bennemann P. Poulopoulos M. Farle F. Wilhelm and K. Baberschke. *Phys. Rev. B*, 60:R14994, 1999.

[98] S. Schwieger J. Kienert K. Lenz J. Lindner K. Baberschke and W. Nolting. *Phys. Rev. Lett.*, 98:057205, 2007.

[99] C. Santos W. Nolting and V. Eyert. *Phys. Rev. B*, 69:214412, 2004.

[100] D.N. Zubarev. *Sov. Phys. Usp.*, 3:320, 1960.

[101] A.L. Fetter and J.D. Walecka. *Quantum Theory of Many-Particle Systems.* McGraw-Hill, New York, 1971.

[102] K. Elk and W. Gasser. *Die Methode der Greenschen Funtionen in der Festkörperphysik.* Akademie-Verlag, 1979.

[103] E.K.U. Gross and E. Runge. *Vielteilchentheorie.* Teubner, Stuttgart, 1986.

[104] W. Nolting. *Grundkurs Theoretische Physik, Band 7.* Springer, Berlin, 2002.

[105] N.W. Ashcroft and N.D. Mermin. *Solid State Physics.* Saunders College Publishing, 1976.

[106] K. Held and D. Vollhardt. *Phys. Rev. Lett.*, 84:5168, 2000.

[107] J. Kienert C. Santos and W. Nolting. *phys. stat. sol. (b)*, 236:515, 2003.

[108] M. Stier and W. Nolting. *Phys. Rev. B*, 75:144409, 2007.

[109] P. Fazekas. *Lecture Notes on Electron Correlation and Magnetism.* World Scientific, 1999.

[110] W. Nolting. *Quantentheorie des Magnetismus, Band 2.* Teubner, Stuttgart, 1986.

[111] W. Müller and W. Nolting. *Phys. Rev. B*, 66:085205, 2002.

[112] T. Holstein and H. Primakoff. *Phys. Rev.*, 58:1098, 1940.

[113] F.J. Dyson. *Phys. Rev.*, 102:1217, 1956.

[114] M.C. Gutzwiller. *Phys. Rev. Lett.*, 10:159, 1963.

[115] J. Hubbard. *Proc. R. Soc. London*, A 276:238, 1963.

[116] J. Kanamori. *Prog. Theor. Phys. (Kyoto)*, 30:275, 1963.

[117] W. Nolting. *Ferromagnetism and Electronic Correlations.* AIP Conference Proceedings, Vol. 527, Melville, New York, 2000.

[118] K. Baberschke M. Donath and W. Nolting, editors. *Band-Ferromagnetism.* Springer, Berlin, 2001.

[119] K. Held et al. *Quantum Simulations of Complex Many-Body Systems: From Theory to Algorithms.* John von Neumann Institute for Computing, Jülich, 2002.

[120] W. Nolting W. Borgiel V. Dose and Th. Fauster. *Phys. Rev. B*, 40:5015, 1989.

[121] F. Gebhard. *The Mott Metal-Insulator Transition.* Springer, Berlin, 1997.

[122] W. Metzner and D. Vollhardt. *Phys. Rev. Lett.*, 62:324, 1989.

[123] E. Müller-Hartmann. *Z. Phys. B*, 74:507, 1989.

[124] A. Georges G. Kotliar W. Krauth and M. J. Rozenberg. *Rev. Mod. Phys.*, 68:13, 1996.

[125] G. Kotliar and D. Vollhardt. *Physics Today*, 57:53, 2004.

[126] W. Nolting G.G. Reddy A. Ramakanth and D. Meyer. *Phys. Rev. B*, 64: 155109, 2001.

[127] W. Nolting G.G. Reddy A. Ramakanth D. Meyer and J. Kienert. *Phys. Rev. B*, 67:024426, 2003.

[128] W. Nolting M. Potthoff T. Herrmann and T. Wegner. *Band-Ferromagnetism.* Springer, Berlin, 2001.

[129] M. Potthoff T. Herrmann T. Wegner and W. Nolting. *phys. stat. sol. (b)*, 210:199, 1998.

[130] S. Schwieger and W. Nolting. *Phys. Rev. B*, 64:144415, 2001.

[131] D. Meyer and W. Nolting. *Eur. Phys. J. B*, 18:385, 2000.

[132] M. Sigrist H. Tsunetsugu and K. Ueda. *Phys. Rev. Lett.*, 67:2211, 1991.

[133] M. Sigrist K. Ueda and H. Tsunetsugu. *Phys. Rev. B*, 46:175, 1992.

[134] M. Sigrist H. Tsunetsugu K. Ueda and T.M. Rice. *Phys. Rev. B*, 46:13838, 1992.

[135] H. Tsunetsugu M. Sigrist and K. Ueda. *Rev. Mod. Phys.*, 69:809, 1997.

[136] M. Gulacsi. *Adv. Phys.*, 53:769, 2004.

[137] H. Tsunetsugu. *Phys. Rev. B*, 55:3042, 1997.

[138] R.E. Brunton and D.M. Edwards. *J. Phys.: Condens. Matter*, 10:5421, 1998.

[139] G.C. Wick. *Phys. Rev.*, 80:268, 1950.

[140] Y.A. Izyumov and Y.N. Skryabin. *Statistical Mechanics of Magnetically Ordered Systems.* New York, 1988.

[141] Y.A. Izyumov. *Basic Models in the Quantum Theory of Magnetism.* AIP Conference Proceedings, Vol. 678, Melville, New York, 2003.

[142] D.I. Golosov. *Phys. Rev. Lett.*, 84:3974, 2000.

[143] N. Furukawa. *J. Phys. Soc. Jpn.*, 65:1174, 1996.

[144] Y. Motome and N. Furukawa. *Phys. Rev. B*, 71:014446, 2005.

[145] A. Auerbach. *Interacting Electrons and Quantum Magnetism.* Springer, New York, 1994.

[146] T. Hickel C. Santos and W. Nolting. *J. Magn. Magn. Mater.*, 272:e263, 2004.

[147] T. Hickel and W. Nolting. *Physica B*, 378:706, 2006.

[148] D. Meyer C. Santos and W. Nolting. *J. Phys.: Condens. Matter*, 13:2531, 2001.

[149] T. Hickel and W. Nolting. *Phys. Rev. B*, 69:085110, 2004.

[150] A.A. Rudermann and C. Kittel. *Phys. Rev.*, 96:99, 1954.

[151] C. Kittel. *Solid State Physics vol.22.* Academic, New York, 1968.

[152] D.N. Aristov. *Phys. Rev. B.*, 55:8064, 1997.

[153] Y. Yafet. *Phys. Rev. B*, 36:3948, 1987.

[154] M.T. Beal-Monod. *Phys. Rev. B*, 36:8835, 1987.

[155] G.F. Giuliani G. Vignale and T. Datta. *Phys. Rev. B*, 72:033411, 2005.

[156] G. Bergmann W. Shieh and M. Huberman. *Phys. Rev. B*, 46:8607, 1992.

[157] J.S. Helman and W. Baltensperger. *Phys. Rev. B*, 50:12682, 1994.

[158] U. Larsen. *Phys. Lett.*, 85A:471, 1981.

[159] P. Mahadevan A. Zunger and D.D. Sarma. *Phys. Rev. Lett.*, 93:177201, 2004.

[160] R. Bouzerar G. Bouzerar and T. Ziman. *Phys. Rev. B*, 73:024411, 2006.

[161] Y. Yafet. *J. Appl. Phys.*, 61:4058, 1987.

[162] Y. Yafet J. Kwo M. Hong C.F. Majkrzak and T. O'Brien. *J. Appl. Phys.*, 63:3453, 1988.

[163] C.F. Majkrzak J.W. Cable J. Kwo M. Hong D.B. McWhan Y. Yafet J.V. Waszczak and C. Vettier. *Phys. Rev. Lett.*, 56:2700, 1986.

[164] J. Kwo M. Hong F.J. di Salvo J.V. Waszczak and C.F. Majkrzak. *Phys. Rev. B*, 35:7295, 1987.

[165] N. Furukawa. *J. Phys. Soc. Jpn.*, 63:3214, 1994.

[166] N. Furukawa. *cond-mat*, page 9812066, 1998.

[167] N. Furukawa. *Physics of Manganites.* Plenum, New York, 1999.

[168] Y.A. Izyumov and Y.N. Skryabin. *Phys. Uspekhi*, 44:109, 2001.

[169] B. Michaelis and A.J. Millis. *Phys. Rev. B*, 68:115111, 2003.

[170] A. Chattopadhyay A.J. Millis and S. Das Sarma. *Phys. Rev. B*, 61:10738, 2000.

[171] E. Kogan and M. Auslender. *Phys. Rev. B*, 67:132410, 2003.

[172] S. Yunoki J. Hu A.L. Malvezzi A. Moreo N. Furukawa and E. Dagotto. *Phys. Rev. Lett.*, 80:845, 1998.

[173] E. Dagotto S. Yunoki A.L. Malvezzi A. Moreo J. Hu S. Capponi D. Poilblanc and N. Furukawa. *Phys. Rev. B*, 58:6414, 1998.

[174] K. Nagai T. Momoi and K. Kubo. *J. Phys. Soc. Jpn.*, 69:1837, 2000.

[175] A. Chattopadhyay A.J. Millis and S. Das Sarma. *Phys. Rev. B*, 64:012416, 2001.

[176] R.S. Fishman F. Popescu G. Alvarez T. Maier and J. Moreno. *Phys. Rev. B*, 73:140405(R), 2006.

[177] C. Lin S. Okamoto and A.J. Millis. *Phys. Rev. B*, 73:041104(R), 2006.

[178] A. Chattopadhyay S. Das Sarma and A.J. Millis. *Phys. Rev. Lett.*, 87:227202, 2001.

[179] E.H. Hwang and S. Das Sarma. *Phys. Rev. B*, 72:035210, 2005.

[180] F. Popescu Y. Yildirim G. Alvarez A. Moreo and E. Dagotto. *Phys. Rev. B*, 73:075206, 2006.

[181] R.S. Fishman and M. Jarrell. *Phys. Rev. B*, 67:100403(R), 2003.

[182] R.S. Fishman F. Popescu G. Alvarez J. Moreno T. Maier and M. Jarrell. *New J. Phys.*, 8:116, 2006.

[183] R.S. Fishman. *Phys. Rev. Lett.*, 97:177204, 2006.

[184] W. Nolting S. Rex and S.M. Jaya. *J. Phys.: Condens. Matter*, 9:1301, 1997.

[185] J. Kienert and W. Nolting. *Phys. Rev. B*, 75:094401, 2007.

[186] C. Santos and W. Nolting. *Phys. Rev. B*, 65:144419, 2002.

[187] V.Y. Irkhin and M.I. Katsnelson. *Phys. Uspekhi*, 37:659, 1994.

[188] J. Zang H. Röder A.R. Bishop and S.A. Trugman. *J. Phys.: Condens. Matter*, 9:L157, 1997.

[189] J. Kienert and W. Nolting. *Phys. Rev. B*, 73:224405, 2006.

[190] R. Peters and T. Pruschke. *Phys. Rev. B*, 76:245101, 2007.

[191] L. Yin. *Phys. Rev. B*, 68:104433, 2003.

[192] H. Fukuyama and H. Ehrenreich. *Phys. Rev. B*, 7:3266, 1973.

[193] J. Hubbard. *Proc. R. Soc. London*, A 281:401, 1964.

[194] A.C.M. Green and D.M. Edwards. *J. Phys.: Condens. Matter*, 11:10511, 1999.

[195] H. Aliaga B. Normand K. Hallberg M. Avignon and B. Alascio. *Phys. Rev. B*, 64:024422, 2001.

[196] H. Yi J. Yu and S.-I. Lee. *Eur. Phys. J. B*, 7:509, 1999.

[197] W. Koller A. Prüll H.G. Evertz and W. v. d. Linden. *Phys. Rev. B*, 67: 104432, 2003.

[198] J.L. Alonso J.A. Capitan L.A. Fernandez F. Guinea and V. Martin-Mayor. *Phys. Rev. B*, 64:054408, 2001.

[199] Y. Motome and N. Furukawa. *J. Phys. Soc. Jpn.*, 69:3785, 2000.

[200] Y. Motome and N. Furukawa. *Phys. Rev. B*, 68:144432, 2003.

[201] I. Peschel X. Wang M. Kaulke and K. Hallberg, editors. *Density Matrix Renormalization.* Springer, New York, 1999.

[202] D.R. Neuber M. Daghofer H.G. Evertz W. v. d. Linden and R.M. Noack. *Phys. Rev. B*, 73:014401, 2006.

[203] D.J. Garcia K. Hallberg C.D. Batista S. Capponi D. Poilblanc M. Avignon and B. Alascio. *Phys. Rev. B.*, 65:134444, 2002.

[204] D.J. Garcia K. Hallberg B. Alascio and M. Avignon. *Phys. Rev. Lett.*, 93: 177204, 2004.

[205] J. Kienert and W. Nolting. *J. Magn. Magn. Mater.*, 272-276:e887–e888, 2004.

[206] W. Nolting and M. Matlak. *phys. stat. sol. (b)*, 123:155, 1984.

[207] D. Meyer. *Electron correlation effects in ferromagnetic local-moment and intermediate-valence systems.* PhD thesis, Humboldt Universität zu Berlin, 2001. Berichte aus der Physik, Shaker Verlag, Aachen 2001.

[208] B.S. Shastry and D.C. Mattis. *Phys. Rev. B*, 24:5340, 1981.

[209] W. Nolting S.M. Jaya and S. Rex. *Phys. Rev. B*, 54:14455, 1996.

[210] W. Nolting. *phys. stat. sol. (b)*, 96:11, 1979.

[211] M. Potthoff. *Correlated Electrons at Metal Surfaces.* Habilitation Thesis, Humboldt-Universität zu Berlin, 2000.

[212] R. Schiller W. Müller and W. Nolting. *J. Mag. Mag. Mater.*, 169:39–55, 1997.

[213] G.D. Mahan. *Many-Particle Physics.* Plenum Press, New York, 1990.

[214] W. Nolting. *Quantentheorie des Magnetismus, Band 1.* Teubner, Stuttgart, 1986.

[215] E.C. Stoner. *Proc. R. Soc. London*, A 154:656, 1936.

[216] R. Schiller and W. Nolting. *Phys. Rev. B*, 60:462, 1999.

[217] R. Schiller. *Correlation Effects and Temperature Dependencies in Thin Ferromagnetic Films: Magnetism and Electronic Structure.* PhD thesis, Humboldt Universität zu Berlin, 2000.

[218] F. Bloch. *Z. Phys.*, 61:206, 1930.

[219] X. Wang. *Phys. Rev. B*, 57:7427, 1998.

[220] N. Bloembergen and T.J. Rowland. *Phys. Rev.*, 97:1679, 1955.

[221] P.G. de Gennes. *Phys. Rev.*, 118:141, 1960.

[222] K. Kubo and N. Ohata. *J. Phys. Soc. Jpn.*, 33:21, 1972.

[223] Jürgen König John Schliemann T. Jungwirth and A.H. MacDonald. *Electronic Structure and Magnetism of Complex Materials.* Springer, Berlin, 2003. cond-mat/0111314.

[224] A. Singh S.K. Das A. Sharma and W. Nolting. *J. Phys.: Condens. Matter*, 19:236213, 2007.

[225] E.L. Nagaev. *Phys. Rev. B*, 58:827, 1998.

[226] W. Haubenreisser W. Brodkorb A. Corciovei and G. Costache. *phys. stat. sol. (b)*, 53:9, 1972.

[227] T. Hickel. *Theory of many-body effects in the Kondo-lattice model: Projection-operator method.* PhD thesis, Humboldt Universität zu Berlin, 2005.

[228] G. Bouzerar J. Kudrnovsky and P. Bruno. *Phys. Rev. B*, 68:205311, 2003.

[229] M.L. Neel. *J. Phys. Radium*, 15:225, 1954.

[230] P. Bruno. *Magnetismus von Festkörpern und Grenzflächen.* Forschungszentrum Jülich, Jülich, 1993.

[231] O. Hjortstam K. Baberschke J.M. Wills B. Johansson and O. Eriksson. *Phys. Rev. B*, 55:15026, 1997.

[232] T. Herrmann M. Potthoff and W. Nolting. *Phys. Rev. B*, 58:831, 1998.

[233] F. Körmann S. Schwieger J. Kienert and W. Nolting. *Eur. Phys. J. B*, 53: 463, 2006.

[234] S. Schwieger J. Kienert and W. Nolting. *Phys. Rev. B*, 71:024428, 2005.

[235] J. Lindner. *Ferromagnetische Resonanz an ultradünnen magnetischen Einfach- und Mehrfachlagen der 3d-Übergangsmetalle - Statik und Dynamik.* PhD thesis, Freie Universität Berlin, 2002.

[236] F.B. Anderson and H.B. Callen. *Phys. Rev.*, 136:A1068–A1087, 1964.

[237] S.V. Tyablikov. *Quantentheoretische Methoden des Magnetismus.* Teubner, Stuttgart, 1969.

[238] R.A. Tahir-Kheli and D. ter Haar. *Phys. Rev.*, 127:88–94, 1962.

[239] H.B. Callen. *Phys. Rev.*, 130:890–898, 1963.

[240] C. Zener. *Phys. Rev.*, 96:1335, 1954.

[241] S. Schwieger J. Kienert and W. Nolting. *Phys. Rev. B*, 71:174441, 2005.

[242] F. Körmann. *Spinreorientierungsübergänge in magnetischen Multilagen.* Diploma Thesis, Humboldt-Universität zu Berlin, 2007.

[243] M.G. Pini P. Politi and R.L. Stamps. *Phys. Rev. B*, 72:014454, 2005.

[244] S. Henning F. Körmann J. Kienert W. Nolting and S. Schwieger. *Phys. Rev. B*, 75:214401, 2007.

[245] P. Henelius P. Fröbrich P.J. Kuntz C. Timm and P.J. Jensen. *Phys. Rev. B*, 66:094407, 2002.

[246] R.P. Erickson and D.L. Mills. *Phys. Rev. B*, 43:11527, 1991.

[247] M. Bander and D.L. Mills. *Phys. Rev. B*, 38:12015, 1988.

[248] T.G. Perring D.T. Adroja G. Chaboussant G. Aeppli T. Kimura and Y. Tokura. *Phys. Rev. Lett.*, 87:217201, 2001.

[249] O. Eriksson R. Ahuja A. Ormeci J. Trygg O. Hjortstam P. Soederlind B. Johansson and J.M. Wills. *Phys. Rev. B*, 52:4420, 1995.

[250] D.M. Bylander and L. Kleinman. *Phys. Rev. B*, 50:4996, 1994.

[251] J. Quinn Y.S. Li F. Jona and D. Fort. *Phys. Rev. B*, 46:9694, 1992.

[252] D.A. Papaconstantopoulos. *Handbook of the Bandstructure of Elemental Solids*. Plenum Press, New York, 1986.

[253] N. Goldenfeld. *Lectures on Phase Transitions and the Renormalization Group*. Addison-Wesley, 1992.

[254] R. Pfandzelter and M. Potthoff. *Phys. Rev. B*, 64:140405, 2001.

[255] M.B. Salamon S. Sinha J.J. Rhyne J.E. Cunningham R.W. Erwin J. Borchers and C.P. Flynn. *Phys. Rev. Lett.*, 56:259, 1986.

[256] S.S.P. Parkin N. More and K.P. Roche. *Phys. Rev. Lett.*, 64:2304, 1990.

[257] S.S.P. Parkin. *Phys. Rev. Lett.*, 67:3598, 1991.

[258] C.F. Majkrzak J. Kwo M. Hong Y. Yafet D. Gibbs C.L. Chien and J. Bohr. *Adv. Phys.*, 40:99, 1991.

[259] Y. Yafet. *Magnetic Multilayers*. World Scientific, Singapore, 1994.

[260] J.J. Rhyne and R.W. Erwin. *Magnetic Materials vol.8*. North-Holland, Amsterdam, 1995.

[261] P. Bruno and C. Chappert. *Phys. Rev. Lett.*, 67:1602 and 2592, 1991.

[262] P. Bruno and C. Chappert. *Phys. Rev. B*, 46:261, 1992.

[263] L.M. Roth H.J. Zeiger and T.A. Kaplan. *Phys. Rev.*, 149:519, 1966.

[264] P. Bruno. *J. Magn. Magn. Mater.*, 121:248, 1993.

[265] P. Bruno. *Phys. Rev. B*, 52:411, 1995.

[266] P. Bruno. *J. Phys.: Condens. Matter*, 11:9403–9419, 1999.

[267] M.D. Stiles. *Phys. Rev. B*, 48:7238, 1993.

[268] M.D. Stiles. *Ultrathin Magnetic Structures III - Fundamentals of Nanomagnetism*. Springer, Berlin Heidelberg, 2005.

[269] M.D. Stiles. *Nanomagnetism*. Elsevier, 2006.

[270] D.M. Edwards J. Mathon R.B. Muniz and M.S. Phan. *Phys. Rev. Lett.*, 67: 493, 1991.

[271] D.M. Edwards J. Mathon R.B. Muniz and M.S. Phan. *J. Phys.: Condens. Matter*, 3:4941, 1991.

[272] J. Mathon M. Villeret and D.M. Edwards. *J. Phys.: Condens. Matter*, 4: 9873, 1992.

[273] J. d'Albuquerque e Castro M.S. Ferreira and R.B. Muniz. *Phys. Rev. B*, 49: 16062, 1994.

[274] J. Mathon M. Villeret A. Umerski R.B. Muniz J. d'Albuquerque e Castro and D.M. Edwards. *Phys. Rev. B*, 56:11797, 1997.

[275] M.S. Ferreira R.B. Muniz J. d'Albuquerque e Castro and D.M. Edwards. *J. Phys.: Condens. Matter*, 6:L619, 1994.

[276] M.S. Ferreira J. d'Albuquerque e Castro D.M. Edwards and J. Mathon. *J. Phys.: Condens. Matter*, 8:11259, 1996.

[277] P. Bruno. *Phys. Rev. Lett.*, 72:3627, 1994.

[278] V. Drchal J. Kudrnovsky P. Bruno I. Turek P.H. Dederichs and P. Weinberger. *Phys. Rev. B*, 60:9588, 1999.

[279] B.C. Lee and Y.-C. Chang. *Phys. Rev. B*, 62:3888, 2000.

[280] T. Ohsawa S. Kubota H. Itoh and J. Inoue. *Phys. Rev. B*, 71:212407, 2005.

[281] J. Lindner and K. Baberschke. *J. Phys.: Condens. Matter*, 15:R193 and S465, 2003.

[282] S. Schwieger and W. Nolting. *Phys. Rev. B*, 69:224413, 2004.

[283] F. Herman J. Sticht and M. van Schilfgaarde. *J. Appl. Phys.*, 69:4783, 1991.

[284] K. Ounadjela C.B. Sommers A. Fert D. Stoeffler F. Gautier and V.L. Moruzzi. *Europhys. Lett.*, 15:875, 1991.

[285] D. Stoeffler and F. Gautier. *Phys. Rev. B*, 44:10389, 1991.

[286] H. Hasegawa. *Phys. Rev. B*, 42:2368, 1990.

[287] H. Hasegawa. *Phys. Rev. B*, 43:10803, 1991.

[288] J. Lindner C. Rüdt E. Kosubek P. Poulopoulos K. Baberschke P. Blomquist R. Wäppling and D.L. Mills. *Phys. Rev. Lett.*, 88:167206, 2002.

[289] M. Weinert R.E. Watson and J.W. Davenport. *Phys. Rev. B*, 32:2115, 1985.

[290] P.J.H. Bloemen M.T. Johnson M.T.H. van de Vorst R. Coehoorn J.J. de Vries R. Jungblut J. aan de Stegge A. Reinders and W.J.M. de Jonge. *Phys. Rev. Lett.*, 72:764, 1994.

[291] C.H. Back W. Weber A. Bischof D. Pescia and R. Allenspach. *Phys. Rev. B*, 52:R13114, 1995.

[292] L. Nordström P. Lang R. Zeller and P. Dederichs. *Phys. Rev. B*, 50:13058, 1994.

[293] P. Lang L. Nordström K. Wildberger R. Zeller, P. Dederichs, and T. Hoshino. *Phys. Rev. B*, 53:9092, 1996.

[294] B. Lee and Y.-C. Chang. *Phys. Rev. B*, 54:13034, 1996.

[295] V. Drchal J. Kudrnovsky I. Turek and P. Weinberger. *Phys. Rev. B*, 53: 15036, 1996.

[296] W.C. Koehler H.R. Child R.M. Nicklow H.G. Smith R.M. Moon and J.W. Cable. *Phys. Rev. Lett.*, 24:16, 1970.

[297] W.E. Evenson and S.H. Liu. *Phys. Rev. Lett.*, 21:432, 1968.

[298] S.H. Liu R.P. Gupta and S.K. Sinha. *Phys. Rev.*, B4:1100, 1971.

[299] M. Wietstruk. *Temperatur- und Schichtdickeneffekte auf magnetische Kopplung in Tb/Y/Gd-Trilagen*. Diploma Thesis, Freie Universität Berlin, 2006.

[300] K.M. Doebrich M. Wietstruk J.E. Prieto F. Heigl O. Krupin K. Starke and G. Kaindl. *cond-mat*, page arXiv:0712.3122v1, 2007.

[301] J. Bünemann and F. Gebhard. *J. Phys.: Condens. Matter*, 13:9985, 2001.

[302] M. Pajda J. Kudrnovsky I. Turek V. Drchal and P. Bruno. *Phys. Rev. B*, 64:174402, 2001.

[303] B.A. Jones and C.B. Hanna. *Phys. Rev. Lett.*, 71:4253, 1993.

[304] M.C. Munoz and J.L. Perez-Diaz. *Phys. Rev. Lett.*, 72:2482, 1994.

[305] P. Bruno M.D. Stiles and Y. Yafet. *Phys. Rev. Lett.*, 74:3087, 1995.

[306] C. Chappert and J.P. Renard. *Eur. Phys. Lett.*, 15:553, 1991.

[307] Y. Huang and W.F. McColl. *J. Phys. A: Math. Gen.*, 30:7919, 1997.

Danksagung

Ich danke allen, die zur Fertigstellung dieser Arbeit beigetragen haben.

Vor allem danke ich Prof. Nolting für die umfassende Betreuung, seinen fachlichen Rat und seine Unterstützung bei der Entstehung der Arbeit. Ich habe die angenehme Atmosphäre an seinem Lehrstuhl stets geschätzt.

Frau Götsch danke ich für ihre große Hilfsbereitschaft und gute Laune.

Allen aktuellen und ehemaligen Mitgliedern der Arbeitsgruppe Festkörpertheorie sei für die vielen fachlichen und auch nicht-fachlichen Gespräche, Anregungen und die sonstige Hilfe im Laufe der letzten Jahre gedankt.

Vor allem Stephan Schwieger sowie Sören Henning und Fritz Körmann danke ich für die schöne Zusammenarbeit. Außerdem bedanke ich mich bei Vadym Bryksa, Tilmann Hickel, Dietrich Meyer, Wolf Müller, Niko Sandschneider, Carlos Santos, Anand Sharma, Peter Sinjukow und Martin Stier.

Für anregende Diskussionen zum Kondo-Gitter-Modell bin ich Dr. Guixin Tang und Prof. Avinash Singh zu Dank verpflichtet.

Prof. Baberschke und Kilian Lenz sei für die interessanten Diskussionen rund um dünne Filme und die Interlagenkopplung gedankt.

Die Arbeit am Rechner wurde durch die wertvolle und unermüdliche Hilfe von Sören Henning, Wolf Müller, Tilmann Hickel und Carlos Santos immens erleichtert. Special thanks to them.

Ein herzliches Dankeschön auch an Prof. Keiper sowie Dr. Suisky.

Bei den Studenten der von mir betreuten Übungsgruppen bedanke ich mich für ihren großen Wissensdurst, ihre Begeisterung und die fiesen Fragen.

Der Friedrich-Naumann-Stiftung danke ich für die finanzielle Förderung und die Möglichkeit gewinnbringender Blicke über den Tellerrand. Ich bedanke mich bei Dr. Röseler für seine Hilfsbereitschaft.

Thanks a lot Sören, Isa and Daddy for the korrekturreading.

Last but not least ein liebes Dankeschön an meine Familie und an Isabelle für die tolle Unterstützung.

List of Publications

J. A. Freund, J. Kienert, L. Schimansky-Geier, B. Beisner, A. Neiman, D. Russel, T. Yakusheva, and F. Moss*, Behavioral Stochastic Resonance: How a noisy army betrays its outpost,* Phys. Rev. E 63, 031910 (2001)

J. Kienert, C. Santos, and W. Nolting, *The correlated Kondo-lattice model*
phys. stat. sol. (b) 236, 515 (2003)

W. Nolting, G. G. Reddy, A. Ramakanth, D. Meyer, and J. Kienert*, Self-energy approach to the correlated Kondo lattice model,* Phys. Rev. B 67, 024426 (2003)

J. Kienert and W. Nolting*, Magnetism of finite-n Kondo-lattice films*
J. Mag. Mag. Mater. 272, 2 (2004)

S. Schwieger, J. Kienert, and W. Nolting*, Theory of field-induced spin reorientation transition in thin Heisenberg films*, Phys. Rev. B 71, 024428 (2005)

S. Schwieger, J. Kienert, and W. Nolting*, Temperature dependence of interlayer exchange coupling: Spin waves versus spacer effects*, Phys. Rev. B 71, 174441 (2005)

J. Kienert and W. Nolting*, Magnetic phase diagram of the Kondo lattice model with quantum localized spins,* Phys. Rev. B 73, 224405 (2006)

F. Körmann, S. Schwieger, J. Kienert, and W. Nolting*, A new type of temperature-driven reorientation transition in magnetic thin films*
Eur. Phys. J. B 53, 463 (2006)

J. Kienert, S. Schwieger, K. Lenz, J. Lindner, K. Baberschke, and W. Nolting
Mechanism of temperature dependence of the magnetic anisotropy energy in ultrathin Cobalt and Nickel films, J. Mag. Mag. Mater. 316, e86 (2007)

S. Schwieger, J. Kienert, K. Lenz, J. Lindner, K. Baberschke, and W. Nolting
Spin wave excitations: The main source of the temperature dependence of interlayer exchange coupling in nanostructures
Phys. Rev. Lett. 98, 057205 (2007)

J. Kienert and W. Nolting*, Curie temperature of Kondo lattice films with finite itinerant charge carrier density*, Phys. Rev. B 75, 094401 (2007)

S. Schwieger, J. Kienert, K. Lenz, J. Lindner, K. Baberschke, and W. Nolting
Temperature dependence of interlayer exchange coupling,
J. Mag. Mag. Mater. 310, 2301 (2007)

S. Henning, F. Körmann, J. Kienert, S. Schwieger, and W. Nolting*, Green function theory versus Quantum Monte Carlo calculations for thin magnetic films*, Phys. Rev. B 75, 214401 (2007)

Selbständigkeitserklärung

Hiermit erkläre ich, dass ich die vorliegende Arbeit selbständig und ohne unerlaubte Hilfe angefertigt habe. Die benutzten Hilfsmittel habe ich vollständig angegeben.

Berlin, 28. März 2008